

2009

Mechanistic foam modeling and simulations: gas injection during surfactant-alternating-gas processes using foam-catastrophe theory

Ali Afsharpoor

Louisiana State University and Agricultural and Mechanical College, aafsha1@tigers.lsu.edu

Follow this and additional works at: https://digitalcommons.lsu.edu/gradschool_theses



Part of the [Petroleum Engineering Commons](#)

Recommended Citation

Afsharpoor, Ali, "Mechanistic foam modeling and simulations: gas injection during surfactant-alternating-gas processes using foam-catastrophe theory" (2009). *LSU Master's Theses*. 2129.

https://digitalcommons.lsu.edu/gradschool_theses/2129

This Thesis is brought to you for free and open access by the Graduate School at LSU Digital Commons. It has been accepted for inclusion in LSU Master's Theses by an authorized graduate school editor of LSU Digital Commons. For more information, please contact gradetd@lsu.edu.

**MECHANISTIC FOAM MODELING AND
SIMULATIONS: GAS INJECTION DURING
SURFACTANT-ALTERNATING-GAS PROCESSES
USING FOAM-CATASTROPHE THEORY**

A Thesis

Submitted to Graduate Faculty of the
Louisiana State University and
Agricultural and Mechanical College
in partial fulfillment of the
requirements for the degree of
Master of Science in Petroleum Engineering
in
The Department of Petroleum Engineering

by

Ali Afsharpoor
B.S., Petroleum University of Technology, Iran, 2006
August, 2009

ACKNOWLEDGEMENTS

Completing this study has definitely been a challenge and could not have been accomplished without an assistance and support of many individuals. I would like to thank the Craft and Hawkins Department of Petroleum Engineering at Louisiana State University (LSU) and the Louisiana Oil Spill Research and Development Program for the financial support to conduct this research. I would like to express my greatest appreciation to my major advisor Dr. Seung Ihl Kam for his guidance, kindness, patience, and encouragement. Besides the research, I learned a lot from him, he has served as a role model to me demonstrating that my goals were achievable.

Additional gratitude is also extended to all professors in petroleum Engineering department, especially my examination committee members, Dr. Christopher D. White, and Dr. Mayank Tyagi.

I am very grateful to all petroleum engineering department staffs, and all my friends who make the friendly environment for me; especially Mr. Fenelon Nunes for his support and presence at the department.

I would like to thank Petroleum University of Technology in Iran which helps me to get academic knowledge to follow my higher education.

This work is dedicated to my parents, Hassan and Maliheh, and my dear brother, Keivan.

TABLE OF CONTENTS

ACKNOWLEDGEMENTS	ii
LIST OF TABLES	vi
LIST OF FIGURES	vii
ABSTRACT.....	xii
1. INTRODUCTION.....	1
1.1. Objectives of This Study	3
1.2. Chapter Description.....	4
2. LITERATURE REVIEW	5
2.1. Foam Fundamentals	5
2.1.1 Foams in Porous Media	5
2.1.2. Weak Foam vs. Strong Foam	5
2.1.3. Lamella Creation and Coalescence in Porous Media	6
2.1.3.1. Lamella Creation Mechanisms	6
2.1.3.2. Lamella Coalescence Mechanisms	6
2.1.4. Gas-Mobility Reduction and Bubble Trapping	9
2.2. Recent Developments.....	9
2.2.1. Two Steady-State Strong-Foam Regimes.....	9
2.2.2. Foam Catastrophe Theory	14
2.2.3. Co-injection vs. Surfactant-Alternating-Gas (SAG)	15
2.2.4. Population-Balance Modeling and Simulation.....	18
3. METHODOLOGY	22
4. RESULTS AND DISCUSSIONS.....	30
4.1. Model Fit and Parameter Determination	30
4.2. Dynamic Foam Simulations at Very Low or High Injection Velocities	33
4.3. Modification of Pressure Profile at the Leading Edge of a Strong-Foam Front	42
4.4. Behaviors at Intermediate Injection Velocities	48
4.5. Determination of Model Parameters	57
4.6. Inlet Effect and System Length in Foam Displacement.....	69

5. CONCLUSIONS AND RECOMMENDATIONS	74
5.1. Conclusions	74
5.2. Recommendations	76
REFERENCES.....	78
APPENDIX A.DETERMINATION OF STEADY-STATE FOAM PARAMETERS	82
A.1. Fit to an S-shaped Curve	82
A.2. Fit to Two Strong-Foam Flow Regimes (High-Quality and Low-Quality Regimes)	85
A.3. Construction of Mechanistic Foam Fractional Flow Curves.....	88
APPENDIX B.NEW FOAM SIMULATION ALGORITHM USING MATRIX SOLVER	89
B.1. Discretization of Material Balance Equation.....	90
B.1.1. Liquid Phase	90
B.1.2. Gas Phase	91
B.2. Construction of Jacobian Matrix	93
B.3. Discretization of Boundary Conditions	97
B.3.1. Fixed-pressure Boundary Condition at the Outlet	97
B.3.2. Fixed-Pressure Boundary Condition at the Inlet.....	100
B.3.3. Fixed-Rate Boundary Condition at the Inlet.....	101
B.3.4. Bubble Population Balance Calculations.....	102
B.4. Flow Chart	103
B.5. Two-Dimensional Simulation.....	105
B.5.1. Discretization of Material Balance Equation	105
B.5.1.1. Liquid Phase.....	106
B.5.1.2. Gas Phase	111
B.5.2. Construction of Jacobian Matrix.....	116
B.5.2.1. Water Phase.....	116
B.5.2.2. Gas Phase	119
B.5.3. Boundary Conditions	124
B.5.3.1. Outlet Boundary Condition- Fixed pressure	124
B.5.3.2. Inlet Boundary Condition.....	128
B.5.3.2.1. Fixed Injection Velocity	128
B.5.3.2.2. Fixed Injection Pressure	130
B.5.3.3. No flow Boundary Condition at the Reservoir Top.....	130
B.5.3.4. No flow Boundary Condition at the Reservoir Bottom.....	137

APPENDIX C.NEW FOAM SIMULATION ALGORITHM RESULTS.....	143
VITA.....	153

LIST OF TABLES

Table 4-1 Base-case (Case 1) model parameters and properties	32
Table 4-2 Foam parameters for Case 2 and Case 3	68

LIST OF FIGURES

Figure 2.1 Schematic of foam flow in porous media (re-drawn from Dholkawala (2006)): (a) conventional gas/liquid two-phase flow (no foam) (b) weak foam (c) strong foam	8
Figure 2.2 Lamella creation mechanisms: Leave-behind (Dholkawala, 2006)	10
Figure 2.3 Lamella creation mechanisms: Snap-off (Dholkawala, 2006)	11
Figure 2.4 Lamella creation mechanisms: Mobilization and division (Dholkawala, 2006)	12
Figure 2.5 The disjoining pressure as a function of film thickness showing the presence of the limiting capillary pressure (P_c^*) (re-drawn from Aronson et al., 1994).....	13
Figure 2.6 Two strong-foam flow regimes observed by Kam et al. (2007): the contour shows the steady-state pressure gradient in psi/ft (1 psi/ft = 22,626 Pa/m)	16
Figure 2.7 Foam catastrophe surface showing three different states (weak-foam, strong-foam, intermediate states) from Gauglitz et al. (2002)	17
Figure 2.8 A schematic showing two possible solution paths for strong foams and weak foams from Rossen and Bruining (2007).....	19
Figure 2.9 an example mechanistic foam fractional flow curve from Dholkawala et al. (2007) .	20
Figure 3.1 Graphical representation of lamella creation function used in this study: (a) the rate of lamella creation (Kam, 2008) and (b) the rate of lamella creation as a function of ∇P at different values of parameter ∇P_0	25
Figure 3.2 Graphical representation of lamella coalescence function used in this study: the rate of lamella coalescence.....	26
Figure 4.1 (a) Fit to experimental data using base-case parameters in Table 1: (a) fit to S-shaped curve and (b) fit to two flow regimes (cf. Fig. 1(b)) – the procedures and plots are essentially the same as those in Kam et al. (2007), and the contour lines represent the steady-state pressure gradient in psi/ft (1 psi/ft = 22,626 Pa/m)	31
Figure 4.2 Mechanistic foam fractional flow curve at $u_t = u_g = 2.8 \times 10^{-5}$ m/s: (a) entire graph and (b) magnified view near the shock front.....	34
Figure 4.3 Results from dynamic simulation (solid line) and fractional flow analysis (dashed line) of gas injection at $u_t = u_g = 2.8 \times 10^{-5}$ m/s: (a) saturation profile and (b) foam texture profile (n_f in m^{-3}).....	35
Figure 4.4 Mechanistic foam fractional flow curve at $u_t = u_g = 1.2 \times 10^{-4}$ m/s: (a) entire graph and (b) magnified view near the shock front.....	37

Figure 4.5 Results from dynamic simulation (solid line) and fractional flow analysis (dashed line) of gas injection at $u_t = u_g = 1.2 \times 10^{-4}$ m/s: (a) saturation profile and (b) foam texture profile (n_f in m^{-3}).....	39
Figure 4.6 Pressure profiles from dynamic simulations (solid line) and fractional flow analysis (dashed line) during gas injection: (a) $u_t = u_g = 2.8 \times 10^{-5}$ m/s and (b) $u_t = u_g = 1.2 \times 10^{-4}$ m/s (1 psi = 6,900 Pa).....	41
Figure 4.7 Results from dynamic foam simulations at $u_t = u_g = 1.2 \times 10^{-4}$ m/s with 50 grid blocks in contrast to the results with 25 grid blocks in Figs. 8(a), 8(b) and 9(b) : (a) water saturation, (b) foam texture (n_f in m^{-3}), and (c) pressure profile (1 psi = 6,900 Pa)...	44
Figure 4.8 Schematic figures to demonstrate the need for pressure modification: (a) effect of grid block size, (b) limitation of discretized system, and (c) modification of pressure response.....	45
Figure 4.9 Simulation results with pressure modification at $u_t = u_g = 1.2 \times 10^{-4}$ m/s: (a) pressure profiles before and after modification, (b) magnified view at the strong-foam front, and (c) inlet injection pressure histories before and after modification (1 psi = 6,900 Pa).....	49
Figure 4.10 Mechanistic fractional flow curves leading to weak-foam propagation in simulation: (a) $u_g = 3.3 \times 10^{-5}$ m/s, (b) $u_g = 4.0 \times 10^{-5}$ m/s, and (c) $u_g = 4.2 \times 10^{-5}$ m/s.....	51
Figure 4.11 Water saturation profile from mechanistic simulations (solid line) and fractional flow analysis (dashed line): (a) $u_g = 3.3 \times 10^{-5}$ m/s, (b) $u_g = 4.0 \times 10^{-5}$ m/s, and (c) $u_g = 4.2 \times 10^{-5}$ m/s	52
Figure 4.12 Foam texture profile from mechanistic simulations (solid line) and fractional flow analysis (dashed line): (a) $u_g = 3.3 \times 10^{-5}$ m/s, (b) $u_g = 4.0 \times 10^{-5}$ m/s, and (c) $u_g = 4.2 \times 10^{-5}$ m/s (n_f in m^{-3})	54
Figure 4.13 Pressure profile from mechanistic simulations (solid line) and fractional flow analysis (dashed line): (a) $u_g = 3.3 \times 10^{-5}$ m/s, (b) $u_g = 4.0 \times 10^{-5}$ m/s, and (c) $u_g = 4.2 \times 10^{-5}$ m/s (1 psi = 6,900 Pa).....	55
Figure 4.14 Schematic figures showing fractional flow analysis during weak-foam propagation.	56
Figure 4.15 Mechanistic fractional flow curves leading to strong-foam propagation in simulation: (a) $u_g = 5.3 \times 10^{-5}$ m/s, (b) $u_g = 7.0 \times 10^{-5}$ m/s, and (c) $u_g = 1.0 \times 10^{-4}$ m/s.....	58
Figure 4.16 Water saturation profile from mechanistic simulations (solid line) and fractional flow analysis (dashed line): (a) $u_g = 5.3 \times 10^{-5}$ m/s, (b) $u_g = 7.0 \times 10^{-5}$ m/s, and (c) $u_g = 1.0 \times 10^{-4}$ m/s	59

Figure 4.17 Foam texture profile from mechanistic simulations (solid line) and fractional flow analysis (dashed line): (a) $u_g = 5.3 \times 10^{-5}$ m/s, (b) $u_g = 7.0 \times 10^{-5}$ m/s, and (c) $u_g = 1.0 \times 10^{-4}$ m/s (n_f in m^{-3})	60
Figure 4.18 Schematic figures showing fractional flow analysis during weak-foam propagation.	62
Figure 4.19 Pressure profile before pressure modification from mechanistic simulations (solid line) and fractional flow analysis (dashed line): (a) $u_g = 5.3 \times 10^{-5}$ m/s, (b) $u_g = 7.0 \times 10^{-5}$ m/s, and (c) $u_g = 1.0 \times 10^{-4}$ m/s (1 psi = 6,900 Pa).....	63
Figure 4.20 Pressure profile after pressure modification from mechanistic simulations (solid line) and fractional flow analysis (dashed line): (a) $u_g = 5.3 \times 10^{-5}$ m/s, (b) $u_g = 7.0 \times 10^{-5}$ m/s, and (c) $u_g = 1.0 \times 10^{-4}$ m/s (1 psi = 6,900 Pa).....	64
Figure 4.21 Two other sets of foam modeling parameters that fit the experimental data equally well (1 psi/ft = 22,626 Pa/m): (a) Case 2 (low ∇P_o and n values) and (b) Case 3 (high ∇P_o and n values)	65
Figure 4.22 Mechanistic foam fractional flow curves with $u_g = 4.2 \times 10^{-5}$ m/s at three different sets of foam model parameters: (a) Case 1, (b) Case 2 (low ∇P_o and n values), and (c) Case 3 (high ∇P_o and n values)	66
Figure 4.23 Water saturation profile with $u_g = 4.2 \times 10^{-5}$ m/s at three different sets of foam model parameters: (a) Case 1, (b) Case 2 (low ∇P_o and n values), and (c) Case 3 (high ∇P_o and n values).	67
Figure 4.24 A schematic of three foam states with the onset of foam generation	70
Figure 4.25 Water saturation profile with $u_g = 7.0 \times 10^{-5}$ m/s at different C_c values (base case, $C_c = 1$): (a) $C_c = 0.1$ and (b) $C_c = 0.01$	72
Figure 4.26 Water saturation profile with $u_g = 7.0 \times 10^{-5}$ m/s at different system lengths: (a) 10 times shorter and (b) 100 times shorter than the base case	73
Figure A.1 Fit to experimental data: fit to S-shaped curve (Kam et al., 2007); 1 psi/ft = 22626 pa/m.....	84
Figure A.2 Fit to experimental data: fit to two flow regimes (Kam et al., 2007) : the contour shows the steady-state pressure gradient in psi/ft (1 psi/ft = 22,626 Pa/m).....	87
Figure B.1 Representation of grid blocks used in the simulation	90
Figure B.2 Formulation of Jacobian, solution, and residual matrices. The term “w” and “nw” represents the equations and terms belongs to wetting (water) and non-wetting (gas),	

respectively. And p_{w1} , S_{w1} at the top of Jacobian matrix represents the derivative of the equations respect to water pressure and water saturation for grid number one 97

Figure B.3 Representation of the first and last grid blocks..... 98

Figure B.4 Flow chart of the new algorithm..... 104

Figure B.5 Schematic figure representing 5×5 grid system in a two-dimensional system..... 107

Figure B.6 A grid block of interest (X or (i,j)) with adjacent grid blocks 108

Figure B.7 A formulation of the Jacobian matrix at grid (i,j) or X. (the first row is the derivative terms related to water phase, and second row is for gas phase.) 120

Figure B.8 Representation of solution scheme using the Jacobian matrix. ΔP terms represent the pressure difference (ΔP_{2X-1}) in consecutive iteration (and saturation difference (ΔP_{2X}) in consecutive iteration)..... 121

Figure B.9 Representation of solution scheme using the Jacobian matrix for a grid block at the inlet. 131

Figure C.1 Results from dynamic simulation and fractional flow analysis of gas injection at $u_t = u_g = 2.8 \times 10^{-5}$ m/s: (a) saturation profile and (b) foam texture profile (from new simulation algorithm (Appendix B) in comparison with Fig. 4.3) 144

Figure C.2 Results from dynamic simulation and fractional flow analysis of gas injection at $u_t = u_g = 12 \times 10^{-5}$ m/s: (a) saturation profile and (b) foam texture profile (from new simulation algorithm (Appendix B) in comparison with Fig. 4.5) 145

Figure C.3 Pressure profiles from dynamic simulations and fractional flow analysis during gas injection: (a) $u_t = u_g = 2.8 \times 10^{-5}$ m/s and (b) $u_t = u_g = 12 \times 10^{-5}$ m/s (from new simulation algorithm (Appendix B) in comparison with Fig. 4.6) 146

Figure C.4 Water saturation profile from mechanistic simulations: (a) $u_g = 3.3 \times 10^{-5}$ m/s, (b) $u_g = 4.0 \times 10^{-5}$ m/s, and (c) $u_g = 4.2 \times 10^{-5}$ m/s (from new simulation algorithm (Appendix B) in comparison with Fig. 4.11)..... 147

Figure C.5 Foam texture profile from mechanistic simulations: (a) $u_g = 3.3 \times 10^{-5}$ m/s, (b) $u_g = 4.0 \times 10^{-5}$ m/s, and (c) $u_g = 4.2 \times 10^{-5}$ m/s (from new simulation algorithm (Appendix B) in comparison with Fig. 4.12)..... 148

Figure C.6 Pressure profile from mechanistic simulations: (a) $u_g = 3.3 \times 10^{-5}$ m/s, (b) $u_g = 4.0 \times 10^{-5}$ m/s, and (c) $u_g = 4.2 \times 10^{-5}$ m/s (from new simulation algorithm (Appendix B) in comparison with Fig. 4.13)..... 149

Figure C.7 Water saturation profile from mechanistic simulations: (a) $u_g = 5.3 \times 10^{-5}$ m/s, (b) $u_g = 7.0 \times 10^{-5}$ m/s, and (c) $u_g = 10.0 \times 10^{-5}$ m/s (from new simulation algorithm (Appendix B) in comparison with Fig. 4.16)..... 150

Figure C.8 Foam texture profile from mechanistic simulations: (a) $u_g = 5.3 \times 10^{-5}$ m/s, (b) $u_g = 7.0 \times 10^{-5}$ m/s, and (c) $u_g = 10.0 \times 10^{-5}$ m/s (from new simulation algorithm (Appendix B) in comparison with Fig. 4.17)..... 151

Figure C.9 Pressure profile without pressure modification from mechanistic simulations: (a) $u_g = 5.3 \times 10^{-5}$ m/s, (b) $u_g = 7.0 \times 10^{-5}$ m/s, and (c) $u_g = 10.0 \times 10^{-5}$ m/s (from new simulation algorithm (Appendix B) in comparison with Fig. 4.19)..... 152

ABSTRACT

The use of foam for mobility control is a promising means to improve sweep efficiency in subsurface applications such as improved/enhanced oil recovery and aquifer remediation. Foam can be introduced into geological formations by injecting gas and surfactant solutions simultaneously or alternatively. Alternating gas and surfactant solutions, which is often referred to as surfactant-alternating-gas (SAG) process, is known to effectively create fine-textured strong foams due to fluctuation in capillary pressure. Recent studies show that foam rheology in porous media can be characterized by foam-catastrophe theory which exhibits three foam states (weak-foam, strong-foam, and intermediate states) and two strong-foam regimes (high-quality and low-quality regimes).

Using both mechanistic foam simulation technique and fractional flow analysis which are consistent with foam catastrophe theory, this study aims to understand the fundamentals of dynamic foam displacement during gas injection in SAG processes. The results revealed some important findings: (1) The complicated mechanistic foam fractional flow curves (f_w vs. S_w) with both positive and negative slopes require a novel approach to solve the problem analytically rather than the typical method of constructing a tangent line from the initial condition; (2) None of the conventional mechanistic foam simulation and fractional flow analysis can fully capture sharply-changing dynamic foam behavior at the leading edge of gas bank, which can be overcome by the pressure-modification algorithm suggested in this study; (3) Four foam model parameters (∇P_o , n , C_g/C_c , and C_f) can be determined systematically by using an S-shaped foam catastrophe curve, a two flow regime map, and a coreflood experiment showing the onset of foam generation; and (4) At given input data set of foam simulation parameters, the inlet effect (i.e., a delay in strong-foam propagation near the core face) is scaled by the system length, and

therefore the change in system length at fixed inlet-effect length requires the change in individual values C_g and C_c at the same C_g / C_c .

This study improves our understanding of foam field applications, especially for gas injection during SAG processes by capturing realistic pressure responses. This study also suggests new fractional flow solutions which do not follow conventional fractional flow analysis.

1. INTRODUCTION

Fluctuation in oil and gas prices in recent years causes the enhanced oil recovery method back in the global spotlight gaining a great deal of attention from the petroleum industry. Enhanced Oil Recovery (EOR), typically defined as oil recovery by the injection of materials not normally present in the reservoir (Lake, 1989), becomes increasingly important because the discovery of a large oil field is coming to be rare and difficult. Venturing into harsher environments such as deepwater, offshore, and remote areas is a new trend, but EOR has merit over a new find in that the oil reserve, already discovered and proven, still remains in the reservoir.

EOR processes can be categorized largely into three different groups which are thermal, chemical, and solvent injections. Many of these processes are associated with the injection of a gas phase. Numerous examples can easily be spotted in both miscible and immiscible displacements such as steam, nitrogen (N_2), hydrocarbon flue gas, carbon dioxide (CO_2), and so on. The sweep efficiency of these gas-assisted EOR processes is often unsatisfactory because of gravity segregation, fingering and channeling. The concept gained in EOR is also implemented in the recovery of non-aqueous phase liquids (NAPLs) such as petroleum oils, trichloroethylene (TCE) and perchloroethylene (PCE) in shallow subsurface remediation treatments. The foreign materials injected into the contaminated formation help displace or dissolve pollutants to clean up groundwater (Rong, 2002; Mamun et al., 2002). The use of such an in-situ remediation technology is believed to be superior to the ex-situ remediation technology in terms of remediation time and process costs. The adverse effect of gas injection during EOR processes is also envisaged and encountered in the aquifer remediation treatments in which gas phase tends to override and channel through the subsurface without contacting the contaminants.

Foam-assisted EOR or remediation processes in subsurface have a capability to greatly improve sweep efficiency by reducing gas mobility (Hirasaki, 1989; Kovsky and Radke, 1994; Rossen, 1996). Examples can be found from many oil field applications including Snorre, Prudhoe Bay, North Sea, San Andres (West Texas), and Oseburg (Hoefner, 1995; Aarra et al., 1994, Aarra and Skauge, 2002; Blaker et al., 2002) and remediation treatments (Hirasaki et al., 2000). For example, Hoefner's work (1995) in San Andres (West Texas) and in Platform Carbonate (southeast Utah) shows about 10 to 30 % increase in oil production by injecting CO₂ as a foam; foam-assisted WAG (water-alternating-gas) process in the North Sea (Aarra and Skauge, 2002) estimates the additional oil production of 217,000 to 650,000 m³ compared to WAG; and foam/surfactant remediation at Utah Air Force base (Hirasaki et al., 2000) shows almost 100 % of contaminants removed from the contaminated site. Foam can be injected into the formation in two different ways: (1) co-injection of gas and surfactant solutions in which foams are pre-generated before entering the formation and (2) surfactant alternating gas (SAG) in which the gas and surfactant solutions are injected one after the other periodically. The SAG process can be advantageous over the co-injection because of easier in-situ foam generation resulting from the fluctuation in capillary pressure (P_c). The use of SAG processes is also shown to be superior to the co-injection in the shallow subsurface applications because the pressure build-up during gas injection can be easily controlled by using pre-specified injection pressure. Prohibiting an excessive subsurface pressure is critical not to expel the contaminants out of the region of interest.

The success of SAG processes strongly relies on whether fine-textured foams are successfully created in porous media, which is not only influenced by the injection rate but also by numerous other field conditions including formulation and concentration of surfactant

solution, wettability of the medium, type and saturation of existing oils, and adsorption and desorption of surfactant molecules on rock faces. Assessing a field SAG process, however, largely counts on a single variable, “inlet injection pressure”, in field operations which is used as a major indicator to judge whether or not strong foams are generated and propagate as intended. As a result, understanding the nature of foam displacement during gas injection in SAG processes is crucial to evaluating the performance of field treatments.

1.1. Objectives of This Study

As a sequel to the previous mechanistic modeling and simulation approaches based on three different foam states and two flow regimes (Kam and Rossen, 2003; Dholkawala et al, 2007; Kam et al., 2007; Kam, 2008), this study is first to investigate the mechanisms of SAG processes by using mechanistic foam-simulation techniques and fractional flow analysis. This study not only aims to show how to resolve the case of gas injection during SAG processes, but also demonstrates why the SAG processes are fundamentally different from the co-injection from the viewpoint of mechanistic modeling and simulation. An effort is also made to reveal why fractional flow methods, which effectively guide a mechanistic foam simulation in the case of co-injection of gas and surfactant solutions (Dholkawala et al, 2007; Kam et al., 2007; Kam, 2008), fail to produce realistic inlet pressure responses by missing foam dynamics at the leading edge of foam front. The mechanistic model is updated from the previous study so that the trapped gas saturation is taken into consideration.

Since the focus of this study is made on the fundamentals of SAG processes, this study narrows down its scope into one-dimensional flow, absence of oil, homogeneous porous medium, and negligible capillary pressure gradient.

1.2. Chapter Description

This study includes five chapters which can be summarized as follows:

Chapter 1 briefly explains the foam application in oil and gas industry, and the implication which exists during SAG process, followed by objective of this study and the chapter description.

Chapter 2 explains the fundamental concepts in foam displacement into porous media together with the review of recent development in terms of catastrophe theory and two strong-foam flow-regime concepts.

Chapter 3 includes the methodology and equations used in this study, covering the governing equations, transport equations, and mechanistic foam functions.

Chapter 4 summarizes the results from simulation and fractional flow solutions, and discusses about them in detail.

Chapter 5 covers the summary of this study followed by recommendations for future work in foam displacement research.

Appendix A and B are attached to describe how to determine model parameters and how to construct a new algorithm using Jacobian matrix, respectively.

2. LITERATURE REVIEW

This chapter describes a brief summary of foam fundamentals to define the terms used in this study followed by recent developments in foam research in terms of foam catastrophe theory, two strong-foam regimes, and SAG processes.

2.1. Foam Fundamentals

2.1.1 Foams in Porous Media

Once foam is present in porous media, it does not form a new “foam” phase. Rather, it splits into two separate phases – (i) a liquid phase with surfactant molecules, taking up a relatively tiny pore space and (ii) a gas phase with thin foam films called “lamellae”, occupying a relatively large pore space. Therefore, foam in porous media, which is basically a gas phase flowing together with foam films in a complicated pore structure, is somewhat different from foam in bulk. According to previous studies (Rossen, 1996; Gauglitz et al., 2002), foam in porous media is defined as the “dispersion of gas phase in the liquid phase such that the liquid phase is connected and at least some part of the gas phase is made discontinuous by the thin liquid films of water”. The number of those foam films in porous media, which is referred to as “foam texture” is the key to understanding the rheological properties of foam including effective gas viscosity, gas relative permeability, yield stress, trapped gas saturation and so on. Since the liquid phase still flows through a relatively small pore space, the relative permeability function to liquid phase is believed to be unaltered (Kovscek and Radke, 1994).

2.1.2. Weak Foam vs. Strong Foam

Previous foam studies use the terms such as “weak foams” and “strong foams” to represent foams with different levels of gas mobility. Weak foams represent coarse-textured foams showing a relatively moderate increase in pressure (or, relatively moderate decrease in gas

mobility), while strong foams represent fine-textured foams showing a drastic increase in pressure (or, drastic decrease in gas mobility). The shift from weak foams to strong foams, which is called “foam generation”, is shown to be often sudden and uncontrollable. The laboratory measured pressure gradients are typically used to infer foam texture in the medium. Fig. 2.1 shows schematics of conventional gas/liquid flow, weak foams, and strong foams in porous media.

2.1.3. Lamella Creation and Coalescence in Porous Media

Foam texture in porous media is an outcome resulting from dynamic lamella creation and coalescence mechanisms because foam films are created or collapsed continuously during the flow. Any parameters, which influence the creation and coalescence of lamellae in the medium, have an impact on foam texture. Parameters such as surfactant concentrations and formulations, rock mineralogy and wettability, pore structures, and temperature are some examples among many.

2.1.3.1. Lamella Creation Mechanisms

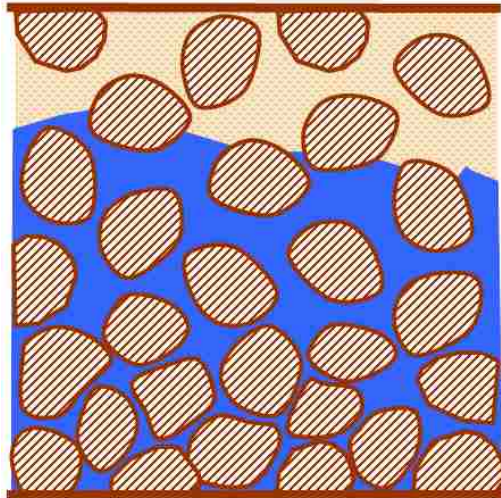
Previous studies show that lamellae can be created by three major mechanisms (Ransohoff and Radke, 1988; Rossen, 1996; Hirasaki et al., 1997): lamellae can be left behind during the invasion of gas into water-saturated media in drainage process (“leave-behind”); a non-wetting gas phase can be snapped off when capillary pressure p_c fluctuate sufficiently (“snap-off”); and pre-existing lamellae can be mobilized by the local pressure gradient and subsequently divided into many at the pore junctions downstream (“lamella mobilization and division”). Figs. 2.2, 2.3, 2.4 show these three mechanisms schematically.

2.1.3.2. Lamella Coalescence Mechanisms

Lamella coalescence is a consequence resulting from the instability of foam films which

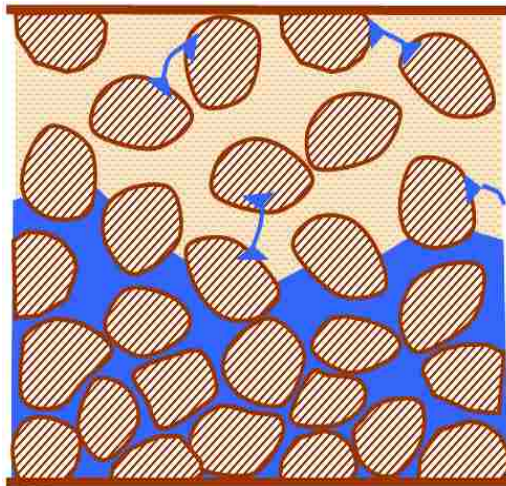
essentially minimizes surface free energy by decreasing interfacial area between immiscible phases (Kovscek and Radke, 1994; Rossen, 1996). High capillary-pressure environments in porous media tend to push the liquid from the thin liquid film to Plateau border (where most of the liquid phase is accumulated), leading to a sudden rupture of the films. Surfactant molecules placed at the gas-liquid interface play an important role in film stability by slowing down the film drainage. Previous experimental studies identify the presence of the limiting capillary pressure (p_c^*) above which foam films cannot survive, which can be translated into the corresponding limiting water saturation (S_w^*). For example, Khatib et al. (1988) shows from their foam-flow experiments in bead packs that there is a threshold value of capillary pressure (p_c) above which foam films become unstable and rupture abruptly. There are other factors that affect films stability which include gas diffusion, liquid evaporation/condensation, presence of another phases, and mechanical disturbance when films are in motion. (Aronson et al., 1994; Kovscek and Radke, 1994; Rossen, 1996; Dholkawala, 2006)

The concept of macroscopic foam stability in porous media is in fact connected to the microscopic film stability that Derjaguin and Obuchov (1936), and Derjaguin and Kussakov (1939) investigated by using the disjoining pressure (π). Their theory, which is often referred to as DLVO theory, combines different types of short-range forces such as van Der Waals attraction and electrostatic repulsion in order to explain a threshold film thickness below which the film coalesces suddenly. As shown schematically in Fig. 2.5, any positive values of π represent a net repulsive force resisting to the rupture of a film whereas any negative values of π represent a net attractive force causing film rupture. The stability condition says that any part that has a negative slope in the right-hand side is physically stable, and the maximum disjoining pressure, which is sometimes called the limiting capillary pressure, coincides



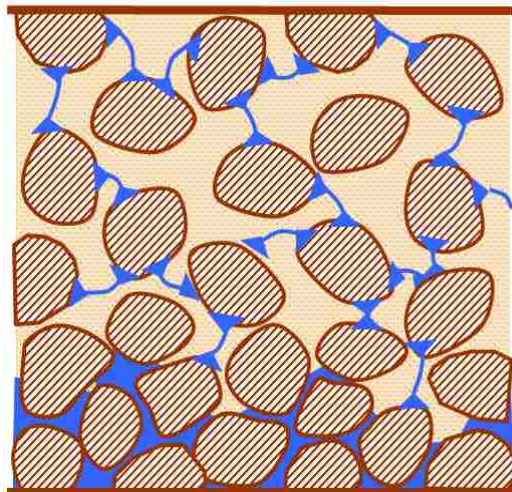
No Foam

(a)



Weak Foam

(b)



Strong Foam

(c)

Figure 2.1 Schematic of foam flow in porous media (re-drawn from Dholkawala (2006)):
(a) conventional gas/liquid two-phase flow (no foam) (b) weak foam (c) strong foam

with the threshold thickness (h^*).

Existing lamellae may disappear due to the diffusion of gas mass into the adjacent larger bubbles. This gas diffusion between bubbles tends to keep a bubble above a certain size (Rossen, 1996). The use of minimum bubble size estimated from pore body and throat sizes is in fact a simplification of this diffusion process.

2.1.4. Gas-Mobility Reduction and Bubble Trapping

Foam has been applied in many different applications. They can be mainly grouped into three major categories: (1) large-scale foam-assisted enhanced oil recovery, (2) small-scale near-wellbore improved oil recovery (for example, gas- and/or water-blocking near the well, foam-acid diversion treatment in well stimulation), and (3) foam/surfactant processes in aquifer remediation for contaminant removal. (Patzek and Koinis, 1990; Djabbarah et al., 1990; Friedmann et al., 1994; Blaker et al., 2002) although slightly different, all these applications share the same fundamentals – reducing gas mobility significantly by increasing effective gas viscosity and decreasing gas relative permeability (Hirasaki and Lawson, 1985; Falls et al., 1989). The decrease in gas mobility by creating strong foams typically leads to a significant fraction of gas phase trapped, not contributing the flow of foams in porous media (Kovscek and Radke, 1994). In reality, effectively gas viscosity, relative permeability, and trapped gas saturation are all inter-connected nonlinearly, therefore separating them from others is regarded as a challenging task.

2.2. Recent Developments

2.2.1. Two Steady-State Strong-Foam Regimes

Earlier foam studies show different interpretations on foam rheology based on laboratory-measured experimental data, many of them conflicting each other. Osterloh and Jante's study

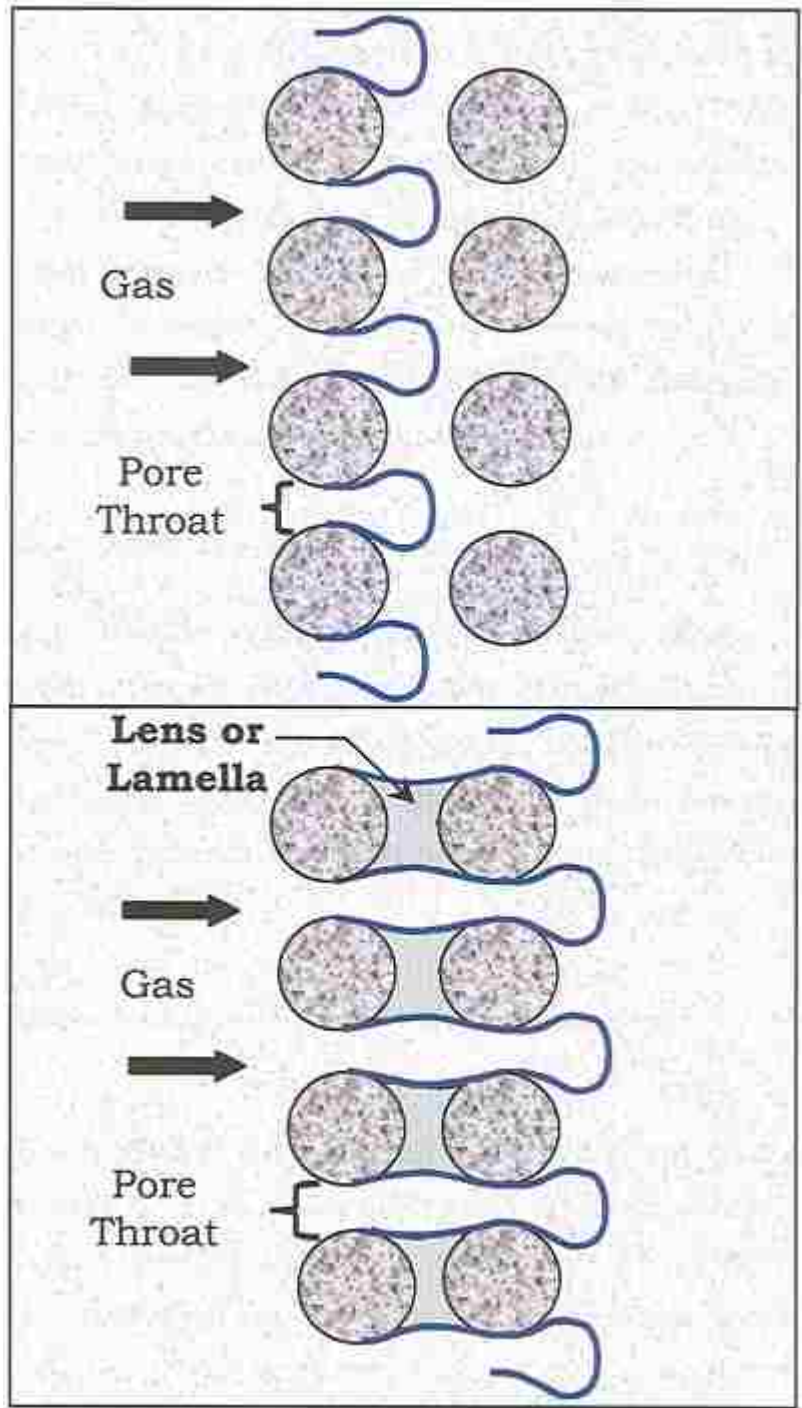


Figure 2.2 Lamella creation mechanisms: Leave-behind (Dholkawala, 2006)

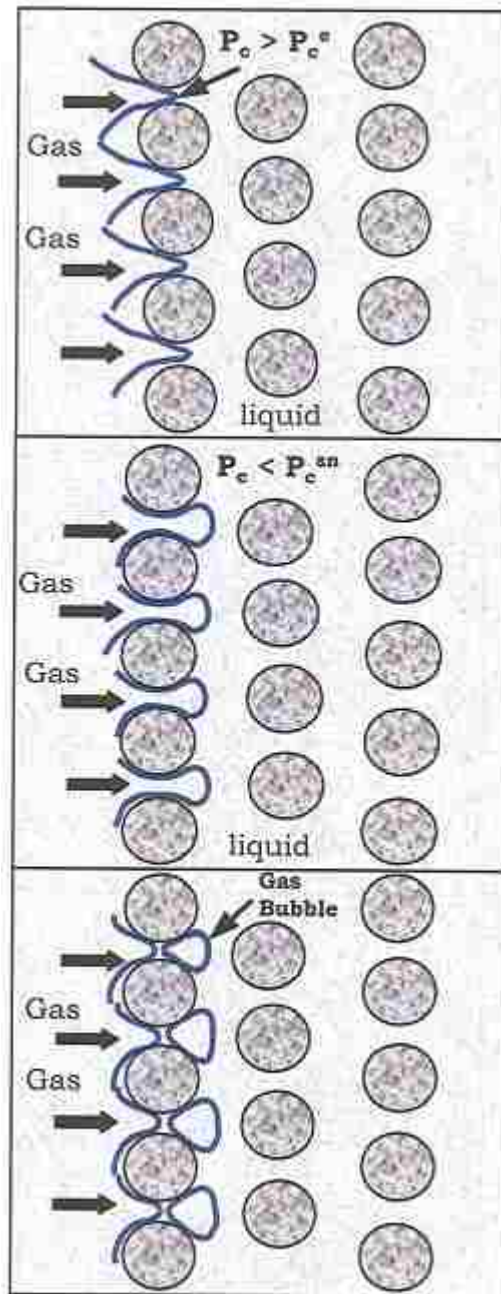


Figure 2.3 Lamella creation mechanisms: Snap-off (Dholkawala, 2006)

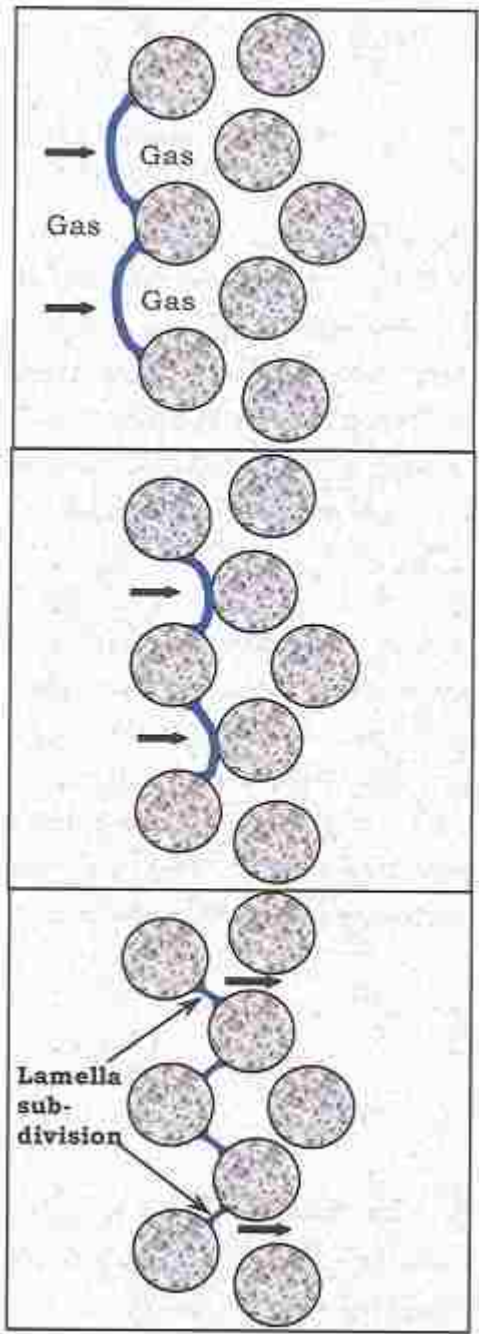


Figure 2.4 Lamella creation mechanisms: Mobilization and division (Dholkawala, 2006)

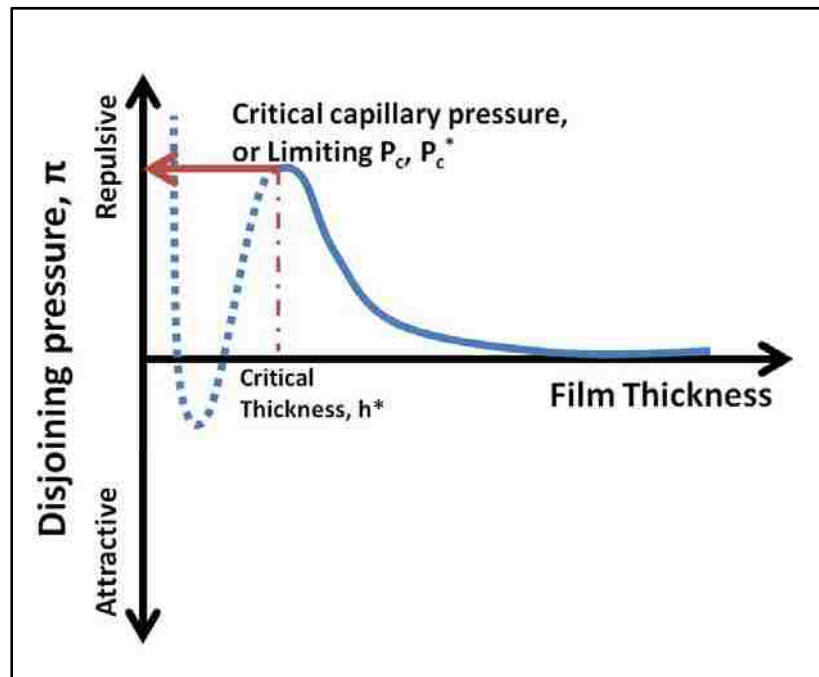


Figure 2.5 The disjoining pressure as a function of film thickness showing the presence of the limiting capillary pressure (P_c^*) (re-drawn from Aronson et al., 1994)

(1992) is perhaps the first to resolve many of the conflicts by plotting the steady-state pressure contours as a function of gas and liquid velocities. The pressure contours show two distinct flow regimes.

Alvarez et al. (2001) repeated the same type of coreflood experiments – measuring the steady-state pressure drops at different velocities – in a wide range of experimental conditions by using different surfactants, surfactant concentrations, porous media, and back pressure. Their study confirms the presence of two flow regimes once strong foams are successfully created, as shown in Fig. 2.6: (1) the low-quality regime (i.e., relatively wet foams) shows that the pressure gradient is almost independent of liquid velocity forming horizontal contours and (2) the high-quality regime (i.e., relatively dry foams) shows that the pressure gradient is almost independent of gas velocity forming vertical contours. These two regimes are separated by a certain foam quality (f_g), called f_g^* . These two regimes are shown to be governed by different mechanisms: bubble coalescence near the limiting capillary pressure in the high-quality regime; and bubble trapping and mobilizations in the low-quality regime. More details on these two regimes can be found elsewhere (Rossen and Wang, 1999; Kam and Rossen, 2003; Kam, 2008)

2.2.2. Foam Catastrophe Theory

A recent experimental study (Gauglitz et al., 2002) shows that foam rheology in porous media follows a trend demonstrated by catastrophe theory which characterizes a physical phenomenon by a sudden and unpredictable shift leading to dramatic changes, often associated with mathematical singularity. Their study proves that such a catastrophic behavior of foams in porous media, which is referred to as “foam catastrophe theory” in later studies, exists in a broad range of experimental conditions including different gas phases (N_2 and CO_2), surfactant formulations and concentrations, back pressures, and porous media (sands, beads, and sand

stones). All three different types of inlet injection conditions (i.e., fixed pressures, fixed rates, and combination of both, which they called type 1, 2, and 3 respectively) exhibit the same tendency consistently as shown in Fig. 2.7 in which the top surface represents strong-foam state with a significant reduction in gas mobility, the bottom surface represents weak-foam state with a moderate reduction in gas mobility, and the surface in between represents an unstable intermediate state. Subsequent experiments at the same experimental conditions (Kam et al., 2007) show that strong-foam rheology represented by the top surface consists of two steady-state strong-foams regimes which agrees well with earlier two flow regime studies of Osterloh and Jante (1992) and Alvarez et al. (2001). Both Figs. 2.6 and 2.7 are consistent with well-known concept of “foam generation” that describes a sudden change from weak-foam to strong-foam state as the injection velocity increases at fixed foam quality (f_g).

2.2.3. Co-injection vs. Surfactant-Alternating-Gas (SAG)

Compared with co-injection of gas and surfactant solutions, the mechanism of the SAG process is believed to be fundamentally different because of two main reasons: (1) There exist two different paths to describe gas injection during SAG processes, one for weak-foam and the other for strong-foam propagation. Of the two, the strong-foam path leads to the propagation of fine-textured foams resulting in enhanced sweep efficiency, while the weak-foam path leads to the propagation of coarse-textured foams resulting in poor sweep efficiency. This concept is well summarized by a schematic figure provided by Rossen and Bruining (2007) as shown in Fig. 2.8; (2) In contrast to the co-injection; the SAG process is more complicated. As the porous media dries, there is a change in foam texture near the limiting water saturation, S_w^* (i.e., water saturation (S_w) that corresponds to the limiting capillary pressure (P_c^*) through the capillary-pressure curve) during gas injection. A mechanistic fractional flow curve from Dholkawala et al. (2007) as shown in Fig. 2.9 shows an example in which the fractional flow curve extends back

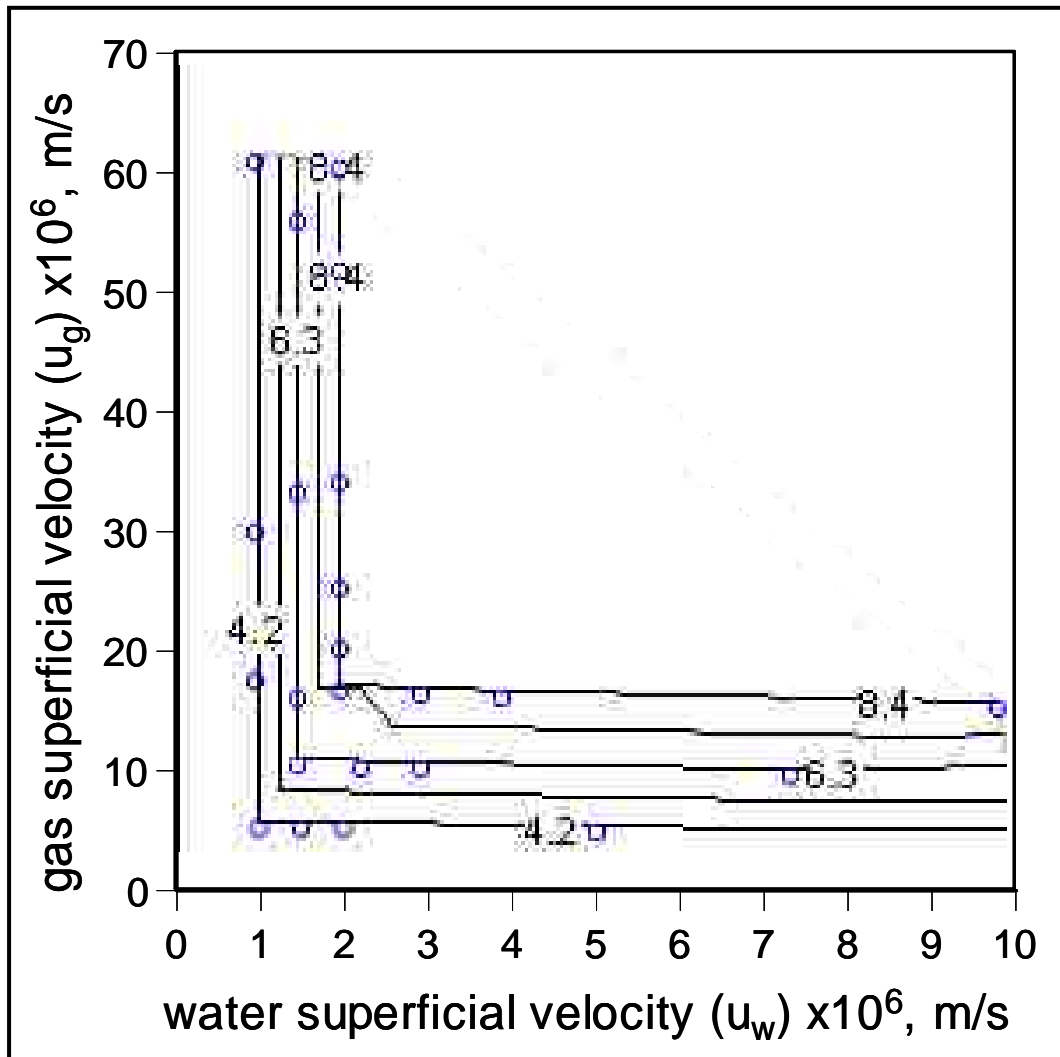


Figure 2.6 Two strong-foam flow regimes observed by Kam et al. (2007): the contour shows the steady-state pressure gradient in psi/ft (1 psi/ft = 22,626 Pa/m)

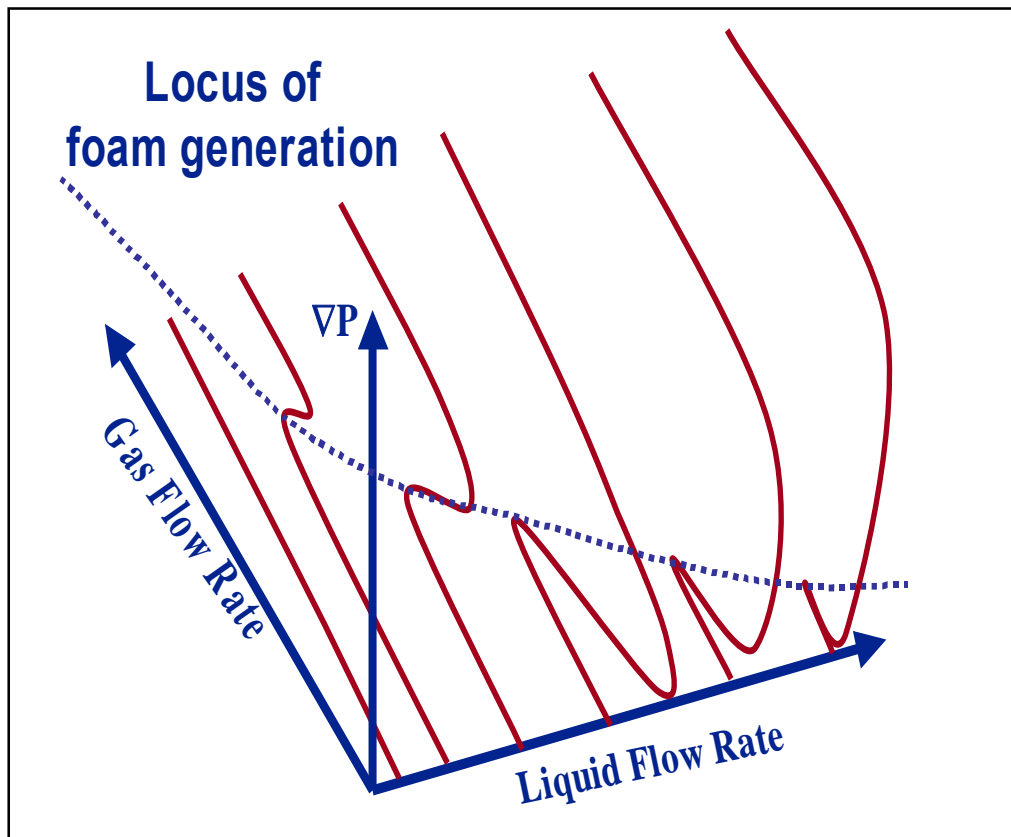


Figure 2.7 Foam catastrophe surface showing three different states (weak-foam, strong-foam, intermediate states) from Gauglitz et al. (2002)

from Dholkawala et al. (2007) as shown in Fig. 2.9 shows an example in which the fractional flow curve extends back and forth at very low values of water fractional flow (f_w), which is basically caused by the three different foam states following foam catastrophe theory (cf. Fig. 2.7). The part in which f_w does not increase monotonically with S_w at low f_w in Fig. 2.9 is also evidenced by earlier experimental studies (Kibodeaux and Rossen, 1997; Wassamuth et al., 2001; Xu and Rossen, 2004). Although fractional flow methods (Buckely and Leverett, 1941; Lake, 1989) have been used actively in order to obtain analytical solutions and physical insights for foam-assisted displacement processes (Martinsen and Vassenden, 1999; Zhou and Rossen, 1995, Mayberry et al., 2008), they are unable to show the complicated foam dynamics near the water limiting saturation (S_w^*).

2.2.4. Population-Balance Modeling and Simulation

Although it is more complicated and time-consuming compared to other local steady-state modeling and simulations, the population-balance foam-simulation technique is known to be the most accurate method. It provides a robust mathematical framework for complex numerical calculations, keeping track of mechanistic descriptions on a broad range of microscopic phenomena encountered in foam displacements. There exist different versions of population-balance simulators in the literature depending on how to mathematically describe those pore-scale events. (Falls et al., 1988; Friedmann et al., 1991; Kovscek and Radke, 1994; Kovscek et al., 1995; Kovscek et al., 1997; Bertin et al., 1998; Myers and Radke, 2000)

In continuation of Gauglitz et al.'s experimental work (2002), the study of Kam and Rossen (2003) attempts modeling efforts using mechanistic descriptions on foam rheology. The study shows that the use of lamella mobilization and division as the major bubble-creation mechanism enables both foam-catastrophe surface and two strong-foam regimes to be

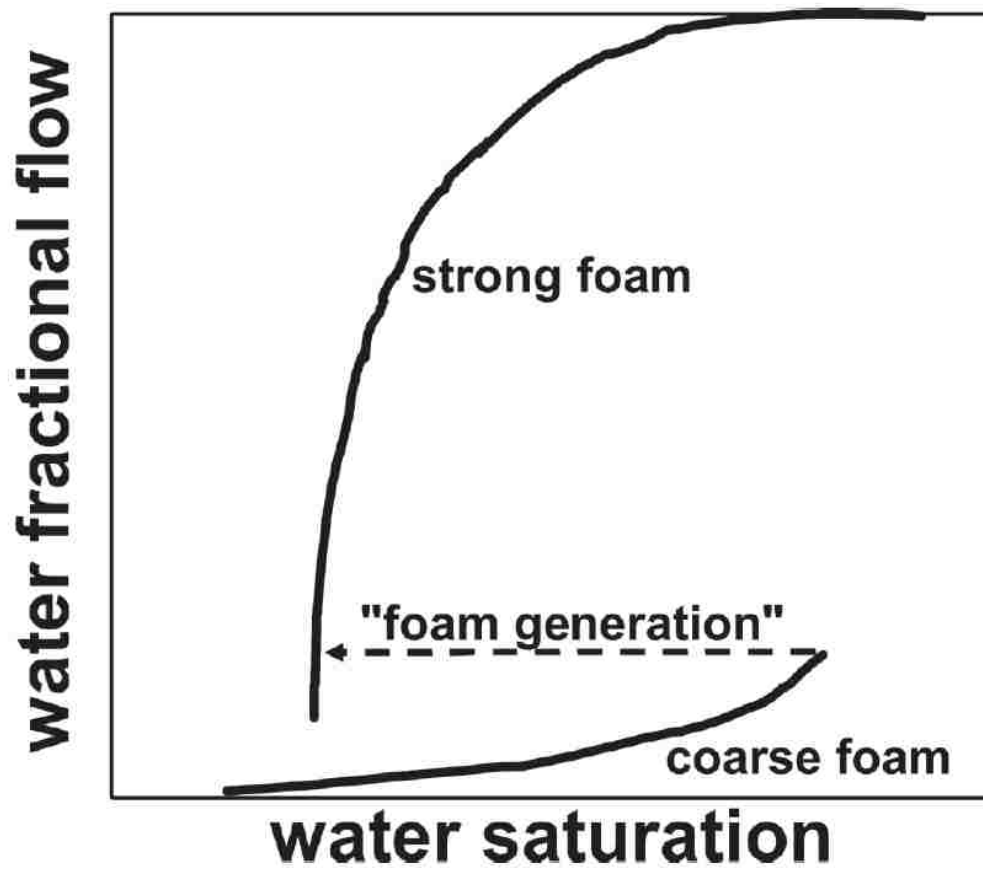


Figure 2.8 A schematic showing two possible solution paths for strong foams and weak foams from Rossen and Bruining (2007).

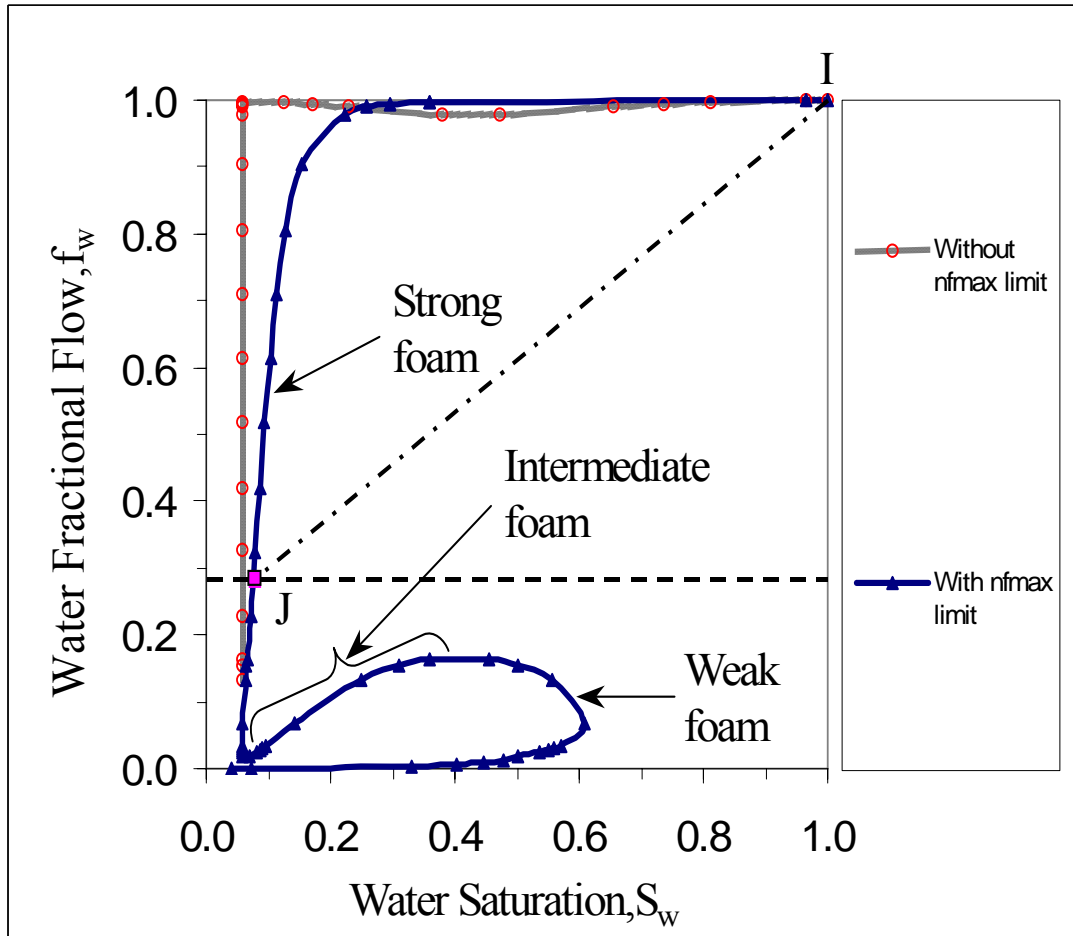


Figure 2.9 an example mechanistic foam fractional flow curve from Dholkawala et al. (2007)

reproduced successfully. Also, their findings are in good agreement with the previous studies in that foam in the high-quality strong-foam regime is governed by bubble coalescence near a limiting capillary pressure (P_c^*) at which bubbles break down abruptly (Aronson et al., 1994; Khatib et al., 1988; Kibodeaux, 1997) whereas foam in the low-quality strong-foam regime is governed by bubble trapping and mobilization with bubbles close to the average pore size (Rossen and Wang, 1999; Alvarez et al., 2001). A mechanistic foam simulator, developed to capture the three different foam states (i.e., strong-foam, weak-foam, intermediate states) and the two flow regimes, is shown to adequately describe the nature of foam displacement during co-injection of gas and surfactant solutions (Kam et al., 2007; Kam, 2008). It should be noted that a series of these mechanistic foam simulators, including a new version developed in this study, is the only mechanistic foam model and simulator so far that is consistent with both foam catastrophe theory and two strong-foam regimes.

This study follows the conventional use of the term, mechanistic simulation, in this field of research, meaning that the important foam parameters such as foam texture, gas effective viscosity, trapped gas saturation, and gas relative permeability are determined by mathematical descriptions of different individual governing mechanisms. Strictly speaking, the term “mechanistic” may not be appropriate, because some of the mathematical descriptions are based on the empirical equations.

3. METHODOLOGY

As shown in the previous mechanistic foam simulations (Falls et al., 1988; Friedmann et al., 1991; Kavscek et al., 1995; Bertin et al., 1998; Kam et al., 2007; Kam, 2008), formulating equations for foam displacement in porous media first requires mass balance and population balance. The mass balance of two immiscible phases in the absence of absorption and mass exchange is given by (Lake, 1989)

$$\frac{\partial}{\partial t}(\phi \rho_j S_j) + \nabla \cdot (\rho_j \vec{u}_j) = G \quad ; \quad j = w \text{ or } g \dots\dots\dots(3.1)$$

This equation can be simplified into

$$\frac{\partial}{\partial t}(S_j) + \frac{u_t}{\phi} \frac{\partial}{\partial x}(f_j) = 0 \quad ; \quad j = w \text{ or } g \dots\dots\dots(3.2)$$

for one-dimensional incompressible flow which is well known as fractional flow equation. Note that ϕ is porosity (kept uniform and constant in this study), G is a sink or source term, u_t is total injection velocity, t and x are time and space, and ρ_j , S_j , u_j , and f_j are the density, saturation, superficial velocity, and fractional flow of phase j , respectively. These two equations for water (w) and gas (g) are commingled through saturations and fractional flows, and therefore only one equation is independent.

Bubble population balance can be handled in a similar way once water saturation is greater than the limiting water saturation (i.e., $S_w > S_w^*$) as follows (Falls et al., 1988; Friedmann et al., 1991; Kavscek et al., 1995):

$$\phi \frac{\partial}{\partial t}(S_g n_f) + \frac{\partial}{\partial x}(n_f u_g) = \phi S_g R \dots\dots\dots(3.3)$$

where n_f is foam texture (i.e., the number of foam films in unit gas volume) and R is the net change of n_f per unit time. This equation allows a mechanistic simulation to keep track of bubble population with time and space based on the accumulation (first term), convection (i.e., flux in

and out; second term), and generation or destruction (third term) of foam films. There are two occasions in which the mechanistic simulation bypasses bubble population balance calculations. First, if water saturation is less than, or equal to, the limiting water saturation ($S_w \leq S_w^*$), foam films can no longer sustain and the condition of the medium spontaneously leads to $n_f = 0$. Second, if the calculated values of foam texture (n_f) goes beyond the maximum foam texture (n_{fmax}), the calculated n_f is forced to be the same as n_{fmax} . This is because bubbles cannot be smaller than the average pore size due to diffusion, and the presence of minimum bubble size imposes an upper limit for the foam texture.

The net rate (R) can be either positive or negative depending on the magnitudes of two competing mechanisms such as the rate of lamella creation (R_g) and the rate of lamella coalescence (R_c), which is given by the following equation:

$$R = R_g - R_c \quad \text{if} \quad S_w > S_w^* \quad , \dots \dots \dots (3.4)$$

where R_g and R_c are expressed by

$$R_g = \frac{C_g}{2} \left\{ \text{erf} \left(\frac{\nabla p - \nabla p_0}{\sqrt{2}} \right) - \text{erf} \left(\frac{-\nabla p_0}{\sqrt{2}} \right) \right\} \quad \dots \dots \dots (3.5)$$

and

$$R_c = C_c n_f \left(\frac{S_w}{S_w - S_w^*} \right)^n \quad \text{if} \quad S_w > S_w^* \quad \dots \dots \dots (3.6)$$

respectively, following the concept of lamella mobilization and division (Rossen and Gauglitz, 1990; Kam and Rossen, 2003) and bubble coalescence near the limiting capillary pressure (Aronson et al., 1994; Khatib et al. 1988). The use of lamella mobilization and division as the major lamella-creation mechanism is fully discussed in other previous studies (Rossen, 2003; Kam and Rossen, 2003; Kam et al., 2007; Kam, 2008). Note that C_g and ∇P_0 are model parameters for bubble creation, C_c and n are model parameters for bubble coalescence, and “erf”

represents the error function.

The selection of lamella-creation function as shown in Eq. 3.5 is based on two constraints: (1) At low pressure gradient (∇P), the rate of lamella creation (R_g) should increase rapidly as ∇P increases; and (2) At high ∇P , R_g should level off and reach a plateau. The former is implicitly related to the concept of the minimum mobilization pressure (Rossen and Gauglitz, 1990) above which foam films can be mobilized easily leading to a rapidly growing bubble population, and the latter represents the condition at which foam films do not multiply actively once fine-textured foams are created at high ∇P holding the bubble size close to the average pore size. Further details on this topic are provided by Kam (2008). Figs. 3.1(a) and 3.1(b) show schematics of the rate of lamella creation as a function of ∇P at different values of parameter ∇P_o (cf. Eq. 3.5) and the rate of lamella coalescence as a function of water saturation (S_w) (cf. Eq. 3.6). The sudden change in rate of bubble coalescence at S_w^* (or P_c^* equivalently) in Fig. 3.2 is represented by the singularity at S_w^* as shown in Eq. 3.6.

For fractional flow analysis which requires local steady-state modeling, foam texture (n_f) can be calculated from Eqs. 3.5 and 3.6 by equating R_g and R_c . Therefore,

$$n_f = \frac{C_g}{2C_c} \left(\frac{S_w - S_w^*}{S_w} \right)^n \left\{ \operatorname{erf} \left(\frac{\nabla p - \nabla p_o}{\sqrt{2}} \right) - \operatorname{erf} \left(\frac{-\nabla p_o}{\sqrt{2}} \right) \right\} \quad \text{if } n_f < n_{fmax} \dots\dots\dots (3.7)$$

In order to accommodate trapped gas saturation, this study follows the approach employed by Kovscek et al. (1995) in which the fraction of trapped gas saturation (X_t) is defined by

$$X_t = X_{tmax} \left(\frac{\beta n_f}{1 + \beta n_f} \right) \dots\dots\dots (3.8)$$

where X_{tmax} and β are model parameters and kept constant in this study. Likewise the fraction of flowing gas saturation (X_f) is defined by

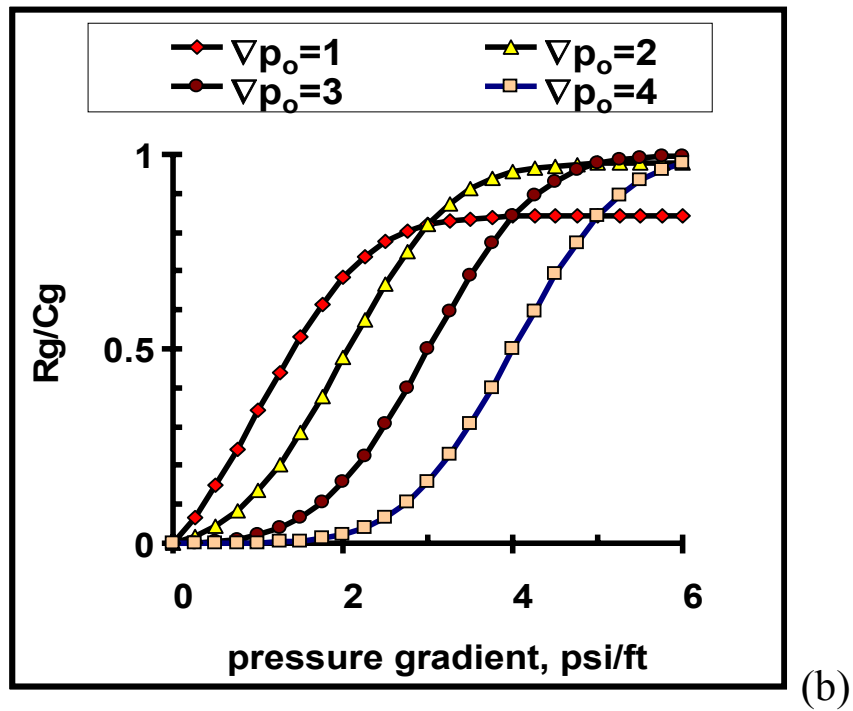
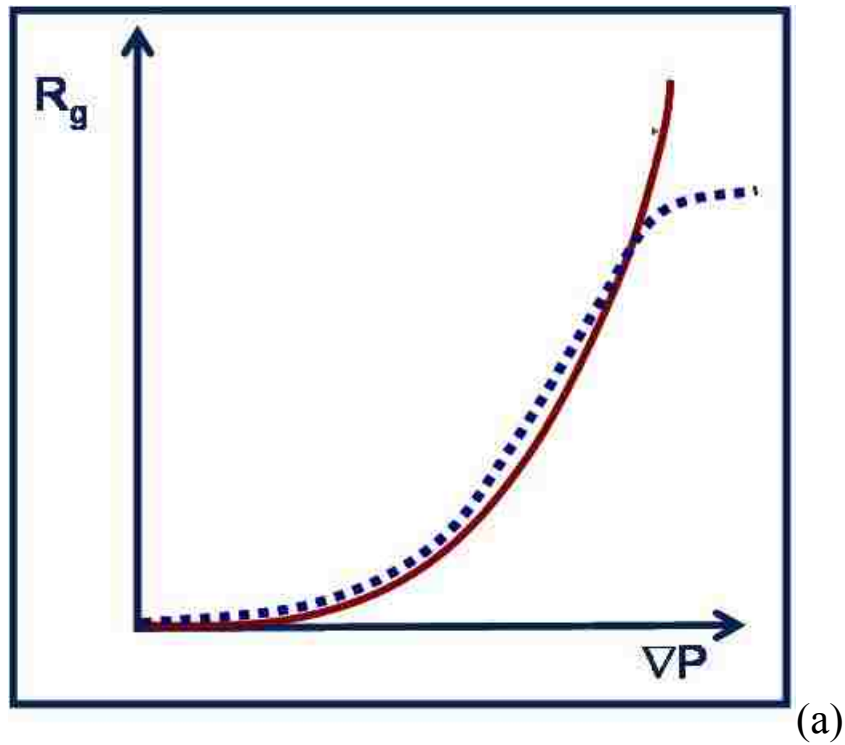


Figure 3.1 Graphical representation of lamella creation function used in this study: (a) the rate of lamella creation (Kam, 2008) and (b) the rate of lamella creation as a function of ∇P at different values of parameter ∇p_o .

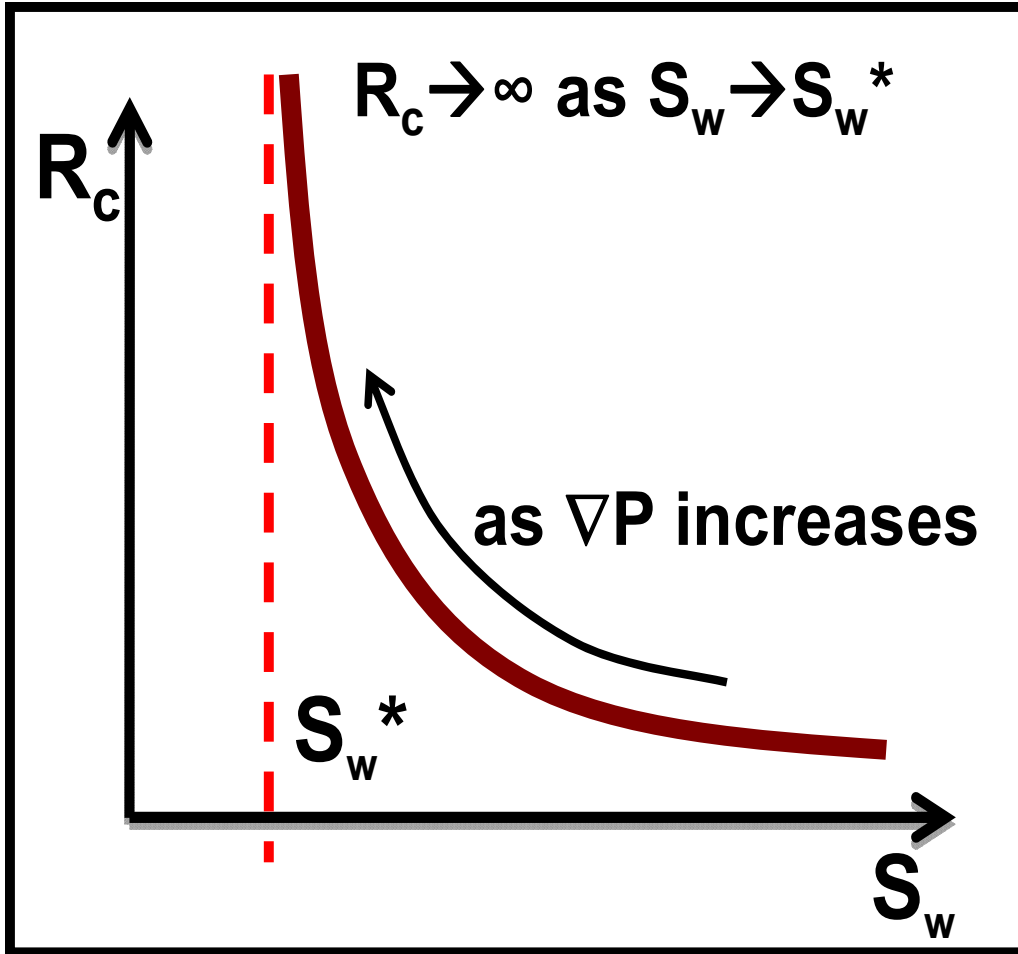


Figure 3.2 Graphical representation of lamella coalescence function used in this study: the rate of lamella coalescence

$$X_f = 1 - X_t \quad \dots\dots\dots(3.9)$$

and both X_t and X_f are related to gas saturation (S_g) as follows:

$$S_g = S_{gt} + S_{gf} = X_t S_g + X_f S_g = X_t S_g + (1 - X_t) S_g \quad \dots\dots\dots(3.10)$$

where S_{gt} and S_{gf} are trapped and flowing gas saturations, respectively.

Because the presence of foam is shown to affect only gas relative permeability function without altering liquid relative permeability function (Friedmann et al., 1991; Kovscek et al., 1995), the following equations are used for liquid relative permeability (k_{rw}), gas relative permeability in the absence of foam (k_{rg}^0), and gas relative permeability in the presence of foam (k_{rg}^f):

$$k_{rw} = 0.7888 \left(\frac{S_w - S_{wc}}{1 - S_{wc} - S_{gr}} \right)^{1.9575} \quad \dots\dots\dots(3.11)$$

$$k_{rg}^0 = \left(\frac{1 - S_w - S_{gr}}{1 - S_{wc} - S_{gr}} \right)^{2.2868} \quad \dots\dots\dots(3.12)$$

and

$$k_{rg}^f = \left(X_f \frac{1 - S_w - S_{gr}}{1 - S_{wc} - S_{gr}} \right)^{2.2868} \quad \dots\dots\dots(3.13)$$

where S_{wc} and S_{gr} are connate water saturation and residual gas saturation, respectively. Water fractional flow (f_w) therefore can be written as

$$f_w = 1 - f_g = \frac{u_w}{u_t} = \frac{u_w}{u_w + u_g} = \left(1 + \frac{k_{rg}/\mu_g}{k_{rw}/\mu_w} \right)^{-1}, \quad \dots\dots\dots(3.14)$$

if the flow is in horizontal direction and the capillary pressure gradient is negligible. Note the gas relative permeability (k_{rg}) can be either k_{rg}^0 or k_{rg}^f , depending on whether foams are absent or present in the media.

Gas viscosity in the presence of foams (μ_g^f) is

$$\mu_g^f = \mu_g^o + \frac{C_f n_f}{\left(u_g / (\phi S_g X_f)\right)^{1/3}} \dots\dots\dots(3.15)$$

following Hirasaki and Lawson’s study (1985), where μ_g^o is no-foam gas viscosity and C_f is a model parameter.

Darcy’s equation describes the transport of gas and liquid phase in porous media, i.e., for gas phase

$$u_g = \frac{k k_{rg}^o(S_w)}{\mu_g^o} \nabla p \dots\dots\dots(3.16)$$

in the absence of foam and

$$u_g = \frac{k k_{rg}^f(S_w)}{\mu_g^f} \nabla p \dots\dots\dots(3.17)$$

in the presence of foam, and for aqueous phase

$$u_w = \frac{k k_{rw}(S_w)}{\mu_w} \nabla p \dots\dots\dots(3.18)$$

Determination of model parameters and construction of mechanistic foam fractional flow curves are shown in Appendix A, and computational method for dynamic foam simulations performed in this study are available in earlier studies (Kam and Rossen, 2003; Kam, 2008). The simulation algorithm used in this study is similar to that described in Kam (2008), which is, the use of finite difference method, updating all saturations, pressures, and gas viscosities in the new time step such that the outer iteration loop for gas viscosity has the inner iteration loop for saturation and pressure. Another algorithm, which is newly developed in this study by using Jacobian matrix, is described in Appendix B. The results from these two algorithms are shown to be comparable.

Because of the complexity of foam rheology in porous media, it is not yet clear how many parameters are needed to model complex foam mechanisms. Furthermore, it is not certain

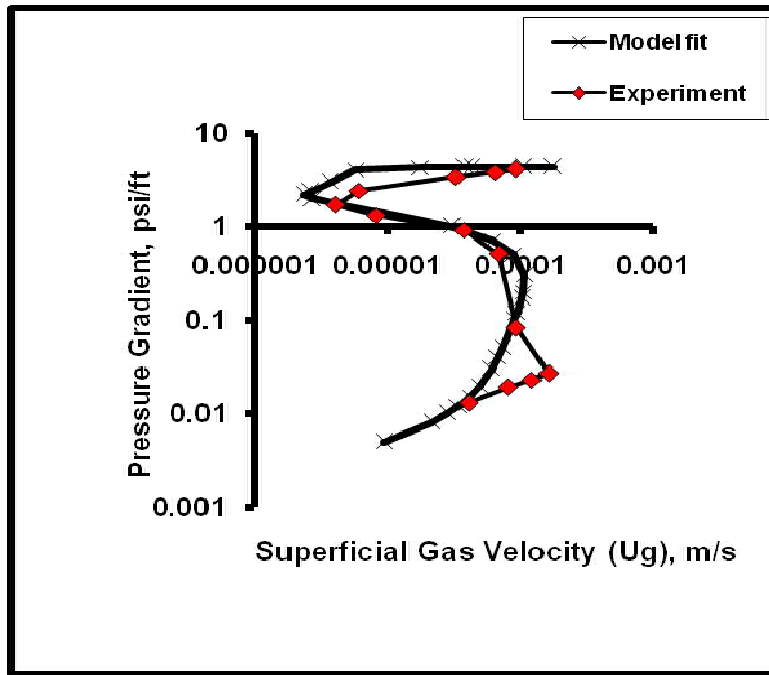
how many of those parameters are independent, and therefore how many dimensionless variables should be used to describe mechanistic foam models.

4. RESULTS AND DISCUSSIONS

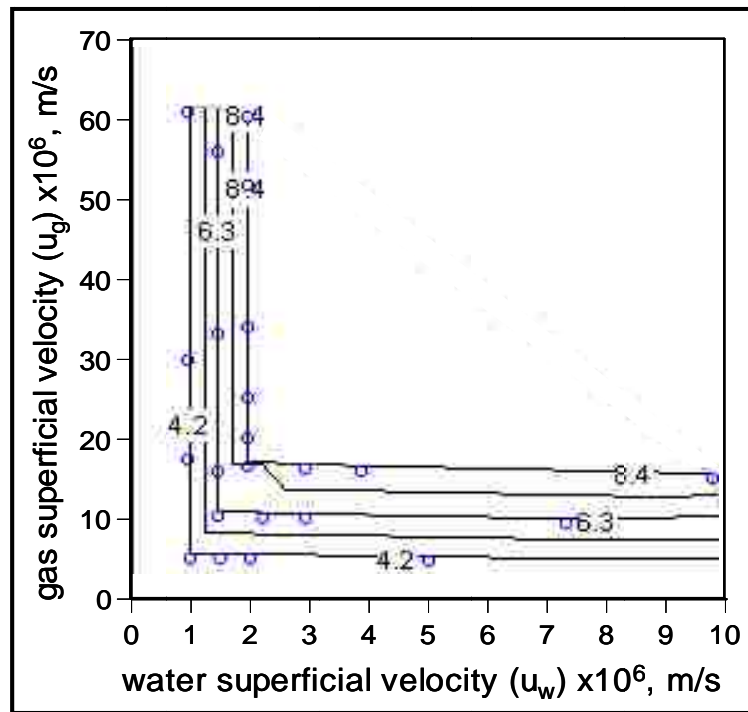
4.1. Model Fit and Parameter Determination

Mechanistic foam modeling and simulation require a fit to experimental data to determine model parameters. An S-shaped curve (i.e., a vertical slice of foam catastrophe surface; cf. Fig. 4.1(a)) and a two steady-state flow regime map (cf. Fig. 4.1(b)), both obtained from the same experimental conditions (i.e., the same gas phase, surfactant formulation and concentration, brine recipe, back pressure, and beadpack with identical porosity and permeability), serve as a basis for parameter determination. This study has three different types of parameters as shown in Table 4.1 : (1) petrophysical properties that define the underlying rock and fluid properties (i.e., k , ϕ , μ_w , μ_g^o , S_{gr} , and S_{wc} ; the first column of Table 1), (2) basic foam properties such as n_{fmax} , S_w^* , X_{tmax} , and β (the second column of Table 1), and (3) mechanistic foam model parameters that fit foam-catastrophe surface and two strong-foam regimes spontaneously (i.e., ∇P_o , n , C_g/C_c , and C_f ; the third column of Table 4.1). These distinctions may not be obvious, nor do they have to, but provide a convenient means to distinguish one from another for the purpose of this study. The parameters in the second column are roughly estimated from existing data in the literature.

Fig. 4 shows an example fit to experimental data, when the base-case parameters (called Case 1) listed in Table 4.1 is used. Fig. 4.1 compares both modeling and experimental results along the S-shaped curve and Fig. 4.1(a) is the fit to two flow regimes in Fig. 1(b). These figures are essentially the same as those in Kam et al. (2007). All mechanistic simulation results shown below are based on the base case parameters (cf. Table 4.1) unless noted otherwise. Because the dynamic foam simulations shown below need individual values of C_g and C_c separately, C_c is assumed to be one in all simulation runs except where the effect of C_g and C_c are investigated.



(a)



(b)

Figure 4.1 (a) Fit to experimental data using base-case parameters in Table 1: (a) fit to S-shaped curve and (b) fit to two flow regimes (cf. Fig. 1(b)) – the procedures and plots are essentially the same as those in Kam et al. (2007), and the contour lines represent the steady-state pressure gradient in psi/ft (1 psi/ft = 22,626 Pa/m)

Table 4-1 Base-case (Case 1) model parameters and properties

Petrophysical Properties		basic foam properties		foam parameters	
k (m ²)	3×10^{-11}	n_{fmax}	8×10^{13}	∇P_o (Psi/ft)	4.2*
ϕ	0.3	S_w^*	0.0585	n	1.0
μ_w (Pa.s)	0.001	X_{tmax}	0.8	C_g / C_c	3.6046×10^{16}
μ_g^o (Pa.s)	0.00002	β	5×10^{-11}	C_f	6.617×10^{-18}
S_{gr}	0.0				
S_{wc}	0.04				

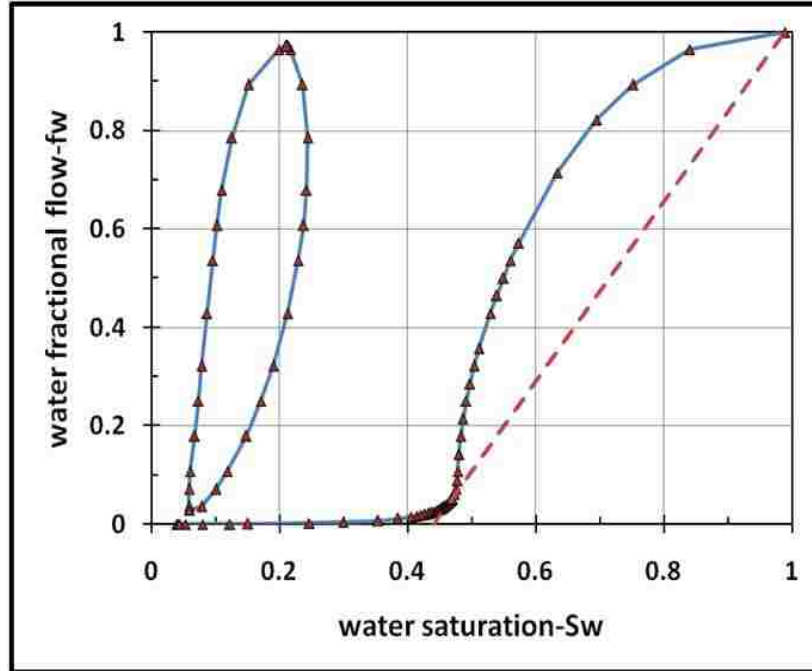
* 4.2 psi/ft = 95,029.2 Pa/m (1 psi/ft = 22,626 Pa/m)

4.2. Dynamic Foam Simulations at Very Low or High Injection Velocities

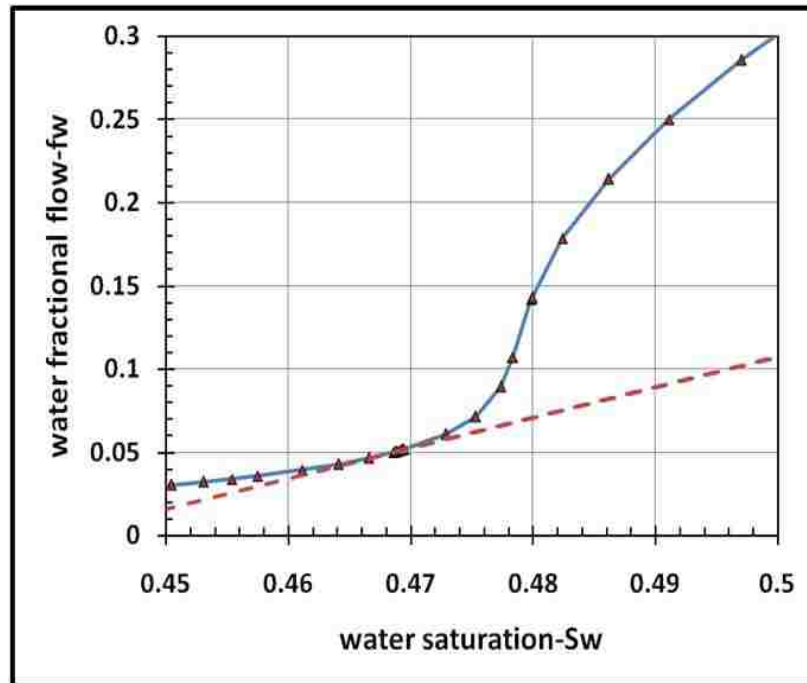
The simulation of gas injection during SAG processes is first investigated at two different gas injection velocities: (1) $u_g = 2.8 \times 10^{-5}$ m/s, which is low enough to lead to weak-foam propagations and (2) $u_g = 1.2 \times 10^{-4}$ m/s, high enough to lead to strong-foam propagations. The initial condition (I) is a medium saturated with surfactant solutions, i.e., $S_w = 1$, and the injection condition (J) is gas only injection, i.e., $u_t = u_g$, $f_g = 1$, or $f_w = 0$. The number of grid blocks in simulations is typically set to be 25, unless noted otherwise.

Fig. 4.2 shows a mechanistic foam fractional flow curve at $u_g = 2.8 \times 10^{-5}$ m/s which leads to weak-foam propagations. The triple valued fractional flow curve within the range of $0.03 < f_w < 0.97$ reflects three different foam states (i.e., the curve far right for weak-foam state, the curve left-hand side of the loop for strong-foam state, and the curve right-hand side of the loop for intermediate state). The saturation behind the shock is about 0.47, as illustrated by the dashed straight line in Figs. 4.2(a) and 4.2(b), and there are spreading waves until the solution reaches J. In other words, the fractional flow solution from J to I by increasing the dimensionless velocity monotonically consists of a shock (from $S_w = 1$ to $S_w = 0.47$) and spreading waves (from $S_w = 0.47$ to $S_w = S_{wc} = 0.04$).

Fig. 4.3 shows the profiles of water saturation (S_w) and foam texture (n_f). The dotted lines in Fig. 4.3 are solutions from fractional flow analysis (corresponding to the fractional flow curve in Fig. 4.2), while the solid lines in Fig. 4.3 are results from mechanistic foam simulations for comparison. Note that the dimensionless time (t_D) shown in the legend is expressed in terms of pore volume injected (PVI). The values of S_w and n_f are in good agreement between the simulation and fractional flow analysis except for two aspects: (1) There is a peak in n_f at the leading edge of gas bank in simulations which results from the dynamics of lamella

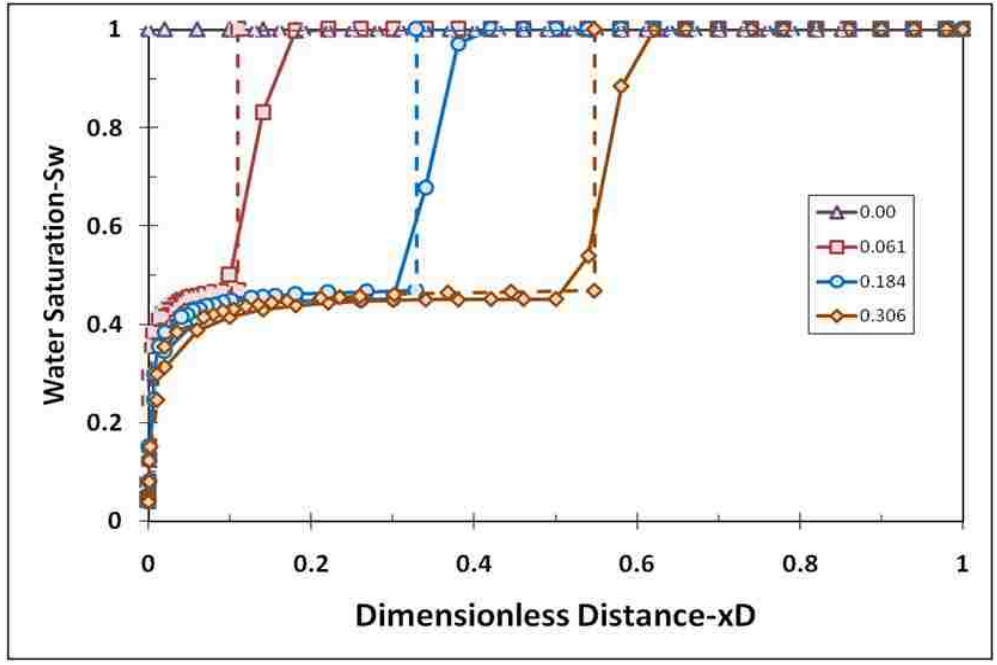


(a)

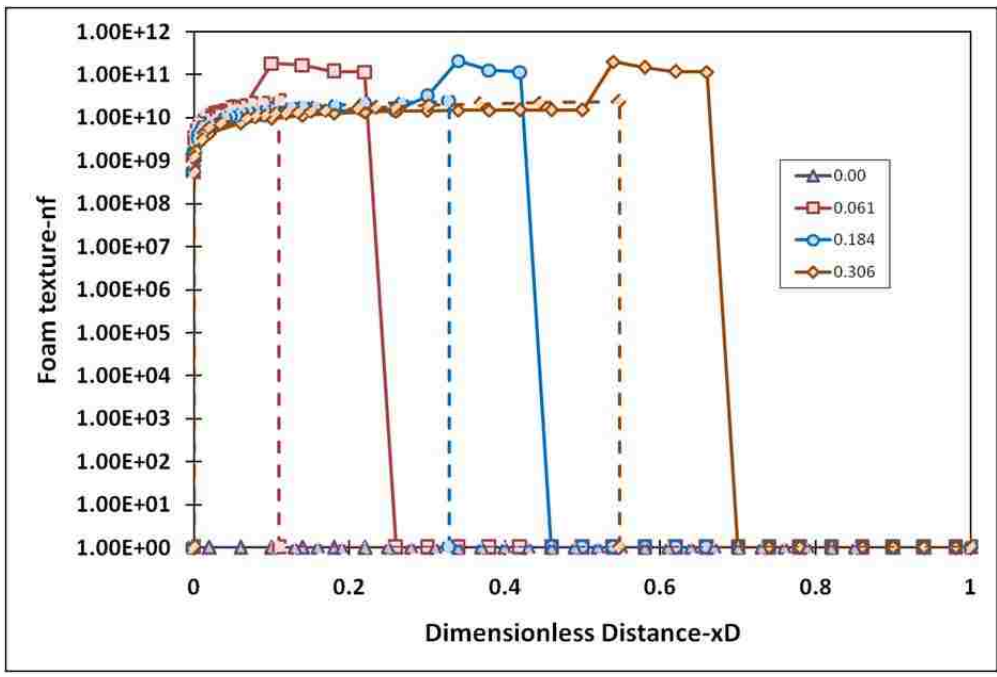


(b)

Figure 4.2 Mechanistic foam fractional flow curve at $u_t = u_g = 2.8 \times 10^{-5}$ m/s: (a) entire graph and (b) magnified view near the shock front



(a)



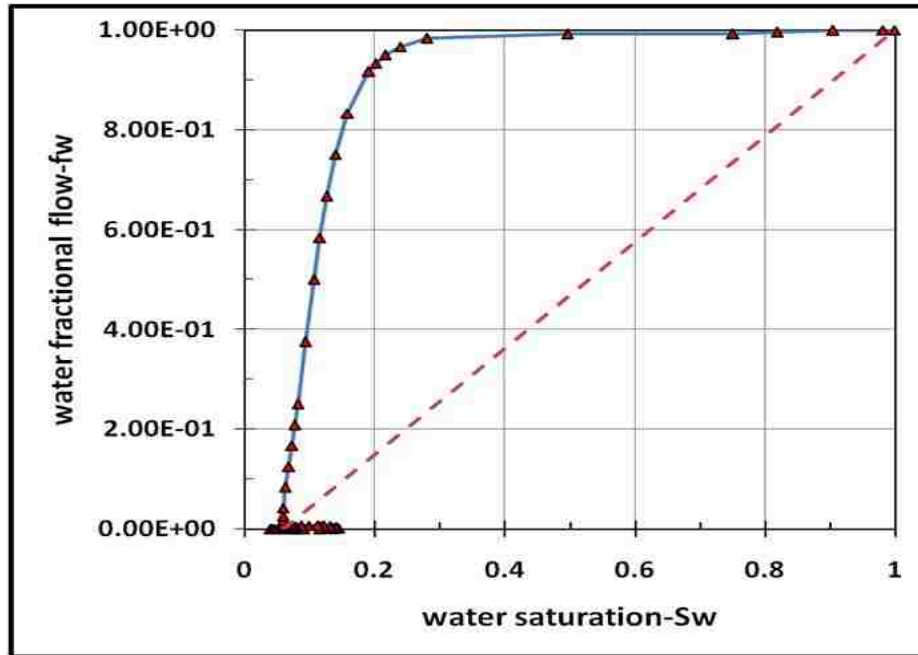
(b)

Figure 4.3 Results from dynamic simulation (solid line) and fractional flow analysis (dashed line) of gas injection at $u_t = u_g = 2.8 \times 10^{-5}$ m/s: (a) saturation profile and (b) foam texture profile (n_f in m^{-3})

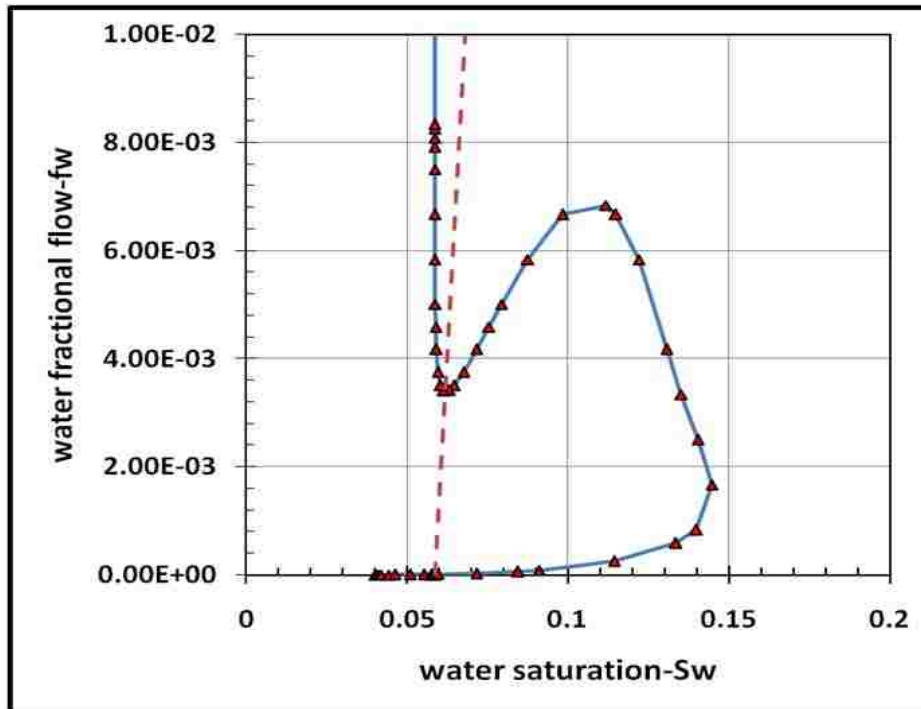
creation and coalescence as gas invades surfactant water-saturated regions. This does not occur in the fractional flow analysis because of its local steady-state approach (see Dholkawala et al. (2007) for more details); and (2) There exist some spreading in saturation (Fig. 4.3(a)) and some offset in foam texture (Fig. 4.3(b)) at the shock front, which can be reduced and eventually eliminated as grid-block size decreases. The former has a significant implication to strong-foam simulations, as is further described in later sections. Note that n_f is assigned to be zero for the region ahead of the shock front because no gas is present there (i.e., $S_w = 1$).

Fig. 4.4 shows a mechanistic fractional flow curve at $u_g = 1.2 \times 10^{-4}$ m/s which leads to strong-foam propagations. In contrast to Fig. 4.2 at $u_g = 2.8 \times 10^{-5}$ m/s, Fig. 4.4 shows that the fractional flow curve is now all connected. This fractional flow curve at relatively high injection velocity has two important characteristics: (1) An intermediate foam state (i.e., the portion from $(S_w, f_w) = (0.06, 3.4 \times 10^{-3})$ to $(S_w, f_w) = (0.11, 6.8 \times 10^{-3})$ in Fig. 4.4(b) cannot be the solution for fixed-rate injection due to its inherent instability (Gauglitz et al., 2002; Kam et al., 2007); and (2) Any part that has a negative slope (i.e., $df_w/dS_w < 0$) in f_w vs. S_w domain might be valid mathematically but not meaningful physically (Rossen and Bruining, 2007). As a result, a reconstructed fractional flow curve after removing those unphysical segments is made up of two distinct and separate curves – (i) strong-foam part from $(S_w, f_w) = (1, 1)$ to $(S_w, f_w) = (0.058535, 8.33 \times 10^{-3})$ and (ii) weak-foam part from $(S_w, f_w) = (0.145, 1.6 \times 10^{-3})$ to $(S_w, f_w) = (0.04, 0)$ of the fractional flow curve in Fig. 4.4. Note that a resulting fractional flow curve reconstructed in this way is very similar to that shown in Fig. 2.8.

Rossen and Bruining (2007) suggest that in the case of strong-foam propagation, the state behind a shock should be the lowest point of the almost-vertical section of strong-foam fractional flow curve (i.e., about $(S_w, f_w) = (0.058535, 8.33 \times 10^{-3})$ in Fig. 4.4(b); cf. Fig. 2.8) followed by



(a)

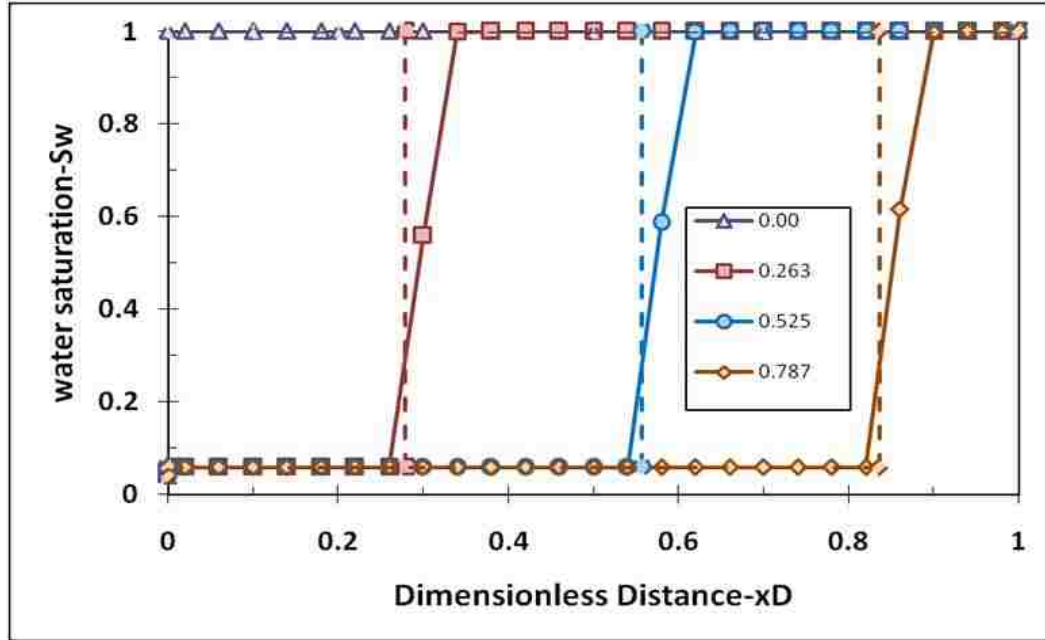


(b)

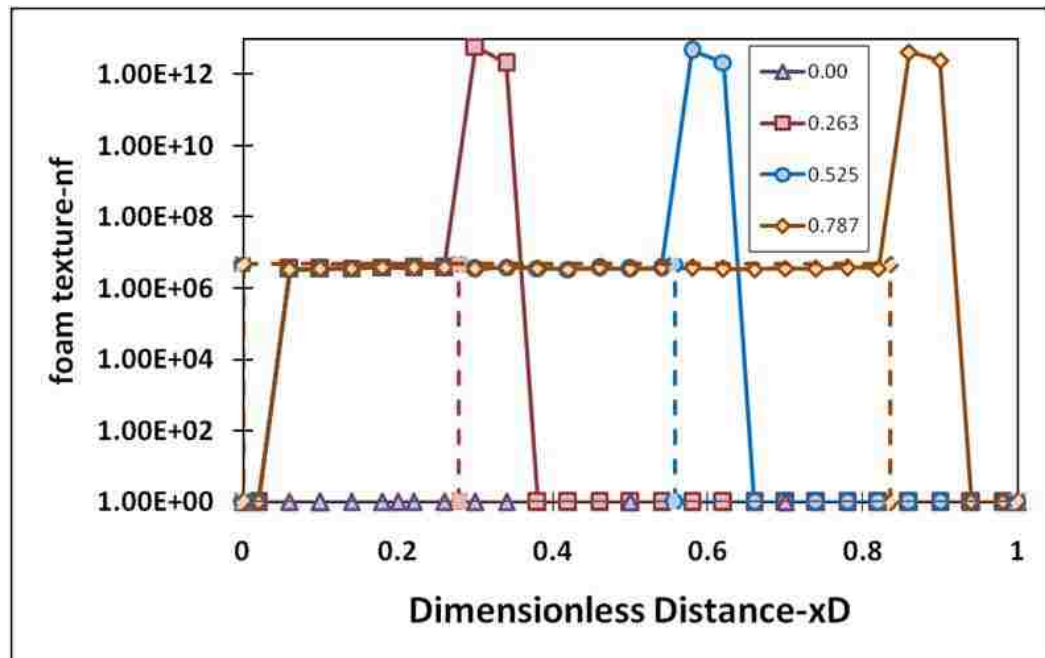
Figure 4.4 Mechanistic foam fractional flow curve at $u_t = u_g = 1.2 \times 10^{-4}$ m/s: (a) entire graph and (b) magnified view near the shock front

another spontaneous jump to the weak-foam part of the fractional flow curve at the same capillary pressure (or at the same water saturation if capillary hysteresis is not present, equivalently). Because this study assumes no hysteresis in capillary pressure, this means that the jump from strong-foam to weak-foam segment, which takes place from $(S_w, f_w) = (0.058535, 8.33 \times 10^{-3})$ to $(S_w, f_w) = (0.058535, 7.28 \times 10^{-6})$ in Fig. 4.4, occurs at the same water saturation (or equivalently, at the same P_c). For the purpose of graphical construction of fractional flow solution, the first jump from I to $(S_w, f_w) = (0.058535, 8.33 \times 10^{-3})$ and the consecutive second jump to $(S_w, f_w) = (0.058535, 7.28 \times 10^{-6})$ can be represented by one straight line from I to $(S_w, f_w) = (0.058535, 7.28 \times 10^{-6})$ as shown in the dashed straight line in Fig. 4.4(b). The shock is followed by very slowly moving spreading waves until the saturation reaches S_{wc} . Additional discussions on the construction of fractional flow solutions for different cases are given in section 4.4.

Fig. 4.5 shows a comparison between simulation results and fractional flow solutions. Good agreement is observed between them in terms of water saturation (Fig. 4.5(a)) and foam texture (Fig. 4.5(b)), successfully capturing the position of the shock and the saturation and foam texture behind the shock. In contrast to the case of weak foam in Fig. 4.3(b), foam texture in strong foam (Fig. 4.5(b)) exhibits a much higher peak in foam texture because active lamella creation at the gas front always pushes n_f to its maximum. Note that the maximum foam texture (n_{fmax}) in this study is set to be $8 \times 10^{13} \text{ m}^{-3}$ following the measurements of pore sizes in the previous study (Kam and Rossen, 2003). Although the hump of n_f at the foam front seems well simulated, the highest peak in foam texture in Fig. 4.5(b), which range from 1.5×10^{12} to $2 \times 10^{12} \text{ m}^{-3}$, is still lower than n_{fmax} because of a relatively coarse grid system used in simulations. The profile of foam texture with a hump in Figs. 4.3(b) and 4.5(b) was confirmed by earlier experimental study of Kovscek et al. (1995) in which nitrogen gas was injected into a surfactant-



(a)

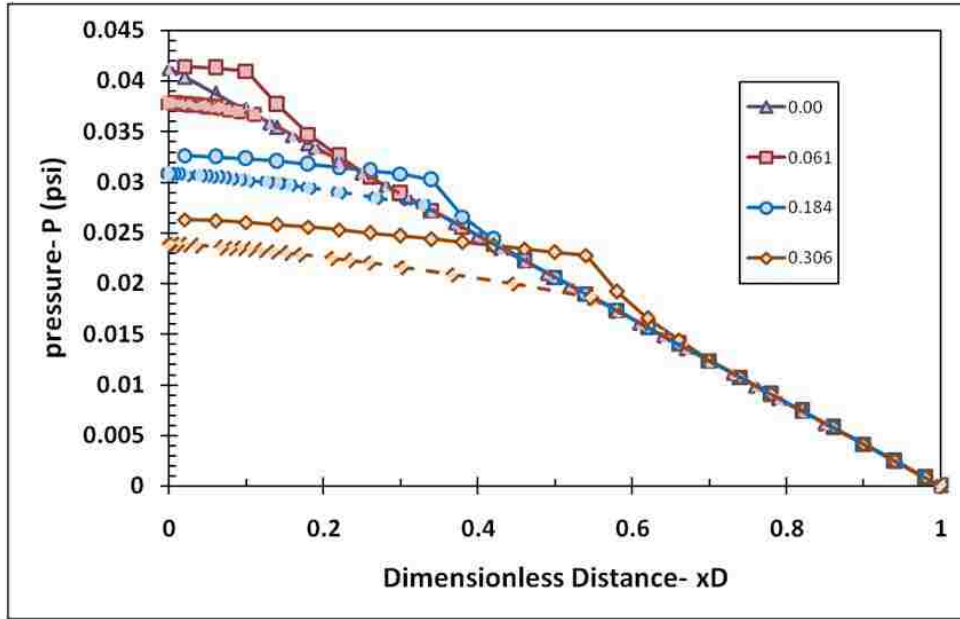


(b)

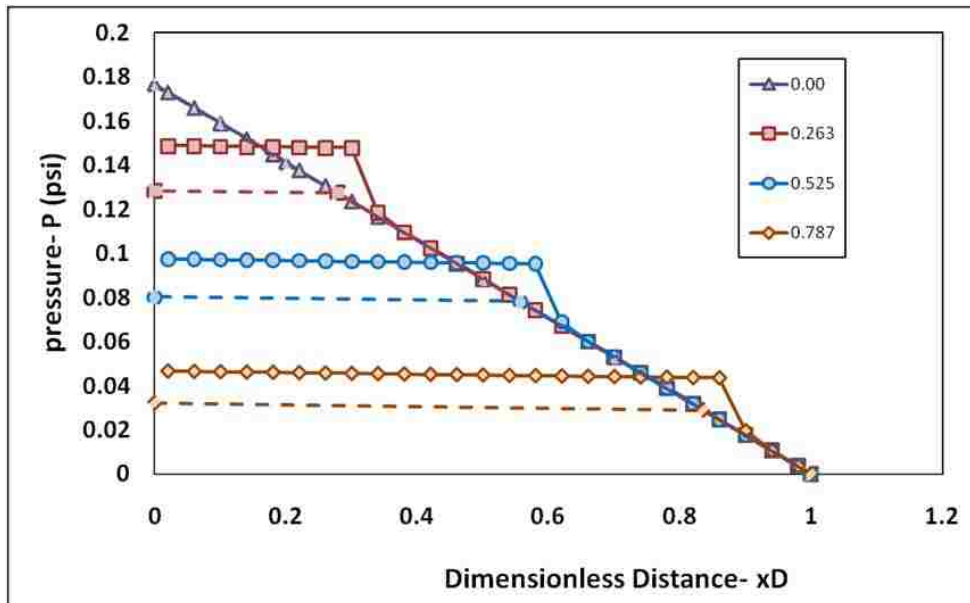
Figure 4.5 Results from dynamic simulation (solid line) and fractional flow analysis (dashed line) of gas injection at $u_t = u_g = 1.2 \times 10^{-4}$ m/s: (a) saturation profile and (b) foam texture profile (n_f in m^{-3})

saturated sandstone in SAG processes. As reported by Dholkawala et al. (2007), the peak in n_f shown in Fig. 4.5(b) reflects the fact that complicated foam dynamics takes place very actively at the leading edge of gas bank over a narrow region. These dynamic mechanisms are summarized as follows: (1) As the gas phase advances into a new grid block saturated with water, lamella creation (r_g) increases rapidly due to the increase in local pressure gradient (cf. Eq. 3.5); (2) The rise in r_g causes an increase in foam texture (n_f) and a reduction in water saturation (S_w) (cf. Eq. 3.7); (3) As the medium dries out and S_w reduces down to near S_w^* (still $S_w > S_w^*$) due to the formation of fine-textured foam, the rate of lamella coalescence (r_c) starts to increase rapidly, essentially leading to foam mechanisms dominated by bubble coalescence (cf. Eq. 3.6); and (4) Once the system undergoes these dynamic behaviors, n_f falls down rapidly reaching a local-steady-state n_f value (cf. Eq. 3.7). The fact that fractional flow analysis cannot reproduce this peak in n_f due to its local steady-state assumption has a huge impact eventually, by limiting the use of fractional flow analysis for SAG processes as is discussed in later sections.

Pressure profiles as a function of dimensionless distance shown in fig 4.6 at different values of PVI (pore volume injection), one at low injection velocity $u_g = 2.8 \times 10^{-5}$ m/s (Fig. 4.6(a); cf. Fig. 4.2) and the other at high injection velocity $u_g = 1.2 \times 10^{-4}$ m/s (Fig. 4.6(b); cf. Fig. 4.4). As demonstrated by the strong-foam case (Fig. 4.6(b)), there are two important the strong-foam case (Fig. 4.6(b)), two important aspects should be emphasized: (1) The pressure profile from fractional flow analysis is different from mechanistic simulation in that the sharp increase in pressure gradient at the foam front in simulation, which results from the peak in n_f (cf. Fig. 4.5(b)), does not appear in fractional flow solutions; and (2) although the simulation result captures part of the change in pressure gradient at the gas front, the simulation fails to capture its magnitude accurately. The sharp change in pressure at the foam front, which roughly ranges from 0.02 to 0.03 psi in Fig. 4.6(b), would have been much more significant (i.e., one or two



(a)



(b)

Figure 4.6 Pressure profiles from dynamic simulations (solid line) and fractional flow analysis (dashed line) during gas injection: (a) $u_t = u_g = 2.8 \times 10^{-5}$ m/s and (b) $u_t = u_g = 1.2 \times 10^{-4}$ m/s (1 psi = 6,900 Pa)

orders of magnitude difference) if the simulation had captured the maximum foam texture (i.e., $n_{f\max} = 8 \times 10^{13} \text{ m}^{-3}$) in Fig. 4.5(b). Closely looking into the weak-foam case (Fig. 4.6(a)), the same problem (i.e., failing to capture the peak in n_f) may occur with weak foams, but the impact is not as significant as that with strong foams because the variation in n_f between the peak and behind the foam bank (i.e., 2.0×10^{11} vs. $1.5 \times 10^{10} \text{ m}^{-3}$ in Fig. 4.3(b)) is less pronounced with weak-foam than with strong-foam (i.e., 8.3×10^{13} vs. $3.5 \times 10^6 \text{ m}^{-3}$ in Fig. 4.5(b)). In other words, a relatively gradual hump of n_f at the leading edge of gas bank for weak foams allows dynamic simulations to capture the change in n_f reasonably well, whereas a very sharp hump of n_f for strong foams does not.

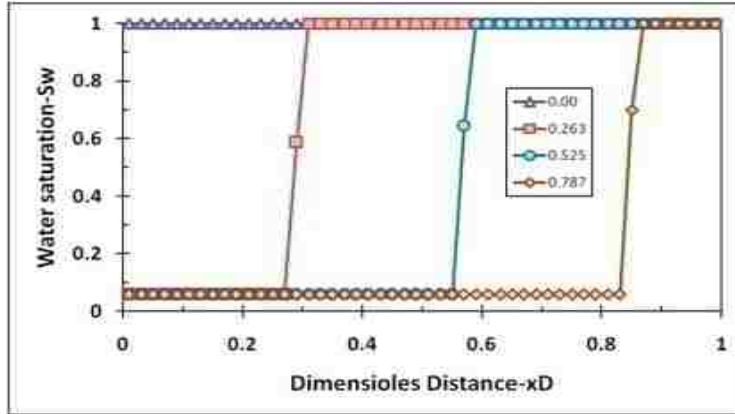
Dynamic simulations and fractional flow analysis (Fig. 4.6) have similar pressure gradient except in the vicinity of the front, where differences in foam dynamics in the simulation are not represented in the fractional flow model. This is because the fractional flow solutions are valid if foam dynamics are relatively muted - there is no foam ahead of shock front, and there is no active lamella creation and coalescence taking place behind the shock due to very dry conditions (i.e., S_w is greater than S_w^* but very close to S_w^*).

4.3. Modification of Pressure Profile at the Leading Edge of a Strong-Foam Front

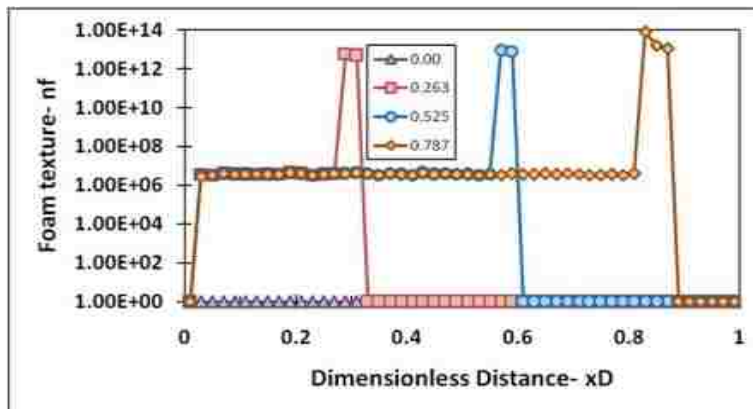
Simulation efforts in finer grid block systems investigated strong-foam propagation. The profiles of water saturation (S_w) and foam texture (n_f) with 50 grid blocks are different from those with 25 grid blocks (Figs. 4.5 and 4.7). The profiles of water saturation in Figs. 4.5(a) and 4.7(a) are consistent, except for the change in S_w at the foam front becoming sharper (as expected as Δx decreases). This suggests that the simulation results are converging to the analytical solution (cf. dotted lines in Fig. 4.5(a)). The peak in n_f is becoming narrower as the

number of grid blocks increases (Figs. 4.5(b) and 4.7(b)). The pressure profile (Fig. 4.7(c)) shows that even with a finer grid, the pressure change at the foam front is not captured in simulations.

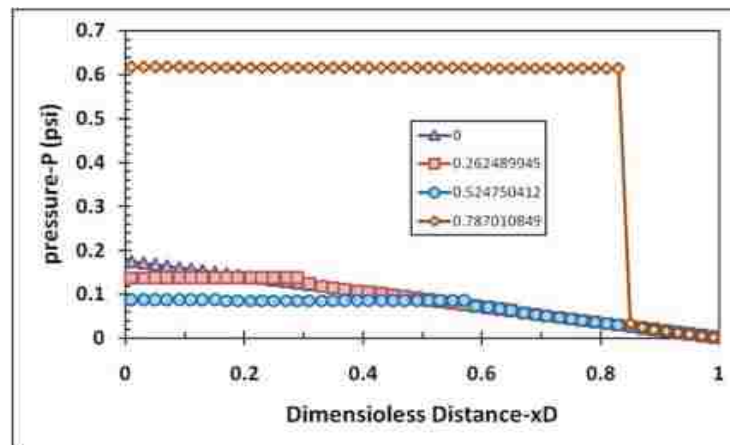
There are few significant implications in the calculation of pressure profile during strong-foam propagation (Fig. 4.7). First, the sharp change at the leading edge of gas bank is a discontinuity (the change might occur over a finite distance in the presence of capillary pressure gradient which is, however, assumed to be negligible in this study), but it tends to spread in simulations due to numerical dispersion in the finite difference calculations. This feature is explained that the peak in n_f at the foam front widens as the grid system becomes coarser (Fig. 4.8(a)). This indicates that the smearing at the front is caused by numerical diffusion, not by physical dispersion. Second, even with finer grid systems, there is no guarantee that the simulation can capture the peak in n_f (i.e., reaching $n_{f\max} = 8 \times 10^{13} \text{ m}^{-3}$) consistently at all time steps. This aspect is illustrated in the schematic (Fig. 4.8(b)) in which the dotted line is a plausible representation of n_f profile if infinite number of grid blocks is used, and the solid line is the profile captured by simulation with a finite-grid system. Although simulation follows the plausible n_f profile reasonably well, the deviation from the true response can be quite significant, failing to capture the maximum foam texture. The peak in n_f in Fig. 4.5(b) would have reached $n_{f\max} = 8 \times 10^{13} \text{ m}^{-3}$, if the grid block size had been infinitesimally small. Third and finally, although the simulation captures the trend of the n_f profile correctly in a discretized system (Fig. 4.8(b)), the resulting pressure gradient at the leading edge of the gas front (which is very sensitive to n_f and μ_g^f ; cf. Eqs. 3.15 and 3.17) can vary significantly depending on how well the peak of n_f is simulated. This numerical artifact of a discretized system is illustrated in Figs. 4.7(b) and 4.7(c): when $n_{f\max}$ is not captured at $t_D = 0.263$ and 0.525 in Fig. 4.7(b), the pressure drop at the gas front is significantly underestimated compared to the pressure drop at $t_D = 0.787$



(a)



(b)



(c)

Figure 4.7 Results from dynamic foam simulations at $u_t = u_g = 1.2 \times 10^{-4}$ m/s with 50 grid blocks in contrast to the results with 25 grid blocks in Figs. 8(a), 8(b) and 9(b) : (a) water saturation, (b) foam texture (n_f in m^{-3}), and (c) pressure profile (1 psi = 6,900 Pa)

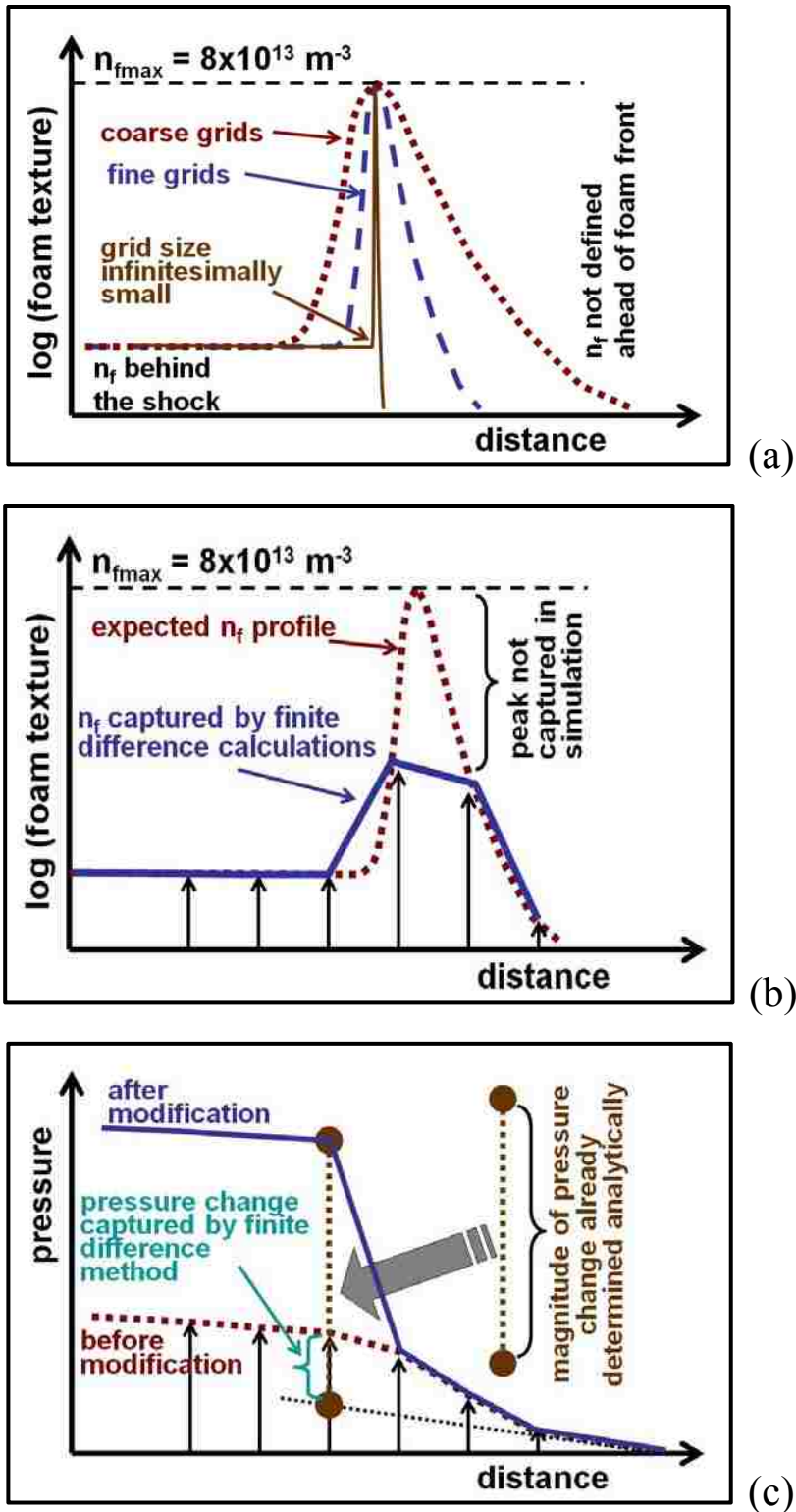


Figure 4.8 Schematic figures to demonstrate the need for pressure modification: (a) effect of grid block size, (b) limitation of discretized system, and (c) modification of pressure response

(Fig. 4.7(c)). Because most pressure drop during gas injection occurs at the strong foam front (cf. $t_D = 0.787$ in Fig. 4.7(c)) and the inlet injection pressure is the only indicator to judge the formation of strong foams in situ during SAG processes, the sensitivity of pressure response to the number of the grid blocks should be modeled properly.

To resolve these unrealistic and unreliable pressure profiles, an algorithm that modifies the pressure response is developed (Fig. 4.8(c)). This pressure modification algorithm resolves the pressure gradient at the leading edge of strong-foam front can be calculated analytically by constructing a mechanistic foam fractional flow curve (Figs. 4.2 and 4.4) and therefore used as an input parameter for simulations. Determining the pressure gradient (and the magnitude of pressure change, equivalently) at the front is possible because: (1) the highest pressure gradient at the strong-foam front coincides with the maximum foam texture (i.e., the peak in n_f , or n_{fmax} , in Fig. 4.8(b)), and thus can be calculated by Eqs. 3.14, 3.15 and 3.17 using corresponding values of S_w and f_w (Fig. 4.4(b)); and (2) the magnitude of pressure change at the front is primarily governed by n_{fmax} rather than the shape of n_f peak - for example, correctly capturing n_{fmax} at $t_D = 0.787$ in Fig. 4.7(b) gives in a realistic pressure response (Fig. 4.7(c)), while missing n_{fmax} at $t_D = 0.263$ and 0.525 (Fig. 4.7(b)) implies an unrealistic pressure response (Fig. 4.7(c)). Fig. 4.7(b) is in log scale and, as a result, the pressure response at the foam front in Fig. 4.7(c) is extremely sensitive to a small change in n_f . The condition that offers the highest pressure gradient does not necessarily have to be the lowest point in the vertical section of the reconstructed strong-foam fractional flow curve after removing unphysical parts (Fig. 4.4(b)). Therefore, the construction of fractional flow solution from I (initial condition) to the lowest point of the vertical strong-foam section, as discussed in Fig. 4.4, does not necessarily capture the highest pressure gradient. If this happens, the pressure response at the foam front tends to be underestimated.

Once the highest pressure gradient is provided, the magnitude of pressure change at the leading edge can be modified as follows (Fig. 4.8(c)): If the magnitude of this pressure change is represented by the vertical dotted line with two filled circles, the mechanistic simulation predicts pressure profile shown by dotted lines (“before modification”, Fig. 4.8(c)), the the pre determined magnitude of the pressure change can added to the pressure profile such that the “modified” pressure profile is accurate at the foam front. Because the sharp pressure change at the front occurs over a few grid blocks in finite-difference calculations, this pressure modification is imposed on the grid block nearest the inlet using the residual of the pressure change not claimed by grid blocks downstream (“after modification” in Fig. 4.8(c)). This method is appealing because (1) the pressure modification procedure does not interfere with the numerical calculations; the current algorithm in the simulations does not require pressure values (it uses the pressure gradient) and (2) there is no change in the pressure profile except for one grid block at which the previously not modeled portion of the pressure change is added (Fig. 4.8(c)). The pressure profile downstream of this grid block is not affected by this pressure modification, and the pressure profile upstream of this grid block (i.e., towards inlet) shifts the profile from “before modification” to “after modification” by the same magnitude as shown in Fig. 4.8 (c).

The magnitude of pressure change at the strong-foam front in mechanistic simulations also depends on the grid block size because the pressure change is calculated by the multiplication of the highest pressure gradient and the width of one grid block. This implies that simulations with a coarse grid system overestimate the inlet injection pressure compared to those with a fine grid system. This overestimation can be reduced by using small grid blocks.

The pressure change at the front after the modification is significantly higher than that before modification (Fig. 4.9 vs. 4.8). Pressure modification improves predictions of inlet injection

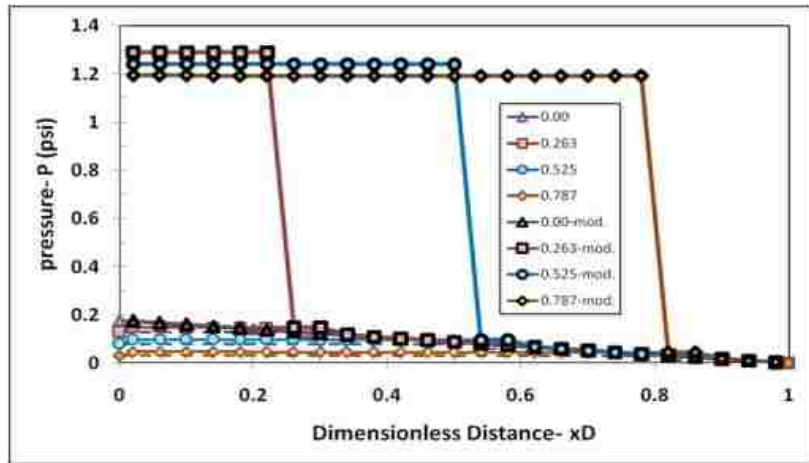
pressure history (Fig. 4.9(c)). The inlet pressure before the modification fluctuates. The simulated inlet pressure decreases as the peak in n_f hump moves away from a grid block (i.e., underestimation of the pressure change at the front), and increases as the peak approaches next grid block (i.e., reduction of such underestimation). This spiky up-and-down pattern of the inlet injection pressure repeats continuously, as the wave of strong-foam front propagates from the inlet to the outlet. If the pressure response is modified, the inlet pressure changes smoothly and monotonically (thick lines in Fig. 4.9(c)) except for the early time period during which in-situ strong foam generation is taking place through active lamella-creation mechanism and the inlet injection pressure builds up significantly.

4.4. Behaviors at Intermediate Injection Velocities

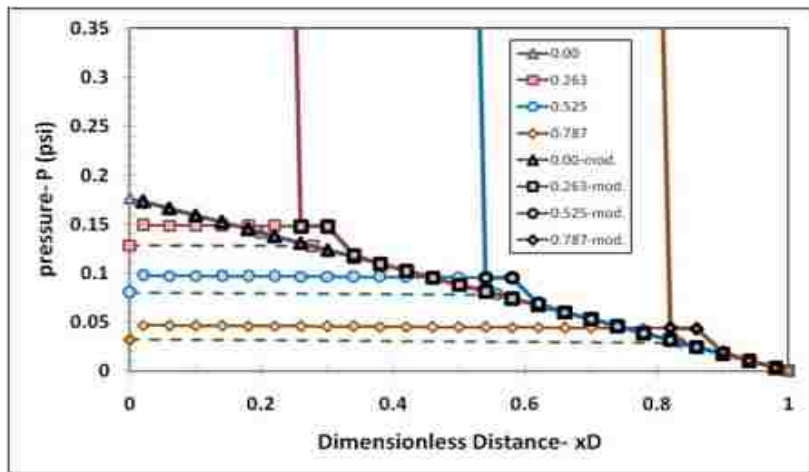
The results (Figs. 4.2- 4.5) show two extremes, illustrating weak-foam propagation at low injection velocity and strong-foam propagation at high injection velocity.

This section shows the behaviors of fractional flow solutions and mechanistic simulation results for the intermediate injection velocities in between (i.e., $2.8 \times 10^{-5} \text{ m/s} < u_g < 12.0 \times 10^{-5} \text{ m/s}$).

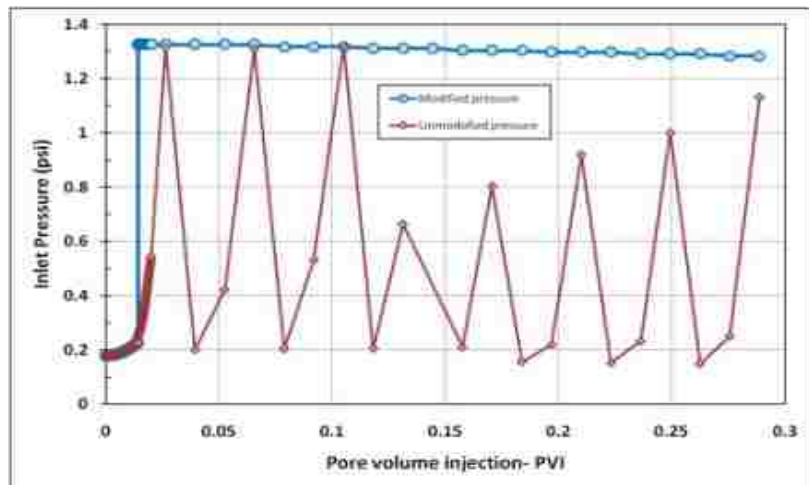
Fractional flow curves at three different injection velocities ($u_g = 3.3 \times 10^{-5}$, 4.0×10^{-5} , and $4.2 \times 10^{-5} \text{ m/s}$; Fig. 4.10) which lead to weak foam propagation in dynamic foam simulations. Except for some minor differences (Figs. 4.10(a) and 4.10(b) have fractional flow curves with isolated loops and Fig. 4.10(c) has a connected fractional flow curve), they are essentially the same. They exhibit two possible solution paths for gas injection: one, strong-foam propagation represented by the near vertical part of the curve in the far left-hand side, and the other weak-form propagation represented by the curve in the far right-hand side. Figs. 4.11(a), 4.11 (b), and 4.11 (c) show saturation profiles at $u_g = 3.3 \times 10^{-5}$, 4.0×10^{-5} , and $4.2 \times 10^{-5} \text{ m/s}$ following Figs.



(a)



(b)



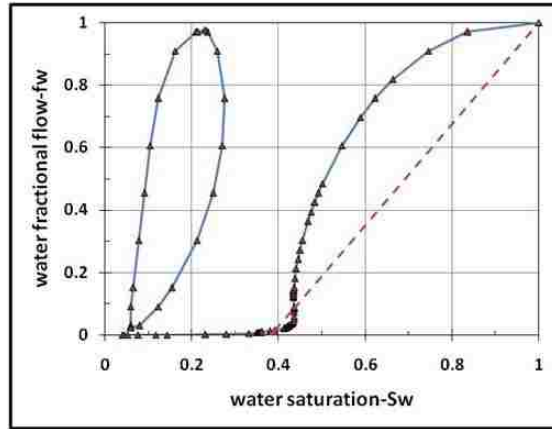
(c)

Figure 4.9 Simulation results with pressure modification at $u_t = u_g = 1.2 \times 10^{-4}$ m/s: (a) pressure profiles before and after modification, (b) magnified view at the strong-foam front, and (c) inlet injection pressure histories before and after modification (1 psi = 6,900 Pa)

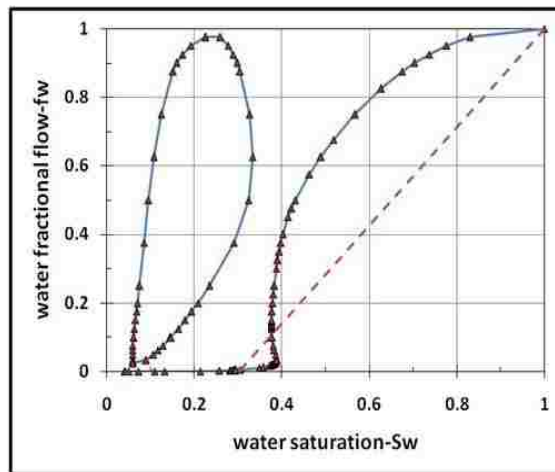
4.10(a), 4.10(b), and 4.10(c), respectively. The comparison between the simulation (solid line) and fractional flow results (dashed line) (Fig. 4.11) shows good agreement in terms of shock velocity (or, shock position) and water saturation behind and ahead of the shock. The same consistency is observed in Figs. 4.12 and 4.13, showing the simulated results in terms of foam texture (n_f) and pressure profile in contrast to the fractional flow solutions.

The responses in these three injection velocities are similar to those in Figs. 4.2, 4.3 and 4.6(a) with $u_g = 2.8 \times 10^{-5}$ m/s, except that the solution path for weak-foam propagation is not a tangent from the initial condition (i.e., $(S_w, f_w) = (1, 1)$) to the weak-foam part of fractional flow curve. This is a deviation from the conventional fractional flow analysis [Lake, 1989] and has not been reported previously. Investigations into the simulation results on the condition behind the saturation shock reveals that the line connecting the initial condition and the condition behind the shock in f_w vs. S_w domain passes through the point at which df_w/dS_w turns from a positive to negative dashed line in Figs. 4.10(a) through 4.10(c).

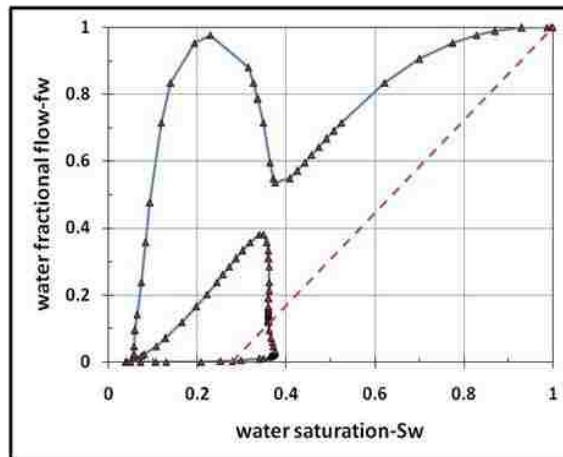
The schematics in Fig. 4.14 clarify the construction of a shock wave. When the injection velocity is very low, the fractional flow curve does not have a region with negative df_w/dS_w and the shock front can be constructed from the initial condition to the corner at high S_w and low f_w using a tangent (dashed straight line in Fig. 4.2). As the injection velocity increases, the fractional flow curve starts to bend as shown in Fig. 4.14(a) and exhibits three regions with $df_w/dS_w > 0$ at high f_w , $df_w/dS_w < 0$ at intermediate f_w , and $df_w/dS_w > 0$ at low f_w . (Any region with $df_w/dS_w < 0$ is physically unstable and therefore is an imaginary part as described in earlier section.) These three regions are split by the two horizontal lines in Fig. 4.14(a) as denoted by “A: $dS_w/df_w = 0$ ” and “B: $dS_w/df_w = 0$ ”. (Between the two, the one at the lower f_w is called A.) In this case, the construction of a shock front to the nose (i.e., at high S_w and low f_w) does not satisfy the mass conservation (cf. Eq. 3.1); instead the mass conservation appears to force the



(a)



(b)



(c)

Figure 4.10 Mechanistic fractional flow curves leading to weak-foam propagation in simulation: (a) $u_g = 3.3 \times 10^{-5}$ m/s, (b) $u_g = 4.0 \times 10^{-5}$ m/s, and (c) $u_g = 4.2 \times 10^{-5}$ m/s

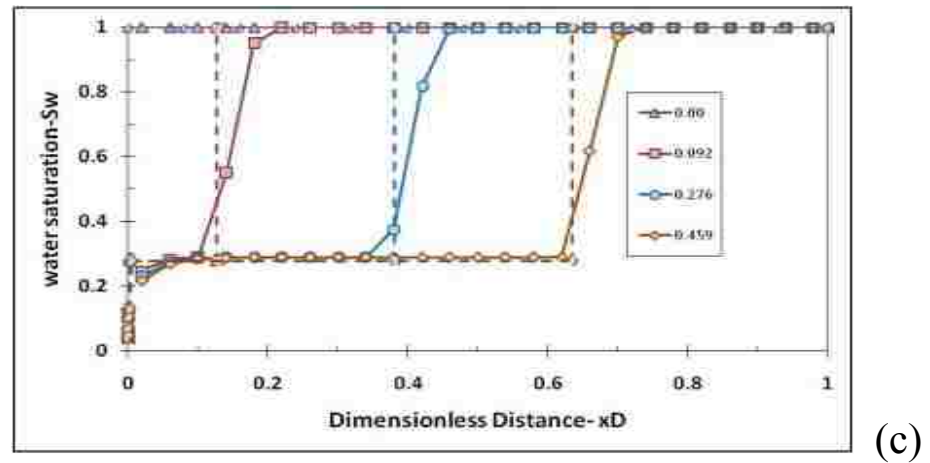
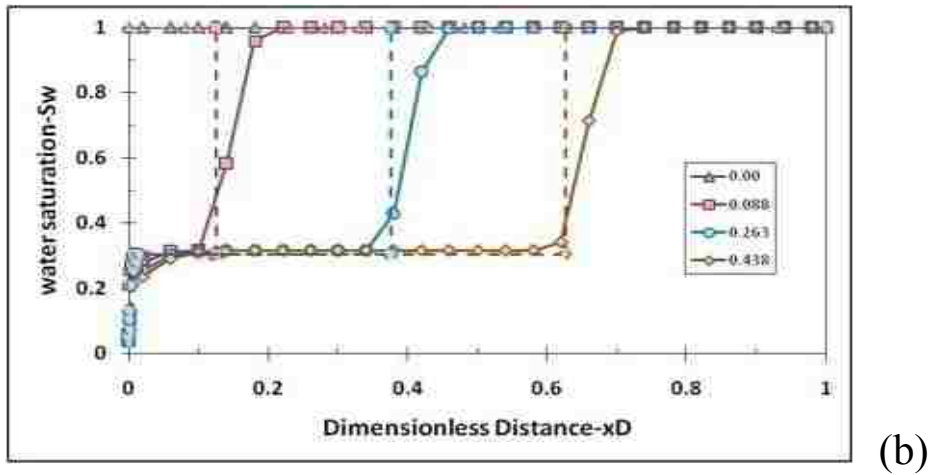
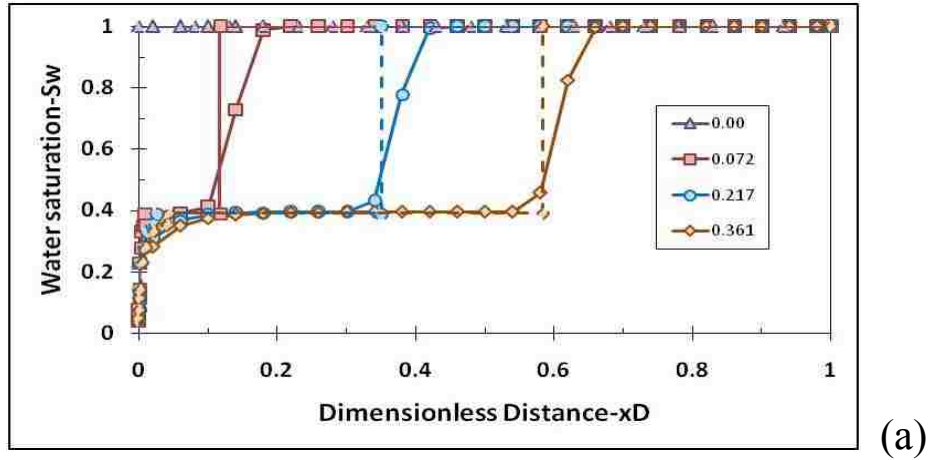


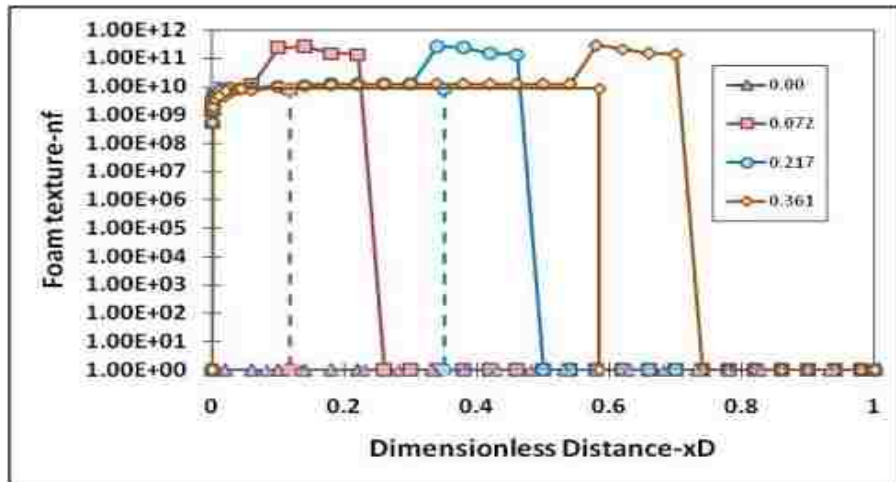
Figure 4.11 Water saturation profile from mechanistic simulations (solid line) and fractional flow analysis (dashed line): (a) $u_g = 3.3 \times 10^{-5}$ m/s, (b) $u_g = 4.0 \times 10^{-5}$ m/s, and (c) $u_g = 4.2 \times 10^{-5}$ m/s

straight line to be constructed through point B (Fig. 4.14(a)). The condition behind a shock is determined by the intersection between the straight line and the lower part of fractional flow curve. Further increases in injection velocity result in fractional flow curves connected (Fig. 4.14(b)). Although the curve looks more complicated, the same solution scheme applies, i.e., drawing a straight line from I through the point B to identify the condition behind the shock. In both Figs. 4.14(a) and 4.14(b), there are slow spreading waves from the condition behind the shock to the injection condition (i.e., $(S_w, f_w) = (S_{wc}, 0)$).

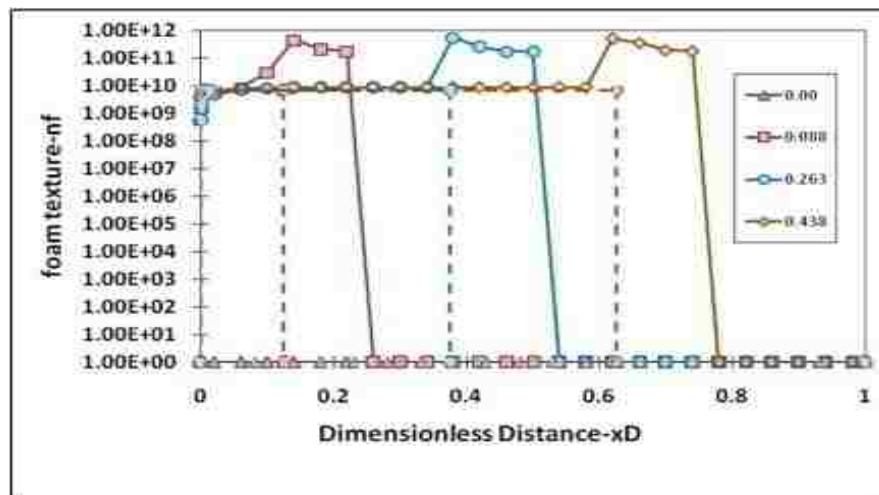
The deviation from the conventional fractional flow analysis occurs when the weak-foam fractional flow curve moves back and forth showing both $df_w/dS_w > 0$ and $df_w/dS_w < 0$ regions. The construction of fractional flow solution is still from a tangent line when there is no change in the slope of df_w/dS_w at low injection velocities (i.e., $df_w/dS_w > 0$ at all S_w values; cf. Fig. 4.2) just like the conventional fractional flow analysis. It is not clear at this stage what causes this deviation and what the implications of this behavior are. The solution for weak-foam propagation suggested above abides by the mass conservation explained in Eq. 3.1.

Fractional flow curves at three different injection velocities ($u_g = 5.3 \times 10^{-5}$, 7.0×10^{-5} , and 1.0×10^{-4} m/s; Fig. 4.15) lead to strong-foam propagation in simulations. The case of $u_g = 5.3 \times 10^{-5}$ m/s is simulated with 150 grid blocks because of its proximity to the injection velocity at which foam generation occurs and therefore numerical calculations become less stable. Corresponding responses in terms of saturation and foam texture are shown in Figs. 4.16 and 4.17. As discussed in Fig. 4.8, the advance of foam front is well simulated, but the maximum foam texture is not always guaranteed to capture.

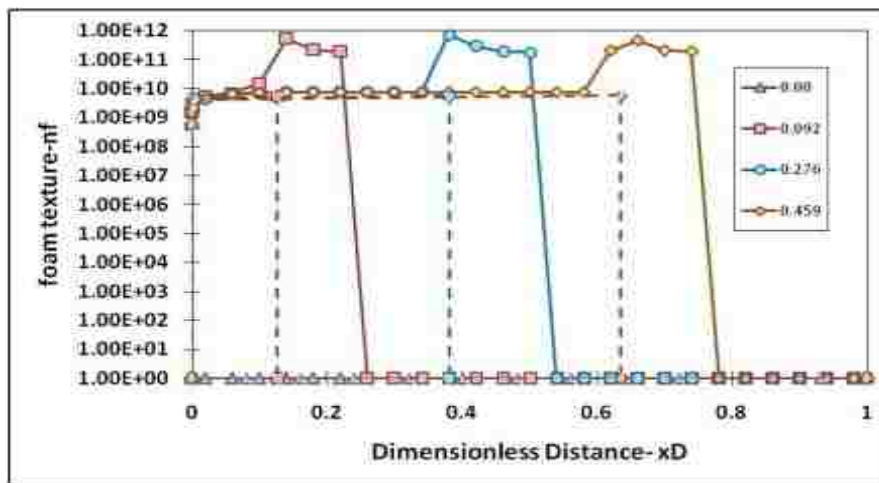
Fig. 4.18 shows schematics of fractional flow solutions for strong-foam propagation. As shown and explained in Fig. 4.4, the fractional flow curve at higher injection velocity tends to be all connected and shifted to the left so that the small bulge that represents weak-foam and



(a)

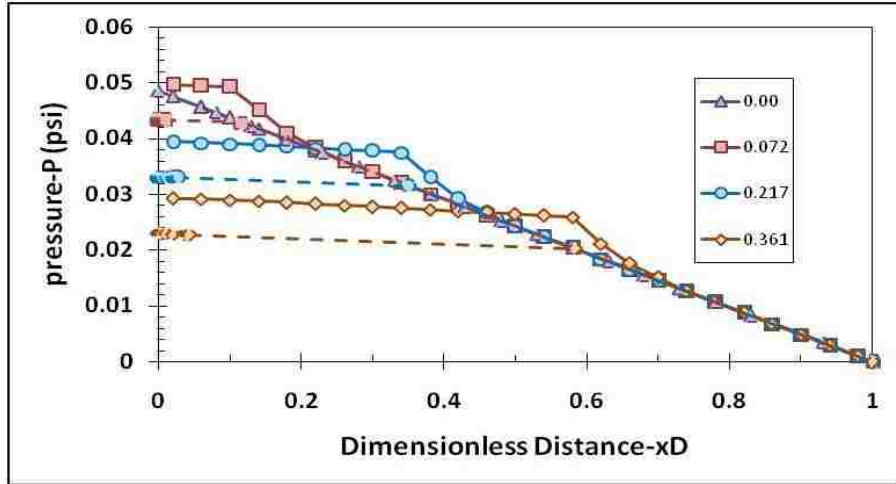


(b)

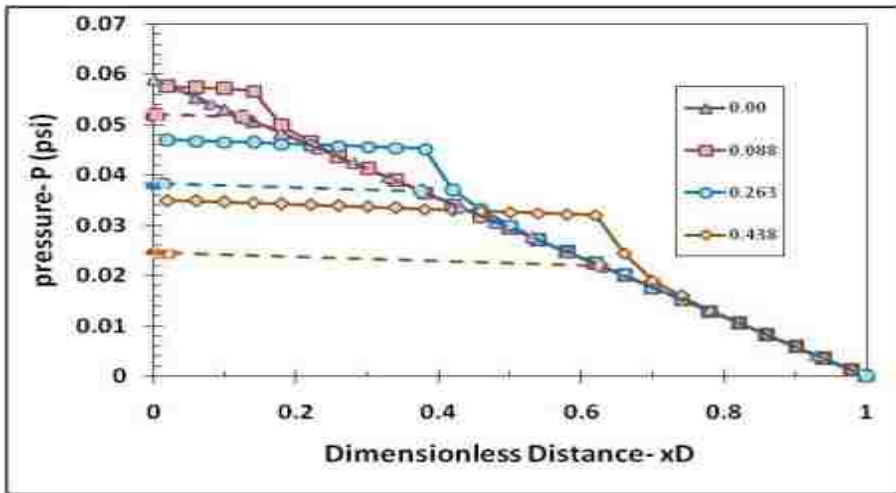


(c)

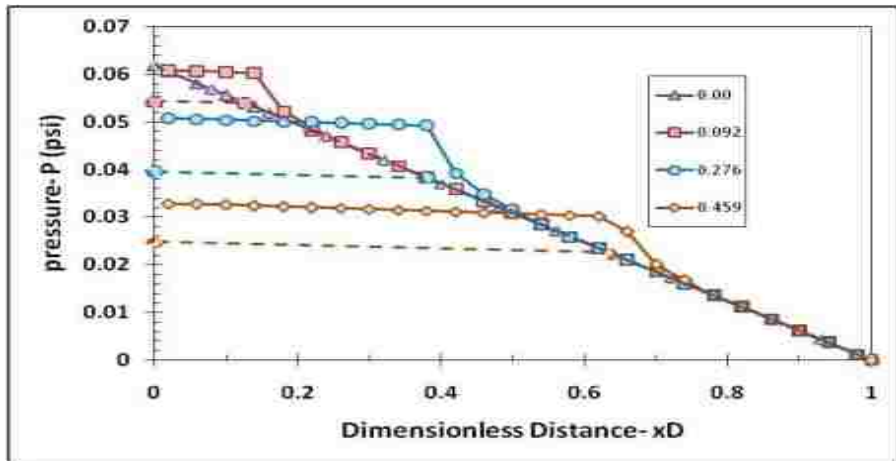
Figure 4.12 Foam texture profile from mechanistic simulations (solid line) and fractional flow analysis (dashed line): (a) $u_g = 3.3 \times 10^{-5}$ m/s, (b) $u_g = 4.0 \times 10^{-5}$ m/s, and (c) $u_g = 4.2 \times 10^{-5}$ m/s (n_f in m^{-3})



(a)



(b)



(c)

Figure 4.13 Pressure profile from mechanistic simulations (solid line) and fractional flow analysis (dashed line): (a) $u_g = 3.3 \times 10^{-5}$ m/s, (b) $u_g = 4.0 \times 10^{-5}$ m/s, and (c) $u_g = 4.2 \times 10^{-5}$ m/s (1 psi = 6,900 Pa)

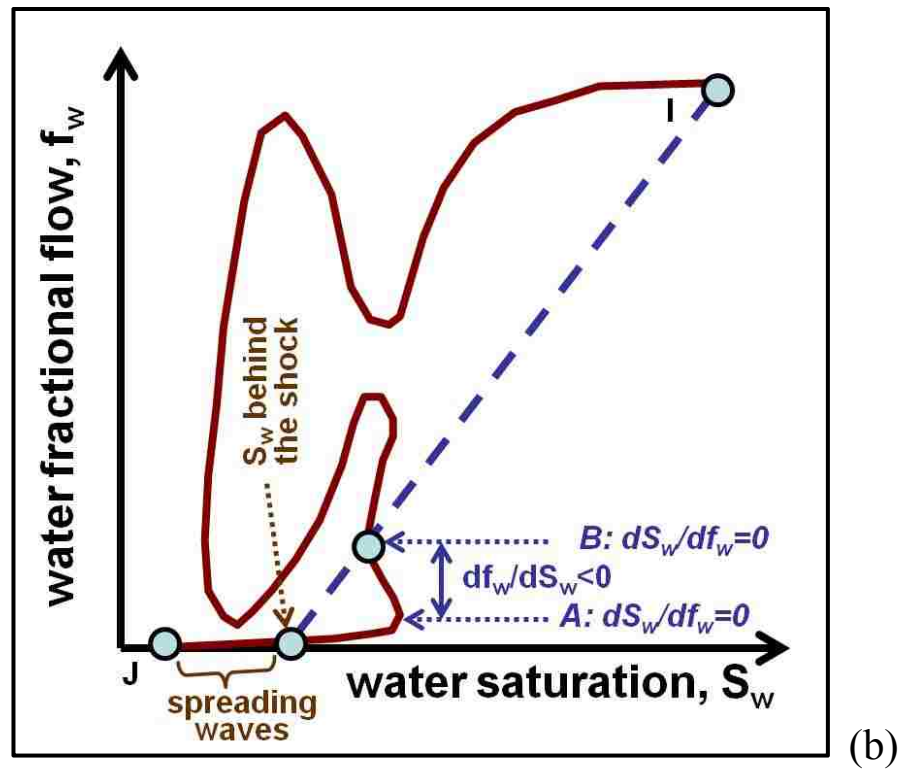
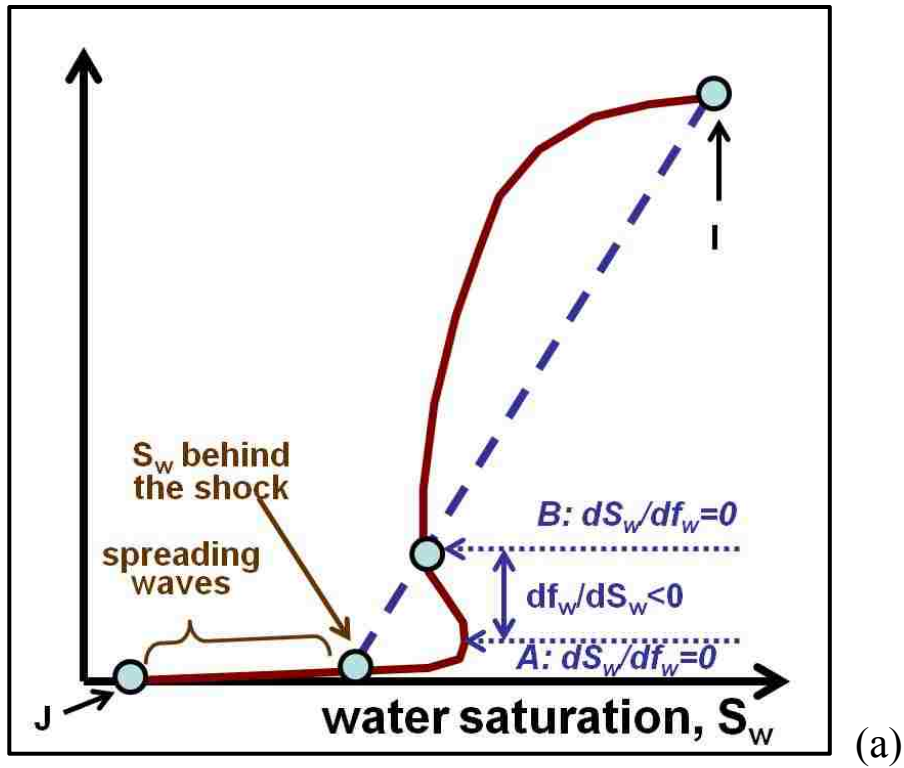


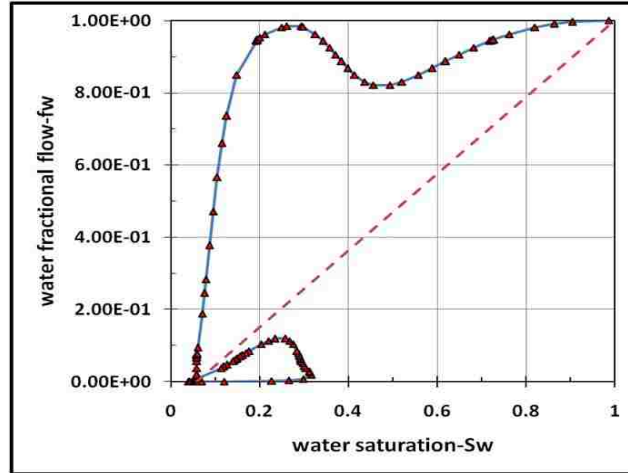
Figure 4.14 Schematic figures showing fractional flow analysis during weak-foam propagation.

intermediate states becomes smaller. The simulations in this study indicate that the condition behind the shock is consistent with point B which is shifted vertically from point A as illustrated in Fig. 4.18(b). Note that point A is the point at which there is a change in slope of the mechanistic fractional flow curve from $df_w/dS_w > 0$ to $df_w/dS_w < 0$ along the vertical segment. (This vertical shift from A to B in Fig. 4.18(b) is consistent with a jump at the same capillary pressure described by Rossen and Bruining (2007).) Saturation values at point A and point B in Fig. 4.18(b) are very close to the limiting water saturation S_w^* , if strong foam is formed.

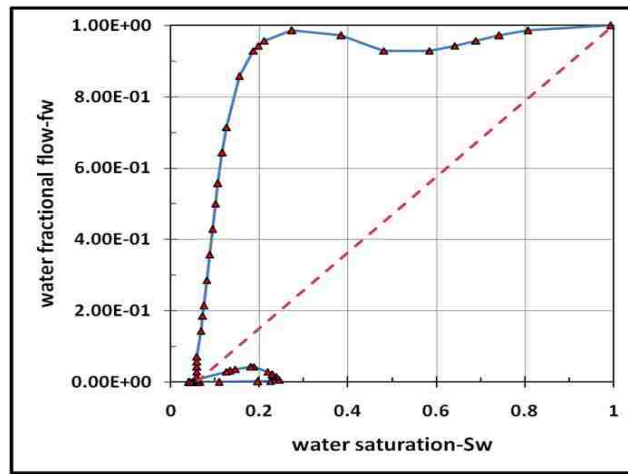
Figs. 4.19(a), 4.19(b), and 4.19(c) show pressure profiles obtained directly from mechanistic simulations at $u_g = 5.3 \times 10^{-5}$, 7.0×10^{-5} , and 1.0×10^{-4} m/s (Figs. 4.15(a), 4.15 (b), and 4.15 (c), respectively). As discussed in Fig. 4.8, the position of foam front is well captured, but the magnitude of pressure change at the foam front is not realistic. The same pressure-profile calculation is shown in Figs. 4.20(a), 4.20(b), and 4.20(c) after pressure modification. In all three cases shown, the benefit of pressure modification procedure is well demonstrated.

4.5. Determination of Model Parameters

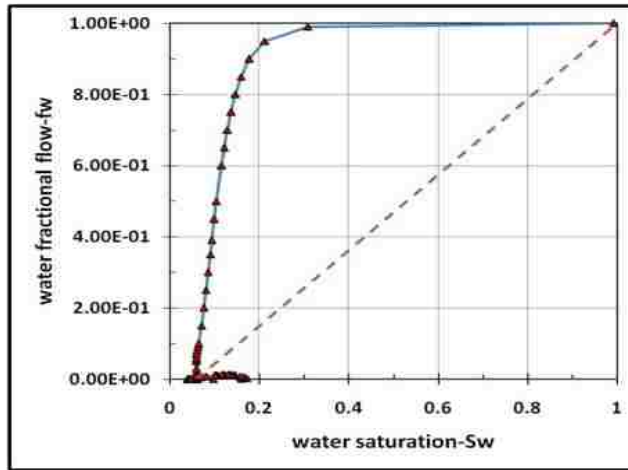
The determination of foam model parameters in foam modeling and simulation is critical in evaluating the performance of foam processes in a wide range of field and laboratory conditions. As illustrated in Fig. 4.1, a set of foam parameters (∇P_o , n , C_g/C_c , and C_f ; cf. the third column of Table 4.1) can be used to fit both steady-state two flow regime contours and the steady-state S-shaped foam catastrophe curve. In addition to the bases case (Case 1) in Table 4.1, Fig. 4.21 shows two other sets of foam model parameters which provide an almost identical fit to the same S-shaped curve in Fig. 4.1(a). These two sets of model parameters for Figs. 4.21(a) and 4.21(b), called Case 2 and Case 3 respectively as shown in Table 4.2, also equally fit the two flow regimes well, similar to the results in Fig. 4.1(b). This result of Figs. 4.21(a) and 4.21(b)



(a)

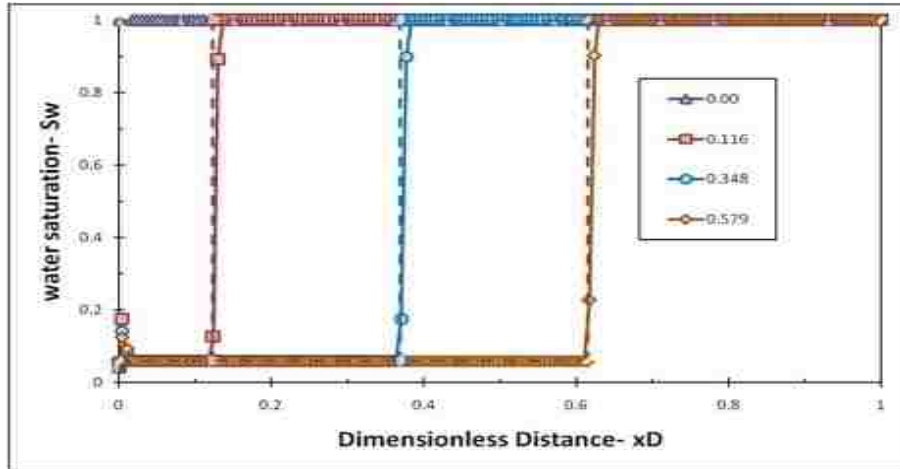


(b)

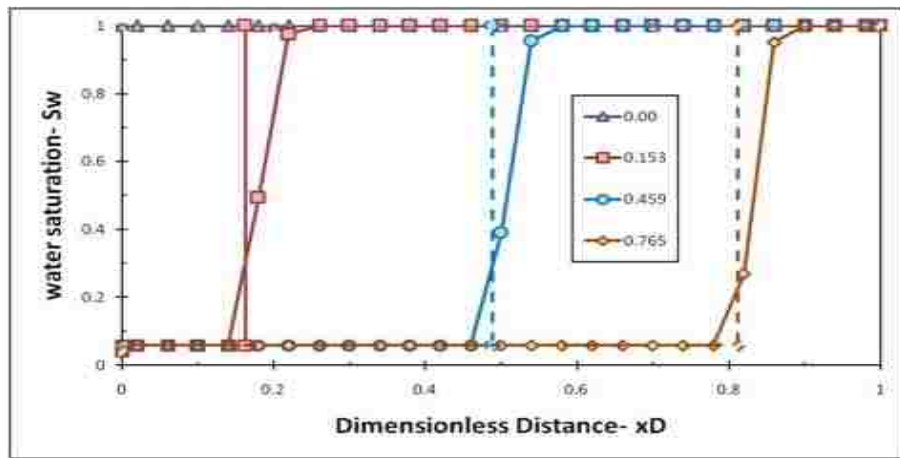


(c)

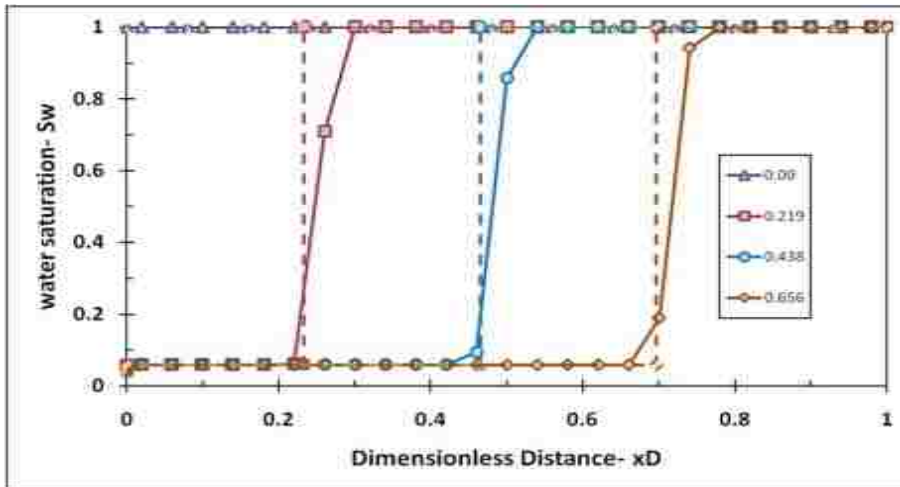
Figure 4.15 Mechanistic fractional flow curves leading to strong-foam propagation in simulation: (a) $u_g = 5.3 \times 10^{-5}$ m/s, (b) $u_g = 7.0 \times 10^{-5}$ m/s, and (c) $u_g = 1.0 \times 10^{-4}$ m/s.



(a)

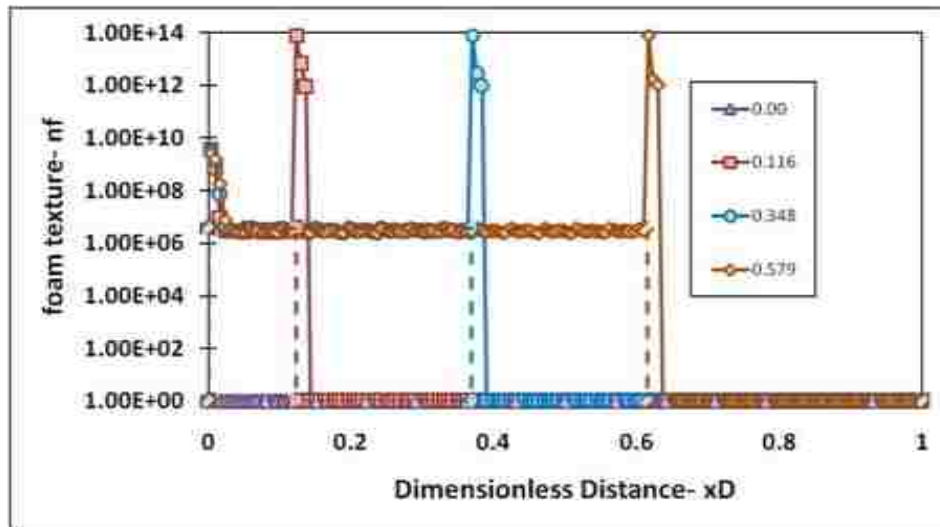


(b)

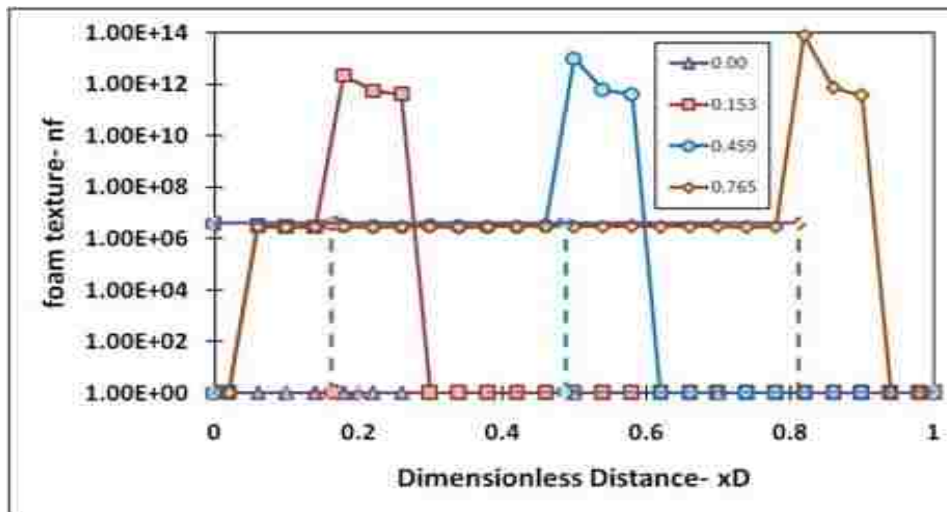


(c)

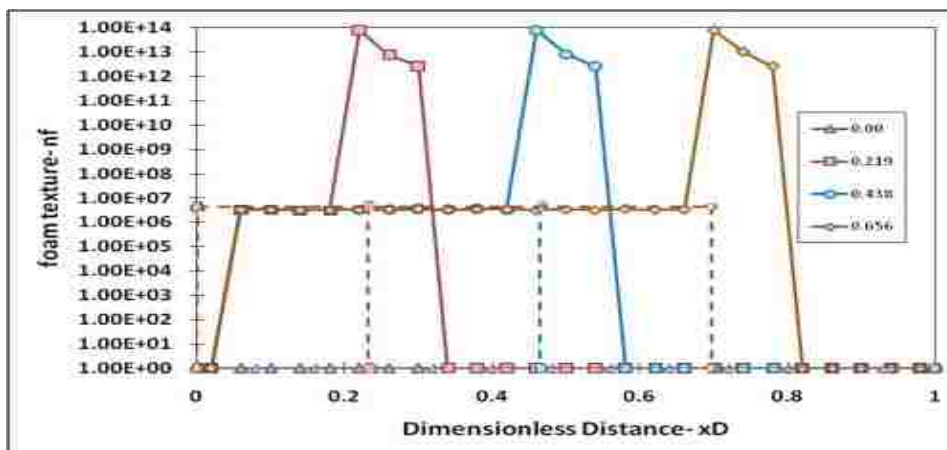
Figure 4.16 Water saturation profile from mechanistic simulations (solid line) and fractional flow analysis (dashed line): (a) $u_g = 5.3 \times 10^{-5}$ m/s, (b) $u_g = 7.0 \times 10^{-5}$ m/s, and (c) $u_g = 1.0 \times 10^{-4}$ m/s



(a)



(b)



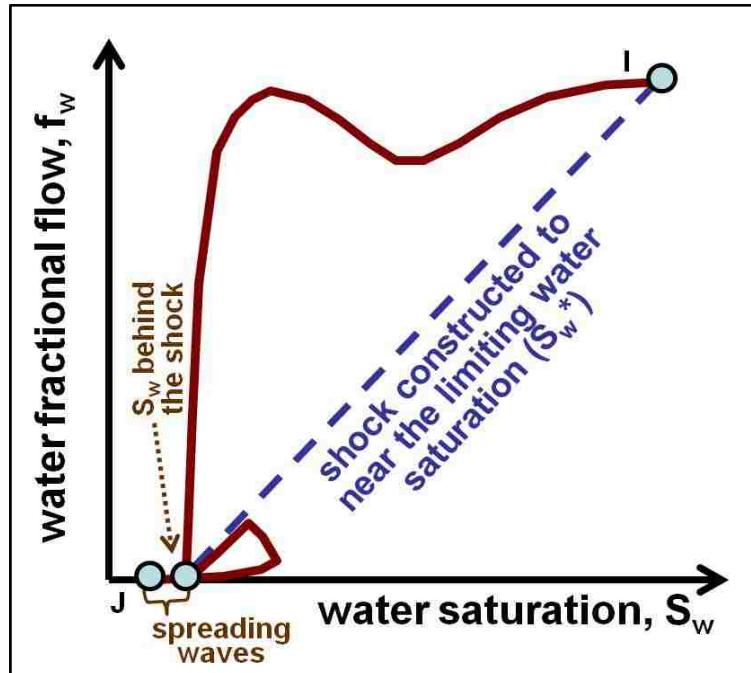
(c)

Figure 4.17 Foam texture profile from mechanistic simulations (solid line) and fractional flow analysis (dashed line): (a) $u_g = 5.3 \times 10^{-5}$ m/s, (b) $u_g = 7.0 \times 10^{-5}$ m/s, and (c) $u_g = 1.0 \times 10^{-4}$ m/s (n_f in m^{-3})

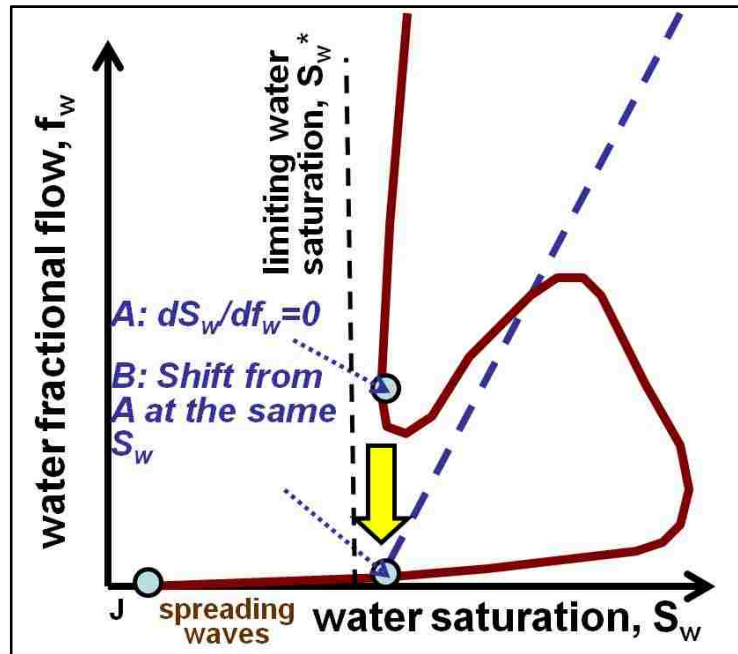
indicates that the use of an S-shaped curve and a two steady-state strong-foam regime map may come up with multiple sets of foam model parameters (i.e., third column of Table 4.1). This implies another important feature of mechanistic foam modeling, which is, the level of lamella creation mechanism can be compensated by the level of lamella coalescence mechanism - less active creation can be paired with less active lamella coalescence (Case 2 with low ∇P_0 and n values) and more active lamella creation can be paired with more active lamella coalescence (Case 3 with high ∇P_0 and n values). This is consistent with the finding in Kam (2008) even when trapped gas saturation is accounted for in this study.

Figs. 4.22(a), 4.22(b), and 4.22(c) show fractional flow curves of Case 1, Case 2, and Case 3, respectively, at the same injection velocity of $u_g = 4.2 \times 10^{-5}$ m/s. Notice that the fractional flow curve in Fig. 4.22(a) is identical to that in Fig. 4.10(c)). As discussed in earlier sections, the fractional flow curve with an isolated loop has a strong tendency to form weak foams in dynamic simulations and, once the loop is connected to the fractional flow curve at higher injection velocities, the curve with a smaller bulge has a stronger tendency to form strong foams. This analysis is proved to be valid as shown by the dynamic simulation results in Figs. 4.23(a), 4.23(b), and 4.23(c), Case 2 leading to the highest water saturation (i.e., weak foam), Case 3 leading to the lowest water saturation behind the shock (i.e., strong foam), and the base case (Case 1) in between (weak foam).

The results in Figs. 4.22 and 4.23 have important implications in foam modeling and simulations: (1) Numerous different sets of foam parameters can fit experimental foam flow data of foam catastrophe and two flow regimes equally at all different levels of lamella creation and coalescence mechanisms. However, steady-state in foam flow does not probe how active lamella creation and coalescence mechanisms are, as long their relative activity is correct. In other words, the same fit given by three cases uses relatively large, relatively small, or

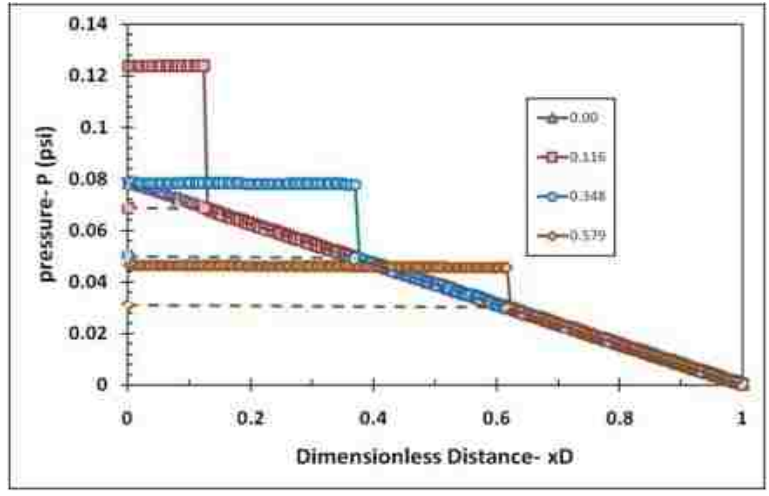


(a)

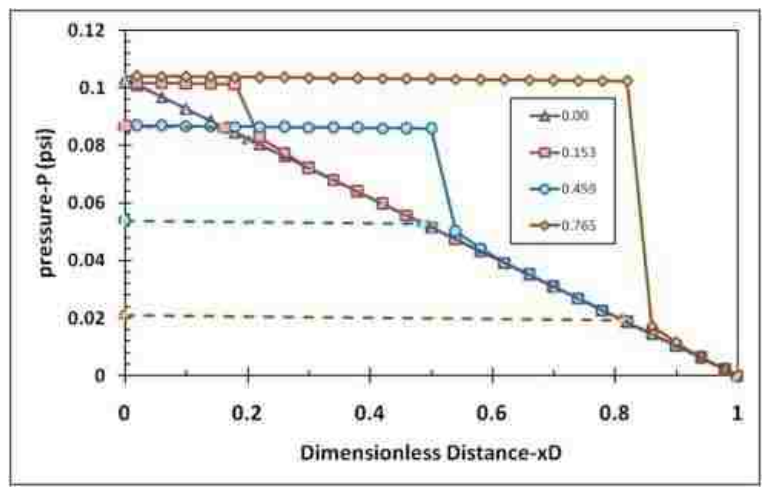


(b)

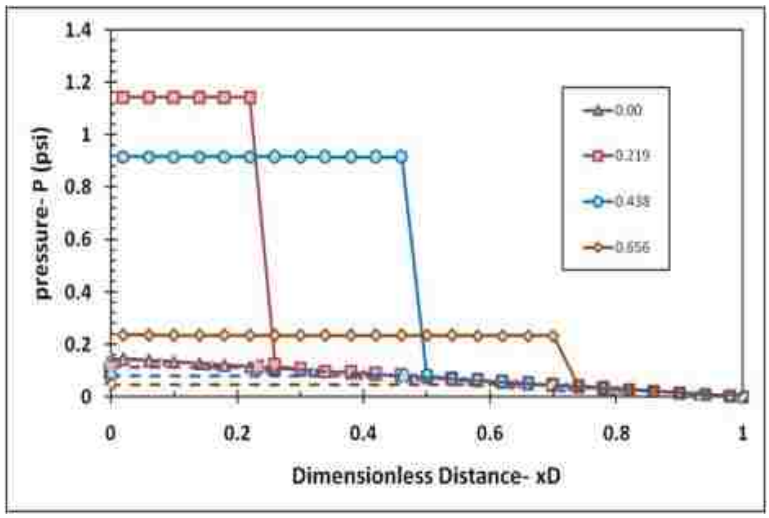
Figure 4.18 Schematic figures showing fractional flow analysis during weak-foam propagation.



(a)



(b)



(c)

Figure 4.19 Pressure profile before pressure modification from mechanistic simulations (solid line) and fractional flow analysis (dashed line): (a) $u_g = 5.3 \times 10^{-5}$ m/s, (b) $u_g = 7.0 \times 10^{-5}$ m/s, and (c) $u_g = 1.0 \times 10^{-4}$ m/s (1 psi = 6,900 Pa)

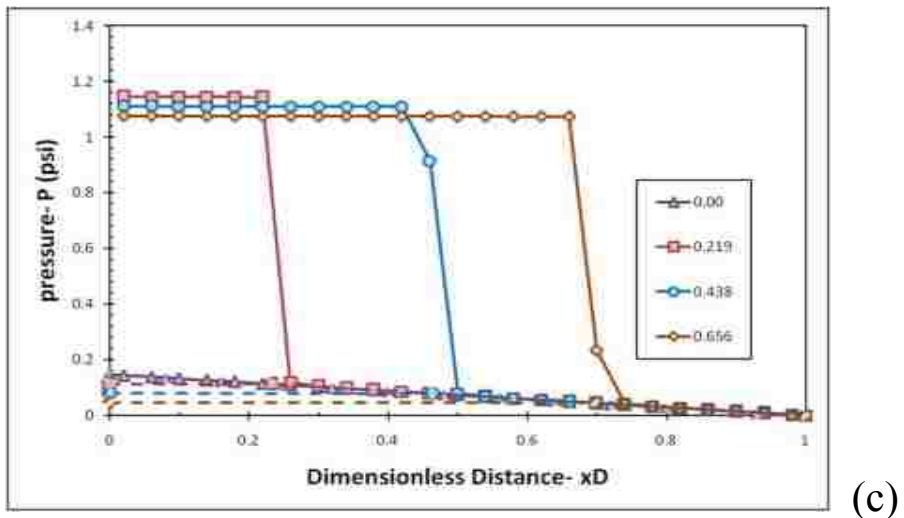
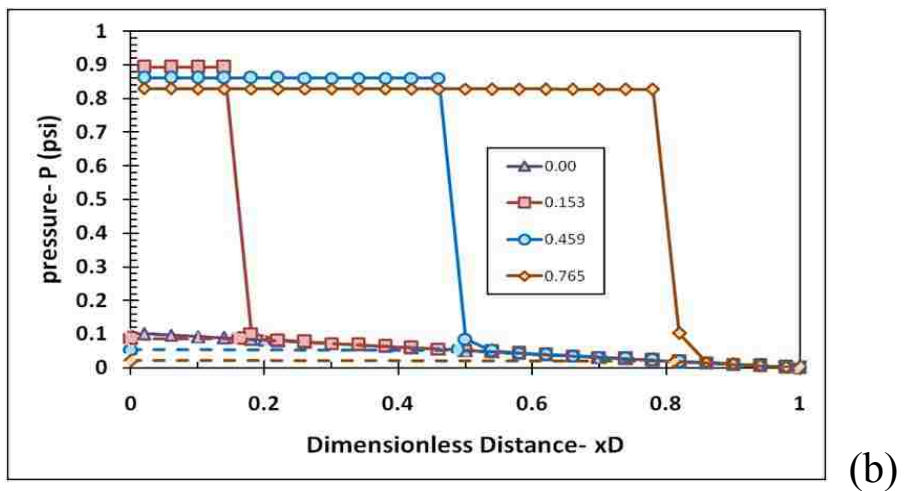
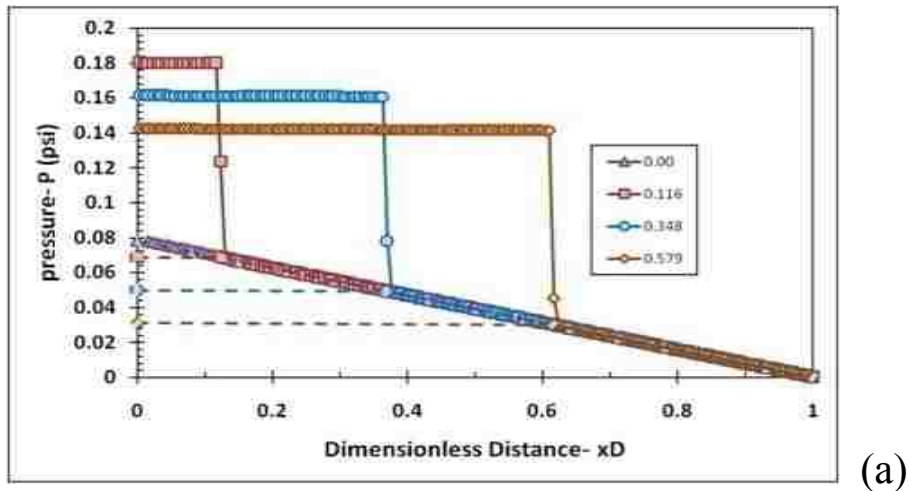
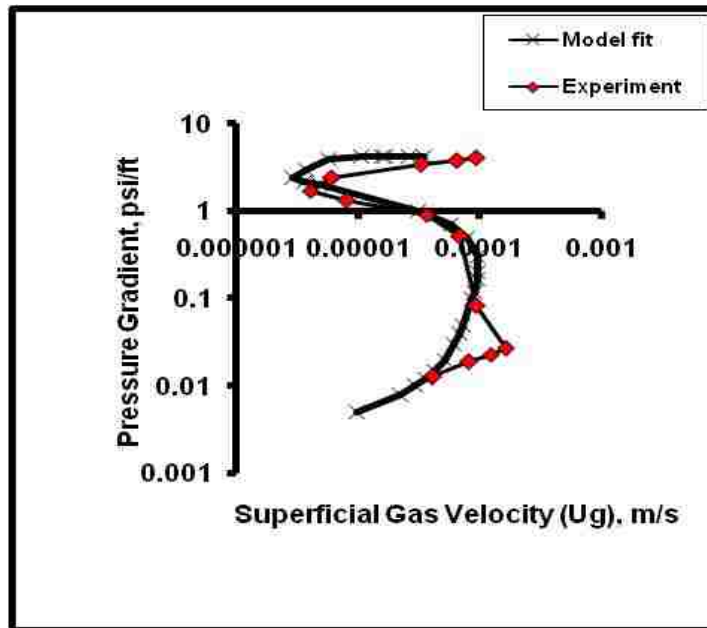
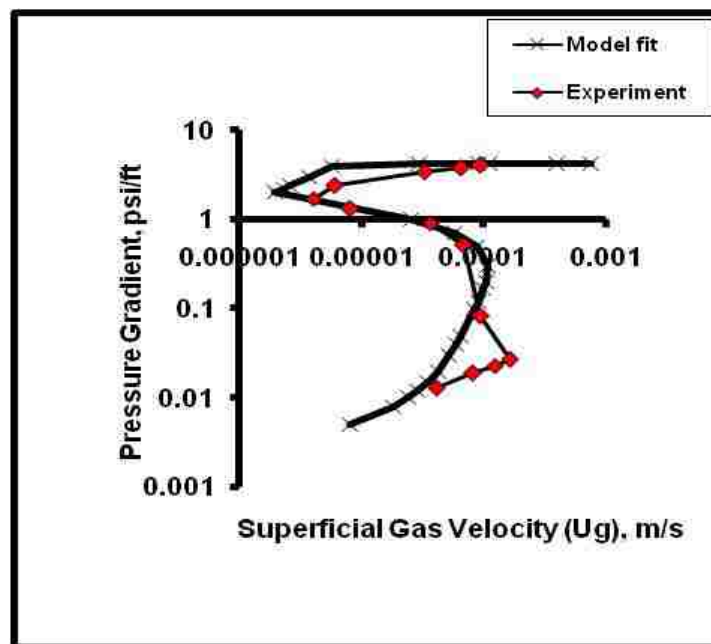


Figure 4.20 Pressure profile after pressure modification from mechanistic simulations (solid line) and fractional flow analysis (dashed line): (a) $u_g = 5.3 \times 10^{-5}$ m/s, (b) $u_g = 7.0 \times 10^{-5}$ m/s, and (c) $u_g = 1.0 \times 10^{-4}$ m/s (1 psi = 6,900 Pa)



(a)



(b)

Figure 4.21 Two other sets of foam modeling parameters that fit the experimental data equally well ($1 \text{ psi/ft} = 22,626 \text{ Pa/m}$): (a) Case 2 (low ∇P_o and n values) and (b) Case 3 (high ∇P_o and n values)

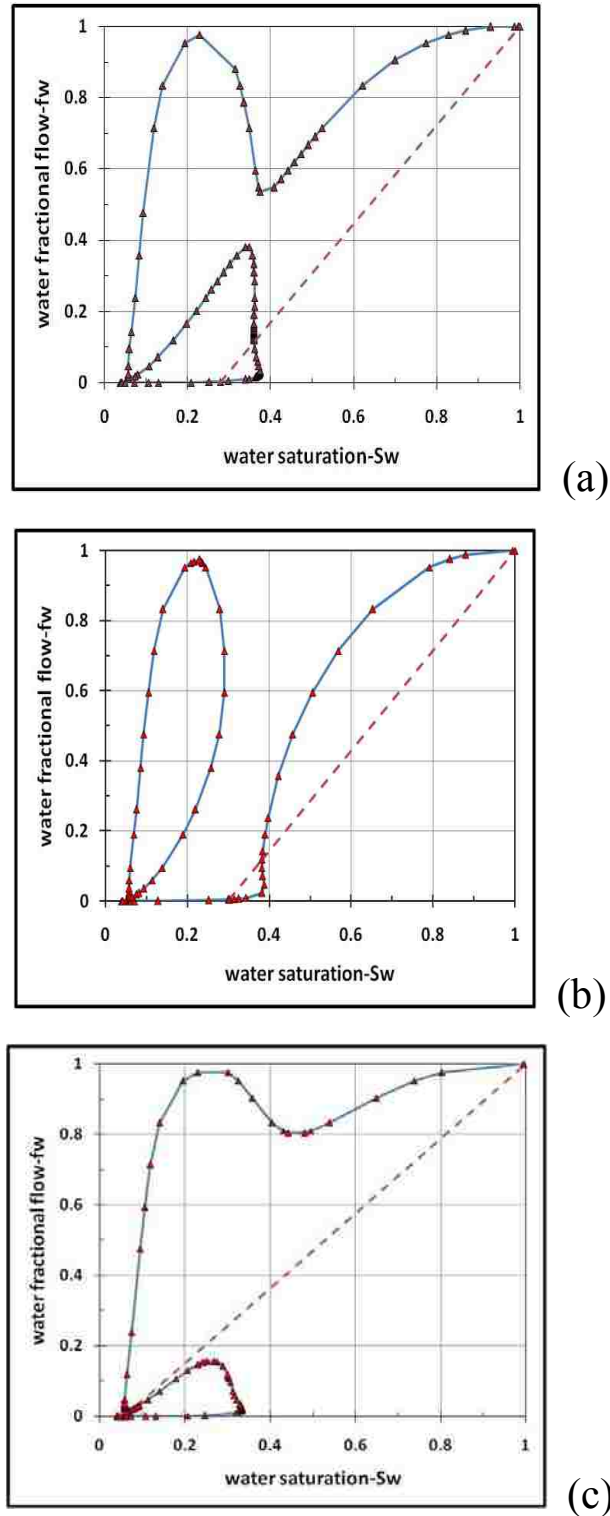
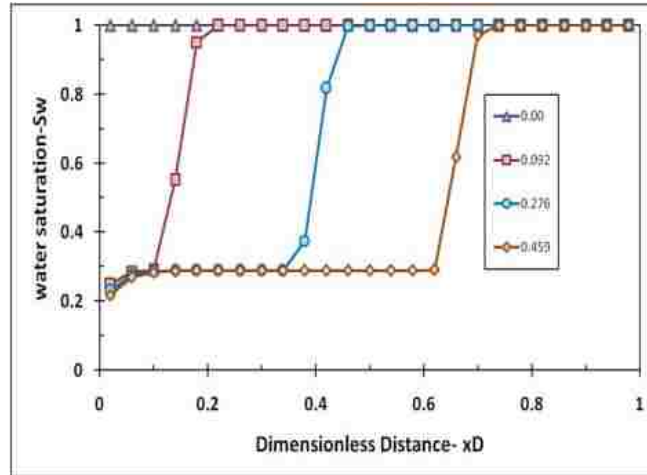
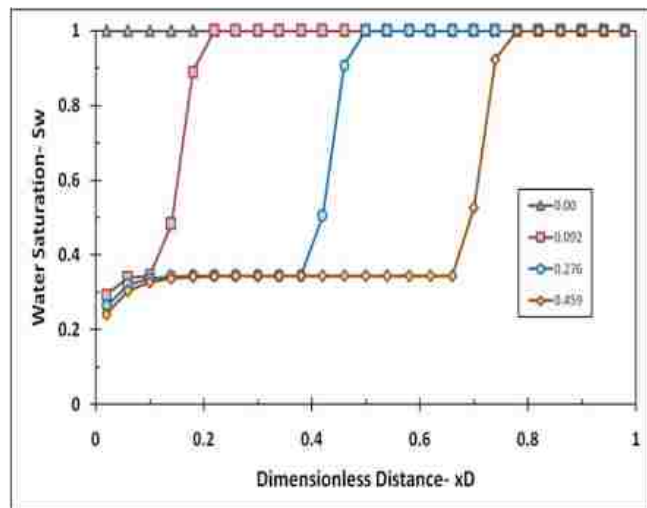


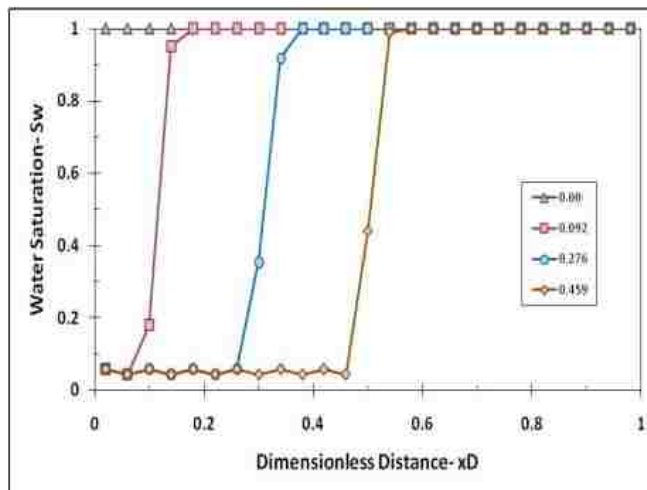
Figure 4.22 Mechanistic foam fractional flow curves with $u_g = 4.2 \times 10^{-5}$ m/s at three different sets of foam model parameters: (a) Case 1, (b) Case 2 (low ∇P_0 and n values), and (c) Case 3 (high ∇P_0 and n values)



(a)



(b)



(c)

Figure 4.23 Water saturation profile with $u_g = 4.2 \times 10^{-5}$ m/s at three different sets of foam model parameters: (a) Case 1, (b) Case 2 (low ∇P_0 and n values), and (c) Case 3 (high ∇P_0 and n values).

Table 4-2 Foam parameters for Case 2 and Case 3

Foam parameters	Case 2	Case 3
∇P_o (Psi/ft)	3.4*	4.9**
n	0.5	1.5
C_g / C_c	1.5242×10^{15}	1.118×10^{18}
C_f	6.617×10^{-18}	6.617×10^{-18}

*3.4 psi/ft = 76,928.4 Pa/m (1 psi/ft = 22,626 Pa/m)

**4.9 psi/ft = 110867.4 Pa/m (1 psi/ft = 22,626 Pa/m)

relatively comparable values of ∇P_o and n as a set as shown in Case 3, Case 2, or Case 1 respectively.; and (2) Although these different parameter sets produce the same fit (cf. Fig. 4.22), they exhibit different levels of foam dynamics (cf. Fig. 4.23) and therefore show different values of injection velocities for the onset of foam generation. By using this injection velocity at which foam generation occurs, one can determine the set of ∇P_o and n to capture the transition from weak-foam to strong-foam propagation.

These two aspects are schematically described in Fig. 4.24 that shows a range of gas injection velocity (u_g) below which there is only one weak-foam state and above which there is only one strong-foam state present. Any u_g in between has multiple foam states. The shift from weak-foam to strong-foam state (i.e. vertical arrows in Fig. 4.24) at any u_g is governed by how active lamella creation is at u_g . If lamella-creation is more prolific, foam is more easily created and strong foam forms at lower u_g . This implies that among many sets of foam parameters to fit the steady-state data, there is one set of foam parameters (∇P_o , n , C_g/C_c , and C_f) which can fit the onset of foam generation during a series of gas injection coreflood experiments.

4.6. Inlet Effect and System Length in Foam Displacement

Even with strong-foam propagation during gas injection, it takes a certain distance at the core inlet for injected foams to reach its fine-textured state, which is referred to as “inlet effect”.

Dynamic foam simulations can handle different levels of inlet effect by adjusting individual values of C_g and C_c , keeping the ratio of C_g/C_c constant (cf. Table 4.1). Figs. 4.25(a) and 4.25 (b) show two examples at $C_c = 0.1$ and 0.01 at $u_g = 7.0 \times 10^{-5}$ m/s in contrast to Fig. 4.16(b) (i.e., at the same u_g with $C_c = 1$). If C_g/C_c is kept constant, smaller C_c (or, smaller C_g equivalently) represents less active lamella creation and coalescence, resulting in a longer transient region (or, the distance for foams to reach strong foams). Therefore, the transient region

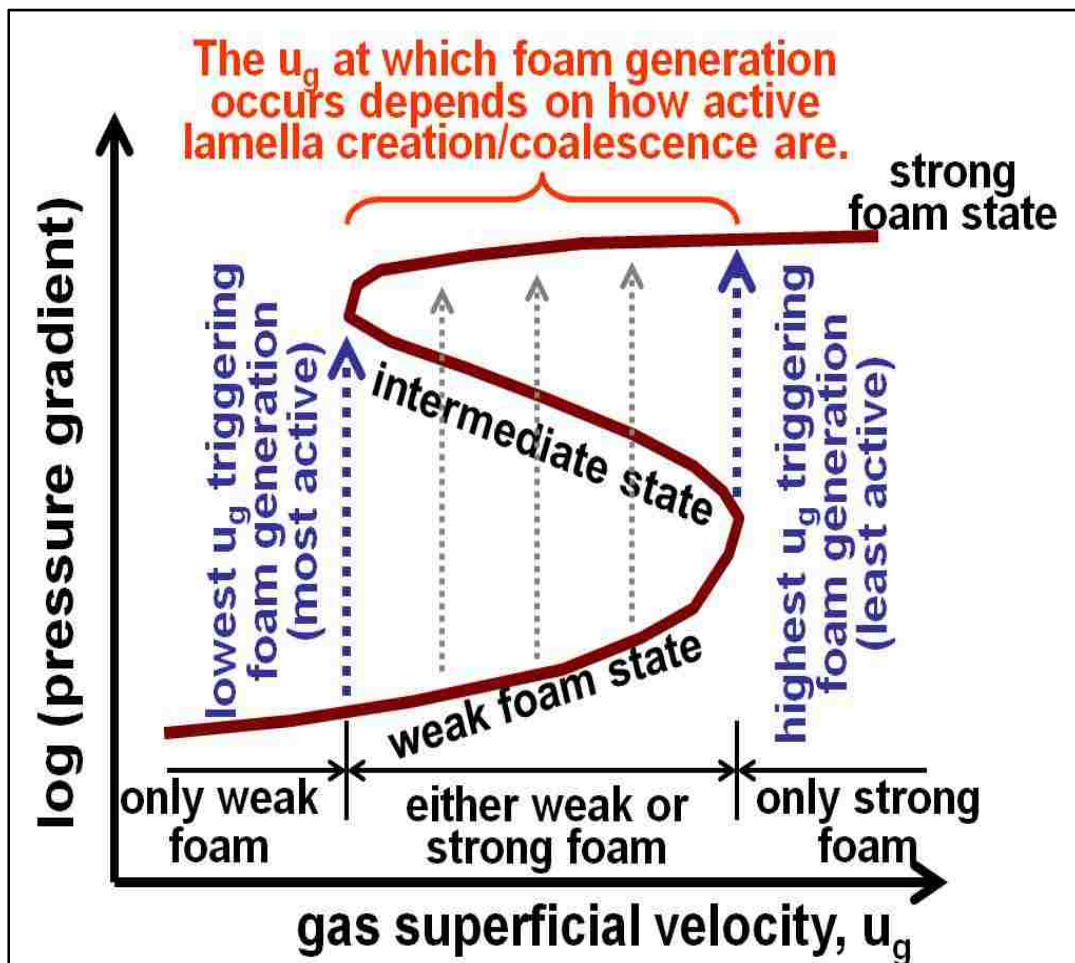


Figure 4.24 A schematic of three foam states with the onset of foam generation

tends to increase with decreasing C_c , as shown in Fig. 4.25. This implies that weak-foam propagation observed in lab-scale coreflood experiments may still end up with strong-foam propagation in the field.

Other mechanistic simulations are conducted to see the impact of system length on dynamic foam simulations. In contrast to Fig. 4.16(b), the core length is reduced by 10 times and 100 times, as shown in Figs. 4.26(a) and 4.26(b) respectively, at the same injection velocity ($u_g = 7.0 \times 10^{-5}$ m/s) and the same number of grid blocks. The results (Fig. 4.26) are almost identical to those in Fig. 4.25, indicating that the effect of reduction in core length is the same as that of reduction in C_c value. This in turn implies that the magnitude of C_c in mechanistic simulations can be used to adjust the relative length of transient region to the length of the system. Therefore, the value of C_g and C_c should be adjusted depending on the scale of the system of interest in mechanistic simulations by keeping C_g/C_c constant.

Another algorithm for foam simulation is proposed in Appendix B. This new algorithm is a fully implicit method solving saturation and pressure at the same time by using Jacobian matrix and matrix solver.

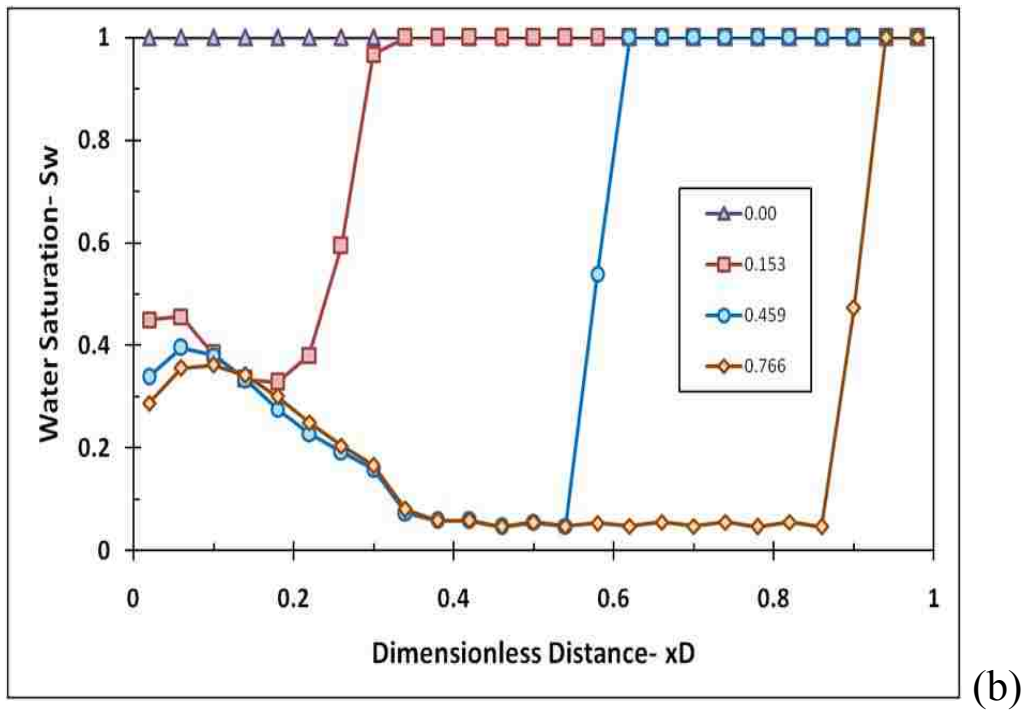
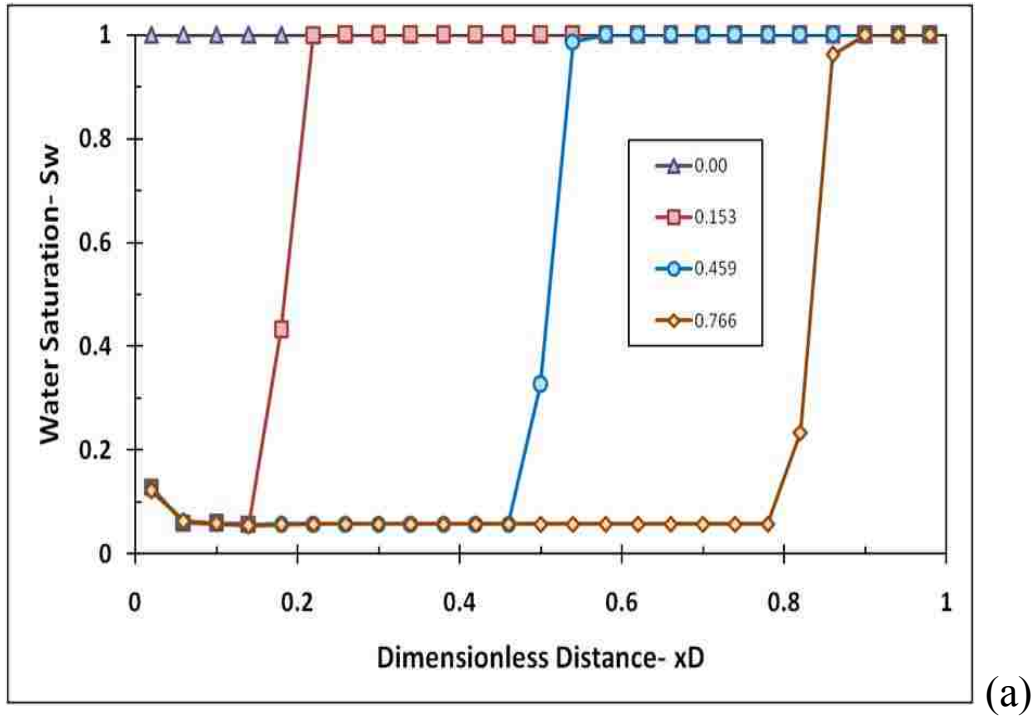


Figure 4.25 Water saturation profile with $u_g = 7.0 \times 10^{-5}$ m/s at different C_c values (base case, $C_c = 1$): (a) $C_c = 0.1$ and (b) $C_c = 0.01$

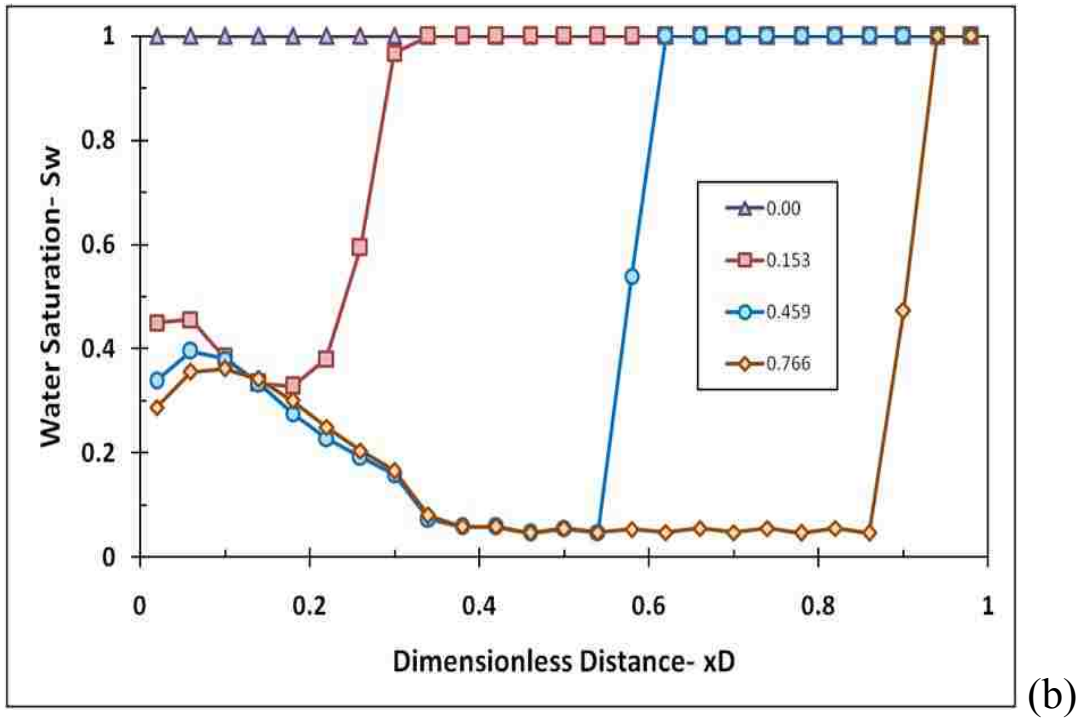
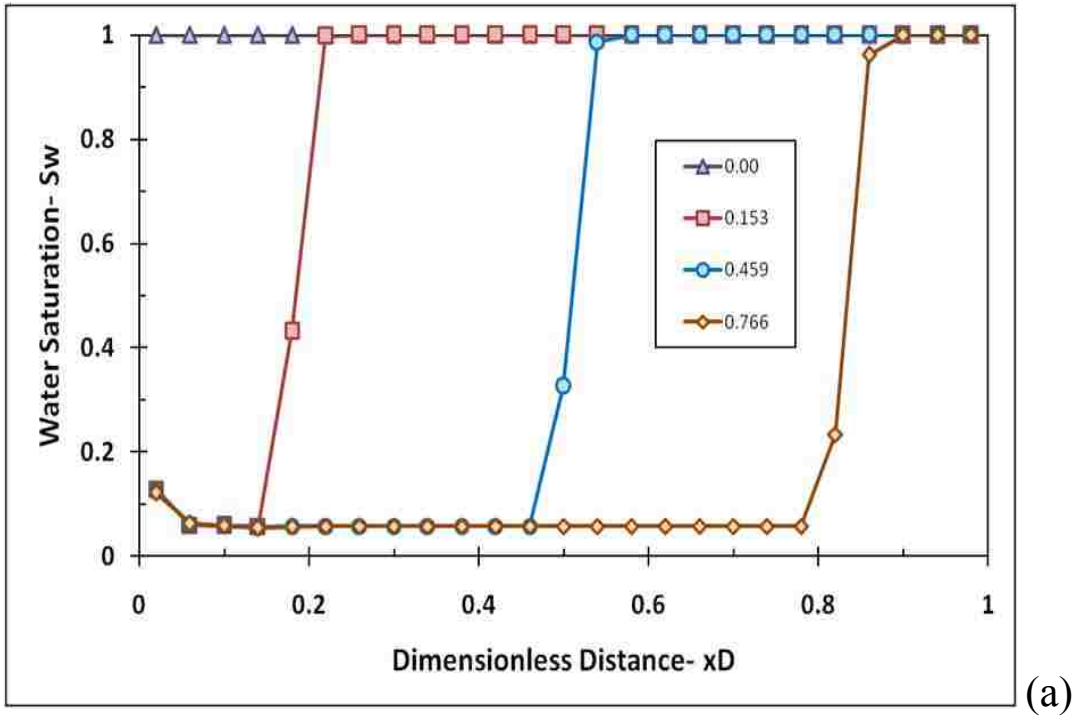


Figure 4.26 Water saturation profile with $u_g = 7.0 \times 10^{-5}$ m/s at different system lengths: (a) 10 times shorter and (b) 100 times shorter than the base case

5. CONCLUSIONS AND RECOMMENDATIONS

Chapter 5 summarizes the outcome of this mechanistic foam-simulation study. The recommendations for future studies are also listed.

5.1. Conclusions

In continuation with the previous mechanistic foam-simulation attempts, this study expands the scope into the surfactant-alternating-gas (SAG) processes. The results show that the underlying physics behind the SAG process is quite different from that behind the co-injection of gas and surfactant solutions. The novel foam modeling and simulation efforts have led to several conclusions:

1. A mechanistic foam modeling and simulation technique is extended to accommodate the trapped gas saturation as observed in many laboratory experiments. This study is first for the mechanistic foam simulation to handle gas injection during surfactant-alternating-gas (SAG) processes, still fitting the steady-state data of three foam states (i.e., weak-foam, strong-foam, and intermediate states) and two strong-foam regimes (high-quality and low-quality regimes). The modeling and simulation results show that the foam mechanism at very low water fractional flow (f_w) is very important to evaluate the efficiency of foam displacement in the SAG processes.
2. Although the simulation of gas injection agrees well with the previous foam studies showing weak-foam propagation at low injection velocity and strong-foam propagation at high injection velocity, details of the solution scheme are much more complicated. It is primarily because mechanistic foam fractional flow curves bend back and forth resulting in regions with $df_w/dS_w \geq 0$ and $df_w/dS_w < 0$ in f_w vs. S_w domain. Except for very low injection velocity, the outcome of mechanistic simulation is different from the

conventional tangent-line construction, showing two different solution paths depending on whether strong foams are formed or not: (1) If strong foams are not formed (i.e., weak-foam propagation), the condition behind the shock on the mechanistic foam fractional flow curve seems to be the extension of the line connecting the initial condition (I) and the point at which $dS_w/df_w=0$ on the weak-foam fractional flow curve; and (2) If strong foams are formed successfully (i.e., strong-foam propagation) the condition behind the shock seems to be the point on the weak-foam fractional flow side which is shifted from the lowest f_w on the physically-meaningful strong-foam fractional flow curve (i.e., $df_w/dS_w=\infty$) at the same capillary pressure. In both cases, the condition behind the shock is followed by very slow spreading waves.

3. Although fractional flow analysis guides dynamic simulations of gas injection during SAG processes, it does not match pressure profile and inlet injection pressure history during strong-foam propagation. Lamella creation and coalescence at the leading edge of gas bank cannot be captured by a local-steady-state assumption of fractional flow analysis. In addition, the dramatic change in lamella creation/coalescence mechanisms at the front, in fact, takes place too rapidly to be properly managed by the finite difference method. The pressure modification algorithm suggested in this study, which utilizes the maximum foam texture (n_{fmax}) and the maximum pressure gradient at the foam front, makes it possible to determine realistic pressure profiles and inlet injection pressure history.
4. This study shows how to determine five foam parameters systematically. In order to determine four foam parameters (∇P_o , n , C_g/C_c , and C_f), it is necessary to have the following experimental data: a steady state strong foam regime map (at least one pressure contour exhibiting both high and low quality regimes), a foam catastrophe surface (at

least one S-shaped curve showing three different foam states), and a series of coreflood experiments showing the onset of foam generation. Different combinations of lamella-creation coefficient (C_g) and lamella-coalescence coefficient (C_c) at the same ratio (C_g/C_c) can be used to adjust the length of transient region at the inlet relative to the length of entire system.

5. Two different numerical algorithms examine whether the mechanistic simulation results are strongly influenced by numerical artifacts; One solves fractional flow equation first, followed by explicit pressure calculations; The other uses an implicit saturation and pressure. The two algorithms give consistent results, including the velocity at which foam generation occurs (i.e., the transition from weak-foam to strong-foam state), the condition behind a shock in both weak-foam and strong-foam propagations, and saturation and foam-texture profiles.

5.2. Recommendations

In addition, mechanistic foam simulation investigated in this study indicates the following subjects are likely to be fruitful ways for future research:

1. The most challenging task in this field of research is perhaps to move forward to construct fully mechanistic foam models and simulators. The mechanistic simulation technique shown in this study is not fully mechanistic at this stage, because it is not clear yet how these model parameters are related to different types of rock and fluid properties. This implies that the model cannot tell easily how the modeling and simulation outcome will be affected by the change in experimental/field conditions. Instead, the model requires a new set of experimental data (foam catastrophe, two flow regimes, onset of foam generation and inlet effect) to obtain new foam parameters for the particular rock

and fluid systems.

2. An addition of third phase such as petroleum oils and/or contaminants is required in order for this simulation technique to be applied to foam-assisted enhanced oil recovery and subsurface-remediation treatments. The three-phase mechanistic foam simulations should be able to account for different types of oil and surfactants.
3. The simulation methods should be extended into two and three dimensions. A critical step towards two- or three-dimensional mechanistic foam models is how to translate the pressure-dependent lamella-creation mechanism extracted from one-dimensional coreflood experiments. A multi dimensional mechanistic foam simulation would enable study of physical phenomena such as gravity segregations, fingering, channeling, and subsurface heterogeneity.
4. The presence of foam-rheology surface following catastrophe theory implies that the outcome of foam displacements in porous media can be quite different depending on whether the injection condition is specified by fixed rates, fixed pressure, or a combination of the two. Further simulation and experimental studies on dynamic foam displacements can be performed to investigate the implication of different injection strategies.

REFERENCES

- 1) Aarra, M. G., Skauge, A., 1994. A foam pilot in a North Sea oil reservoir: preparation for a production well treatment. SPE 28599 presented at the SPE Annual Technical Conference and Exhibition, New Orleans, Louisiana.
- 2) Aarra, M. G., Skauge, A., Martinsen, H. A., 2002. FAWAG: A breakthrough for EOR in the North Sea. SPE 77695 presented at the SPE Annual Technical Conference and Exhibition, San Antonio, Texas.
- 3) Alvarez, J. M., Rivas, H., Rossen, W. R., 2001. A unified model for steady-state foam behavior at high and low foam qualities. SPE Journal, 325–333 (September).
- 4) Aronson, A. S., Bergeron, V., Fagan, M. E., Radke, C. J., 1994. The influence of disjoining pressure on foam stability and flow in porous media. Colloids Surface A: Physicochemical and Engineering Aspects 83, 109.
- 5) Aziz, K., Settari, A., 1979. Petroleum Reservoir Simulation. Elsevier Applied Science Publishers, London and New York.
- 6) Bertin, H. J., Quintard, M. Y., Castanier, L. M., 1998. Development of a bubble-population correlation for foam-flow modeling in porous media. SPE Journal , 356–362 (December).
- 7) Blaker, T., Morten, G., Skauge, A., Rasmussen, L., Celius, Harald K., Martinsen, H. A., Vassenden, F., 2002. Foam for gas mobility control in the Snorre Field: the FAWAG project, SPE Reservoir Evaluation and Engineering, 317–323(August).
- 8) Buckley, S. E., Leverett, M. C., 1941. Mechanism of fluid displacement in sands. Transactions of American Institute of Mechanical Engineering Journal 146, 107–116.
- 9) Derjaguin, B. V., Obuchov, E., 1936. Acta Physicochimica. URSS 5, 1.
- 10) Derjaguin, B. V., Kussakov, M. M., 1939. Acta Physicochimica. URSS 10, 153.
- 11) Dholkawala, Z. F., 2006. Application of fractional flow theory to foams in porous media. Master's Thesis, The University of Adelaide, Australia.
- 12) Dholkawala, Z. F., Sarma, H. K., Kam, S. I., 2007. Application of fractional flow theory to foams in porous media. Journal of Petroleum Science and Engineering 57, 152–165.
- 13) Djabbarah, N. F., 1990. Laboratory design and field demonstration of steam diversion with foam. SPE 20097 presented at The 60th California Regional Meeting, Ventura, California.

- 14) Falls, A. H., Hirasaki, G. J., Patzek, T. W., Gauglitz, P. A., Miller, D. D., Ratulowski, J., 1988. Development of a mechanistic foam simulator: The population balance and generation by snap-Off. *SPE Reservoir Engineering*, 884–892 (August).
- 15) Falls, A. H., Musters, J. J., 1989. The apparent viscosity of foams in homogenous Bead packs. *SPE Reservoir Engineering*, 155-164 (May).
- 16) Friedmann, F., 1994. Steam-foam mechanistic field trial in the Midway-Sunset field. *SPE Reservoir Engineering*, 297-304 (November).
- 17) Friedmann, F., Chen, W. H., Gauglitz, P. A., 1991. Experimental and simulation study of high-temperature foam displacement in porous media. *SPE Reservoir Engineering*, 37–45 (February).
- 18) Gauglitz, P. A., Friedmann, F., Kam, S. I., Rossen, W. R., 2002. Foam generation in homogeneous porous media. *Chemical Engineering Science* 57, 4037–4052.
- 19) Hirasaki, G. J., Lawson, J. B., 1985. Mechanisms of foam flow through porous media – apparent viscosity in smooth capillaries. *SPE Journal*, 176–190 (April).
- 20) Hirasaki, G. J., 1989. Supplement to SPE 19505, the Steam-Foam Process-Review of Steam-Foam Process Mechanisms. SPE 19518.
- 21) Hirasaki, G. J., Miller, C. A., Lawson, J. B., Akiya, N., Szafranski, R., 1997. Surfactant/foam process for Aquifer Remediation. SPE 37257 presented at the SPE Symposium on Oilfield Chemistry, Houston, Texas.
- 22) Hirasaki, G. J., Jackson, R. E., Jin, M., Lawson, J. B., Londergan, J., Meinardus, H., Miller, C. A., Pope, G. A., Szafranski, R., Tanzil, D., 2000. Field demonstration of the surfactant/foam process for remediation of a heterogeneous aquifer contaminated with DNAPL, in NAPL removal: surfactants, foams, and microemulsions. in: Fiorenza, S., Miller, C.A., Oubre, C.L., Ward, C.H. (Eds.), Lewis Publishers, Boca Raton.
- 23) Hoefner, M. L., Evans, E. M., 1995. CO₂ foam: results from four developmental field trials. *SPE Reservoir Engineering Journal*, 273-281 (November).
- 24) Kam, S. I., Rossen, W. R., 2003. A Model for Foam Generation in Homogeneous Porous Media. *SPE Journal* , 417-425 (December).
- 25) Kam, S. I., Nguyen, Q. P., Rossen, W. R., 2007. Dynamic simulations with an improved model for foam generation. *SPE Journal* , 35-48 (March).
- 26) Kam, S. I., 2008. Improved mechanistic foam simulation with foam catastrophe theory. *Colloids and Surfaces A: Physicochemical Engineering Aspects* 318, 62–77.

- 27) Khatib, Z. I., Hirasaki, G. J., Falls, A. H., 1988. Effects of capillary pressure on coalescence and phase mobilities in foams flowing through porous media. SPE Reservoir Engineering, 919–926 (August).
- 28) Kibodeaux, K. R., Rossen, W. R., 1997. Coreflood study of surfactant-alternating-gas foam processes. SPE 38318 presented at the SPE western regional meeting, Long Beach, California.
- 29) Kovscek, A. R., Radke, C. J., 1994. Fundamentals of foam transport in porous media, in foams: fundamentals and applications in the petroleum industry. in: Schramm, L.L. (Ed.), ACS Advances in Chemistry Series, vol. 242. American Chemistry Society, Washington, DC.
- 30) Kovscek, A. R., Patzek, T. W., Radke, C. J., 1995. A mechanistic population balance model for transient and steady-state foam flow in Boise sandstone. Chemical Engineering Science 50, 3783–3799.
- 31) Lake, L. , 1989. Enhanced oil recovery. Prentice Hall, Englewood Cliffs, New Jersey.
- 32) Mamun, C. K., Rong, J. G., Kam, S. I., Liljestr and, H. M., Rossen, W. R., 2002. Extending foam technology from improved oil recovery to environmental remediation. SPE 77557 presented at the SPE Annual Technical Conference, San Antonio, Texas.
- 33) Martinsen, H. A., Vassenden, F., 1999. Foam-assisted water alternating gas (FAWAG) process on Snorre, in: Presented at the 10th European symposium on improved oil recovery, Brighton, UK (August).
- 34) Mayberry, D. J., Afsharpoor, A., Kam, S. I., 2008. The use of fractional-flow theory for foam displacement in presence of oil. SPE Reservoir Evaluation and Engineering, 707-718 (August).
- 35) Osterloh, W. T., Jante, M. J., 1992. Effects of gas and liquid velocity on steady-state foam flow at high temperature. SPE 24179 presented at the SPE/DOE symposium on enhanced oil recovery, Tulsa, Oklahoma (April).
- 36) Patzek, T. W., Koinis, M. T., 1990. Kern River steam-foam pilots. Journal of Petroleum Technology, 496-503 (April).
- 37) Ransohoff, T. C., Radke, C. J., 1988. Mechanisms of foam generation in Glass-Bead packs. SPE Reservoir Engineering, 573-585 (May).
- 38) Rong, J. G., 2002. Experimental Result of Foam in Environmental Remediation. PhD dissertation, University of Texas at Austin, Austin, Texas.

- 40) Rossen, W. R., Gauglitz, P. A., 1990. Percolation theory of creation and mobilization of foam in porous media. *American Institute of Chemical Engineering Journal* 36, 1176–1188.
- 41) Rossen, W. R., Zhou, Z. H., 1995a. Modeling foam mobility at the limiting capillary pressure. *SPE Advanced Technology*, 3, 146-153.
- 42) Rossen, W. R., Zhou, Z. H., 1995b. Applying fractional-flow theory to foam processes at the “limiting capillary pressure”. *SPE Advanced Technology*, 3, 154-162.
- 43) Rossen, W. R., 1996. Foams in enhanced oil recovery, in: Prud'homme, R.K., Khan, S. (Eds.) , *In foams: theory, measurements and applications*. Marcel Dekker, New York.
- 44) Rossen, W. R., Wang, M. W., 1999. Modeling foams for acid diversion. *SPE Journal*, 92–100 (June).
- 45) Rossen, W. R., 2003. A critical review of roof snap-off as a mechanism of steady-state foam generation in homogeneous porous media. *Colloids and Surfaces A: Physicochemical Engineering Aspects* ,225, 1–24.
- 46) Rossen, W. R., Bruining, J., 2007. Foam displacements with multiple steady states. *SPE Journal*, 5-18 (March).
- 47) Rossen, W. R., Kibodeaux, K. R., 1997. Coreflood study of surfactant-alternating-gas foam processes: implication for field design. SPE 38318 presented at 1997 SPE Western Regional Meeting, Long Beach, California.
- 48) Wassmuth, F. R., Green, K. A., Randall, L., 2001. Details of in-situ foam propagation exposed with magnetic resonance imaging. *SPE Reservoir Evaluation and Engineering*, 135-145 (April).
- 49) Xu, Q., Rossen, W. R., 2004. Experimental study of gas injection in a surfactant-alternating-gas foam process. *SPE Reservoir Evaluation and Engineering*, 438-448 (December).

APPENDIX A. DETERMINATION OF STEADY-STATE FOAM PARAMETERS

Four steady-state foam model parameters (C_g/C_c , C_f , ∇P_o , n) are determined from the fit to the steady-state experimental data such as foam-catastrophe surface and two steady-state strong-foam regimes. It is necessary to have at least (1) one S-shaped curve from the catastrophe surface showing three different foam states and (2) one pressure contour showing both high-quality and low-quality regimes. There are two different pieces of program which chase up with those two aspects separately, and then they are put together because the two strong-foam regimes are interconnected with the characteristics of upper foam-catastrophe surface. The calculation procedures described below are currently carried out by Microsoft Excel.

A.1. Fit to an S-shaped Curve

Suppose two foam parameters such as C_g/C_c and C_f are determined from the fit to two strong-foam regimes. Then the objective of this section is to determine two other model parameters (∇P_o , n) by matching experimental data as shown by the S-shaped curve in Fig. A.1. Notice that the plot shows how gas velocity (u_g ; x axis) changes with the pressure gradient (∇P ; y axis) at fixed liquid velocity (u_w). The initial guess for ∇P_o and n should be updated repeatedly by the trial-and-error process to find the optimum set of ∇P_o and n to best fit the S-shaped curve.

If the first column of Excel program is available with the pressure gradients imposed in the experiments, liquid relative permeability (k_{rw}) can be calculated from Darcy's equation directly as follows:

$$k_{rw}(S_w) = \frac{u_w \mu_w}{k \nabla p} \dots\dots\dots (A.1)$$

where μ_w , k , and ∇P represent liquid viscosity, absolute permeability, and liquid-phase pressure gradient, respectively. This study does not distinguish, for simplicity, liquid-phase pressure gradient from gas-phase pressure gradient, by assuming the magnitude of capillary pressure is negligible compared to the magnitude of pressure values. The use of Eq. A.1 is supported by the previous experimental studies which show that the presence of foam films does not impact the flow of liquid because the liquid phase still flows in a relatively small pore space. The liquid relative permeability calculated from Eq. A.1 provides the corresponding values of liquid saturation (S_w) and gas relative permeability in the absence of foam (μ_g^0), i.e.,

$$S_w = \left(\frac{k_{rw}}{0.7888} \right)^{\frac{1}{1.9575}} (1 - S_{wc} - S_{gr}) + S_{wc} \quad \dots\dots\dots (A.2)$$

$$k_{rg}^0 = \left(\frac{1 - S_w - S_{gr}}{1 - S_{wc} - S_{gr}} \right)^{2.2868} \quad \dots\dots\dots (A.3)$$

where, S_{wc} and S_{gr} are connate water saturation and residual gas saturation, respectively.

In local-steady-state foam modeling, the steady-state foam texture (n_f) can be calculated by putting the rate of lamella creation (R_g) and the rate of lamella coalescence (R_c) the same, i.e., $R_g = R_c$.

$$R_g = \frac{C_g}{2} \left\{ \operatorname{erf} \left(\frac{\nabla p - \nabla p_0}{\sqrt{2}} \right) - \operatorname{erf} \left(\frac{-\nabla p_0}{\sqrt{2}} \right) \right\} \quad \dots\dots\dots (A.4)$$

$$R_c = C_c n_f \left(\frac{S_w}{S_w - S_w^*} \right)^n \quad \text{if } S_w > S_w^* \quad \dots\dots\dots (A.5)$$

$$n_f = \frac{C_g}{2C_c} \left(\frac{S_w - S_w^*}{S_w} \right)^n \left\{ \operatorname{erf} \left(\frac{\nabla p - \nabla p_0}{\sqrt{2}} \right) - \operatorname{erf} \left(\frac{-\nabla p_0}{\sqrt{2}} \right) \right\} \quad \text{if } n_f < n_{fmax} \quad \dots\dots\dots (A.6)$$

where S_w^* is the limiting water saturation, and ‘erf’ is the error function.

The presence of lamellae affects gas relative permeability (k_{rg}^f) as follows:

$$k_{rg}^f = \left(X_f \frac{1 - S_w - S_{gr}}{1 - S_{wc} - S_{gr}} \right)^{2.2868} = k_{rg}^0 (1 - X_t)^{2.2868} \quad \dots\dots\dots (A.7)$$

where the fraction of trapped gas (X_t) is given by

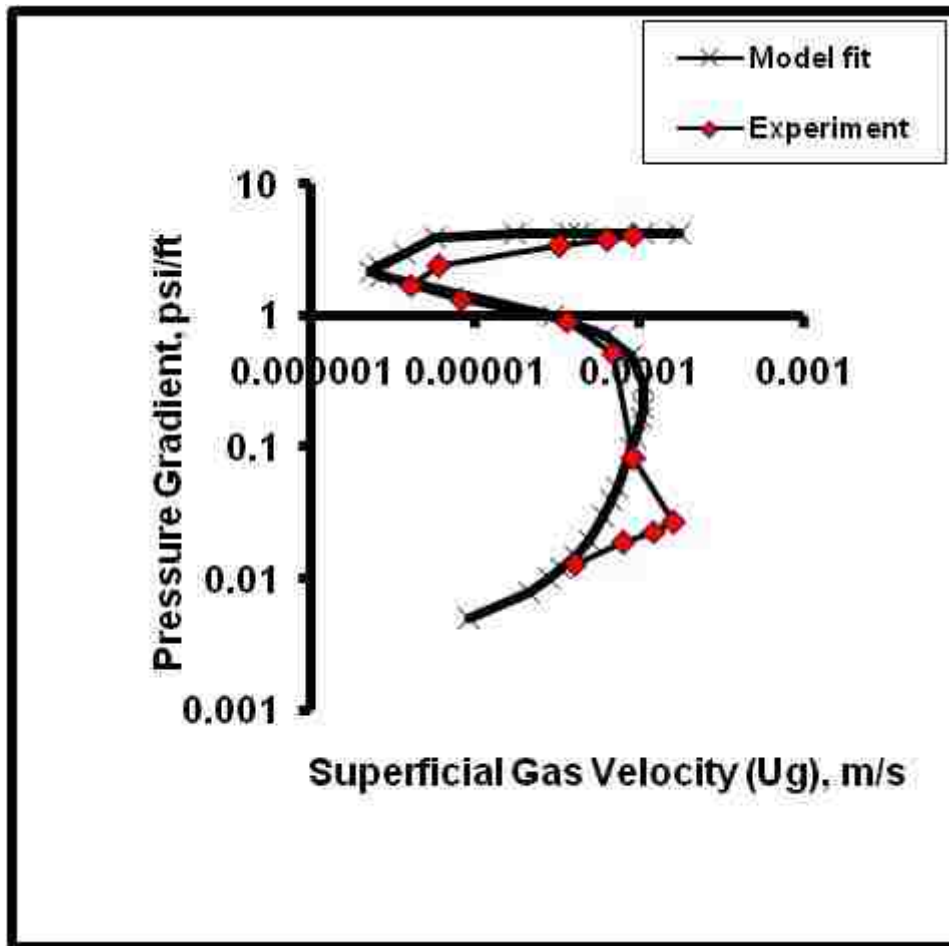


Figure A.1 Fit to experimental data: fit to S-shaped curve (Kam et al., 2007); 1 psi/ft = 22626 pa/m

$$X_t = X_{tmax} \left(\frac{\beta n_t}{1 + \beta n_t} \right) \quad (A.8)$$

where X_{tmax} and β are model parameters determined by surfactant adsorption experiments and n_t is the texture of trapped foam. Note that $n_t = n_f$ in this study. Flowing gas fraction (X_f) can then be calculated by $X_f = 1 - X_t$.

Once gas viscosity in the presence of foam (μ_g^f) is calculated by

$$\mu_g^f = \mu_g^0 + \frac{C_f n_f}{\left(\frac{u_g}{(\phi S_g X_f)} \right)^{1/3}} \quad \dots\dots\dots (A.9)$$

then the corresponding gas velocity (u_g) can be determined by Darcy's equation for gas phase as follows:

$$u_g = \frac{k k_{rg}^f(S_w)}{\mu_g^f} \nabla p \quad \dots\dots\dots (A.10)$$

Since Eqs. A.9 and A.10 are coupled one needs to determine gas velocity (u_g) and gas viscosity in the presence of foam (μ_g^f) simultaneously by solving both equations together.

A.2. Fit to Two Strong-Foam Flow Regimes (High-Quality and Low-Quality Regimes)

This section assumes that two foam parameters such as ∇P_0 and n are determined as described in the previous section and therefore focuses on the determination of C_g/C_c and C_f from the pressure contour. The model currently is capable of incorporating different shear-thinning exponents in the low-quality regime as observed in laboratory coreflood experiments, but assumes near-Newtonian behavior in the high-quality regime. Most of the equations explained in the previous section are valid for the descriptions given in this section.

To begin with, it should be mentioned that both C_g/C_c and C_f are determined from the intersection (i.e., f_g^*) between vertical contour and horizontal contour as shown in Fig. A.2.

Based on the previous experimental and theoretical studies, it is believed that (1) the bubble size becomes smaller (or foam texture becomes higher, equivalently) as gas velocity decreases along the vertical pressure contour; (2) once it reaches the lowest gas velocity along the vertical contour (i.e., f_g^*), bubble size reaches its minimum (approximately average pore size) and foam texture reaches its maximum (n_{fmax}); and (3) bubble size remains the same at its minimum (or foam texture remain the same at its maximum, equivalently) along the horizontal pressure contour.

Suppose the value of f_g^* is available from experimental data at given pressure gradient along a pressure contour. Then, the magnitude of C_g/C_c can be determined directly by re-writing Eq. A.6 which is,

$$\frac{C_g}{C_c} = 2n_{fmax} \left(\frac{\left(\frac{S_w}{S_w - S_w^*}\right)^n}{\left\{\operatorname{erf}\left(\frac{\sqrt{p} - \sqrt{p_0}}{\sqrt{2}}\right) - \operatorname{erf}\left(\frac{-\sqrt{p_0}}{\sqrt{2}}\right)\right\}} \right)_{\text{at } f_g = f_g^*} \dots\dots\dots (A.11)$$

The steps described in Section A.1 enable other physical properties determined at that particular value of pressure gradient assigned by the pressure contour (i.e., pressure gradient \rightarrow liquid permeability \rightarrow water saturation). Since gas velocity at f_g^* is experimentally determined and the trapped gas fraction is computed from Eq. A.8 (note that $n_f = n_{fmax}$), there is only one unknown variable, μ_g^f , in both Eqs. A.9 and A.10. Equating those two equations and re-writing the equation for C_f leads to the following expression:

$$C_f = \left(\left[\left(\frac{k k_{rg}^f(S_w) \nabla p}{u_g} - \mu_g^o \right) / n_{fmax} \right] \left[\frac{u_g}{\phi S_g X_f} \right]^{\frac{1}{3}} \right)_{\text{at } f_g = f_g^*} \dots\dots\dots (A.12)$$

Once C_g/C_c and C_f are determined, one can move on to the high-quality and low-quality regimes in order to investigate how foam rheology changes as a function of different gas and liquid velocities.

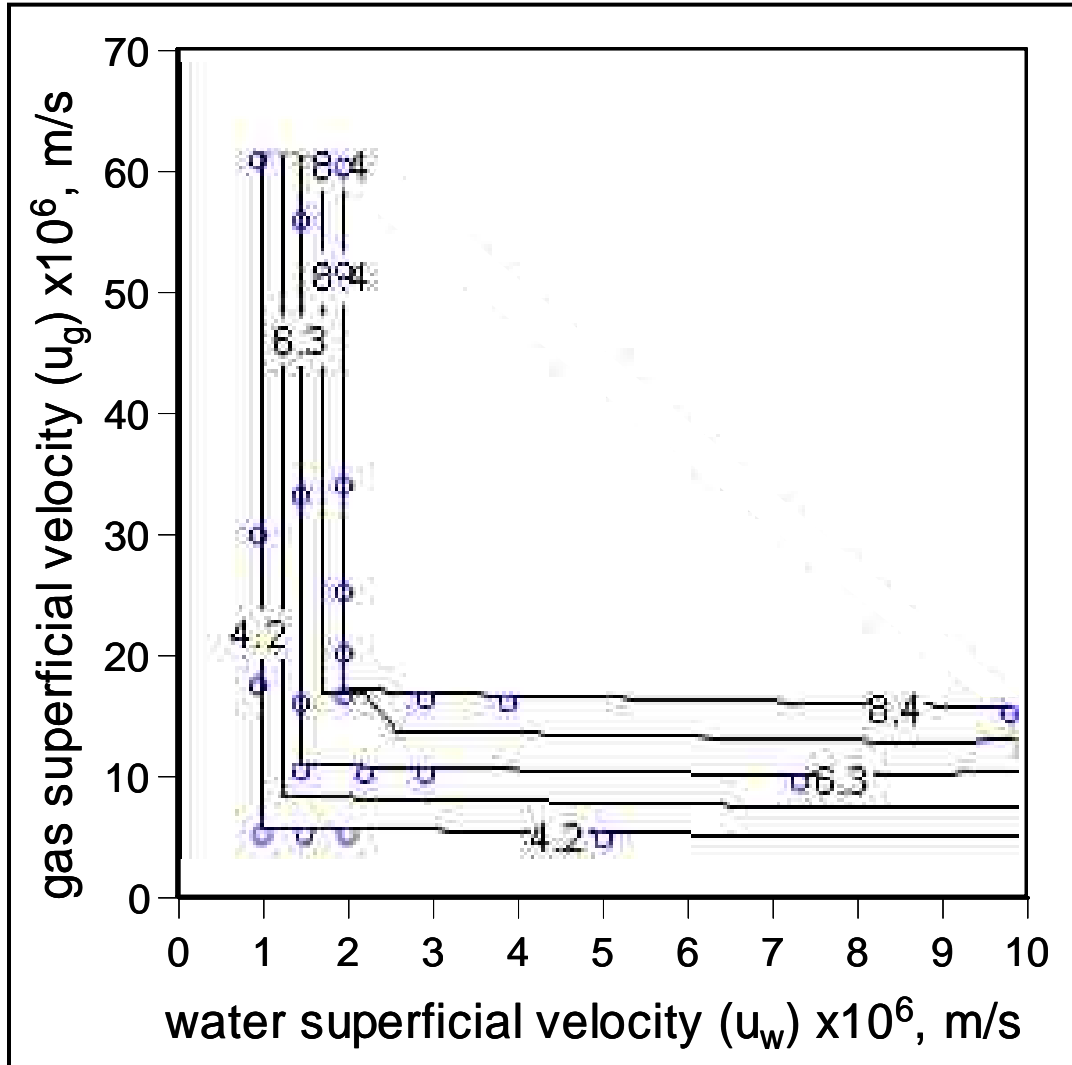


Figure A.2 Fit to experimental data: fit to two flow regimes (Kam et al., 2007) : the contour shows the steady-state pressure gradient in psi/ft (1 psi/ft = 22,626 Pa/m)

A.3. Construction of Mechanistic Foam Fractional Flow Curves

Once the parameters are determined, one can construct mechanistic foam fractional flow curves by using the above-mentioned equations in a similar manner. There exist a few different methods, and the approach described below serves as one possible example among them.

Because mechanistic foam fractional flow curves are sensitive to velocity, the first step is to set a certain total injection velocity (u_t) of interest. One can come up with a column with different values of u_w in Excel which determines another column with the values of u_g simultaneously (note that $u_g = u_t - u_w$). The goal is to determine the value of water saturation that satisfies a given set of (u_g, u_w). The following steps are followed to meet this goal:

- Assume water saturation (S_w).
- Calculate liquid relative permeability (Eq. A.1) and gas relative permeability in the absence of foams (Eq. A.3).
- Calculate the pressure gradient from Darcy's equation for water (Eq. A.1).
- Determine foam texture (Eq. A.6) and trapped gas fraction (Eq. A.8).
- Solve Darcy's equation for gas (Eq. A.10) and gas viscosity (Eq. A.9) simultaneously to determine u_g and μ_g^f .
- Conduct iterations by changing S_w until the calculated value of u_g is close enough to the assumed u_g .

APPENDIX B. NEW FOAM SIMULATION ALGORITHM USING MATRIX SOLVER

Much of the mechanistic simulation in this study follows the upgraded algorithm shown by Kam (2008) which determines liquid/gas fractional flows and saturations separated from the subsequent pressure calculations within a major iteration loop for effective gas viscosity. This study developed a new simulation algorithm which allows the calculation of saturations and pressures at the same time by using a matrix solver following modified Gaussian elimination technique for Block Tri-diagonal matrix- BITRI subroutine (Aziz and Settari, 1979). This algorithm is fully implicit in a sense that saturations and pressures are updated at a new time step, but still uses effective gas viscosity determined in the previous time step. Although none of these two algorithms experienced poor convergence and/or instability issues, the new version provides the simulation with a better stability near the onset of foam generation with the help of a matrix solver (Figs. 4.17(a) vs. C.7 (a)). For example, when $u_f=u_g=5.3 \times 10^{-5}$ m/s with 25 grids, the previous algorithm does not converge (It converges with 150 grids (Fig. 4.17(a))), but the new algorithm does (Fig. C.7 (a)). The results from both algorithms were basically the same, and the following sections briefly describe the new algorithm with the matrix solver.

The new algorithm also starts with material balance as described in Chapter 3, i.e.,

$$\frac{\partial}{\partial t}(\phi S_j) + \nabla \cdot (\bar{u}_j) = 0 \quad , \quad j = g \text{ and } w \quad \dots\dots\dots (B.1)$$

which can be combined with transport equations for different phases. For example, in the case of liquid phase,

$$u_w = - \frac{k k_{rw}(S_w)}{\mu_w} \nabla \phi_w = -\lambda_w(S_w) \nabla \phi_w \quad \dots\dots\dots (B.2)$$

Note that λ_w and Φ_w represent liquid-phase mobility and fluid potential along the liquid phase.

Therefore Eq. B.1 can be re-written as follows for liquid phase.

$$\frac{\partial}{\partial t}(\phi S_w) = \nabla \cdot (\lambda_w \nabla \phi_w) = \nabla \cdot (\lambda_w (\nabla p_w - \gamma_w \nabla h)) \dots\dots\dots (B.3)$$

A similar equation can be derived from gas phase. The term “h” accounts for the pressure drop caused by the hydrostatic head.

B.1. Discretization of Material Balance Equation

A grid system used in this study is shown below in Fig. B.1 with three consecutive grid blocks, (i-1)-th, i-th and (i+1)-th nodes. Some transport properties defined at the boundary between adjacent grid blocks (i.e., relative permeability, mobility, and transmissibility) use the notation of i+ and i- to represent (i+ 1/2) and (i - 1/2).

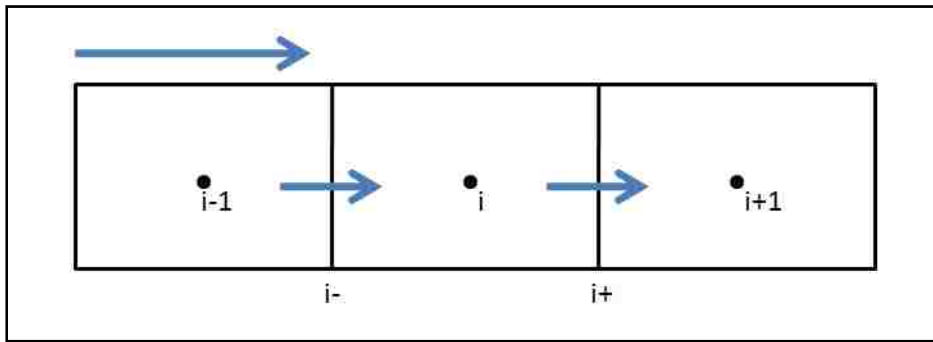


Figure B.1 Representation of grid blocks used in the simulation

B.1.1. Liquid Phase

Once fully implicit CSFT (central in space and forward in time) is applied assuming that the system in x-direction is horizontal (i.e., $\frac{\partial h}{\partial x} = 0$), then the right-hand-side (RHS) term becomes

$$\begin{aligned} \frac{\partial}{\partial x} \left(\lambda_w \left(\frac{\partial p_w}{\partial x} - \gamma_w \frac{\partial h}{\partial x} \right) \right) &= \partial_x (\lambda_w \partial_x p_w) \\ &= \frac{1}{\Delta x^2} [\lambda_{wi+} p_{w(i+1)} - (\lambda_{wi+} + \lambda_{wi-}) p_{w(i)} + \lambda_{wi-} p_{w(i-1)}] \dots\dots\dots (B.4) \end{aligned}$$

Note that the pressure terms are defined at the center of each grid block, and the relative mobility is defined at the boundary between grid blocks, i.e.,

$$\lambda_{w,i+} = \lambda_w(S_{w,i+1/2}) = \lambda_w(S_{w,i+}) = \frac{kk_{rw}(S_{w,i})}{\mu_w} \dots\dots\dots (B.5)$$

$$\lambda_{w,i-} = \lambda_w(S_{w,i-1/2}) = \lambda_w(S_{w,i-}) = \frac{kk_{rw}(S_{w,i-1})}{\mu_w} \dots\dots\dots (B.6)$$

The left-hand-side (LHS) term can be discretized as follows:

$$\partial_t(\phi S_w) = \frac{\phi}{\Delta t} [S_{wi}^{t+} - S_{wi}^t] \dots\dots\dots (B.7)$$

The grid block size is assumed uniform, i.e., $\Delta x = x_i - x_{i-1} = x_{i+1} - x_i$. Putting Eqs. B.4 and B.7 together ends up with the final equation for water phase as follows:

$$[\lambda_{wi+}p_{w(i+1)} - (\lambda_{wi+} + \lambda_{wi-})p_{w(i)} + \lambda_{wi-}p_{w(i-1)}] = \frac{\phi(\Delta x)^2}{\Delta t} [S_{wi}^{t+} - S_{wi}^t] \dots\dots\dots (B.8)$$

B.1.2. Gas Phase

Gas-phase pressure (p_g) and liquid-phase pressure (p_w) are related through capillary pressure (p_c) as follows:

$$p_g = p_w + p_c \dots\dots\dots (B.9)$$

where p_c is defined by

$$p_{c_i} = \alpha e^{-\left(\frac{S_{w_i}}{\beta}\right)} \dots\dots\dots (B.10)$$

with two model parameters α and β .

From material balance for gas phase which can be written as

$$\frac{\partial}{\partial t} (\phi S_g) = \nabla \cdot (\lambda_g \nabla \phi) = \nabla \cdot (\lambda_g (\nabla p - \gamma_g \nabla h)) \dots\dots\dots (B.11)$$

The RHS becomes

$$\begin{aligned}
(\lambda_g \partial_x(p_w + p_c))_{i+\frac{1}{2}} &= \lambda_{g(i+\frac{1}{2})} [\partial_x(p_w) + \partial_x(p_c)]_{(i+\frac{1}{2})} \\
&= \lambda_{g(i+\frac{1}{2})} \left[\partial_x(p_w) + \left(p'_c \times \frac{\partial S_w}{\partial x} \right) \right]_{(i+\frac{1}{2})} \\
&= \frac{\lambda_{g(i+\frac{1}{2})}}{\Delta x} \left[(p_{w,i+1} - p_{w,i}) + p'_{c,i+\frac{1}{2}} (S_{w,i+1} - S_{w,i}) \right] \\
&\dots\dots\dots (B.12)
\end{aligned}$$

$$\begin{aligned}
\partial_x(\lambda_g \partial_x p_g)_i &= \frac{(\lambda_g \partial_x p_g)_{i+\frac{1}{2}} - (\lambda_g \partial_x p_g)_{i-\frac{1}{2}}}{\Delta x} \\
&= \frac{(\lambda_g \partial_x(p_w + p_c))_{i+\frac{1}{2}} - (\lambda_g \partial_x(p_w + p_c))_{i-\frac{1}{2}}}{\Delta x} \\
&= \frac{\lambda_{g(i+\frac{1}{2})} \left[(p_{w,i+1} - p_{w,i}) + p'_{c,i+\frac{1}{2}} (S_{w,i+1} - S_{w,i}) \right]}{\Delta x^2} \\
&\quad - \frac{\lambda_{g(i-\frac{1}{2})} \left[(p_{w,i} - p_{w,i-1}) + p'_{c,i-\frac{1}{2}} (S_{w,i} - S_{w,i-1}) \right]}{\Delta x^2} \\
&\dots\dots\dots (B.13)
\end{aligned}$$

Note that the Chain rule is applied to the capillary pressure such that

$$\frac{\partial p_c}{\partial x} = \frac{\partial p_c}{\partial S_w} \times \frac{\partial S_w}{\partial x} = p'_c \times \frac{\partial S_w}{\partial x} \dots\dots\dots (B.14)$$

As was discussed in the previous section, the mobility terms are defined by

$$\lambda_{g,i+} = \lambda_g(S_{w,i+\frac{1}{2}}) = \lambda_g(S_{w,i+}) = \frac{kk_{rg}(S_{w,i})}{\mu_g} \dots\dots\dots (B.15)$$

$$\lambda_{g,i-} = \lambda_g(S_{w,i-\frac{1}{2}}) = \lambda_g(S_{w,i-}) = \frac{kk_{rg}(S_{w,i-1})}{\mu_g} \dots\dots\dots (B.16)$$

In addition, the capillary pressure term is discretized as

$$p_{c_{i+1/2}} = \alpha e^{-\left(\frac{S_{w_i}}{\beta}\right)} \dots\dots\dots (B.17)$$

The capillary pressure derivative with respect with water saturation (which will be used in the formation of Jacobian matrix later) is then given by

$$p'_{c_{i+1/2}} = -\left(\frac{\alpha}{\beta}\right) e^{-\left(\frac{S_{w_i}}{\beta}\right)} \dots\dots\dots (B.18)$$

and

$$p''_{c_{i+1/2}} = \left(\frac{\alpha}{\beta^2}\right) e^{-\left(\frac{S_{w_i}}{\beta}\right)} \dots\dots\dots (B.19)$$

The LHS term becomes

$$\frac{\partial}{\partial t} (\phi S_g) = \frac{\phi}{\Delta t} (S_{g,i}^{t+1} - S_{g,i}^t) = \frac{\phi}{\Delta t} (S_{w,i}^t - S_{w,i}^{t+1}) \dots\dots\dots (B.20)$$

Therefore, the final discretized material-balance equation for gas becomes as follows:

$$\begin{aligned} & \lambda_{g(i+\frac{1}{2})} \left[(p_{w,i+1} - p_{w,i}) + p'_{c,i+\frac{1}{2}} (S_{w,i+1} - S_{w,i}) \right] \\ & - \lambda_{g(i-\frac{1}{2})} \left[(p_{w,i} - p_{w,i-1}) + p'_{c,i-\frac{1}{2}} (S_{w,i} - S_{w,i-1}) \right] \\ & = \frac{\phi(\Delta x)^2}{\Delta t} [S_{wi}^t - S_{wi}^{t+}] \dots\dots\dots (B.21) \end{aligned}$$

B.2. Construction of Jacobian Matrix

Discretized finite difference equation for liquid phase can be re-arranged as follows:

$$F_{2i-1} = \left[\lambda_{wi+} p_{w(i+1)} - (\lambda_{wi+} + \lambda_{wi-}) p_{w(i)} + \lambda_{wi-} p_{w(i-1)} \right] - \frac{\phi(\Delta x)^2}{\Delta t} [S_{wi}^{t+} - S_{wi}^t] \dots\dots\dots (B.22)$$

Notice that the subscript (2i-1) for residual vector (F) represents the vector for liquid phase, and liquid relative permeability and its derivative are shown to be

$$k_{rwi} = 0.7888 \left(\frac{S_{wi} - S_{wc}}{1 - S_{wc} - S_{gr}} \right)^{1.9575} \dots\dots\dots (B.23)$$

and

$$k'_{rwi} = \frac{1.5441}{(1-S_{wc}-S_{gr})^{1.9575}} (S_{wi} - S_{wc})^{0.9575} \dots\dots\dots (B.24)$$

Derivatives of F_{2i-1} are expressed as follows:

With respect to upstream pressure

$$\frac{\partial F_{2i-1}}{\partial p_{w(i-1)}} = \frac{\partial F_{2i-1}}{\partial P_{(2i-3)}} = \lambda_{wi-} ; \dots\dots\dots (B.25)$$

With respect to upstream saturation

$$\frac{\partial F_{2i-1}}{\partial S_{w(i-1)}} = \frac{\partial F_{2i-1}}{\partial P_{(2i-2)}} = \lambda'_{w(i-1)} (p_{w(i-1)} - p_{wi}); \dots\dots\dots (B.26)$$

With respect to pressure at the grid of interest

$$\frac{\partial F_{2i-1}}{\partial p_{w(i)}} = \frac{\partial F_{2i-1}}{\partial P_{(2i-1)}} = -(\lambda_{wi+} + \lambda_{wi-}) ; \dots\dots\dots (B.27)$$

With respect to saturation at the grid of interest

$$\frac{\partial F_{2i-1}}{\partial S_{wi}} = \frac{\partial F_{2i-1}}{\partial P_{(2i)}} = \lambda'_{wi} (p_{w(i+1)} - p_{wi}) - \frac{\phi(\Delta x)^2}{\Delta t} ; \dots\dots\dots (B.28)$$

With respect to downstream pressure

$$\frac{\partial F_{2i-1}}{\partial p_{w(i+1)}} = \frac{\partial F_{2i-1}}{\partial P_{(2i+1)}} = \lambda_{wi+} ; \text{ and } \dots\dots\dots (B.29)$$

With respect to downstream saturation

$$\frac{\partial F_{2i-1}}{\partial S_{w(i+1)}} = \frac{\partial F_{2i-1}}{\partial P_{(2i+2)}} = 0 , \dots\dots\dots (B.30)$$

where P is the solution matrix to be defined in the following section.

Similarly, discretized finite difference equation for gas phase can be re-arranged as follows:

$$F_{2i} = \lambda_{g(i+\frac{1}{2})} \left[(p_{w,i+1} - p_{w,i}) + p'_{c,i+\frac{1}{2}} (S_{w,i+1} - S_{w,i}) \right] \\ - \lambda_{g(i-\frac{1}{2})} \left[(p_{w,i} - p_{w,i-1}) + p'_{c,i-\frac{1}{2}} (S_{w,i} - S_{w,i-1}) \right]$$

$$-\frac{\phi(\Delta x)^2}{\Delta t} [S_{wi}^t - S_{wi}^{t+}] \dots\dots\dots (B.31)$$

The subscript (2i) for residual vector (F) represents the vector for gas phase, and gas relative permeability and its derivative are shown to be

$$k_{rgi} = \left(\frac{1-S_{wi}-S_{gr}}{1-S_{wc}-S_{gr}} \right)^{2.2868} \dots\dots\dots (B.32)$$

and

$$k'_{rgi} = \frac{-2.2868}{(1-S_{wc}-S_{gr})^{2.2868}} (1 - S_{wi} - S_{gr})^{1.2868} \dots\dots\dots (B.33)$$

Derivatives of F_{2i} are expressed as follows:

With respect to upstream pressure

$$\frac{\partial F_{2i}}{\partial p_{w(i-1)}} = \frac{\partial F_{2i}}{\partial P_{(2i-3)}} = \lambda_{gi-} \dots\dots\dots (B.34)$$

With respect to upstream saturation

$$\begin{aligned} \frac{\partial F_{2i}}{\partial S_{w(i-1)}} = \frac{\partial F_{2i}}{\partial P_{(2i-2)}} = & -\lambda'_{g,i-1} (p_{w(i)} - p_{w,i-1}) - \lambda'_{g,i-1} p'_{c,i-1} S_{w(i)} - p''_{c,i-1} \lambda_{g,i-1} S_{w(i)} \\ & + \lambda'_{g,i-1} p'_{c,i-1} S_{w,i-1} + p''_{c,i-1} \lambda_{g,i-1} S_{w,i-1} + \lambda_{g,i-1} p'_{c,i-1} \\ & ; \dots\dots\dots (B.35) \end{aligned}$$

With respect to pressure at the grid of interest

$$\frac{\partial F_{2i}}{\partial p_{w(i)}} = \frac{\partial F_{2i}}{\partial P_{(2i-1)}} = -(\lambda_{gi+} + \lambda_{gi-}) \dots\dots\dots (B.36)$$

With respect to saturation at the grid of interest

$$\begin{aligned} \frac{\partial F_{2i}}{\partial S_{wi}} = \frac{\partial F_{2i}}{\partial P_{(2i)}} = & \lambda'_{gi} (p_{w(i+1)} - p_{w,i}) + \lambda'_{gi} p'_{ci} S_{w(i+1)} + p''_{ci} \lambda_{gi} S_{w(i+1)} - \lambda'_{gi} p'_{ci} S_{w,i} \\ & - p''_{ci} \lambda_{gi} S_{w,i} - \lambda_{gi} p'_{ci} - \lambda_{g,i-1} p'_{c,i-1} + \frac{\phi(\Delta x)^2}{\Delta t} ; \dots\dots\dots (B.37) \end{aligned}$$

With respect to downstream pressure

$$\frac{\partial F_{2i}}{\partial p_{w(i+1)}} = \frac{\partial F_{2i}}{\partial P_{(2i+1)}} = \lambda_{gi+} \quad ; \text{ and} \quad \dots\dots\dots (B.38)$$

With respect to downstream saturation

$$\frac{\partial F_{2i}}{\partial S_{w(i+1)}} = \frac{\partial F_{2i}}{\partial P_{(2i+2)}} = p'_{c(i)} \lambda_{gi} \quad \dots\dots\dots (B.39)$$

Pressure and saturations are related to the solution matrix (P) as follows:

$$p_{w(i-1)} = P_{2(i-1)-1} = P_{2i-3} \quad \dots\dots\dots (B.40)$$

$$S_{w(i-1)} = P_{2(i-1)} = P_{2i-2} \quad \dots\dots\dots (B.41)$$

$$p_{wi} = P_{2i-1} \quad \dots\dots\dots (B.42)$$

$$S_{wi} = P_{2i} \quad \dots\dots\dots B.43$$

$$p_{w(i+1)} = P_{2(i+1)-1} = P_{2i+1} \quad \dots\dots\dots (B.44)$$

$$S_{w(i+1)} = P_{2(i+1)} = P_{2i+2} \quad \dots\dots\dots (B.45)$$

Nicholson-Raphson method can solve the nonlinear equations. Note that all derivatives in Jacobian matrix and all residual terms are related to the solution matrix as schematically shown in Fig. B.2. The Jacobian matrix formed in this algorithm is a block tri-diagonal matrix. The BITRI matrix solver (Aziz and Settari, 1979) was used to solve the block tri-diagonal more efficiently. In other words, the formulated discretized equation becomes as follows:

$$J^k \delta P^{k+1} = -F^k \quad \dots\dots\dots (B.46)$$

$$P^{k+1} = P^k + \delta P^{k+1} \quad \dots\dots\dots (B.47)$$

Where, k and k+1 represent the previous and the new iterations, respectively. J is Jacobian matrix, F is the residual term, and P and δP are the solution matrix and its increment/decrement.

The P matrix can be updated at each iteration step from δP (or ΔP in Fig. B.2) as follows.

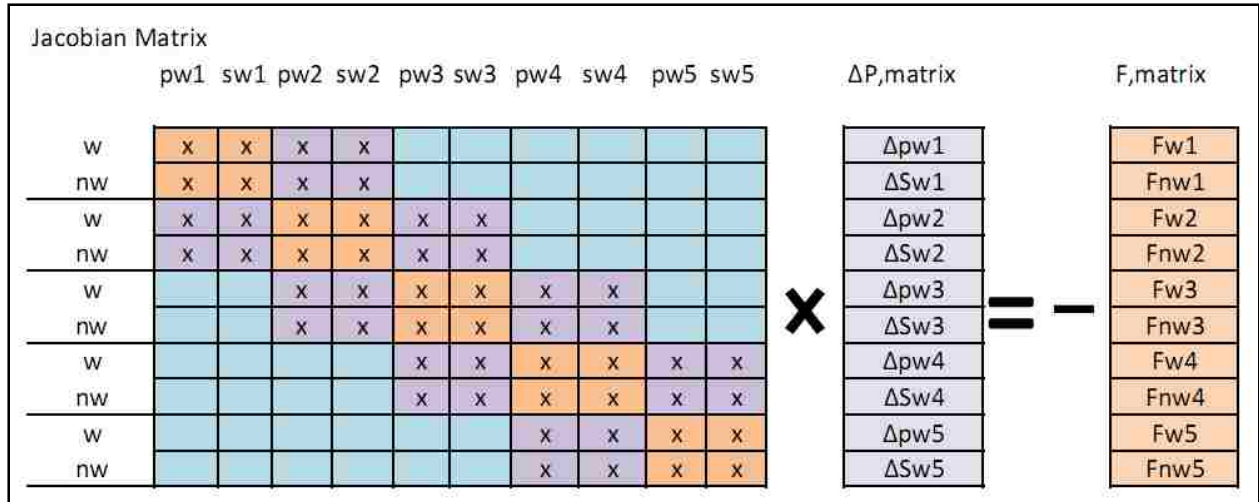


Figure B.2 Formulation of Jacobian, solution, and residual matrices. The term “w” and “nw” represents the equations and terms belongs to wetting (water) and non-wetting (gas), respectively. And p_{w1} , S_{w1} at the top of Jacobian matrix represents the derivative of the equations respect to water pressure and water saturation for grid number one

B.3. Discretization of Boundary Conditions

The finite-difference equations formulated for the matrix solver need a special treatment when the first and last grid blocks are concerned. Fig. B.3 show how those two grid blocks are taken into consideration in this algorithm. The boundary condition at the outlet is given by fixed outlet pressure (or backpressure), but the inlet boundary condition can be either fixed inlet pressure or fixed inlet injection rates.

B.3.1. Fixed-pressure Boundary Condition at the Outlet

The finite difference equation at the outlet at which $i = nx$ can be written as follows for liquid phase:

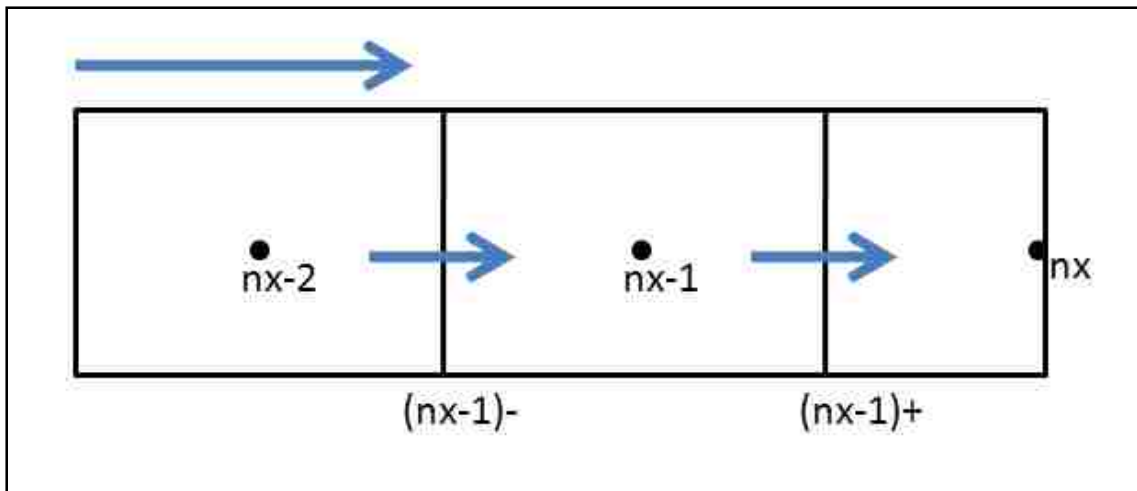
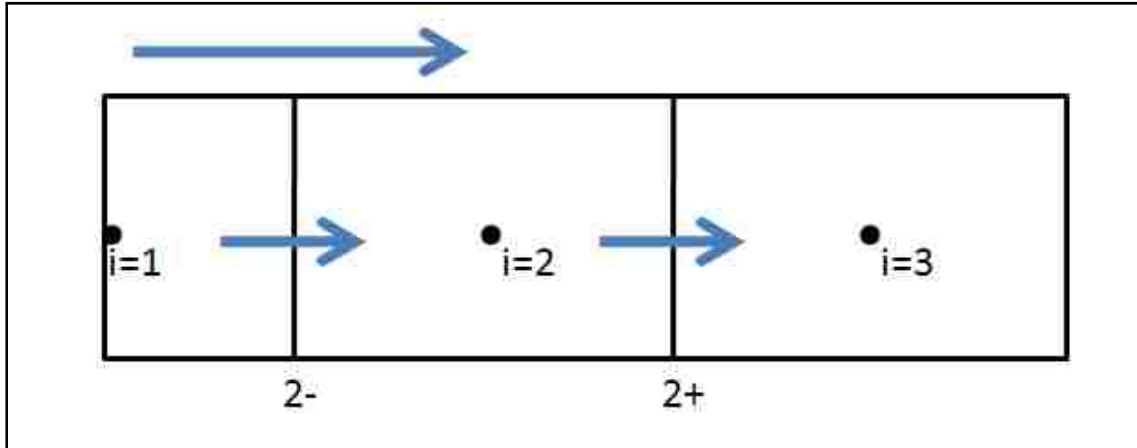


Figure B.3 Representation of the first and last grid blocks

$$F_{2(nx)-1} = [-(\lambda_{w,nx-1})p_{w(nx)} + \lambda_{w,nx-1}p_{w(nx-1)}] - \frac{\phi(\Delta x)^2}{\Delta t} [S_{w,nx}^{t+} - S_{w,nx}^t] \quad \dots\dots\dots (B.48)$$

The derivatives are given by

$$\frac{\partial F_{2nx-1}}{\partial p_{w(nx-1)}} = \frac{\partial F_{2nx-1}}{\partial P_{(2nx-3)}} = \lambda_{w,nx-1} \quad \dots\dots\dots (B.49)$$

$$\frac{\partial F_{2nx-1}}{\partial S_{w(nx-1)}} = \frac{\partial F_{2nx-1}}{\partial P_{(2nx-2)}} = \lambda'_{w(nx-1)}(p_{w(nx-1)} - p_{w,nx}) \quad \dots\dots\dots (B.50)$$

$$\frac{\partial F_{2nx-1}}{\partial p_{w(nx)}} = \frac{\partial F_{2nx-1}}{\partial P_{(2nx-1)}} = -(\lambda_{w,nx-1}) \quad \dots\dots\dots (B.51)$$

and

$$\frac{\partial F_{2nx-1}}{\partial S_{w,nx}} = \frac{\partial F_{2nx-1}}{\partial P_{(2nx)}} = \lambda'_{w,nx}(-p_{w,nx}) - \frac{\phi(\Delta x)^2}{\Delta t} \quad \dots\dots\dots (B.52)$$

For gas phase, the formulation becomes

$$F_{2,nx} = -\lambda_{g(nx-\frac{1}{2})} \left[(p_{w,nx} - p_{w,nx-1}) + P'_{c,nx-\frac{1}{2}}(S_{w,nx} - S_{w,nx-1}) \right] - \frac{\phi(\Delta x)^2}{\Delta t} [S_{w,nx}^t - S_{w,nx}^{t+}] \quad \dots\dots\dots (B.53)$$

with the following derivatives:

$$\frac{\partial F_{2,nx}}{\partial p_{w(nx-1)}} = \frac{\partial F_{2,nx}}{\partial P_{(2nx-3)}} = \lambda_{g,nx-1} \quad \dots\dots\dots (B.54)$$

$$\begin{aligned} \frac{\partial F_{2,nx}}{\partial S_{w(nx-1)}} = \frac{\partial F_{2,nx}}{\partial P_{(2nx-2)}} = & -\lambda'_{g,nx-1}(p_{w(nx)} - p_{w,nx-1}) - \lambda'_{g,nx-1}P'_{c,nx-1}S_{w(nx)} \\ & -P''_{c,nx-1}\lambda_{g,nx-1}S_{w(nx)} + \lambda'_{g,nx-1}P'_{c,nx-1}S_{w,nx-1} \\ & +P''_{c,nx-1}\lambda_{g,nx-1}S_{w,nx-1} + \lambda_{g,nx-1}P'_{c,nx-1} \quad \dots\dots\dots (B.55) \end{aligned}$$

$$\frac{\partial F_{2,nx}}{\partial p_{w(nx)}} = \frac{\partial F_{2,nx}}{\partial P_{(2nx-1)}} = -(\lambda_{g,nx-1}) \quad \dots\dots\dots (B.56)$$

and

$$\frac{\partial F_{2nx}}{\partial S_{w,nx}} = \frac{\partial F_{2nx}}{\partial P_{(2nx)}} = -\lambda_{g,nx-1} P'_{c,nx-1} + \frac{\phi(\Delta x)^2}{\Delta t} \dots \dots \dots (B.57)$$

B.3.2. Fixed-Pressure Boundary Condition at the Inlet

For the fixed inlet boundary condition with pressure fixed, the saturation at the formation face (i.e., first node) is already determined if gas or liquid fraction is specified and if no foam films are present. This implies that S_w at the first node is directly calculated from no-foam gas-liquid fractional flow curve and is invariant with time (i.e., $S_{w,1}^{t+} - S_{w,1}^t = 0$).

The finite difference equation at the inlet at which $i = 1$ can be written as follows for liquid phase:

$$F_1 = [\lambda_{w,1} p_{w(2)} - (\lambda_{w,1}) p_{w(1)}] - \frac{\phi(\Delta x)^2}{\Delta t} [S_{w,1}^{t+} - S_{w,1}^t] \dots \dots \dots (B.58)$$

where the derivatives are

$$\frac{\partial F_1}{\partial p_{w(1)}} = \frac{\partial F_1}{\partial P_{(1)}} = -(\lambda_{w,1}) \dots \dots \dots (B.59)$$

$$\frac{\partial F_1}{\partial S_{w,1}} = \frac{\partial F_1}{\partial P_{(2)}} = \lambda'_{w,1} (p_{w(2)} - p_{w,1}) - \frac{\phi(\Delta x)^2}{\Delta t} \dots \dots \dots (B.60)$$

$$\frac{\partial F_1}{\partial p_{w(2)}} = \frac{\partial F_1}{\partial P_{(3)}} = \lambda_{w,1} \dots \dots \dots (B.61)$$

and

$$\frac{\partial F_1}{\partial S_{w(2)}} = \frac{\partial F_1}{\partial P_{(4)}} = 0 \dots \dots \dots (B.62)$$

The finite difference for gas phase is

$$F_2 = \lambda_{g(1)} [(p_{w,2} - p_{w,1}) + P'_{c,1} (S_{w,2} - S_{w,1})] - \frac{\phi(\Delta x)^2}{\Delta t} [S_{w,1}^t - S_{w,1}^{t+}] \dots \dots \dots (B.63)$$

where the derivatives are

$$\frac{\partial F_2}{\partial p_{w(1)}} = \frac{\partial F_2}{\partial P(1)} = -(\lambda_{g,1}) \dots\dots\dots (B.64)$$

$$\begin{aligned} \frac{\partial F_2}{\partial S_{w,1}} = \frac{\partial F_2}{\partial P(2)} = & \lambda'_{g,1}(p_{w(2)} - p_{w,1}) + \lambda'_{g,1}P'_{c,1}S_{w(2)} + P'_{c,1}\lambda_{g,1}S_{w(2)} \\ & - \lambda'_{g,1}P'_{c,1}S_{w,1} - P'_{c,1}\lambda_{g,1}S_{w,1} - \lambda_{g,1}P'_{c,1} + \frac{\phi(\Delta x)^2}{\Delta t} \dots\dots\dots (B.65) \end{aligned}$$

$$\frac{\partial F_2}{\partial p_{w(2)}} = \frac{\partial F_2}{\partial P(3)} = \lambda_{g,1} \dots\dots\dots (B.66)$$

and

$$\frac{\partial F_2}{\partial S_{w(2)}} = \frac{\partial F_2}{\partial P(4)} = P'_{c(1)}\lambda_{g,1} \dots\dots\dots (B.67)$$

B.3.3. Fixed-Rate Boundary Condition at the Inlet

If the boundary condition at the inlet is given by fixed injection rate (i.e., fixed gas velocity because this study focuses on gas only injection), the program should be modified such that the finite difference equation at the inlet at which $i = 1$ should be written as follows. Note that u_{win} and u_{gin} represent water and gas injection velocities, respectively.

More specifically, for liquid phase:

$$F_1 = [\lambda_{w,1}p_{w(2)} - (\lambda_{w,1})p_{w(1)}] - \frac{\phi(\Delta x)^2}{\Delta t} [S_{w,1}^{t+} - S_{w,1}^t] + u_{win} \dots\dots\dots (B.68)$$

where the derivatives are

$$\frac{\partial F_1}{\partial p_{w(1)}} = \frac{\partial F_1}{\partial P(1)} = -(\lambda_{w,1}) \dots\dots\dots (B.69)$$

$$\frac{\partial F_1}{\partial S_{w,1}} = \frac{\partial F_1}{\partial P(2)} = \lambda'_{w,1}(p_{w(2)} - p_{w,1}) - \frac{\phi(\Delta x)^2}{\Delta t} \dots\dots\dots (B.70)$$

$$\frac{\partial F_1}{\partial p_{w(2)}} = \frac{\partial F_1}{\partial P(3)} = \lambda_{w,1} \dots\dots\dots (B.71)$$

and

$$\frac{\partial F_1}{\partial S_{w(2)}} = \frac{\partial F_1}{\partial P(4)} = 0 \dots\dots\dots (B.72)$$

For gas phase,

$$F_2 = \lambda_{g(1)}[(p_{w,2} - p_{w,1}) + P'_{c,1}(S_{w,2} - S_{w,1})] - \frac{\phi(\Delta x)^2}{\Delta t}[S_{w,1}^t - S_{w,1}^{t+}] + u_{gin} \quad \dots\dots\dots (B.73)$$

where the derivatives are

$$\frac{\partial F_2}{\partial p_{w(1)}} = \frac{\partial F_2}{\partial P(1)} = -(\lambda_{g,1}) \quad \dots\dots\dots (B.74)$$

$$\begin{aligned} \frac{\partial F_2}{\partial S_{w,1}} = \frac{\partial F_2}{\partial P(2)} = & \lambda'_{g,1}(p_{w(2)} - p_{w,1}) + \lambda'_{g,1}P'_{c,1}S_{w(2)} + P'_{c,1}\lambda_{g,1}S_{w(2)} - \lambda'_{g,1}P'_{c,1}S_{w,1} \\ & - P'_{c,1}\lambda_{g,1}S_{w,1} - \lambda_{g,1}P'_{c,1} + \frac{\phi(\Delta x)^2}{\Delta t} \quad \dots\dots\dots (B.75) \end{aligned}$$

$$\frac{\partial F_2}{\partial p_{w(2)}} = \frac{\partial F_2}{\partial P(3)} = \lambda_{g,1} \quad \dots\dots\dots (B.76)$$

and

$$\frac{\partial F_2}{\partial S_{w(2)}} = \frac{\partial F_2}{\partial P(4)} = P'_{c(1)}\lambda_{g,1} \quad \dots\dots\dots (B.77)$$

B.3.4. Bubble Population Balance Calculations

Bubble population balance is given by the following equation.

$$\begin{aligned} \frac{\partial}{\partial t}(\phi S_g n_f) + \frac{\partial}{\partial x}(u_g n_f) &= \phi S_g (r_g - r_c) \\ &= \phi S_g \left(\frac{C_g}{2} \left\{ erf \left(\frac{\nabla p - \nabla p_o}{\sqrt{2}} \right) - erf \left(\frac{-\nabla p_o}{\sqrt{2}} \right) \right\} - C_c n_f \left(\frac{S_w}{S_w - S_w^*} \right)^n \right) \quad \dots\dots\dots (B.78) \end{aligned}$$

Note that the error function can be replaced with the cumulative distribution function, F, and therefore

$$\frac{C_g}{2} \left\{ erf \left(\frac{\nabla p_i - \nabla p_o}{\sqrt{2}} \right) - erf \left(\frac{-\nabla p_o}{\sqrt{2}} \right) \right\} = C_g \{ F(\nabla p_i - \nabla p_o) - F(-\nabla p_o) \} \quad \dots\dots\dots (B.79)$$

For bubble population balance equation, BSBT (backward in space and backward in time) is applied for discretization as shown below. Foam texture at the new time step, then, can be calculated by

$$\begin{aligned} & \frac{(S_g n_f)_i^t - (S_g n_f)_i^{t-1}}{\Delta t} + \frac{1}{\phi} \frac{(u_g n_f)_i^t - (u_g n_f)_{i-1}^t}{\Delta x} \\ &= S_{g,i}^t \left(\frac{C_g}{2} \left\{ \operatorname{erf} \left(\frac{\nabla p_i^t - \nabla p_o}{\sqrt{2}} \right) - \operatorname{erf} \left(\frac{-\nabla p_o}{\sqrt{2}} \right) \right\} - C_c n_{f,i}^t \left(\frac{S_{w,i}^t}{S_{w,i}^t - S_w^*} \right)^n \right) \end{aligned}$$

..... (B.80 a)

$$\begin{aligned} n_{f,i}^t = & \frac{(S_g n_f)_i^{t-1} + \frac{\Delta t}{\phi \Delta x} (u_g n_f)_{i-1}^t + \Delta t S_{g,i}^t \left(\frac{C_g}{2} \left\{ \operatorname{erf} \left(\frac{\nabla p_i^t - \nabla p_o}{\sqrt{2}} \right) - \operatorname{erf} \left(\frac{-\nabla p_o}{\sqrt{2}} \right) \right\} \right)}{S_{g,i}^t + \frac{\Delta t}{\phi \Delta x} u_{g,i}^t + C_c \Delta t S_{g,i}^t \left(\frac{S_{w,i}^t}{S_{w,i}^t - S_w^*} \right)^n} \end{aligned}$$

..... (B.80 b)

Because no foam is flowing into the media, $n_{f,1}^t = 0$.

B.4. Flow Chart

The chart shown in Fig. B.4 summarizes the procedure to determine variables at the new time step, (n-th), if the information at the previous time step, (n-1)-th, is known. The algorithm has an iteration loop for saturations and pressures. Once the iteration converges, it is followed by a bubble-population-balance loop which does not need iterations. Gas viscosity in the presence of foam (μ_g^f) is one time step behind, which eliminates another loop for μ_g^f calculations and thus saves computation time significantly.

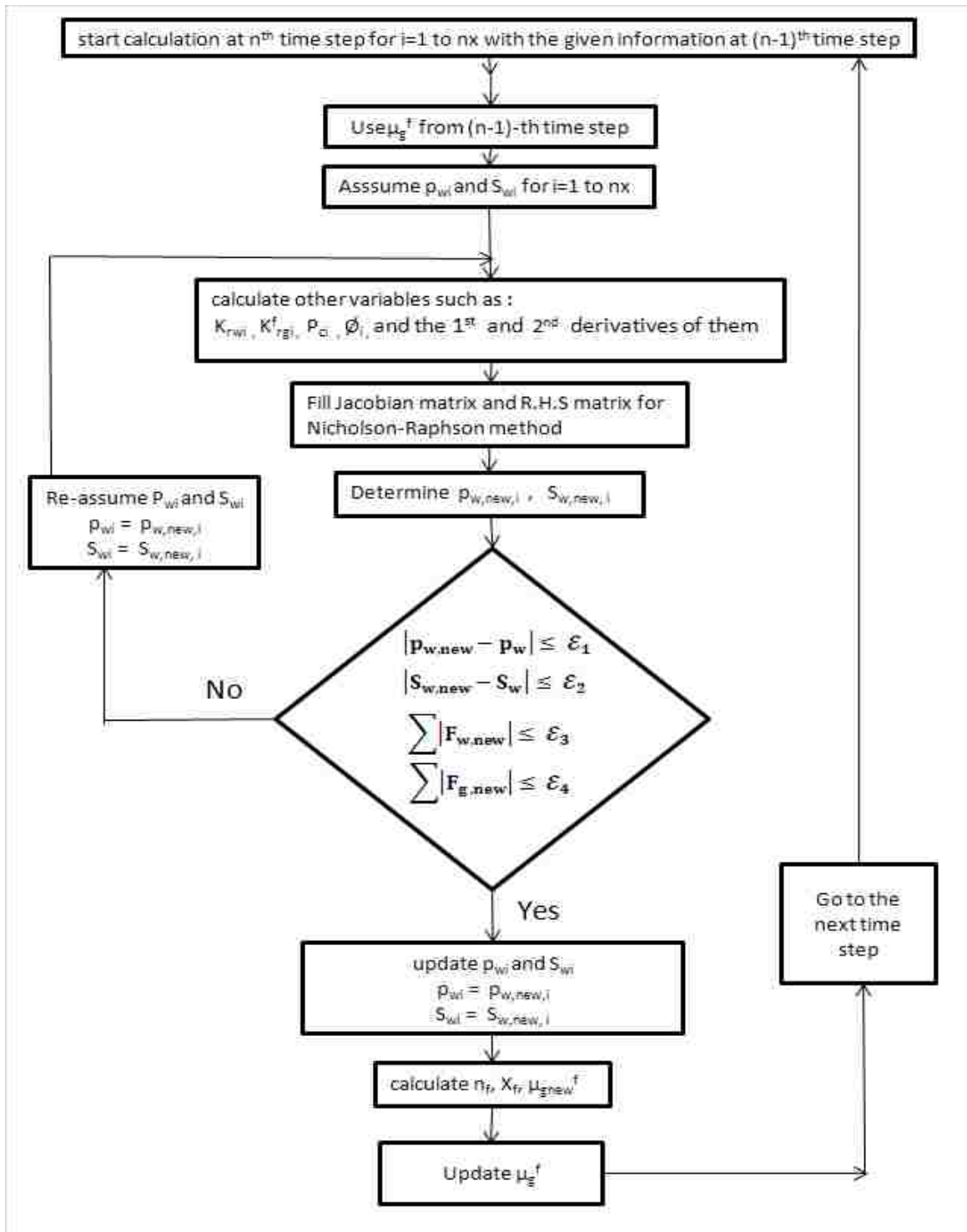


Figure B.4 Flow chart of the new algorithm

B.5. Two-Dimensional Simulation

The concept introduced in B.1 through B.4 for one-dimensional simulation can be extended into multi-dimensional space as described in this section.

As a first step, two mass balance equations are considered for gas and liquid phases as follows:

$$\frac{\partial}{\partial t}(\phi S_j) + \nabla \cdot (\bar{u}_j) = 0 \quad , \quad \dots\dots\dots (B.81)$$

where j represents either water or gas phase. The mass balance equations for water and gas phases are

$$\frac{\partial}{\partial t}(\phi S_w) = \nabla \cdot (\lambda_w \nabla \phi) = \nabla \cdot (\lambda_w (\nabla p_w - \gamma_w \nabla h)) \quad \dots\dots\dots (B.82 a)$$

and

$$\frac{\partial}{\partial t}(\phi S_g) = \nabla \cdot (\lambda_g \nabla \phi) = \nabla \cdot (\lambda_g (\nabla p_g - \gamma_g \nabla h)) \quad \dots\dots\dots (B.82 b)$$

B.5.1. Discretization of Material Balance Equation

In order to explain the way the system is discretized, an example 5×5 two-dimensional system is shown in Figs. B. 5 and B. 6. The (i, j) configuration represents i-th grid in horizontal direction from left-hand side boundary and j-th grid in vertical direction from the top. Each grid has a serial number which is written in the square in Fig. B.5. This number is counted by rows, left to right first, then top to bottom.

Following definitions help the contents in the subsequent sections:

$$\lambda_w(S_w) = \frac{k k_{rw}(S_w)}{\mu_w} \quad \dots\dots\dots (B.83)$$

$$\lambda_g(S_w) = \frac{k k_{rg}(S_w)}{\mu_g} \dots\dots\dots (B.84)$$

$$\gamma_w = \rho_w \frac{g}{g_c} \dots\dots\dots (B.85)$$

$$\gamma_g = \rho_g \frac{g}{g_c} \dots\dots\dots (B.86)$$

B.5.1.1. Liquid Phase

By using the fully implicit CSFT (central in space and forward in time) scheme, the discretization for water phase becomes

$$\frac{\partial}{\partial t} (\phi S_w) = \nabla \cdot (\lambda_w \nabla \phi_w) = \nabla \cdot (\lambda_w (\nabla p_w - \gamma_w \nabla h)) \dots\dots\dots (B.87)$$

where the right-hand side is defined as

$$\nabla \cdot (\lambda_w (\nabla p_w - \gamma_w \nabla z)) = \frac{\partial}{\partial x} \left(\lambda_w \left(\frac{\partial p_w}{\partial x} - \gamma_w \frac{\partial h}{\partial x} \right) \right) + \frac{\partial}{\partial z} \left(\lambda_w \left(\frac{\partial p_w}{\partial z} - \gamma_w \frac{\partial h}{\partial z} \right) \right) \dots\dots\dots (B.88)$$

By using the point-distributed equal-distance grid system in x direction,

$$\frac{\partial}{\partial x} \left(\lambda_w \left(\frac{\partial p_w}{\partial x} \right) \right) = \frac{\lambda_{w,(i+\frac{1}{2},j)} \left(\frac{\partial p}{\partial x} \right)_{w,(i+\frac{1}{2},j)} - \lambda_{w,(i-\frac{1}{2},j)} \left(\frac{\partial p}{\partial x} \right)_{w,(i-\frac{1}{2},j)}}{\Delta x} \dots\dots\dots (B.89)$$

where

$$\left(\frac{\partial p}{\partial x} \right)_{w,(i+\frac{1}{2},j)} = \frac{p_{w,(i+1,j)} - p_{w,(i,j)}}{\Delta x} \dots\dots\dots (B.90)$$

$$\left(\frac{\partial p}{\partial x} \right)_{w,(i-\frac{1}{2},j)} = \frac{p_{w,(i,j)} - p_{w,(i-1,j)}}{\Delta x} \dots\dots\dots (B.91)$$

Note that $\frac{\partial h}{\partial x} = 0$ because there is no variation in depth along horizontal x-direction. Therefore,

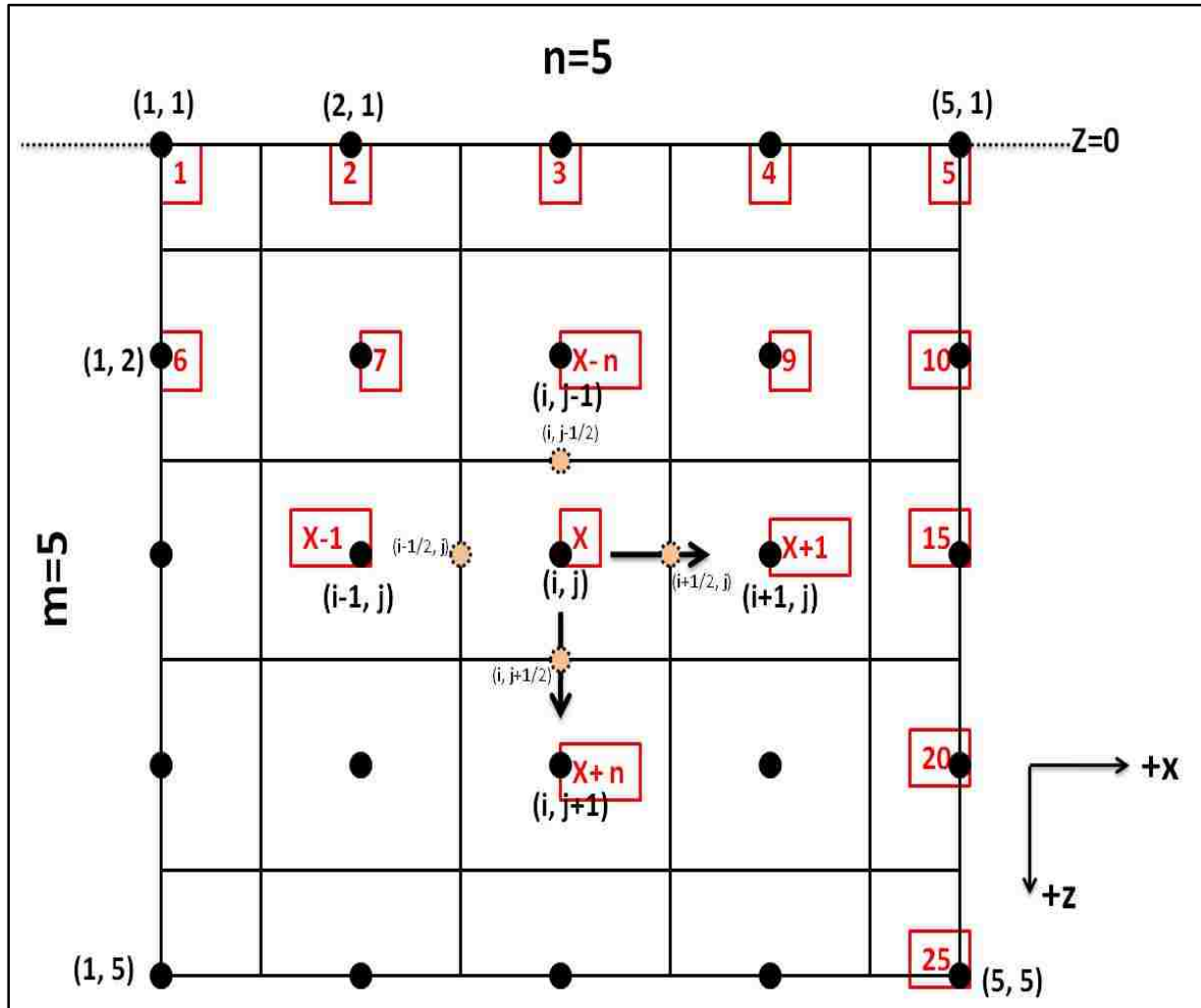


Figure B.5 Schematic figure representing 5x5 grid system in a two-dimensional system

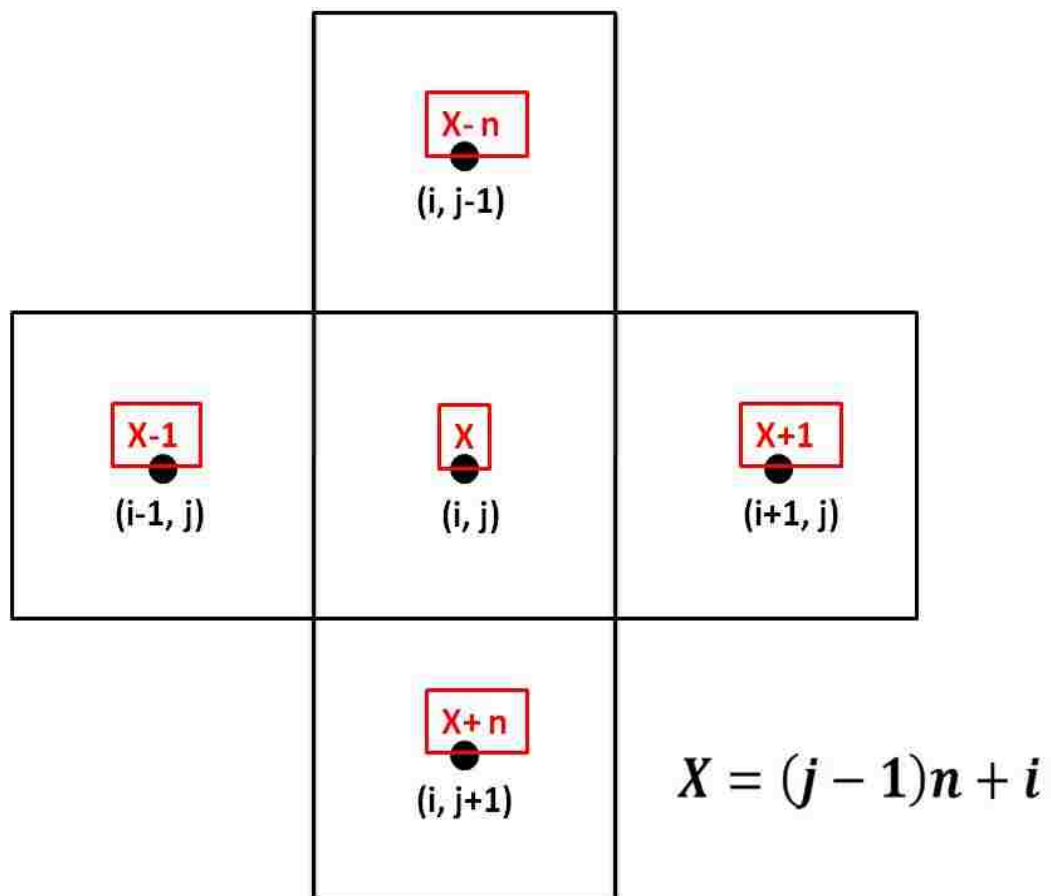


Figure B.6 A grid block of interest (X or (i,j)) with adjacent grid blocks

$$\begin{aligned}
& - \left[\left(\lambda_{w,(i,j+\frac{1}{2})} + \lambda_{w,(i,j-\frac{1}{2})} \right) (p_{w,(i,j)} - \gamma_w z_{w,(i,j)}) \right]^{t+1} \\
& + \left[\lambda_{w,(i,j-\frac{1}{2})} (p_{w,(i,j-1)} - \gamma_w z_{w,(i,j-1)}) \right]^{t+1} \\
& = \Phi (S_{w,(i,j)}^{t+1} - S_{w,(i,j)}^t) \dots\dots\dots (B.96)
\end{aligned}$$

If upstream weighting is applied in both x and z directions, those mobility terms can be written as

$$\lambda_{w,(i+\frac{1}{2},j)} = \lambda_{w,(i,j)} \dots\dots\dots (B.97)$$

$$\lambda_{w,(i-\frac{1}{2},j)} = \lambda_{w,(i-1,j)} \dots\dots\dots (B.98)$$

$$\lambda_{w,(i,j-1/2)} = \lambda_{w,(i,j-1)} \dots\dots\dots (B.99)$$

and

$$\lambda_{w,(i,j+1/2)} = \lambda_{w,(i,j)} \dots\dots\dots (B.100)$$

The final difference equation for water phase becomes

$$\begin{aligned}
& \lambda_{w,(i,j)}^{t+1} p_{w,(i+1,j)}^{t+1} + \lambda_{w,(i,j)}^{t+1} p_{w,(i,j+1)}^{t+1} \\
& - \left(\lambda_{w,(i,j)}^{t+1} + \lambda_{w,(i-1,j)}^{t+1} + \lambda_{w,(i,j)}^{t+1} + \lambda_{w,(i,j-1)}^{t+1} \right) p_{w,(i,j)}^{t+1} \\
& + \lambda_{w,(i-1,j)}^{t+1} p_{w,(i-1,j)}^{t+1} + \lambda_{w,(i,j-1)}^{t+1} p_{w,(i,j-1)}^{t+1} - \Phi S_{w,(i,j)}^{t+1} + G_w \\
& = -\Phi S_{w,(i,j)}^t \dots\dots\dots (B.101)
\end{aligned}$$

where the gravity term G_w is defined as

$$G_w = \lambda_{w,(i,j)}^{t+1} \gamma_w (z_{w,(i,j)}^{t+1} - z_{w,(i,j+1)}^{t+1}) + \lambda_{w,(i,j-1)}^{t+1} \gamma_w (z_{w,(i,j)}^{t+1} - z_{w,(i,j-1)}^{t+1})$$

..... (B.102)

Note that all terms in the left-hand side of Eq. B.101 are in new time step which should be calculated in new time step, and RHS terms are known for new time step because it is calculated in previous time step.

B.5.1.2. Gas Phase

The same approach can be applied to gas phase. First, gas-phase pressure is determined by capillary pressure and liquid pressure, i.e.,

$$p_g = p_w + p_c \quad , \quad \text{..... (B.103)}$$

where p_c is capillary pressure given by

$$P_{c,(i,j)} = \alpha e^{-\left(\frac{S_{w,(i,j)}}{\beta}\right)} \quad . \quad \text{..... (B.104)}$$

If upstream weighting is used for capillary pressure, then the expression in x-direction becomes

$$P_{c,(i+\frac{1}{2},j)} = \alpha e^{-\left(\frac{S_{w,(i,j)}}{\beta}\right)} \quad , \quad \text{..... (B.105)}$$

and the expression in z-direction becomes

$$P_{c,(i,j+\frac{1}{2})} = \alpha e^{-\left(\frac{S_{w,(i,j)}}{\beta}\right)} \quad . \quad \text{..... (B.106)}$$

In order to build the Jacobian matrix, the first and second derivatives of capillary pressure with respect to water saturation are required as shown below.

$$P'_{c,(i,j)} = -\left(\frac{\alpha}{\beta}\right) e^{-\left(\frac{S_{w,(i,j)}}{\beta}\right)}, \dots\dots\dots (B.107)$$

$$P''_{c,(i,j)} = \left(\frac{\alpha}{\beta^2}\right) e^{-\left(\frac{S_{w,(i,j)}}{\beta}\right)}, \dots\dots\dots (B.108)$$

The governing mass-balance equation for gas phase is as follows:

$$\frac{\partial}{\partial t}(\phi S_g) = \nabla \cdot (\lambda_g \nabla \phi) = \nabla \cdot (\lambda_g (\nabla p - \gamma_g \nabla h)) \dots\dots\dots (B.109)$$

By using the chain rule,

$$\frac{\partial P_c}{\partial x} = \frac{\partial P_c}{\partial S_w} \times \frac{\partial S_w}{\partial x} = P'_c \times \frac{\partial S_w}{\partial x} \dots\dots\dots (B.110)$$

The right-hand side of Eq. B.109 becomes

$$\nabla \cdot (\lambda_g (\nabla p_g - \gamma_g \nabla z)) = \frac{\partial}{\partial x} \left(\lambda_g \left(\frac{\partial p_g}{\partial x} - \gamma_g \frac{\partial h}{\partial x} \right) \right) + \frac{\partial}{\partial z} \left(\lambda_g \left(\frac{\partial p_g}{\partial z} - \gamma_g \frac{\partial h}{\partial z} \right) \right) \dots\dots\dots (B.111)$$

By using fully implicit CSFT (central in space and forward in time) and point-distributed equal-distance grid system, the term in x-direction in Eq. B.111 becomes

$$\frac{\partial}{\partial x} \left(\lambda_g \left(\frac{\partial p_g}{\partial x} \right) \right) = \frac{\lambda_{g,(i+\frac{1}{2},j)} \left(\frac{\partial p_g}{\partial x} \right)_{i+\frac{1}{2},j} - \lambda_{g,(i-\frac{1}{2},j)} \left(\frac{\partial p_g}{\partial x} \right)_{i-\frac{1}{2},j}}{\Delta x} \dots\dots\dots (B.112)$$

where

$$\left(\frac{\partial p_g}{\partial x} \right)_{g,(i+\frac{1}{2},j)} = \frac{p_{w,(i+1,j)} - p_{w,(i,j)}}{\Delta x} + P'_{c,(i+\frac{1}{2},j)} \frac{S_{w,(i+1,j)} - S_{w,(i,j)}}{\Delta x} \dots\dots\dots (B.113)$$

and

$$\left(\frac{\partial p_g}{\partial x}\right)_{g,(i-\frac{1}{2},j)} = \frac{p_{w,(i,j)} - p_{w,(i-1,j)}}{\Delta x} + P'_{c,(i-\frac{1}{2},j)} \frac{S_{w,(i,j)} - S_{w,(i-1,j)}}{\Delta x} \dots\dots\dots (B.114)$$

Because $\frac{\partial h}{\partial x} = 0$ due to no variation along x-direction, the first term in the right-hand side of Eq.

B. 111 writes

$$\begin{aligned} & \frac{\partial}{\partial x} \left(\lambda_g \left(\frac{\partial p_g}{\partial x} - \gamma_g \frac{\partial h}{\partial x} \right) \right) \\ &= \frac{\lambda_{g,(i+\frac{1}{2},j)} \left(\frac{p_{w,(i+1,j)} - p_{w,(i,j)} + P'_{c,(i+\frac{1}{2},j)} \frac{S_{w,(i+1,j)} - S_{w,(i,j)}}{\Delta x}}{\Delta x} \right)}{\Delta x} \\ & - \frac{\lambda_{g,(i-\frac{1}{2},j)} \left(\frac{p_{w,(i,j)} - p_{w,(i-1,j)} + P'_{c,(i-\frac{1}{2},j)} \frac{S_{w,(i,j)} - S_{w,(i-1,j)}}{\Delta x}}{\Delta x} \right)}{\Delta x}, \dots\dots\dots (B.115) \end{aligned}$$

which further becomes

$$\begin{aligned} & \frac{\partial}{\partial x} \left(\lambda_g \left(\frac{\partial p_g}{\partial x} - \gamma_g \frac{\partial h}{\partial x} \right) \right) \\ &= \frac{1}{\Delta x^2} \left[\lambda_{g,(i+\frac{1}{2},j)} p_{w,(i+1,j)} - \left(\lambda_{g,(i+\frac{1}{2},j)} + \lambda_{g,(i-\frac{1}{2},j)} \right) p_{w,(i,j)} + \lambda_{g,(i-\frac{1}{2},j)} p_{w,(i-1,j)} \right] \\ & + \frac{1}{\Delta x^2} \left[\lambda_{g,(i+\frac{1}{2},j)} P'_{c,(i+\frac{1}{2},j)} S_{w,(i+1,j)} - \left(\lambda_{g,(i+\frac{1}{2},j)} P'_{c,(i+\frac{1}{2},j)} + \lambda_{g,(i-\frac{1}{2},j)} P'_{c,(i-\frac{1}{2},j)} \right) S_{w,(i,j)} + \right. \\ & \left. \lambda_{g,(i-\frac{1}{2},j)} P'_{c,(i-\frac{1}{2},j)} S_{w,(i-1,j)} \right] \dots\dots\dots (B.116) \end{aligned}$$

Similarly, the term in z-direction with gravity in Eq. B. 111 becomes

$$\frac{\partial}{\partial z} \left(\lambda_g \left(\frac{\partial p_g}{\partial z} - \gamma_g \frac{\partial h}{\partial z} \right) \right) =$$

$$\begin{aligned}
& \frac{1}{\Delta z^2} \left[\lambda_{g,(i,j+\frac{1}{2})} (p_{w,(i,j+1)} - \gamma_g Z_{g,(i,j+1)}) - \left(\lambda_{g,(i,j+\frac{1}{2})} + \lambda_{g,(i,j-\frac{1}{2})} \right) (p_{w,(i,j)} - \gamma_g Z_{g,(i,j)}) + \right. \\
& \left. \lambda_{g,(i,j-\frac{1}{2})} (p_{w,(i,j-1)} - \gamma_g Z_{g,(i,j-1)}) \right] \\
& + \frac{1}{\Delta z^2} \left[\lambda_{g,(i,j+\frac{1}{2})} P'_{c,(i,j+\frac{1}{2})} S_{w,(i,j+1)} - \left(\lambda_{g,(i,j+\frac{1}{2})} P'_{c,(i,j+\frac{1}{2})} + \lambda_{g,(i,j-\frac{1}{2})} P'_{c,(i,j-\frac{1}{2})} \right) S_{w,(i,j)} + \right. \\
& \left. \lambda_{g,(i,j-\frac{1}{2})} P'_{c,(i,j-\frac{1}{2})} S_{w,(i,j-1)} \right] \dots\dots\dots (B.117)
\end{aligned}$$

The left-hand side of Eq. B.111 can be written as follows:

$$S_g = 1 - S_w \dots\dots\dots (B.118)$$

$$\frac{\partial}{\partial t} (\phi S_g) = \frac{\phi}{\Delta t} (S_{g,(i,j)}^{t+1} - S_{g,(i,j)}^t) = \frac{\phi}{\Delta t} (S_{w,(i,j)}^t - S_{w,(i,j)}^{t+1}) \dots\dots\dots (B.119)$$

Assuming that $\Delta x = x_i - x_{i-1} = x_{i+1} - x_i = \Delta z = z_i - z_{i-1} = z_{i+1} - z_i$ and defining a new term Φ as

$$\frac{\phi \Delta x^2}{\Delta t} = \Phi, \dots\dots\dots (B.118)$$

the finite difference equation for gas phase becomes as follows by putting Eqs. B.116, B.117, and B.119 together:

$$\begin{aligned}
& \left(\lambda_{g,(i+\frac{1}{2},j)}^{t+1} \right) p_{w,(i+1,j)}^{t+1} + \left(\lambda_{g,(i,j+\frac{1}{2})}^{t+1} \right) p_{w,(i,j+1)}^{t+1} \\
& - \left(\lambda_{g,(i+\frac{1}{2},j)}^{t+1} + \lambda_{g,(i-\frac{1}{2},j)}^{t+1} + \lambda_{g,(i,j+\frac{1}{2})}^{t+1} + \lambda_{g,(i,j-\frac{1}{2})}^{t+1} \right) p_{w,(i,j)}^{t+1} + \left(\lambda_{g,(i-\frac{1}{2},j)}^{t+1} \right) p_{w,(i-1,j)}^{t+1} \\
& + \left(\lambda_{g,(i,j-\frac{1}{2})}^{t+1} \right) p_{w,(i,j-1)}^{t+1} + \left(\lambda_{g,(i+\frac{1}{2},j)}^{t+1} P'_{c,(i+\frac{1}{2},j)} \right) S_{w,(i+1,j)}^{t+1}
\end{aligned}$$

$$\begin{aligned}
& + \left(\lambda_{g,(i,j+\frac{1}{2})}^{t+1} P'_{c,(i,j+\frac{1}{2})} \right) S_{w,(i,j+1)}^{t+1} \\
& - \left(\lambda_{g,(i+\frac{1}{2},j)}^{t+1} P'_{c,(i+\frac{1}{2},j)} + \lambda_{g,(i-\frac{1}{2},j)}^{t+1} P'_{c,(i-\frac{1}{2},j)} + \lambda_{g,(i,j+\frac{1}{2})}^{t+1} P'_{c,(i,j+\frac{1}{2})} + \lambda_{g,(i,j-\frac{1}{2})}^{t+1} P'_{c,(i,j-\frac{1}{2})} - \right. \\
& \left. \Phi \right) S_{w,(i,j)}^{t+1} \\
& + \left(\lambda_{g,(i-\frac{1}{2},j)}^{t+1} P'_{c,(i-\frac{1}{2},j)} \right) S_{w,(i-1,j)}^{t+1} + \left(\lambda_{g,(i,j-\frac{1}{2})}^{t+1} P'_{c,(i,j-\frac{1}{2})} \right) S_{w,(i,j-1)}^{t+1} + G_g \\
& = \Phi S_{w,(i,j)}^t \dots \dots \dots (B. 121)
\end{aligned}$$

Upstream weighting makes the mobility terms as shown below:

$$\lambda_{g,(i+\frac{1}{2},j)} = \lambda_{g,(i,j)} \dots \dots \dots (B.122)$$

$$\lambda_{g,(i-\frac{1}{2},j)} = \lambda_{g,(i-1,j)} \dots \dots \dots (B.123)$$

$$\lambda_{g,(i,j-1/2)} = \lambda_{g,(i,j-1)} \dots \dots \dots (B.124)$$

and

$$\lambda_{g,(i,j+1/2)} = \lambda_{g,(i,j)} \dots \dots \dots (B.125)$$

And the gravity term G_g is defined as

$$G_g = \lambda_{g,(i,j)}^{t+1} \gamma_g (z_{g,(i,j)}^{t+1} - z_{g,(i,j+1)}^{t+1}) + \lambda_{g,(i,j-1)}^{t+1} \gamma_g (z_{g,(i,j)}^{t+1} - z_{g,(i,j-1)}^{t+1}) \dots (B.126)$$

Note that all terms in the left-hand side of Eq. B.121 are evaluated at the new time step, while all terms in the right-hand side are evaluated at the previous time step. Finally, the difference equation for gas becomes

$$\begin{aligned}
& (\lambda_{g,(i,j)}^{t+1})p_{w,(i+1,j)}^{t+1} + (\lambda_{g,(i,j)}^{t+1})p_{w,(i,j+1)}^{t+1} - (\lambda_{g,(i,j)}^{t+1} + \lambda_{g,(i-1,j)}^{t+1} + \lambda_{g,(i,j)}^{t+1} + \lambda_{g,(i,j-1)}^{t+1})p_{w,(i,j)}^{t+1} \\
& + (\lambda_{g,(i-1,j)}^{t+1})p_{w,(i-1,j)}^{t+1} + (\lambda_{g,(i,j-1)}^{t+1})p_{w,(i,j-1)}^{t+1} + (\lambda_{g,(i,j)}^{t+1}P'_{c,(i,j)})S_{w,(i+1,j)}^{t+1} + \\
& (\lambda_{g,(i,j)}^{t+1}P'_{c,(i,j)})S_{w,(i,j+1)}^{t+1} \\
& - (\lambda_{g,(i,j)}^{t+1}P'_{c,(i,j)} + \lambda_{g,(i-1,j)}^{t+1}P'_{c,(i-1,j)} + \lambda_{g,(i,j)}^{t+1}P'_{c,(i,j)} + \lambda_{g,(i,j-1)}^{t+1}P'_{c,(i,j-1)} - \Phi)S_{w,(i,j)}^{t+1} \\
& + (\lambda_{g,(i-1,j)}^{t+1}P'_{c,(i-1,j)})S_{w,(i-1,j)}^{t+1} + (\lambda_{g,(i,j-1)}^{t+1}P'_{c,(i,j-1)})S_{w,(i,j-1)}^{t+1} + G_g \\
& = \Phi S_{w,(i,j)}^t \cdot \dots\dots\dots (B. 127)
\end{aligned}$$

B.5.2. Construction of Jacobian Matrix

The Jacobian matrix can be formulated by using the finite difference equations derived in earlier sections.

B.5.2.1. Water Phase

For water phase,

$$\begin{aligned}
F_{2i-1} &= \lambda_{w,(i,j)}^{t+1}p_{w,(i+1,j)}^{t+1} + \lambda_{w,(i,j)}^{t+1}p_{w,(i,j+1)}^{t+1} - \\
& (\lambda_{w,(i-1,j)}^{t+1} + 2\lambda_{w,(i,j)}^{t+1} + \lambda_{w,(i,j-1)}^{t+1})p_{w,(i,j)}^{t+1} + \lambda_{w,(i-1,j)}^{t+1}p_{w,(i-1,j)}^{t+1} + \lambda_{w,(i,j-1)}^{t+1}p_{w,(i,j-1)}^{t+1} - \\
& \Phi S_{w,(i,j)}^{t+1} + G_w + \Phi S_{w,(i,j)}^t \dots\dots\dots (B. 128)
\end{aligned}$$

with

$$G_w = \lambda_{w,(i,j)}^{t+1}\gamma_w(z_{w,(i,j)}^{t+1} - z_{w,(i,j+1)}^{t+1}) + \lambda_{w,(i,j-1)}^{t+1}\gamma_w(z_{w,(i,j)}^{t+1} - z_{w,(i,j-1)}^{t+1}) \ , \dots\dots\dots (B.129)$$

$$\frac{\emptyset\Delta x^2}{\Delta t} = \Phi \ , \dots\dots\dots (B. 130)$$

$$\lambda_w(S_w) = \frac{kk_{rw}(S_w)}{\mu_w}, \dots\dots\dots (B. 131)$$

$$\lambda'_w(S_w) = \frac{kk'_{rw}(S_w)}{\mu_w}, \dots\dots\dots (B. 132)$$

$$\gamma_w = \rho_w \frac{g}{g_c}, \dots\dots\dots (B. 133)$$

$$k_{rw,(i,j)} = 0.7888 \left(\frac{S_{w,(i,j)} - S_{wc}}{1 - S_{wc} - S_{gr}} \right)^{1.9575}, \dots\dots\dots (B. 134)$$

and

$$k'_{rw,(i,j)} = \frac{1.5441}{(1 - S_{wc} - S_{gr})^{1.9575}} (S_{w,(i,j)} - S_{wc})^{0.9575} \dots\dots\dots (B. 135)$$

The solution scheme requires the derivatives of Eq. B.128 with respect to the pressures and saturations at different grid blocks. In the equations shown below, all those terms with “ / ” are evaluated at the new (t+1) time step. The formulation of the Jacobian matrix and the solution methodology is represented by Figs. B.7 and B.8 schematically. The specific derivative terms are expressed as follows:

With respect to upstream pressure in x direction (c(X, 1) in Fig. B.7),

$$\frac{\partial F_{2i-1}}{\partial p_{w,(i-1,j)}} = \lambda_{w,(i-1,j)}^{t+1} \dots\dots\dots (B. 136)$$

With respect to upstream saturation in x direction (c(X, 2) in Fig. B.7),

$$\frac{\partial F_{2i-1}}{\partial S_{w,(i-1,j)}} = \lambda'_{w,(i-1,j)} (p_{w,(i-1,j)}^{t+1} - p_{w,(i,j)}^{t+1}) \dots\dots\dots (B. 137)$$

With respect to upstream pressure in z direction (e(X, 1) in Fig. B.7),

$$\frac{\partial F_{2i-1}}{\partial p_{w(i,j-1)}} = \lambda_{w,(i,j-1)}^{t+1} \dots\dots\dots (B. 138)$$

With respect to upstream saturation in z direction (e(X, 2) in Fig. B.7),

$$\frac{\partial F_{2i-1}}{\partial S_{w(i,j-1)}} = \lambda'_{w,(i,j-1)} \left(p_{w,(i,j-1)}^{t+1} - p_{w,(i,j)}^{t+1} + \gamma_w (z_{w,(i,j)}^{t+1} - z_{w,(i,j-1)}^{t+1}) \right) \dots\dots\dots (B. 139)$$

With respect to pressure at the grid of interest (a(X, 1) in Fig. B.7),

$$\frac{\partial F_{2i-1}}{\partial p_{w(i,j)}} = -\left(\lambda_{w,(i-1,j)}^{t+1} + 2\lambda_{w,(i,j)}^{t+1} + \lambda_{w,(i,j-1)}^{t+1} \right) \dots\dots\dots (B. 140)$$

With respect to saturation at the grid of interest (a(X, 2) in Fig. B.7),

$$\frac{\partial F_{2i-1}}{\partial S_{w(i,j)}} = \lambda'_{w,(i,j)} \left(p_{w,(i+1,j)}^{t+1} + p_{w,(i,j+1)}^{t+1} - 2p_{w,(i,j)}^{t+1} + \gamma_w (z_{w,(i,j)}^{t+1} - z_{w,(i,j+1)}^{t+1}) \right) - \Phi \dots\dots\dots (B. 141)$$

With respect to downstream pressure in x direction (b(X, 1) in Fig. B.7),

$$\frac{\partial F_{2i-1}}{\partial p_{w(i+1,j)}} = \lambda_{w,(i,j)}^{t+1} \dots\dots\dots (B. 142)$$

With respect to downstream saturation in x direction (b(X, 2) in Fig. B.7),

$$\frac{\partial F_{2i-1}}{\partial S_{w(i+1,j)}} = 0 \dots\dots\dots (B. 143)$$

With respect to downstream pressure in z direction (d(X, 1) in Fig. B.7),

$$\frac{\partial F_{2i-1}}{\partial p_{w(i,j+1)}} = \lambda_{w,(i,j)}^{t+1} \dots\dots\dots (B. 144)$$

and, with respect to downstream saturation in z direction (d(X, 2) in Fig. B.7),

$$\frac{\partial F_{2i-1}}{\partial S_{w(i,j+1)}} = 0 \quad \dots\dots\dots (B. 145)$$

Note that $P_{2x-1} = p_{w,x} = p_{w, (i,j)}$, and $P_{2x} = S_{w,x} = S_{w, (i,j)}$ as shown in Fig. B.8.

B.5.2.2. Gas Phase

For gas phase,

$$\begin{aligned} F_{2i} = & (\lambda_{g,(i,j)}^{t+1})p_{w,(i+1,j)}^{t+1} + (\lambda_{g,(i,j)}^{t+1})p_{w,(i,j+1)}^{t+1} - (\lambda_{g,(i-1,j)}^{t+1} + 2\lambda_{g,(i,j)}^{t+1} + \lambda_{g,(i,j-1)}^{t+1}) p_{w,(i,j)}^{t+1} \\ & + (\lambda_{g,(i-1,j)}^{t+1})p_{w,(i-1,j)}^{t+1} + (\lambda_{g,(i,j-1)}^{t+1})p_{w,(i,j-1)}^{t+1} + (\lambda_{g,(i,j)}^{t+1}P'_{c,(i,j)}) S_{w,(i+1,j)}^{t+1} \\ & + (\lambda_{g,(i,j)}^{t+1}P'_{c,(i,j)}) S_{w,(i,j+1)}^{t+1} \\ & - (\lambda_{g,(i-1,j)}^{t+1}P'_{c,(i-1,j)} + 2\lambda_{g,(i,j)}^{t+1}P'_{c,(i,j)} + \lambda_{g,(i,j-1)}^{t+1}P'_{c,(i,j-1)} - \Phi) S_{w,(i,j)}^{t+1} \\ & + (\lambda_{g,(i-1,j)}^{t+1}P'_{c,(i-1,j)}) S_{w,(i-1,j)}^{t+1} + (\lambda_{g,(i,j-1)}^{t+1}P'_{c,(i,j-1)}) S_{w,(i,j-1)}^{t+1} + G_g \\ & - \Phi S_{w,(i,j)}^t \end{aligned} \quad \dots\dots\dots (B. 146)$$

with

$$G_g = \lambda_{g,(i,j)}^{t+1}\gamma_g(z_{g,(i,j)}^{t+1} - z_{g,(i,j+1)}^{t+1}) + \lambda_{g,(i,j-1)}^{t+1}\gamma_g(z_{g,(i,j)}^{t+1} - z_{g,(i,j-1)}^{t+1}) \quad \dots\dots (B. 147)$$

$$\frac{\emptyset\Delta x^2}{\Delta t} = \Phi \quad \dots\dots\dots (B. 148)$$

$$\lambda_g(S_w) = \frac{kk_{rg}(S_w)}{\mu_g} \quad \dots\dots\dots (B. 149)$$

$$\lambda'_g(S_w) = \frac{kk'_{rg}(S_w)}{\mu_g} \quad \dots\dots\dots (B. 150)$$

$$\gamma_g = \rho_g \frac{g}{g_c} \quad \dots\dots\dots (B. 151)$$

For example,

$$a(X, 1) = \frac{\partial F_{2X-1}}{\partial p_{w,X}} = \frac{\partial F_{2X-1}}{\partial P_{2X-1}} ; a(X, 2) = \frac{\partial F_{2X-1}}{\partial S_{w,X}} = \frac{\partial F_{2X-1}}{\partial P_{2X}} ; a(X, 3) = \frac{\partial F_{2X}}{\partial p_{w,X}} = \frac{\partial F_{2X}}{\partial P_{2X-1}} ;$$

$$a(X, 4) = \frac{\partial F_{2X}}{\partial S_{w,X}} = \frac{\partial F_{2X}}{\partial P_{2X}} ; b(X, 1) = \frac{\partial F_{2X-1}}{\partial p_{w,X+1}} = \frac{\partial F_{2X-1}}{\partial P_{2X+1}} ; b(X, 2) = \frac{\partial F_{2X-1}}{\partial S_{w,X+1}} = \frac{\partial F_{2X-1}}{\partial P_{2X+2}}$$

$$b(X, 3) = \frac{\partial F_{2X}}{\partial p_{w,X+1}} = \frac{\partial F_{2X}}{\partial P_{2X+1}} ; b(X, 4) = \frac{\partial F_{2X}}{\partial S_{w,X+1}} = \frac{\partial F_{2X}}{\partial P_{2X+2}} ; c(X, 1) = \frac{\partial F_{2X-1}}{\partial p_{w,X-1}} = \frac{\partial F_{2X-1}}{\partial P_{2X-3}}$$

$$c(X, 2) = \frac{\partial F_{2X-1}}{\partial S_{w,X-1}} = \frac{\partial F_{2X-1}}{\partial P_{2X-2}} ; c(X, 3) = \frac{\partial F_{2X}}{\partial p_{w,X-1}} = \frac{\partial F_{2X}}{\partial P_{2X-3}} ; c(X, 4) = \frac{\partial F_{2X}}{\partial S_{w,X-1}} = \frac{\partial F_{2X}}{\partial P_{2X-2}}$$

$$d(X, 1) = \frac{\partial F_{2X-1}}{\partial p_{w,X+n}} = \frac{\partial F_{2X-1}}{\partial P_{2(X+n)-1}} ; d(X, 2) = \frac{\partial F_{2X-1}}{\partial S_{w,X+n}} = \frac{\partial F_{2X-1}}{\partial P_{2(X+n)}} ; d(X, 3) = \frac{\partial F_{2X}}{\partial p_{w,X+n}} = \frac{\partial F_{2X}}{\partial P_{2(X+n)-1}}$$

$$d(X, 4) = \frac{\partial F_{2X}}{\partial S_{w,X+n}} = \frac{\partial F_{2X}}{\partial P_{2(X+n)}} ; e(X, 1) = \frac{\partial F_{2X-1}}{\partial p_{w,X-n}} = \frac{\partial F_{2X-1}}{\partial P_{2(X-n)-1}} ; e(X, 2) = \frac{\partial F_{2X-1}}{\partial S_{w,X-n}} = \frac{\partial F_{2X-1}}{\partial P_{2(X-n)}}$$

$$e(X, 3) = \frac{\partial F_{2X}}{\partial p_{w,X-n}} = \frac{\partial F_{2X}}{\partial P_{2(X-n)-1}} ; e(X, 4) = \frac{\partial F_{2X}}{\partial S_{w,X-n}} = \frac{\partial F_{2X}}{\partial P_{2(X-n)}}$$

		$\frac{\partial}{\partial p_w}$	$\frac{\partial}{\partial S_w}$			$\frac{\partial}{\partial p_w}$	$\frac{\partial}{\partial S_w}$							
F_{2X-1}		e(X,1)	e(X,2)		c(X,1)	c(X,2)	a(X,1)	a(X,2)	b(X,1)	b(X,2)	d(X,1)	d(X,2)
F_{2X}		e(X,3)	e(X,4)		c(X,3)	c(X,4)	a(X,3)	a(X,4)	b(X,3)	b(X,4)	d(X,3)	d(X,4)

Figure B.7 A formulation of the Jacobian matrix at grid (i,j) or X. (the first row is the derivative terms related to water phase, and second row is for gas phase.)

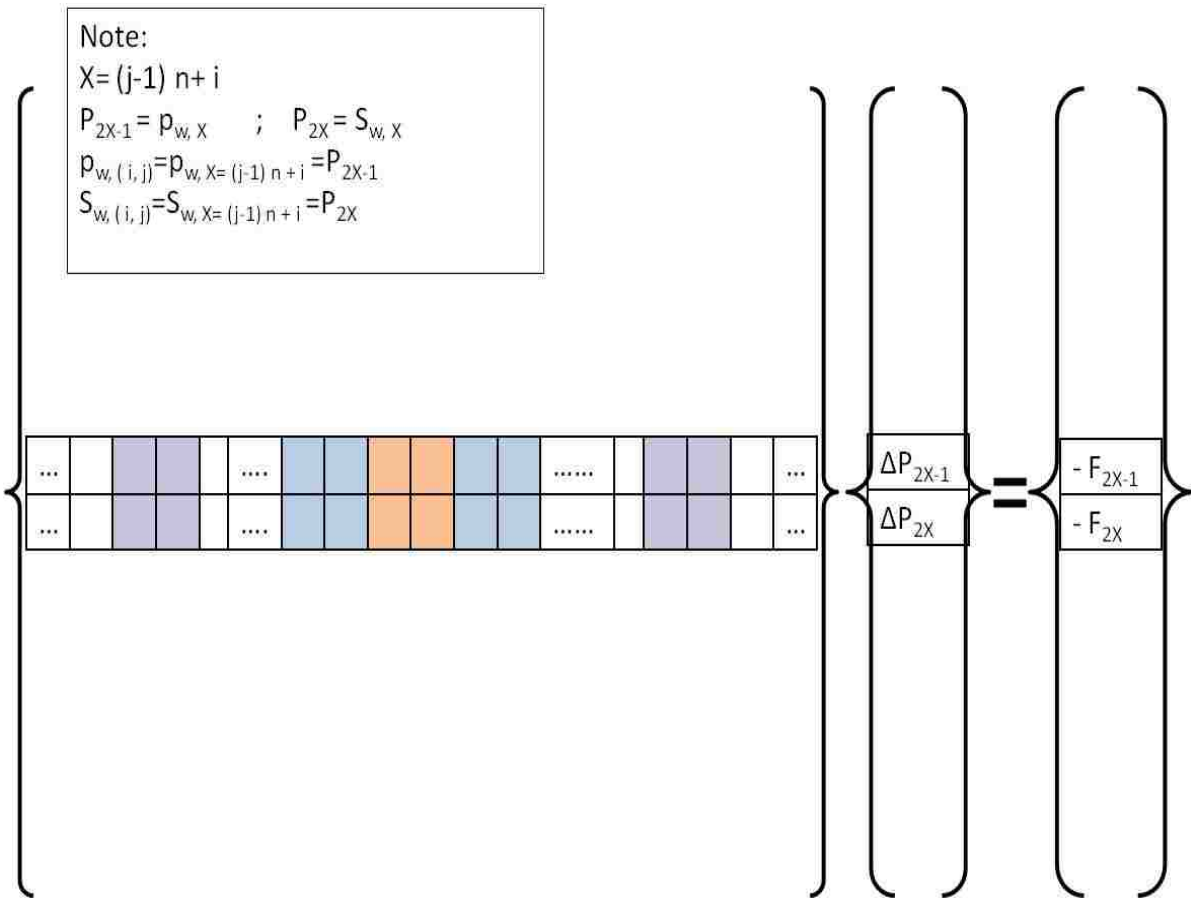


Figure B.8 Representation of solution scheme using the Jacobian matrix. ΔP terms represent the pressure difference (ΔP_{2X-1}) in consecutive iteration (and saturation difference (ΔP_{2X}) in consecutive iteration).

$$k_{rgi} = \left(\frac{1 - S_{wi} - S_{gr}}{1 - S_{wc} - S_{gr}} \right)^{2.2868} \dots \dots \dots (B. 152)$$

and

$$k'_{rgi} = \frac{-2.2868}{(1 - S_{wc} - S_{gr})^{2.2868}} (1 - S_{wi} - S_{gr})^{1.2868} \dots \dots \dots (B. 153)$$

The capillary pressure is defined as

$$P_{c,(i, j)} = \alpha e^{-\left(\frac{S_{w,(i, j)}}{\beta}\right)} \dots \dots \dots (B. 154)$$

And the derivatives of capillary pressure using upstream weighting are

$$P'_{c,(i, j)} = \frac{\partial P_c}{\partial S_w} = - \left(\frac{\alpha}{\beta} \right) e^{-\left(\frac{S_{w,(i, j)}}{\beta}\right)} \dots \dots \dots (B. 155)$$

and

$$P''_{c,(i, j)} = \left(\frac{\alpha}{\beta^2} \right) e^{-\left(\frac{S_{w,(i, j)}}{\beta}\right)} \dots \dots \dots (B. 156)$$

By following similar procedure in the previous section, the derivative terms are given as follows:

With respect to upstream pressure in x direction (c(X, 3) in Fig. B.7),

$$\frac{\partial F_{2i}}{\partial p_{w(i-1, j)}} = \lambda_{g,(i-1, j)}^{t+1} \dots \dots \dots (B. 157)$$

With respect to upstream saturation in x direction (c(X, 4) in Fig. B.7),

$$\begin{aligned} \frac{\partial F_{2i}}{\partial S_{w(i-1, j)}} = & \lambda'_{g,(i-1, j)} \left(p_{w,(i-1, j)}^{t+1} - p_{w,(i, j)}^{t+1} - P'_{c,(i-1, j)} S_{w,(i, j)}^{t+1} + P'_{c,(i-1, j)} S_{w,(i-1, j)}^{t+1} \right) + \\ & \lambda_{g,(i-1, j)}^{t+1} P''_{c,(i-1, j)} \left(S_{w,(i-1, j)}^{t+1} - S_{w,(i, j)}^{t+1} \right) + \lambda_{g,(i-1, j)}^{t+1} P'_{c,(i-1, j)} \dots \dots \dots (B. 158) \end{aligned}$$

With respect to upstream pressure in z direction (e(X, 3) in Fig. B.7),

$$\frac{\partial F_{2i}}{\partial p_{w(i,j-1)}} = \lambda_{g,(i,j-1)}^{t+1} \dots\dots\dots (B. 159)$$

With respect to upstream saturation in z direction (e(X, 4) in Fig. B.7),

$$\begin{aligned} \frac{\partial F_{2i}}{\partial S_{w(i,j-1)}} = & \lambda'_{g,(i,j-1)} \left(p_{w,(i,j-1)}^{t+1} - p_{w,(i,j)}^{t+1} - P'_{c,(i,j-1)} S_{w,(i,j)}^{t+1} + P'_{c,(i,j-1)} S_{w,(i,j-1)}^{t+1} + \right. \\ & \left. \gamma_g(z_{g,(i,j)}^{t+1} - z_{g,(i,j-1)}^{t+1}) \right) + \lambda_{g,(i,j-1)}^{t+1} P'_{c,(i,j-1)} (S_{w,(i,j-1)}^{t+1} - S_{w,(i,j)}^{t+1}) + \lambda_{g,(i,j-1)}^{t+1} P'_{c,(i,j-1)} \\ & \dots\dots\dots (B. 160) \end{aligned}$$

With respect to pressure at the grid of interest (a(X, 3) in Fig. B.7),

$$\frac{\partial F_{2i}}{\partial p_{w(i,j)}} = -(\lambda_{g,(i-1,j)}^{t+1} + 2\lambda_{g,(i,j)}^{t+1} + \lambda_{g,(i,j-1)}^{t+1}) \dots\dots\dots (B. 161)$$

With respect to saturation at the grid of interest (a(X, 4) in Fig. B.7),

$$\begin{aligned} \frac{\partial F_{2i}}{\partial S_{w(i,j)}} = & \lambda'_{g,(i,j)} \left(p_{w,(i+1,j)}^{t+1} + p_{w,(i,j+1)}^{t+1} - 2p_{w,(i,j)}^{t+1} + P'_{c,(i,j)} S_{w,(i+1,j)}^{t+1} + P'_{c,(i,j)} S_{w,(i,j+1)}^{t+1} - \right. \\ & \left. 2P'_{c,(i,j)} S_{w,(i,j)}^{t+1} + \gamma_g(z_{g,(i,j)}^{t+1} - z_{g,(i,j+1)}^{t+1}) \right) + \lambda_{g,(i,j)}^{t+1} P'_{c,(i,j)} (S_{w,(i+1,j)}^{t+1} + S_{w,(i,j+1)}^{t+1} - \\ & \left. 2S_{w,(i,j)}^{t+1}) - 2P'_{c,(i,j)} \lambda_{g,(i,j)}^{t+1} - \left[\lambda_{g,(i-1,j)}^{t+1} P'_{c,(i-1,j)} + \lambda_{g,(i,j-1)}^{t+1} P'_{c,(i,j-1)} - \Phi \right] \\ & \dots\dots\dots (B. 162) \end{aligned}$$

With respect to downstream pressure in x direction (b(X, 3) in Fig. B.7),

$$\frac{\partial F_{2i}}{\partial p_{w(i+1,j)}} = \lambda_{g,(i,j)}^{t+1} \dots\dots\dots (B. 163)$$

With respect to downstream saturation in x direction (b(X, 4) in Fig. B.7),

$$\frac{\partial F_{2i}}{\partial S_{w(i+1,j)}} = \lambda_{g,(i,j)}^{t+1} P'_{c,(i,j)} \dots\dots\dots (B. 164)$$

With respect to downstream pressure in z direction (d(X, 3) in Fig. B.7),

$$\frac{\partial F_{2i}}{\partial p_{w(i,j+1)}} = \lambda_{g,(i,j)}^{t+1} \dots\dots\dots (B. 165)$$

And, with respect to downstream saturation in z direction (d(X, 4) in Fig. B.7),

$$\frac{\partial F_{2i}}{\partial S_{w(i,j+1)}} = \lambda_{g,(i,j)}^{t+1} P'_{c,(i,j)} \dots\dots\dots (B. 166)$$

B.5.3. Boundary Conditions

There are four different types of boundary conditions to be specified – inlet (injection condition), outlet (production condition), and top and bottom of the reservoir (no flow).

B.5.3.1. Outlet Boundary Condition- Fixed pressure

Outlet boundary condition is given by a pre-specified value of production well pressure. This condition can be incorporated into the simulation by applying the well model concept such a way the production well is placed at the outlet with fixed pressure (p_{well}). To incorporate the well model the equations and Jacobian matrix will be modified as follows for outlet grids.

For water phase,

$$\begin{aligned} F_{2i-1} = & \lambda_{w,(i,j)}^{t+1} p_{w,(i+1,j)}^{t+1} + \lambda_{w,(i,j)}^{t+1} p_{w,(i,j+1)}^{t+1} - \\ & (\lambda_{w,(i-1,j)}^{t+1} + 2\lambda_{w,(i,j)}^{t+1} + \lambda_{w,(i,j-1)}^{t+1}) p_{w,(i,j)}^{t+1} + \lambda_{w,(i-1,j)}^{t+1} p_{w,(i-1,j)}^{t+1} + \lambda_{w,(i,j-1)}^{t+1} p_{w,(i,j-1)}^{t+1} - \\ & \Phi S_{w,(i,j)}^{t+1} + G_w + \Phi S_{w,(i,j)}^t \dots\dots\dots (B. 167) \end{aligned}$$

and in Jacobian matrix, with respect to pressure at the grid of interest (a(X, 1) in Fig. B.7),

$$\frac{\partial F_{2i-1}}{\partial p_{w(i,j)}} = -(\lambda_{w,(i-1,j)}^{t+1} + 2\lambda_{w,(i,j)}^{t+1} + \lambda_{w,(i,j-1)}^{t+1}) \dots\dots\dots (B. 168)$$

With respect to saturation at the grid of interest (a(X, 2) in Fig. B.7),

$$\frac{\partial F_{2i-1}}{\partial S_{w(i,j)}} = \lambda'_{w(i,j)} \left(p_{w(i+1,j)}^{t+1} + p_{w(i,j+1)}^{t+1} - 2p_{w(i,j)}^{t+1} + \gamma_w (z_{w(i,j)}^{t+1} - z_{w(i,j+1)}^{t+1}) \right) - \Phi$$

..... (B. 169)

With respect to downstream pressure in x direction (b(X, 1) in Fig. B.7),

$$\frac{\partial F_{2i-1}}{\partial p_{w(i+1,j)}} = \lambda_{w(i,j)}^{t+1} \cdot \dots\dots\dots (B. 170)$$

Eq. B. 167 further becomes

$$F_{2i-1} =$$

$$\lambda_{w(i,j)}^{t+1} p_{w(i,j+1)}^{t+1} - (\lambda_{w(i-1,j)}^{t+1} + \lambda_{w(i,j)}^{t+1} + \lambda_{w(i,j-1)}^{t+1}) p_{w(i,j)}^{t+1} + \lambda_{w(i-1,j)}^{t+1} p_{w(i-1,j)}^{t+1} +$$

$$\lambda_{w(i,j-1)}^{t+1} p_{w(i,j-1)}^{t+1} - \Phi S_{w(i,j)}^{t+1} + G_w + \Phi S_{w(i,j)}^t - J_{well} \frac{k_{rw(i,j)}^{t+1}}{\mu_w} (p_{w(i,j)}^{t+1} - p_{well}) \quad (B. 171)$$

and in Jacobian matrix, with respect to pressure at the grid of interest (a(X, 1) in Fig. B.7),

$$\frac{\partial F_{2i-1}}{\partial p_{w(i,j)}} = -(\lambda_{w(i-1,j)}^{t+1} + \lambda_{w(i,j)}^{t+1} + \lambda_{w(i,j-1)}^{t+1}) - J_{well} \frac{k_{rw(i,j)}^{t+1}}{\mu_w} \dots\dots\dots (B. 172)$$

With respect to saturation at the grid of interest (a(X, 2) in Fig. B.7),

$$\frac{\partial F_{2i-1}}{\partial S_{w(i,j)}} = \lambda'_{w(i,j)} \left(p_{w(i,j+1)}^{t+1} - p_{w(i,j)}^{t+1} + \gamma_w (z_{w(i,j)}^{t+1} - z_{w(i,j+1)}^{t+1}) \right) - \Phi$$

..... (B. 173)

With respect to downstream pressure in x direction (b(X, 1) in Fig. B.7),

$$\frac{\partial F_{2i-1}}{\partial p_{w(i+1,j)}} = 0 \quad \dots\dots\dots (B. 174)$$

For gas phase,

$$\begin{aligned} F_{2i} = & (\lambda_{g,(i,j)}^{t+1}) p_{w,(i+1,j)}^{t+1} + (\lambda_{g,(i,j)}^{t+1}) p_{w,(i,j+1)}^{t+1} - (\lambda_{g,(i-1,j)}^{t+1} + 2\lambda_{g,(i,j)}^{t+1} + \lambda_{g,(i,j-1)}^{t+1}) p_{w,(i,j)}^{t+1} \\ & + (\lambda_{g,(i-1,j)}^{t+1}) p_{w,(i-1,j)}^{t+1} + (\lambda_{g,(i,j-1)}^{t+1}) p_{w,(i,j-1)}^{t+1} + (\lambda_{g,(i,j)}^{t+1} P'_{c,(i,j)}) S_{w,(i+1,j)}^{t+1} \\ & + (\lambda_{g,(i,j)}^{t+1} P'_{c,(i,j)}) S_{w,(i,j+1)}^{t+1} \\ & - (\lambda_{g,(i-1,j)}^{t+1} P'_{c,(i-1,j)} + 2\lambda_{g,(i,j)}^{t+1} P'_{c,(i,j)} + \lambda_{g,(i,j-1)}^{t+1} P'_{c,(i,j-1)} - \Phi) S_{w,(i,j)}^{t+1} \\ & + (\lambda_{g,(i-1,j)}^{t+1} P'_{c,(i-1,j)}) S_{w,(i-1,j)}^{t+1} + (\lambda_{g,(i,j-1)}^{t+1} P'_{c,(i,j-1)}) S_{w,(i,j-1)}^{t+1} + G_g \\ & - \Phi S_{w,(i,j)}^t \end{aligned} \quad \dots\dots\dots (B. 175)$$

and in Jacobian matrix, with respect to pressure at the grid of interest (a(X, 1) in Fig. B.7),

$$\frac{\partial F_{2i}}{\partial p_{w(i,j)}} = -(\lambda_{g,(i-1,j)}^{t+1} + 2\lambda_{g,(i,j)}^{t+1} + \lambda_{g,(i,j-1)}^{t+1}) \quad \dots\dots\dots (B. 176)$$

With respect to saturation at the grid of interest (a(X, 4) in Fig. B.7),

$$\begin{aligned} \frac{\partial F_{2i}}{\partial S_{w(i,j)}} = & \lambda'_{g,(i,j)} \left(p_{w,(i+1,j)}^{t+1} + p_{w,(i,j+1)}^{t+1} - 2p_{w,(i,j)}^{t+1} + P'_{c,(i,j)} S_{w,(i+1,j)}^{t+1} + P'_{c,(i,j)} S_{w,(i,j+1)}^{t+1} - \right. \\ & \left. 2P'_{c,(i,j)} S_{w,(i,j)}^{t+1} + \gamma_g (z_{g,(i,j)}^{t+1} - z_{g,(i,j+1)}^{t+1}) \right) + \lambda_{g,(i,j)}^{t+1} P''_{c,(i,j)} (S_{w,(i+1,j)}^{t+1} + S_{w,(i,j+1)}^{t+1} - \\ & \left. 2S_{w,(i,j)}^{t+1}) - 2P'_{c,(i,j)} \lambda_{g,(i,j)}^{t+1} - \left[\lambda_{g,(i-1,j)}^{t+1} P'_{c,(i-1,j)} + \lambda_{g,(i,j-1)}^{t+1} P'_{c,(i,j-1)} - \Phi \right] \end{aligned} \quad \dots\dots\dots (B. 177)$$

With respect to downstream pressure in x direction (b(X, 3) in Fig. B.7),

$$\frac{\partial F_{2i}}{\partial p_{w(i+1,j)}} = \lambda_{g,(i,j)}^{t+1} \dots\dots\dots (B. 178)$$

With respect to downstream saturation in x direction (b(X, 4) in Fig. B.7),

$$\frac{\partial F_{2i}}{\partial S_{w(i+1,j)}} = \lambda_{g,(i,j)}^{t+1} P'_{c,(i,j)} \dots\dots\dots (B. 179)$$

Eq. B. 175 further becomes

$$\begin{aligned} F_{2i} = & (\lambda_{g,(i,j)}^{t+1}) p_{w,(i+1,j)}^{t+1} + (\lambda_{g,(i,j)}^{t+1}) p_{w,(i,j+1)}^{t+1} - (\lambda_{g,(i-1,j)}^{t+1} + 2\lambda_{g,(i,j)}^{t+1} + \lambda_{g,(i,j-1)}^{t+1}) p_{w,(i,j)}^{t+1} \\ & + (\lambda_{g,(i-1,j)}^{t+1}) p_{w,(i-1,j)}^{t+1} + (\lambda_{g,(i,j-1)}^{t+1}) p_{w,(i,j-1)}^{t+1} + (\lambda_{g,(i,j)}^{t+1} P'_{c,(i,j)}) S_{w,(i+1,j)}^{t+1} \\ & + (\lambda_{g,(i,j)}^{t+1} P'_{c,(i,j)}) S_{w,(i,j+1)}^{t+1} \\ & - (\lambda_{g,(i-1,j)}^{t+1} P'_{c,(i-1,j)} + 2\lambda_{g,(i,j)}^{t+1} P'_{c,(i,j)} + \lambda_{g,(i,j-1)}^{t+1} P'_{c,(i,j-1)} - \Phi) S_{w,(i,j)}^{t+1} \\ & + (\lambda_{g,(i-1,j)}^{t+1} P'_{c,(i-1,j)}) S_{w,(i-1,j)}^{t+1} + (\lambda_{g,(i,j-1)}^{t+1} P'_{c,(i,j-1)}) S_{w,(i,j-1)}^{t+1} + G_g \\ & - \Phi S_{w,(i,j)}^t - J_{well} \frac{k_{rg,(i,j)}^{t+1}}{\mu_g} (p_{w,(i,j)}^{t+1} - p_{well}) \end{aligned} \dots\dots\dots (B. 180)$$

and in Jacobian matrix, with respect to pressure at the grid of interest (a(X, 1) in Fig. B.7),

$$\frac{\partial F_{2i}}{\partial p_{w(i,j)}} = -(\lambda_{g,(i-1,j)}^{t+1} + \lambda_{g,(i,j)}^{t+1} + \lambda_{g,(i,j-1)}^{t+1}) - J_{well} \frac{k_{rg,(i,j)}^{t+1}}{\mu_g} \dots\dots\dots (B. 181)$$

With respect to saturation at the grid of interest (a(X, 4) in Fig. B.7),

$$\begin{aligned} \frac{\partial F_{2i}}{\partial S_{w(i,j)}} = & \lambda'_{g,(i,j)} \left(p_{w,(i,j+1)}^{t+1} - p_{w,(i,j)}^{t+1} + P'_{c,(i,j)} S_{w,(i+1,j)}^{t+1} - P'_{c,(i,j)} S_{w,(i,j)}^{t+1} + \gamma_g (z_{g,(i,j)}^{t+1} - \right. \\ & \left. z_{g,(i,j+1)}^{t+1}) \right) + \lambda_{g,(i,j)}^{t+1} P'_{c,(i,j)} (S_{w,(i,j+1)}^{t+1} - S_{w,(i,j)}^{t+1}) - P'_{c,(i,j)} \lambda_{g,(i,j)}^{t+1} - \left[\lambda_{g,(i-1,j)}^{t+1} P'_{c,(i-1,j)} + \right. \\ & \left. \lambda_{g,(i,j-1)}^{t+1} P'_{c,(i,j-1)} - \Phi \right] \end{aligned} \quad \dots\dots\dots (B. 182)$$

With respect to downstream pressure in x direction (b(X, 3) in Fig. B.7),

$$\frac{\partial F_{2i}}{\partial p_{w(i+1,j)}} = 0 \quad \dots\dots\dots (B. 183)$$

With respect to downstream saturation in x direction (b(X, 4) in Fig. B.7),

$$\frac{\partial F_{2i}}{\partial S_{w(i+1,j)}} = 0 \quad \dots\dots\dots (B. 184)$$

B.5.3.2. Inlet Boundary Condition

There are two different inlet boundary conditions such as fixed injection velocity and fixed injection pressure.

B.5.3.2.1. Fixed Injection Velocity

For simplicity the total injection rate can be assumed to be evenly distributed at the inlet face if the media is homogenous. Then, for water phase,

$$\begin{aligned} F_{2i-1} = & \lambda_{w,(i,j)}^{t+1} p_{w,(i+1,j)}^{t+1} + \lambda_{w,(i,j)}^{t+1} p_{w,(i,j+1)}^{t+1} - \\ & (\lambda_{w,(i-1,j)}^{t+1} + 2\lambda_{w,(i,j)}^{t+1} + \lambda_{w,(i,j-1)}^{t+1}) p_{w,(i,j)}^{t+1} + \lambda_{w,(i-1,j)}^{t+1} p_{w,(i-1,j)}^{t+1} + \lambda_{w,(i,j-1)}^{t+1} p_{w,(i,j-1)}^{t+1} - \\ & \Phi S_{w,(i,j)}^{t+1} + G_w + \Phi S_{w,(i,j)}^t \quad \dots\dots\dots (B. 185) \end{aligned}$$

which further becomes

$$F_{2i-1} = \lambda_{w,(i,j)}^{t+1} p_{w,(i+1,j)}^{t+1} + \lambda_{w,(i,j)}^{t+1} p_{w,(i,j+1)}^{t+1} - (2\lambda_{w,(i,j)}^{t+1} + \lambda_{w,(i,j-1)}^{t+1}) p_{w,(i,j)}^{t+1} + \lambda_{w,(i,j-1)}^{t+1} p_{w,(i,j-1)}^{t+1} - \Phi S_{w,(i,j)}^{t+1} + G_w + \Phi S_{w,(i,j)}^t + u_{win} \quad \dots \dots \dots (B. 186)$$

Note that u_{win} has a positive sign for flow into the formation. And for gas phase,

$$F_{2i} = (\lambda_{g,(i,j)}^{t+1}) p_{w,(i+1,j)}^{t+1} + (\lambda_{g,(i,j)}^{t+1}) p_{w,(i,j+1)}^{t+1} - (\lambda_{g,(i-1,j)}^{t+1} + 2\lambda_{g,(i,j)}^{t+1} + \lambda_{g,(i,j-1)}^{t+1}) p_{w,(i,j)}^{t+1} + (\lambda_{g,(i-1,j)}^{t+1}) p_{w,(i-1,j)}^{t+1} + (\lambda_{g,(i,j-1)}^{t+1}) p_{w,(i,j-1)}^{t+1} + (\lambda_{g,(i,j)}^{t+1} P'_{c,(i,j)}) S_{w,(i+1,j)}^{t+1} + (\lambda_{g,(i,j)}^{t+1} P'_{c,(i,j)}) S_{w,(i,j+1)}^{t+1} - (\lambda_{g,(i-1,j)}^{t+1} P'_{c,(i-1,j)} + 2\lambda_{g,(i,j)}^{t+1} P'_{c,(i,j)} + \lambda_{g,(i,j-1)}^{t+1} P'_{c,(i,j-1)} - \Phi) S_{w,(i,j)}^{t+1} + (\lambda_{g,(i-1,j)}^{t+1} P'_{c,(i-1,j)}) S_{w,(i-1,j)}^{t+1} + (\lambda_{g,(i,j-1)}^{t+1} P'_{c,(i,j-1)}) S_{w,(i,j-1)}^{t+1} + G_g - \Phi S_{w,(i,j)}^t \quad \dots \dots \dots (B. 187)$$

which further becomes

$$F_{2i} = (\lambda_{g,(i,j)}^{t+1}) p_{w,(i+1,j)}^{t+1} + (\lambda_{g,(i,j)}^{t+1}) p_{w,(i,j+1)}^{t+1} - (2\lambda_{g,(i,j)}^{t+1} + \lambda_{g,(i,j-1)}^{t+1}) p_{w,(i,j)}^{t+1} + (\lambda_{g,(i,j-1)}^{t+1}) p_{w,(i,j-1)}^{t+1} + (\lambda_{g,(i,j)}^{t+1} P'_{c,(i,j)}) S_{w,(i+1,j)}^{t+1} + (\lambda_{g,(i,j)}^{t+1} P'_{c,(i,j)}) S_{w,(i,j+1)}^{t+1} - (2\lambda_{g,(i,j)}^{t+1} P'_{c,(i,j)} + \lambda_{g,(i,j-1)}^{t+1} P'_{c,(i,j-1)} - \Phi) S_{w,(i,j)}^{t+1} + (\lambda_{g,(i,j-1)}^{t+1} P'_{c,(i,j-1)}) S_{w,(i,j-1)}^{t+1} + G_g - \Phi S_{w,(i,j)}^t + u_{gin} \quad \dots \dots \dots (B. 188)$$

Note that u_{gin} has a positive sign for flow into the formation.

B.5.3.2.2. Fixed Injection Pressure

For fixed pressure boundary condition the pressures and gas fractions (f_g) for all grids at the inlet are pre-determined. These gas fractions at the inlet, in turn, allow water saturations to be determined. These conditions can be incorporated into the Jacobian matrix by using

$$p_{w,(i,j)}^{t+1} - p_{w,(i,j)}^t = 0 \quad \text{for any } t; \text{ for any } i \text{ and } j \text{ at the inlet}$$

..... (B. 189)

$$S_{w,(i,j)}^{t+1} - S_{w,(i,j)}^t = 0 \quad \text{for any } t; \text{ for any } i \text{ and } j \text{ at the inlet}$$

..... (B. 190)

Therefore, the Jacobian is modified for those grids at the inlet such that their pressures and saturations kept fixed irrespective of iterations and time steps as shown in Fig. B.9.

B.5.3.3. No flow Boundary Condition at the Reservoir Top

To incorporate no-flow boundary condition at the top of the reservoir, the mirror image concept is applied. Therefore, the Jacobian matrix should be modified accordingly as explained below.

For water phase,

$$F_{2i-1} = \lambda_{w,(i,j)}^{t+1} p_{w,(i+1,j)}^{t+1} + 2\lambda_{w,(i,j)}^{t+1} p_{w,(i,j+1)}^{t+1} - (\lambda_{w,(i-1,j)}^{t+1} + 3\lambda_{w,(i,j)}^{t+1}) p_{w,(i,j)}^{t+1}$$

$$+ \lambda_{w,(i-1,j)}^{t+1} p_{w,(i-1,j)}^{t+1} - \Phi S_{w,(i,j)}^{t+1} + G_w + \Phi S_{w,(i,j)}^t$$

..... (B. 191)

with

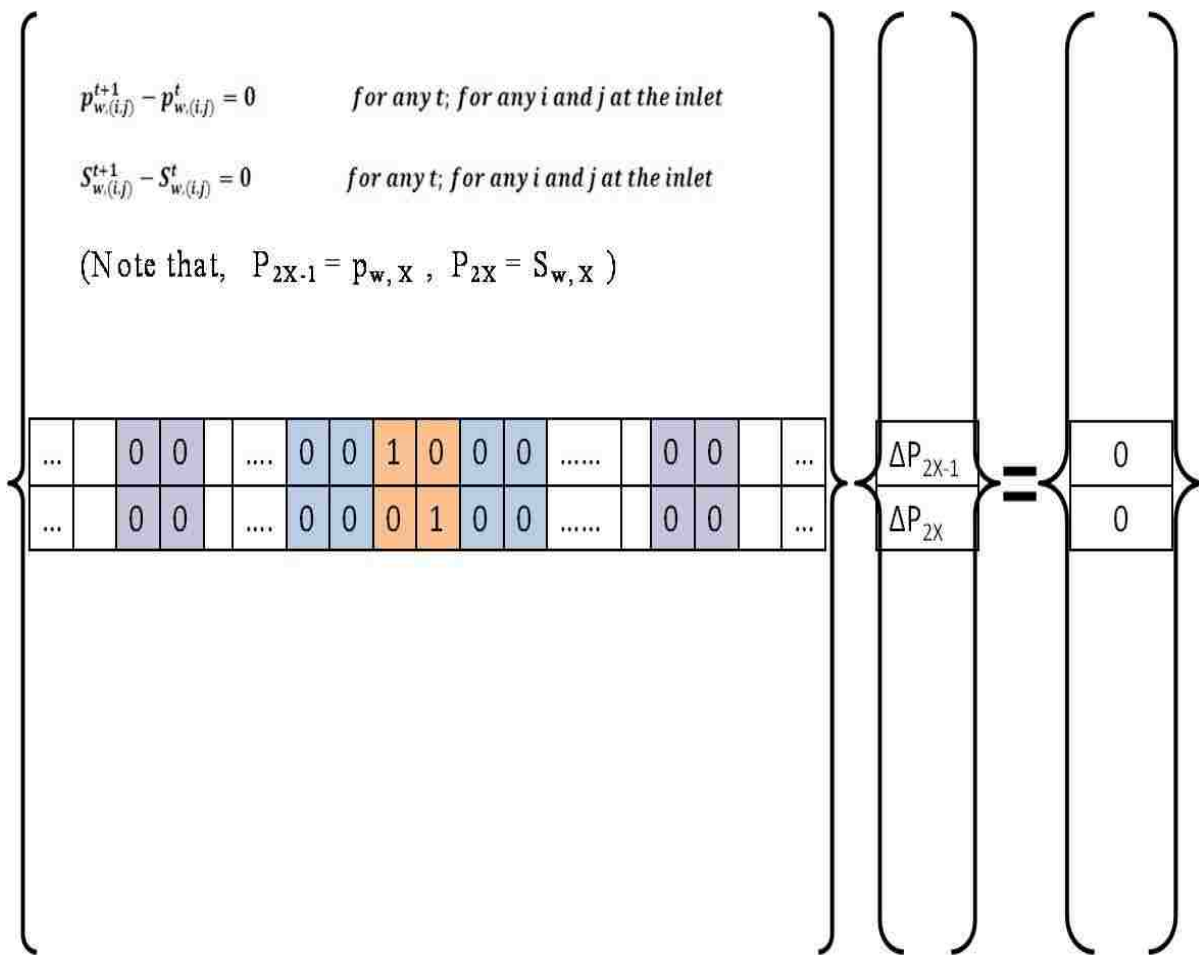


Figure B.9 Representation of solution scheme using the Jacobian matrix for a grid block at the inlet.

$$G_w = 2\lambda_{w,(i,j)}^{t+1} \gamma_w (z_{w,(i,j)}^{t+1} - z_{w,(i,j+1)}^{t+1}) , \dots\dots\dots (B.192)$$

$$\frac{\emptyset \Delta x^2}{\Delta t} = \Phi , \dots\dots\dots (B.193)$$

$$\lambda_w(S_w) = \frac{k k_{rw}(S_w)}{\mu_w} , \dots\dots\dots (B.194)$$

$$\lambda'_w(S_w) = \frac{k k'_{rw}(S_w)}{\mu_w} , \dots\dots\dots (B.195)$$

$$\gamma_w = \rho_w \frac{g}{g_c} , \dots\dots\dots (B.196)$$

$$k_{rw,(i,j)} = 0.7888 \left(\frac{S_{w,(i,j)} - S_{wc}}{1 - S_{wc} - S_{gr}} \right)^{1.9575} , \dots\dots\dots (B.197)$$

and

$$k'_{rw,(i,j)} = \frac{1.5441}{(1 - S_{wc} - S_{gr})^{1.9575}} (S_{w,(i,j)} - S_{wc})^{0.9575} . \dots\dots\dots (B.198)$$

In the equations shown below, all those terms with “ / ” are evaluated at the new (t+1) time step.

The formulation of the Jacobian matrix and the solution methodology is represented by Figs. B.7 and B.8 schematically. The specific derivative terms are expressed as follows:

With respect to upstream pressure in x direction (c(X, 1) in Fig. B.7),

$$\frac{\partial F_{2i-1}}{\partial p_{w(i-1,j)}} = \lambda_{w,(i-1,j)}^{t+1} \dots\dots\dots (B.199)$$

With respect to upstream saturation in x direction (c(X, 2) in Fig. B.7),

$$\frac{\partial F_{2i-1}}{\partial S_{w(i-1,j)}} = \lambda'_{w,(i-1,j)} (p_{w,(i-1,j)}^{t+1} - p_{w,(i,j)}^{t+1}) \dots\dots\dots (B.200)$$

With respect to upstream pressure in z direction (e(X, 1) in Fig. B.7),

$$\frac{\partial F_{2i-1}}{\partial p_{w(i,j-1)}} = 0 \quad \dots\dots\dots (B. 201)$$

With respect to upstream saturation in z direction (e(X, 2) in Fig. B.7),

$$\frac{\partial F_{2i-1}}{\partial S_{w(i,j-1)}} = 0 \quad \dots\dots\dots (B. 202)$$

With respect to pressure at the grid of interest (a(X, 1) in Fig. B.7),

$$\frac{\partial F_{2i-1}}{\partial p_{w(i,j)}} = -(\lambda_{w,(i-1,j)}^{t+1} + 3\lambda_{w,(i,j)}^{t+1}) \quad \dots\dots\dots (B. 203)$$

With respect to saturation at the grid of interest (a(X, 2) in Fig. B.7),

$$\frac{\partial F_{2i-1}}{\partial S_{w(i,j)}} = \lambda'_{w,(i,j)} \left(p_{w,(i+1,j)}^{t+1} + 2p_{w,(i,j+1)}^{t+1} - 3p_{w,(i,j)}^{t+1} + 2\gamma_w(z_{w,(i,j)}^{t+1} - z_{w,(i,j+1)}^{t+1}) \right) - \Phi$$

\dots\dots\dots (B. 204)

With respect to downstream pressure in x direction (b(X, 1) in Fig. B.7),

$$\frac{\partial F_{2i-1}}{\partial p_{w(i+1,j)}} = \lambda_{w,(i,j)}^{t+1} \quad \dots\dots\dots (B. 205)$$

With respect to downstream saturation in x direction (b(X, 2) in Fig. B.7),

$$\frac{\partial F_{2i-1}}{\partial S_{w(i+1,j)}} = 0 \quad \dots\dots\dots (B. 206)$$

With respect to downstream pressure in z direction (d(X, 1) in Fig. B.7),

$$\frac{\partial F_{2i-1}}{\partial p_{w(i,j+1)}} = \lambda_{w,(i,j)}^{t+1} \quad \dots\dots\dots (B. 207)$$

and, with respect to downstream saturation in z direction (d(X, 2) in Fig. B.7),

$$\frac{\partial F_{2i-1}}{\partial S_{w(i,j+1)}} = 0 \quad \dots\dots\dots (B. 208)$$

For gas phase,

$$\begin{aligned} F_{2i} = & (\lambda_{g,(i,j)}^{t+1}) p_{w,(i+1,j)}^{t+1} + 2(\lambda_{g,(i,j)}^{t+1}) p_{w,(i,j+1)}^{t+1} - (\lambda_{g,(i-1,j)}^{t+1} + 3\lambda_{g,(i,j)}^{t+1}) p_{w,(i,j)}^{t+1} + \\ & (\lambda_{g,(i-1,j)}^{t+1}) p_{w,(i-1,j)}^{t+1} + (\lambda_{g,(i,j)}^{t+1} P'_{c,(i,j)}) S_{w,(i+1,j)}^{t+1} + 2(\lambda_{g,(i,j)}^{t+1} P'_{c,(i,j)}) S_{w,(i,j+1)}^{t+1} - \\ & (\lambda_{g,(i-1,j)}^{t+1} P'_{c,(i-1,j)} + 3\lambda_{g,(i,j)}^{t+1} P'_{c,(i,j)} - \Phi) S_{w,(i,j)}^{t+1} + (\lambda_{g,(i-1,j)}^{t+1} P'_{c,(i-1,j)}) S_{w,(i-1,j)}^{t+1} + \\ & G_g - \Phi S_{w,(i,j)}^t \quad \dots\dots\dots (B. 209) \end{aligned}$$

with

$$G_g = 2\lambda_{g,(i,j)}^{t+1} \gamma_g (z_{g,(i,j)}^{t+1} - z_{g,(i,j+1)}^{t+1}) \quad \dots\dots\dots (B. 210)$$

$$\frac{\emptyset \Delta x^2}{\Delta t} = \Phi \quad \dots\dots\dots (B. 211)$$

$$\lambda_g(S_w) = \frac{k k_{rg}(S_w)}{\mu_g} \quad \dots\dots\dots (B. 212)$$

$$\lambda'_g(S_w) = \frac{k k'_{rg}(S_w)}{\mu_g} \quad \dots\dots\dots (B. 213)$$

$$\gamma_g = \rho_g \frac{g}{g_c} \quad \dots\dots\dots (B. 214)$$

$$k_{rgi} = \left(\frac{1 - S_{wi} - S_{gr}}{1 - S_{wc} - S_{gr}} \right)^{2.2868} \quad \dots\dots\dots (B. 215)$$

and

$$k_{rgi}' = \frac{-2.2868}{(1-S_{wc}-S_{gr})^{2.2868}} (1 - S_{wi} - S_{gr})^{1.2868} \dots\dots\dots (B. 216)$$

The capillary pressure is defined as

$$P_{c,(i, j)} = \alpha e^{-\left(\frac{S_{w,(i, j)}}{\beta}\right)} \dots\dots\dots (B. 217)$$

And the derivatives of capillary pressure using upstream weighting are

$$P_{c,(i, j)}' = \frac{\partial P_c}{\partial S_w} = -\left(\frac{\alpha}{\beta}\right) e^{-\left(\frac{S_{w,(i, j)}}{\beta}\right)} \dots\dots\dots (B. 218)$$

and

$$P_{c,(i, j)}'' = \left(\frac{\alpha}{\beta^2}\right) e^{-\left(\frac{S_{w,(i, j)}}{\beta}\right)} \dots\dots\dots (B. 219)$$

By following the same procedure in the previous section, the derivative terms are given as follows:

With respect to upstream pressure in x direction (c(X, 3) in Fig. B.7),

$$\frac{\partial F_{2i}}{\partial p_{w(i-1, j)}} = \lambda_{g,(i-1, j)}^{t+1} \dots\dots\dots (B. 220)$$

With respect to upstream saturation in x direction (c(X, 4) in Fig. B.7),

$$\begin{aligned} \frac{\partial F_{2i}}{\partial S_{w(i-1, j)}} &= \lambda_{g,(i-1, j)}' \left(p_{w,(i-1, j)}^{t+1} - p_{w,(i, j)}^{t+1} - P_{c,(i-1, j)}' S_{w,(i, j)}^{t+1} + P_{c,(i-1, j)}' S_{w,(i-1, j)}^{t+1} \right) + \\ &\lambda_{g,(i-1, j)}^{t+1} P_{c,(i-1, j)}'' (S_{w,(i-1, j)}^{t+1} - S_{w,(i, j)}^{t+1}) + \lambda_{g,(i-1, j)}^{t+1} P_{c,(i-1, j)}' \dots\dots\dots (B. 221) \end{aligned}$$

With respect to upstream pressure in z direction (e(X, 3) in Fig. B.7),

$$\frac{\partial F_{2i}}{\partial p_{w(i, j-1)}} = 0 \dots\dots\dots (B. 222)$$

With respect to upstream saturation in z direction (e(X, 4) in Fig. B.7),

$$\frac{\partial F_{2i}}{\partial S_{w(i,j-1)}} = 0 \quad \dots\dots\dots (B. 223)$$

With respect to pressure at the grid of interest (a(X, 3) in Fig. B.7),

$$\frac{\partial F_{2i}}{\partial p_{w(i,j)}} = -(\lambda_{g,(i-1,j)}^{t+1} + 3\lambda_{g,(i,j)}^{t+1}) \quad \dots\dots\dots (B. 224)$$

With respect to saturation at the grid of interest (a(X, 4) in Fig. B.7),

$$\begin{aligned} \frac{\partial F_{2i}}{\partial S_{w(i,j)}} = & \\ & \lambda'_{g,(i,j)} \left(p_{w,(i+1,j)}^{t+1} + 2p_{w,(i,j+1)}^{t+1} - 3p_{w,(i,j)}^{t+1} + P'_{c,(i,j)} S_{w,(i+1,j)}^{t+1} + 2P'_{c,(i,j)} S_{w,(i,j+1)}^{t+1} - \right. \\ & \left. 3P'_{c,(i,j)} S_{w,(i,j)}^{t+1} + 2\gamma_g (z_{g,(i,j)}^{t+1} - z_{g,(i,j+1)}^{t+1}) \right) + \lambda_{g,(i,j)}^{t+1} P'_{c,(i,j)} (S_{w,(i+1,j)}^{t+1} + 2S_{w,(i,j+1)}^{t+1} - \\ & \left. 3S_{w,(i,j)}^{t+1}) - 3P'_{c,(i,j)} \lambda_{g,(i,j)}^{t+1} - \left[\lambda_{g,(i-1,j)}^{t+1} P'_{c,(i-1,j)} - \Phi \right] \right. \\ & \dots\dots\dots (B. 225) \end{aligned}$$

With respect to downstream pressure in x direction (b(X, 3) in Fig. B.7),

$$\frac{\partial F_{2i}}{\partial p_{w(i+1,j)}} = \lambda_{g,(i,j)}^{t+1} \quad \dots\dots\dots (B. 226)$$

With respect to downstream saturation in x direction (b(X, 4) in Fig. B.7),

$$\frac{\partial F_{2i}}{\partial S_{w(i+1,j)}} = \left(\lambda_{g,(i,j)}^{t+1} P'_{c,(i,j)} \right) \quad \dots\dots\dots (B. 227)$$

With respect to downstream pressure in z direction (d(X, 3) in Fig. B.7),

$$\frac{\partial F_{2i}}{\partial p_{w(i,j+1)}} = \lambda_{g,(i,j)}^{t+1} \quad \dots\dots\dots (B. 228)$$

And, with respect to downstream saturation in z direction (d(X, 4) in Fig. B.7),

$$\frac{\partial F_{2i}}{\partial S_{w(i,j+1)}} = 2 \left(\lambda_{g,(i,j)}^{t+1} P'_{c,(i,j)} \right) \cdot \dots \dots \dots (B. 229)$$

B.5.3.4. No flow Boundary Condition at the Reservoir Bottom

Similar to no flow boundary condition at the reservoir top, the mirror image concept is applied. For instance, the term in the left-hand side of Eq. B.93 is written as

$$\begin{aligned} \frac{\partial}{\partial z} \left(\lambda_w \left(\frac{\partial p_w}{\partial z} - \gamma_w \frac{\partial h}{\partial z} \right) \right) = \\ \frac{1}{\Delta z^2} \left[- (2\lambda_{w,(i,j-1/2)}) (p_{w,(i,j)} - \gamma_w z_{w,(i,j)}) + 2\lambda_{w,(i,j-1/2)} (p_{w,(i,j-1)} - \gamma_w z_{w,(i,j-1)}) \right] \end{aligned} \dots \dots \dots (B. 230)$$

Therefore, for water phase,

$$\begin{aligned} F_{2i-1} = \lambda_{w,(i,j)}^{t+1} p_{w,(i+1,j)}^{t+1} - \left(\lambda_{w,(i-1,j)}^{t+1} + \lambda_{w,(i,j)}^{t+1} + 2\lambda_{w,(i,j-1)}^{t+1} \right) p_{w,(i,j)}^{t+1} + \lambda_{w,(i-1,j)}^{t+1} p_{w,(i-1,j)}^{t+1} \\ + 2\lambda_{w,(i,j-1)}^{t+1} p_{w,(i,j-1)}^{t+1} - \Phi S_{w,(i,j)}^{t+1} + G_w + \Phi S_{w,(i,j)}^t \end{aligned} \dots \dots \dots (B. 231)$$

with

$$G_w = 2\lambda_{w,(i,j-1)}^{t+1} \gamma_w (z_{w,(i,j)}^{t+1} - z_{w,(i,j-1)}^{t+1}) , \dots \dots \dots (B.232)$$

$$\frac{\emptyset \Delta x^2}{\Delta t} = \Phi , \dots \dots \dots (B. 233)$$

$$\lambda_w(S_w) = \frac{k k_{rw}(S_w)}{\mu_w} , \dots \dots \dots (B. 234)$$

$$\lambda'_w(S_w) = \frac{k k'_{rw}(S_w)}{\mu_w} , \dots \dots \dots (B. 235)$$

$$\gamma_w = \rho_w \frac{g}{g_c} , \dots\dots\dots (B. 236)$$

$$k_{rw,(i,j)} = 0.7888 \left(\frac{S_{w,(i,j)} - S_{wc}}{1 - S_{wc} - S_{gr}} \right)^{1.9575} , \dots\dots\dots (B. 237)$$

and

$$k'_{rw,(i,j)} = \frac{1.5441}{(1 - S_{wc} - S_{gr})^{1.9575}} (S_{w,(i,j)} - S_{wc})^{0.9575} . \dots\dots\dots (B. 238)$$

In the equations shown below, all those terms with “'” are evaluated at the new (t+1) time step.

The formulation of the Jacobian matrix and the solution methodology is represented by Figs B.7 and B.8 schematically. The specific derivative terms are expressed as follows:

With respect to upstream pressure in x direction (c(X, 1) in Fig. B.7),

$$\frac{\partial F_{2i-1}}{\partial p_{w(i-1,j)}} = \lambda_{w,(i-1,j)}^{t+1} \dots\dots\dots (B. 239)$$

With respect to upstream saturation in x direction (c(X, 2) in Fig. B.7),

$$\frac{\partial F_{2i-1}}{\partial S_{w(i-1,j)}} = \lambda'_{w,(i-1,j)} (p_{w,(i-1,j)}^{t+1} - p_{w,(i,j)}^{t+1}) \dots\dots\dots (B. 240)$$

With respect to upstream pressure in z direction (e(X, 1) in Fig. B.7),

$$\frac{\partial F_{2i-1}}{\partial p_{w(i,j-1)}} = 2\lambda_{w,(i,j-1)}^{t+1} \dots\dots\dots (B. 241)$$

With respect to upstream saturation in z direction (e(X, 2) in Fig. B.7),

$$\frac{\partial F_{2i-1}}{\partial S_{w(i,j-1)}} = \lambda'_{w,(i,j-1)} \left(2p_{w,(i,j-1)}^{t+1} - 2p_{w,(i,j)}^{t+1} + 2\gamma_w (z_{w,(i,j)}^{t+1} - z_{w,(i,j-1)}^{t+1}) \right) \dots\dots\dots (B. 242)$$

With respect to pressure at the grid of interest (a(X, 1) in Fig. B.7),

$$\frac{\partial F_{2i-1}}{\partial p_{w(i,j)}} = -(\lambda_{w,(i-1,j)}^{t+1} + \lambda_{w,(i,j)}^{t+1} + 2\lambda_{w,(i,j-1)}^{t+1}) \dots\dots\dots (B. 243)$$

With respect to saturation at the grid of interest (a(X, 2) in Fig. B.7),

$$\frac{\partial F_{2i-1}}{\partial S_{w(i,j)}} = \lambda'_{w,(i,j)} (p_{w,(i+1,j)}^{t+1} - p_{w,(i,j)}^{t+1}) - \Phi \dots\dots\dots (B. 244)$$

With respect to downstream pressure in x direction (b(X, 1) in Fig. B.7),

$$\frac{\partial F_{2i-1}}{\partial p_{w(i+1,j)}} = \lambda_{w,(i,j)}^{t+1} \dots\dots\dots (B. 245)$$

With respect to downstream saturation in x direction (b(X, 2) in Fig. B.7),

$$\frac{\partial F_{2i-1}}{\partial S_{w(i+1,j)}} = 0 \dots\dots\dots (B. 246)$$

With respect to downstream pressure in z direction (d(X, 1) in Fig. B.7),

$$\frac{\partial F_{2i-1}}{\partial p_{w(i,j+1)}} = 0 \dots\dots\dots (B. 247)$$

And, with respect to downstream saturation in z direction (d(X, 2) in Fig. B.7),

$$\frac{\partial F_{2i-1}}{\partial S_{w(i,j+1)}} = 0 \dots\dots\dots (B. 248)$$

For gas phase,

$$F_{2i} = (\lambda_{g,(i,j)}^{t+1}) p_{w,(i+1,j)}^{t+1} - (\lambda_{g,(i-1,j)}^{t+1} + \lambda_{g,(i,j)}^{t+1} + 2\lambda_{g,(i,j-1)}^{t+1}) p_{w,(i,j)}^{t+1} +$$

$$(\lambda_{g,(i-1,j)}^{t+1}) p_{w,(i-1,j)}^{t+1} + 2(\lambda_{g,(i,j-1)}^{t+1}) p_{w,(i,j-1)}^{t+1} + (\lambda_{g,(i,j)}^{t+1} P'_{c,(i,j)}) S_{w,(i+1,j)}^{t+1} -$$

$$\begin{aligned}
& \left(\lambda_{g,(i-1,j)}^{t+1} P'_{c,(i-1,j)} + \lambda_{g,(i,j)}^{t+1} P'_{c,(i,j)} + 2\lambda_{g,(i,j-1)}^{t+1} P'_{c,(i,j-1)} - \Phi \right) S_{w,(i,j)}^{t+1} + \\
& \left(\lambda_{g,(i-1,j)}^{t+1} P'_{c,(i-1,j)} \right) S_{w,(i-1,j)}^{t+1} + 2 \left(\lambda_{g,(i,j-1)}^{t+1} P'_{c,(i,j-1)} \right) S_{w,(i,j-1)}^{t+1} + G_g - \Phi S_{w,(i,j)}^t
\end{aligned}
\tag{B. 249}$$

with

$$G_g = 2\lambda_{g,(i,j-1)}^{t+1} \gamma_g (z_{g,(i,j)}^{t+1} - z_{g,(i,j-1)}^{t+1}) \tag{B. 250}$$

$$\frac{\emptyset \Delta x^2}{\Delta t} = \Phi \tag{B. 251}$$

$$\lambda_g(S_w) = \frac{k k_{rg}(S_w)}{\mu_g} \tag{B. 252}$$

$$\lambda'_g(S_w) = \frac{k k'_{rg}(S_w)}{\mu_g} \tag{B. 253}$$

$$\gamma_g = \rho_g \frac{g}{g_c} \tag{B. 254}$$

$$k_{rgi} = \left(\frac{1 - S_{wi} - S_{gr}}{1 - S_{wc} - S_{gr}} \right)^{2.2868} \tag{B. 255}$$

and

$$k'_{rgi} = \frac{-2.2868}{(1 - S_{wc} - S_{gr})^{2.2868}} (1 - S_{wi} - S_{gr})^{1.2868} \tag{B. 256}$$

The capillary pressure is defined as

$$P_{c,(i,j)} = \alpha e^{-\left(\frac{S_{w,(i,j)}}{\beta}\right)} \tag{B. 257}$$

And the derivatives of capillary pressure using upstream weighting are

$$P'_{c,(i,j)} = \frac{\partial P_c}{\partial S_w} = - \left(\frac{\alpha}{\beta} \right) e^{-\left(\frac{S_{w,(i,j)}}{\beta} \right)}, \dots \dots \dots (B. 258)$$

and

$$P''_{c,(i,j)} = \left(\frac{\alpha}{\beta^2} \right) e^{-\left(\frac{S_{w,(i,j)}}{\beta} \right)} \dots \dots \dots (B. 259)$$

By following similar procedure in the previous section, the derivative terms are given as follows:

With respect to upstream pressure in x direction (c(X, 3) in Fig. B.7),

$$\frac{\partial F_{2i}}{\partial p_{w(i-1,j)}} = \lambda_{g,(i-1,j)}^{t+1} \dots \dots \dots (B. 260)$$

With respect to upstream saturation in x direction (c(X, 4) in Fig. B.7),

$$\begin{aligned} \frac{\partial F_{2i}}{\partial S_{w(i-1,j)}} = & \lambda'_{g,(i-1,j)} \left(p_{w,(i-1,j)}^{t+1} - p_{w,(i,j)}^{t+1} - P'_{c,(i-1,j)} S_{w,(i,j)}^{t+1} + P'_{c,(i-1,j)} S_{w,(i-1,j)}^{t+1} \right) + \\ & \lambda_{g,(i-1,j)}^{t+1} P''_{c,(i-1,j)} \left(S_{w,(i-1,j)}^{t+1} - S_{w,(i,j)}^{t+1} \right) + \lambda_{g,(i-1,j)}^{t+1} P'_{c,(i-1,j)} \dots \dots \dots (B. 261) \end{aligned}$$

With respect to upstream pressure in z direction (e(X, 3) in Fig. B.7),

$$\frac{\partial F_{2i}}{\partial p_{w(i,j-1)}} = 2\lambda_{g,(i,j-1)}^{t+1} \dots \dots \dots (B. 262)$$

With respect to upstream saturation in z direction (e(X, 4) in Fig. B.7),

$$\begin{aligned} \frac{\partial F_{2i}}{\partial S_{w(i,j-1)}} = & \lambda'_{g,(i,j-1)} \left(2p_{w,(i,j-1)}^{t+1} - 2p_{w,(i,j)}^{t+1} - 2P'_{c,(i,j-1)} S_{w,(i,j)}^{t+1} + 2P'_{c,(i,j-1)} S_{w,(i,j-1)}^{t+1} + \right. \\ & \left. 2\gamma_g \left(z_{g,(i,j)}^{t+1} - z_{g,(i,j-1)}^{t+1} \right) \right) + \lambda_{g,(i,j-1)}^{t+1} P''_{c,(i,j-1)} \left(2S_{w,(i,j-1)}^{t+1} - 2S_{w,(i,j)}^{t+1} \right) + \lambda_{g,(i,j-1)}^{t+1} P'_{c,(i,j-1)} \dots \dots \dots (B. 263) \end{aligned}$$

With respect to pressure at the grid of interest (a(X, 3) in Fig. B.7),

$$\frac{\partial F_{2i}}{\partial p_{w(i,j)}} = -(\lambda_{g,(i-1,j)}^{t+1} + \lambda_{g,(i,j)}^{t+1} + 2\lambda_{g,(i,j-1)}^{t+1}) \quad \dots\dots\dots (B. 264)$$

With respect to saturation at the grid of interest (a(X, 4) in Fig. B.7),

$$\begin{aligned} \frac{\partial F_{2i}}{\partial S_{w(i,j)}} &= \lambda'_{g,(i,j)} \left(p_{w,(i+1,j)}^{t+1} - p_{w,(i,j)}^{t+1} + P'_{c,(i,j)} S_{w,(i+1,j)}^{t+1} - P'_{c,(i,j)} S_{w,(i,j)}^{t+1} \right) \\ &\quad + \lambda_{g,(i,j)}^{t+1} P'_{c,(i,j)} \left(S_{w,(i+1,j)}^{t+1} - S_{w,(i,j)}^{t+1} \right) - P'_{c,(i,j)} \lambda_{g,(i,j)}^{t+1} \\ &\quad - \left[\lambda_{g,(i-1,j)}^{t+1} P'_{c,(i-1,j)} + 2\lambda_{g,(i,j-1)}^{t+1} P'_{c,(i,j-1)} - \Phi \right] \\ &\quad \dots\dots\dots (B. 265) \end{aligned}$$

With respect to downstream pressure in x direction (b(X, 3) in Fig. B.7),

$$\frac{\partial F_{2i}}{\partial p_{w(i+1,j)}} = \lambda_{g,(i,j)}^{t+1} \quad \dots\dots\dots (B. 266)$$

With respect to downstream saturation in x direction (b(X, 4) in Fig. B.7),

$$\frac{\partial F_{2i}}{\partial S_{w(i+1,j)}} = \lambda_{g,(i,j)}^{t+1} P'_{c,(i,j)} \quad \dots\dots\dots (B. 267)$$

With respect to downstream pressure in z direction (d(X, 3) in Fig. B.7),

$$\frac{\partial F_{2i}}{\partial p_{w(i,j+1)}} = 0 \quad \dots\dots\dots (B. 268)$$

And, with respect to downstream saturation in z direction (d(X, 4) in Fig. B.7),

$$\frac{\partial F_{2i}}{\partial S_{w(i,j+1)}} = 0 \quad \dots\dots\dots (B. 269)$$

APPENDIX C. NEW FOAM SIMULATION ALGORITHM RESULTS

The results shown in Figs. C.1 through C.9 are produced with a new foam simulation algorithm with matrix solver as shown in Appendix B. These figures can be compared with Figs 4.3, 4.5, 4.6, 4.11, 4.12, 4.13, 4.16, 4.17, and 4.19, respectively. These figures show nearly the same responses at different injection conditions, implying that the earlier discussions on pressure-modification and unconventional fractional flow curve analysis (both weak foams and strong foams) are still valid irrespective of discretization methods and different solution algorithms.

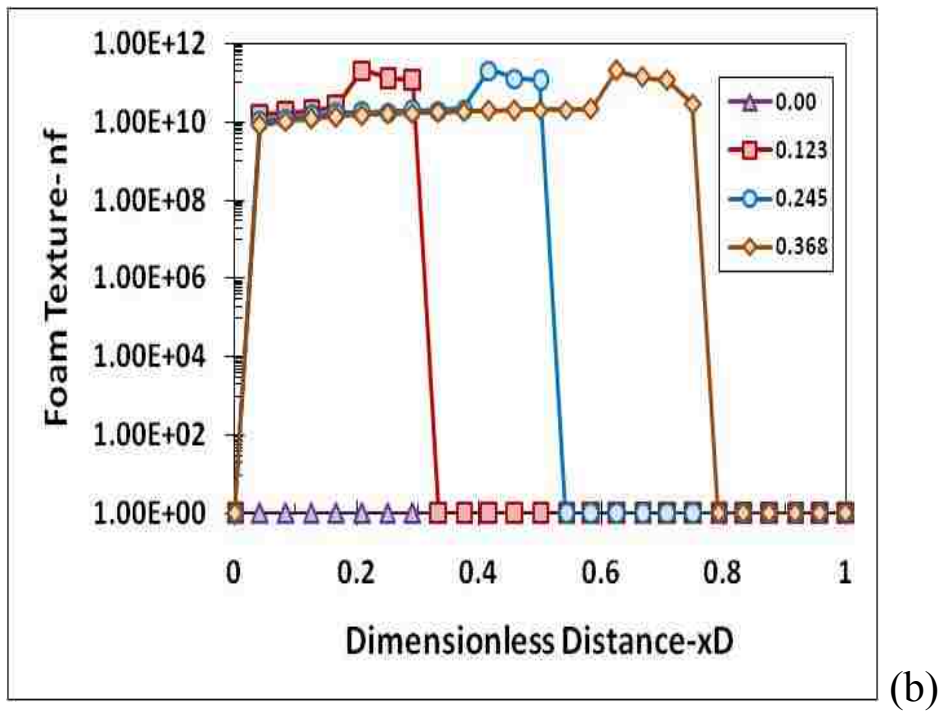
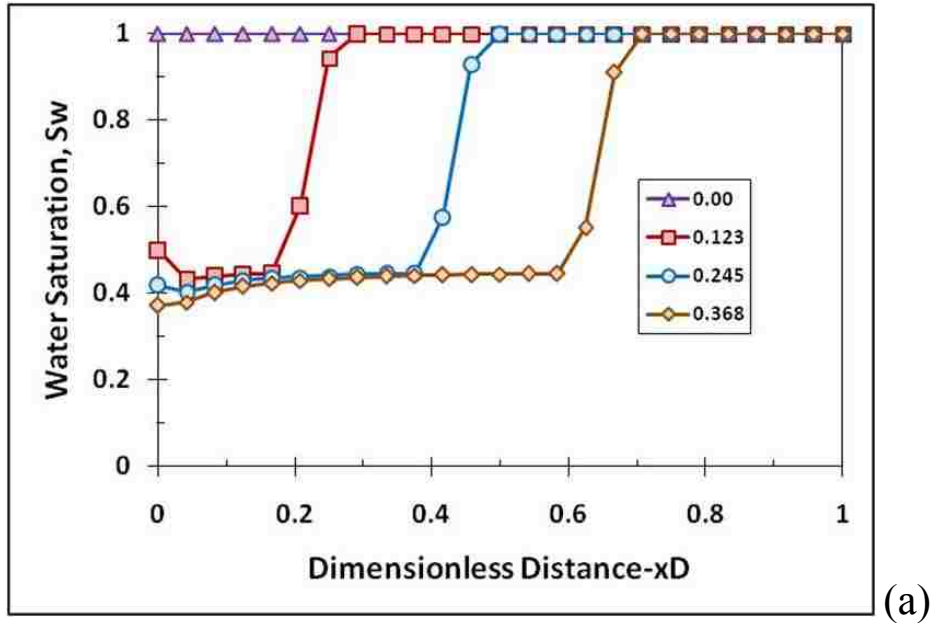


Figure C.1 Results from dynamic simulation and fractional flow analysis of gas injection at $u_t = u_g = 2.8 \times 10^{-5}$ m/s: (a) saturation profile and (b) foam texture profile (from new simulation algorithm (Appendix B) in comparison with Fig. 4.3)

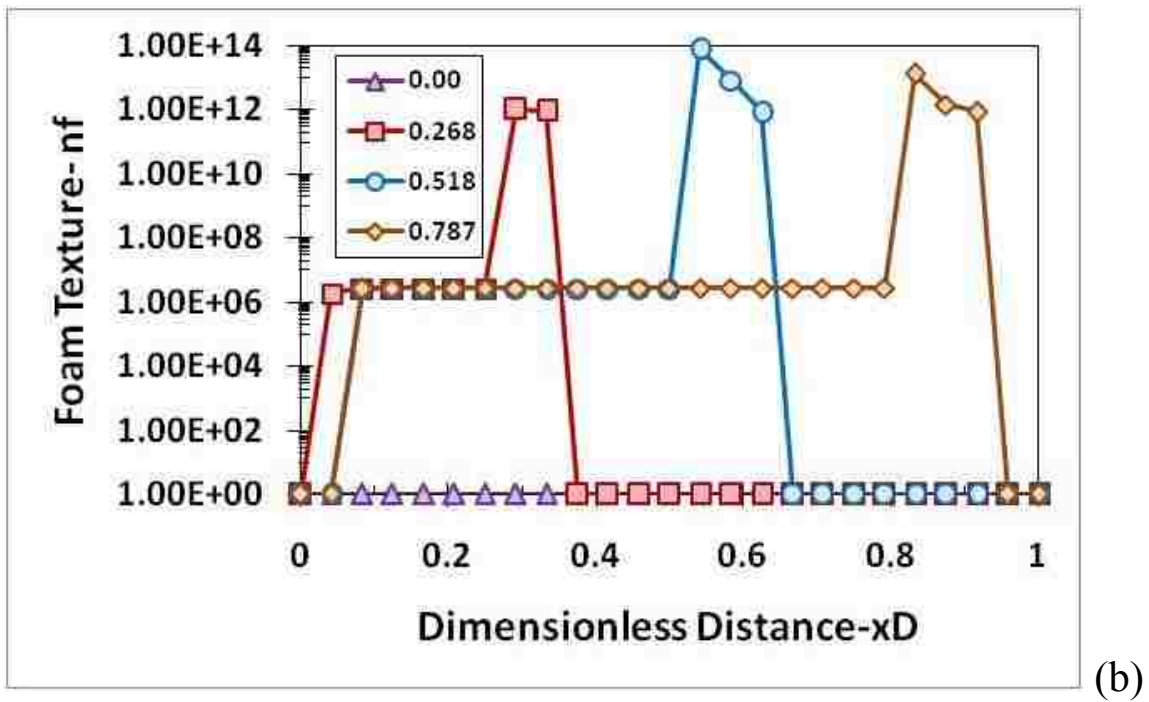
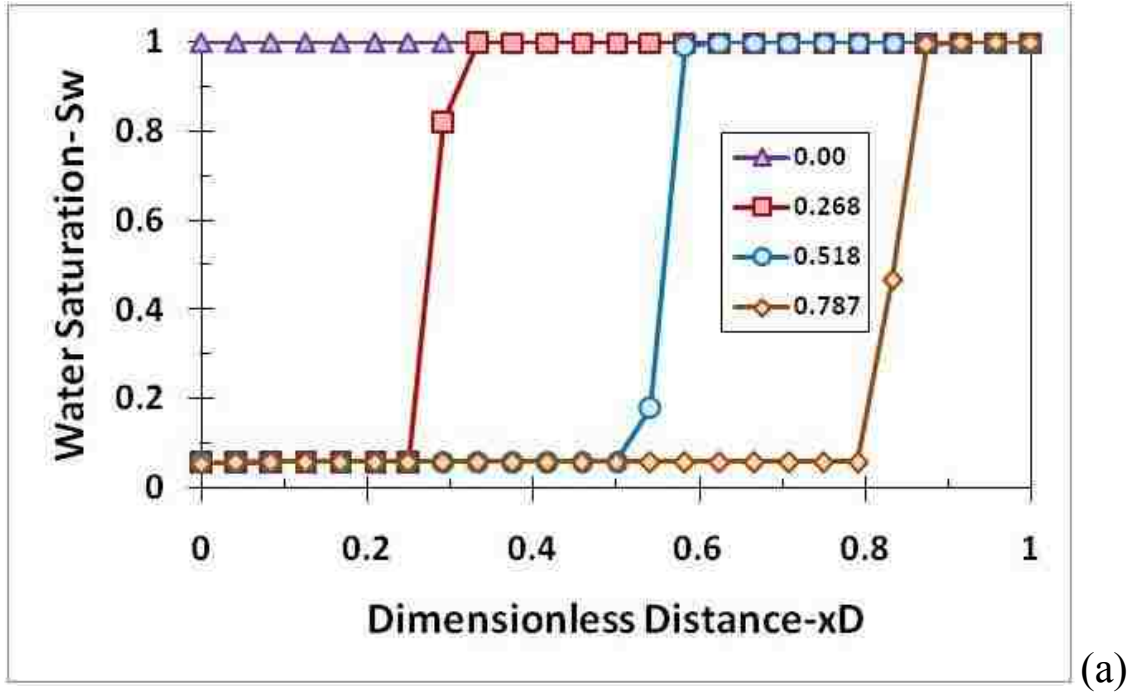


Figure C.2 Results from dynamic simulation and fractional flow analysis of gas injection at $u_t = u_g = 12 \times 10^{-5}$ m/s: (a) saturation profile and (b) foam texture profile (from new simulation algorithm (Appendix B) in comparison with Fig. 4.5)

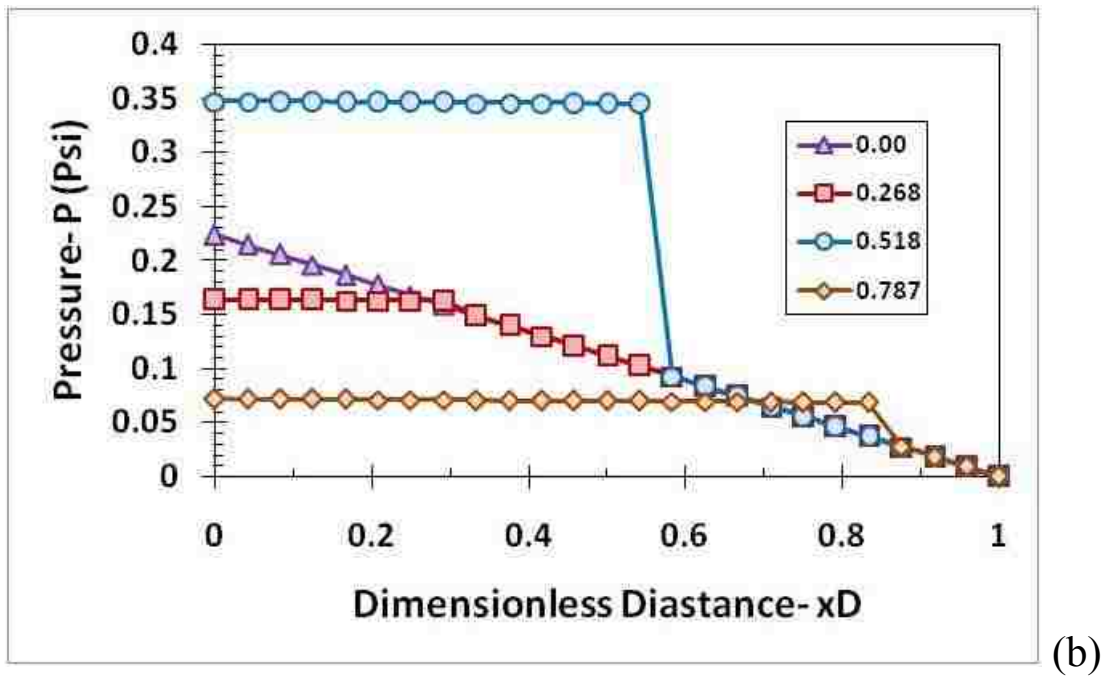
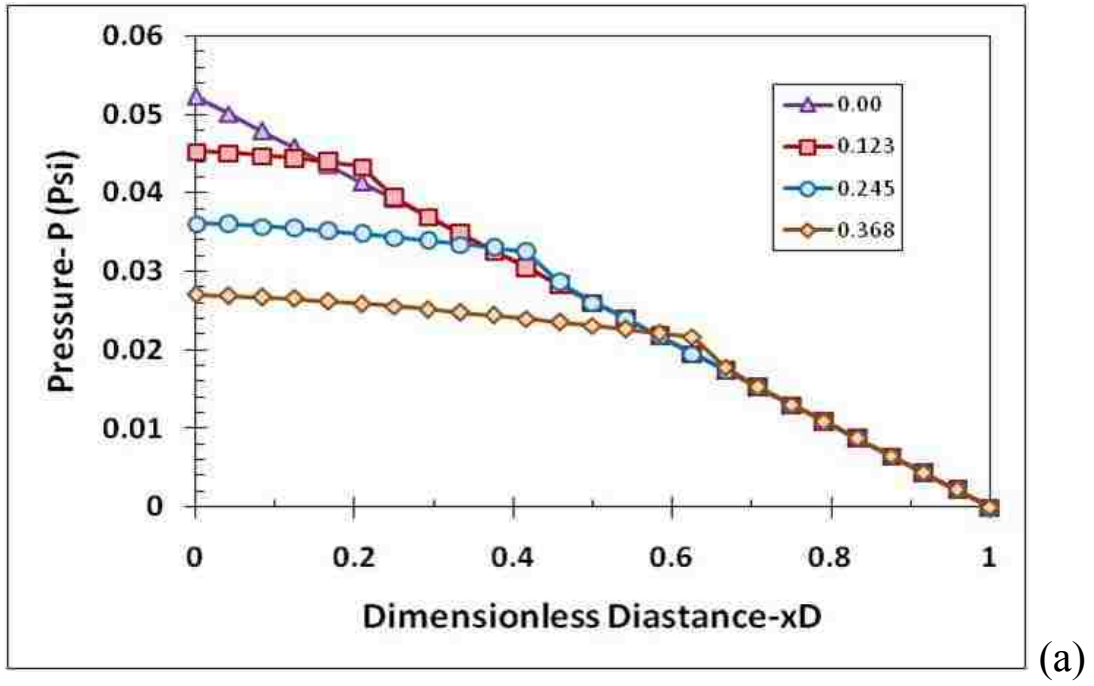
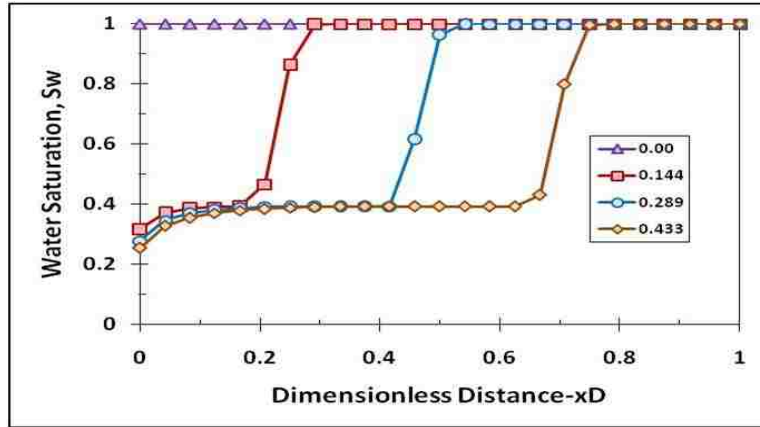
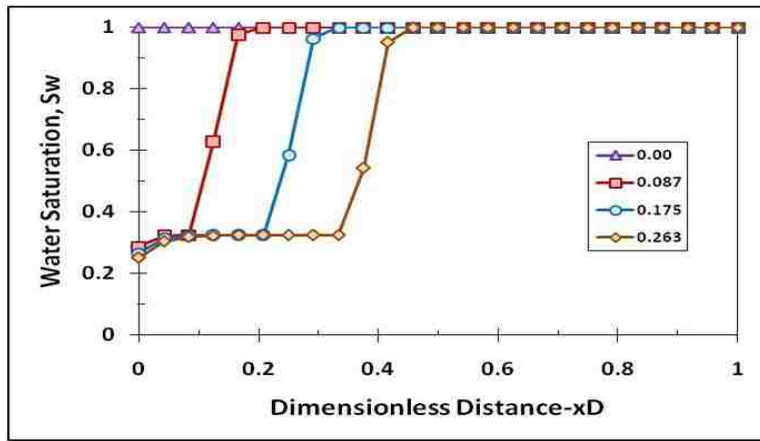


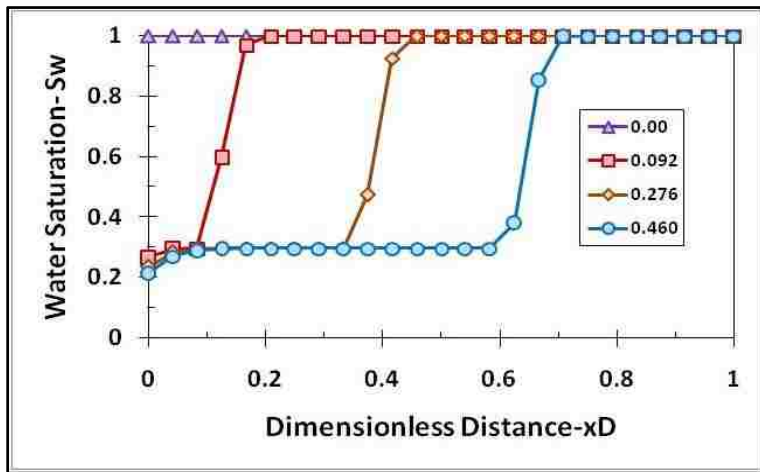
Figure C.3 Pressure profiles from dynamic simulations and fractional flow analysis during gas injection: (a) $u_t = u_g = 2.8 \times 10^{-5}$ m/s and (b) $u_t = u_g = 12 \times 10^{-5}$ m/s (from new simulation algorithm (Appendix B) in comparison with Fig. 4.6)



(a)



(b)



(c)

Figure C.4 Water saturation profile from mechanistic simulations: (a) $u_g = 3.3 \times 10^{-5}$ m/s, (b) $u_g = 4.0 \times 10^{-5}$ m/s, and (c) $u_g = 4.2 \times 10^{-5}$ m/s (from new simulation algorithm (Appendix B) in comparison with Fig. 4.11)

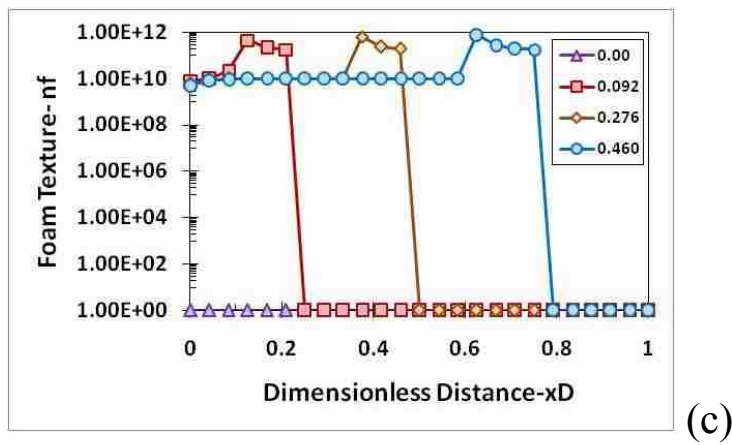
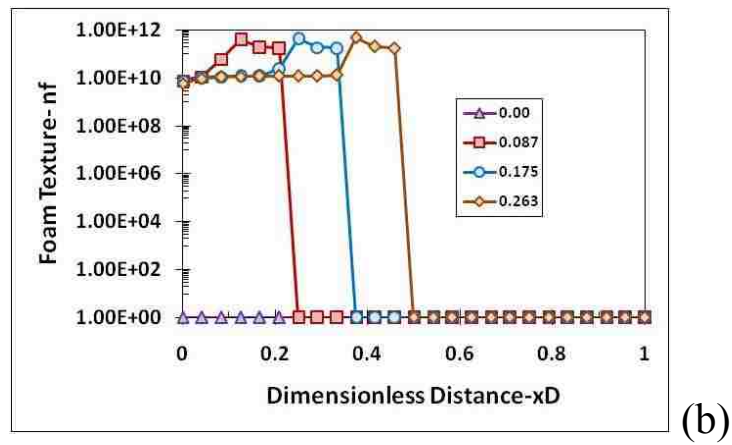
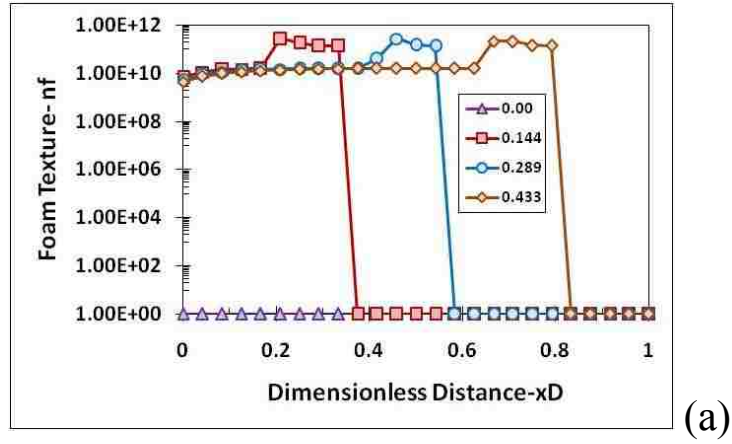


Figure C.5 Foam texture profile from mechanistic simulations: (a) $u_g = 3.3 \times 10^{-5}$ m/s, (b) $u_g = 4.0 \times 10^{-5}$ m/s, and (c) $u_g = 4.2 \times 10^{-5}$ m/s (from new simulation algorithm (Appendix B) in comparison with Fig. 4.12)

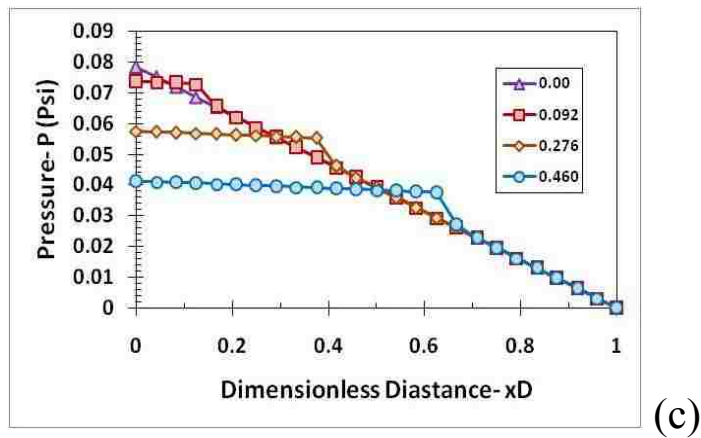
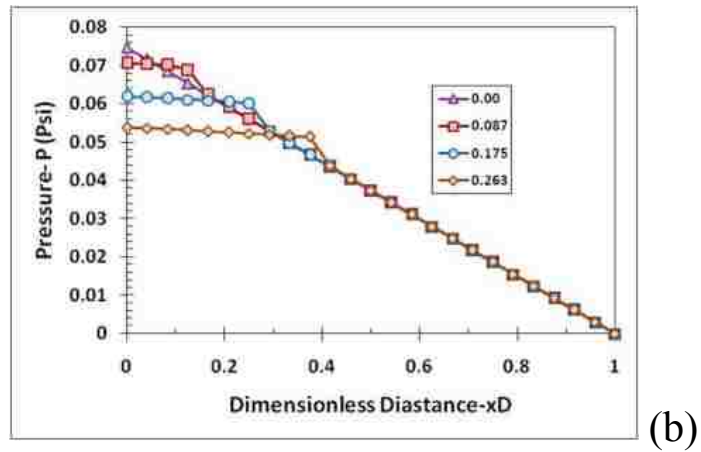
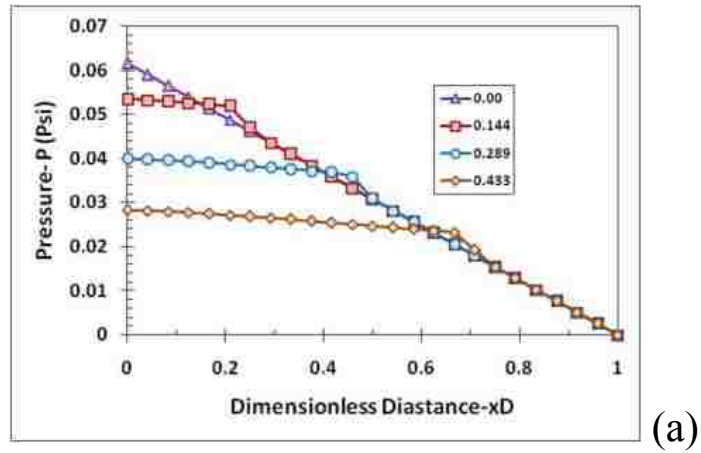


Figure C.6 Pressure profile from mechanistic simulations: (a) $u_g = 3.3 \times 10^{-5}$ m/s, (b) $u_g = 4.0 \times 10^{-5}$ m/s, and (c) $u_g = 4.2 \times 10^{-5}$ m/s (from new simulation algorithm (Appendix B) in comparison with Fig. 4.13)

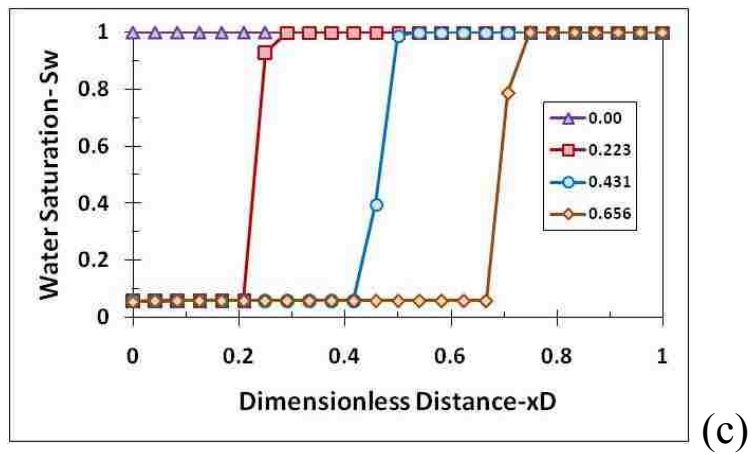
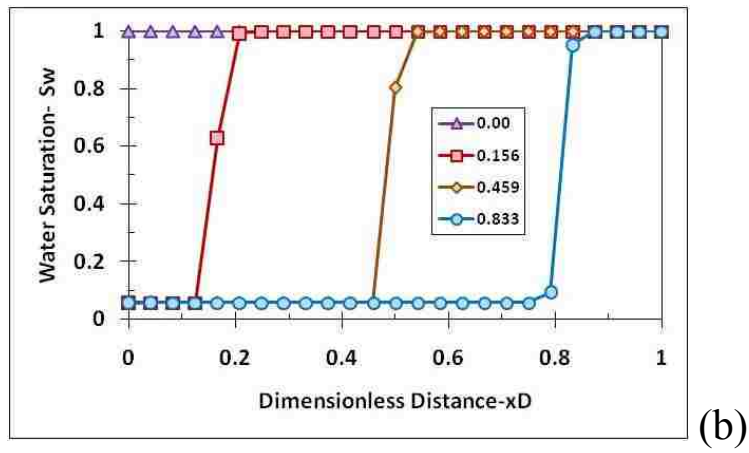
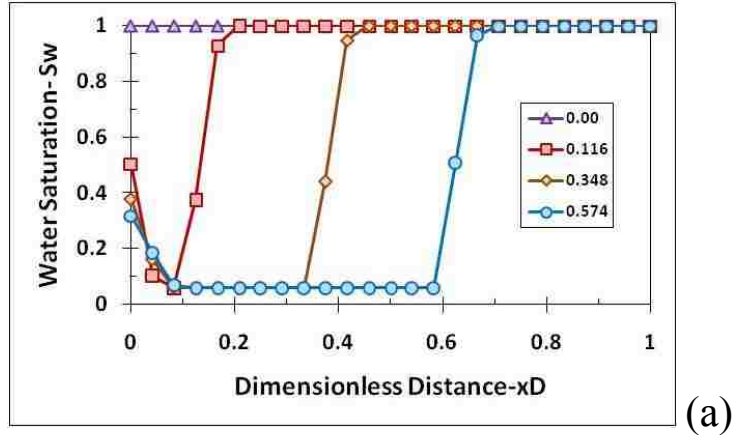
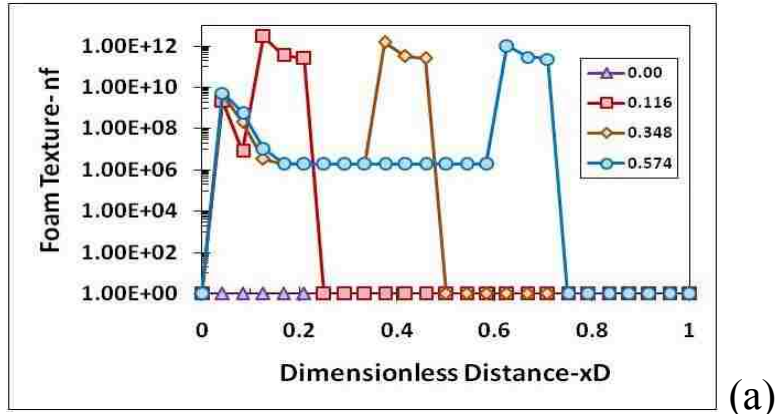
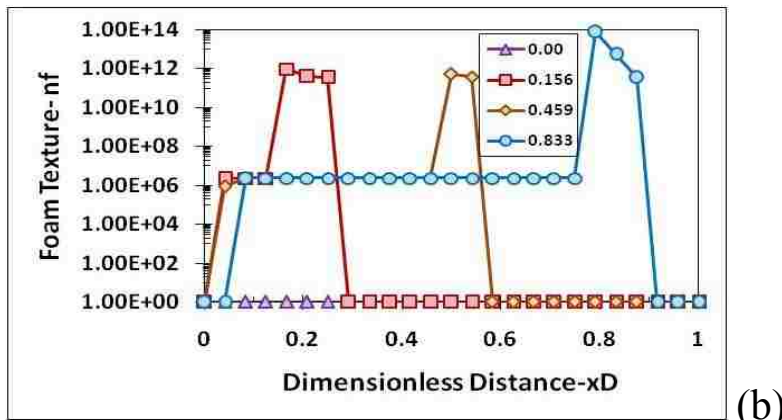


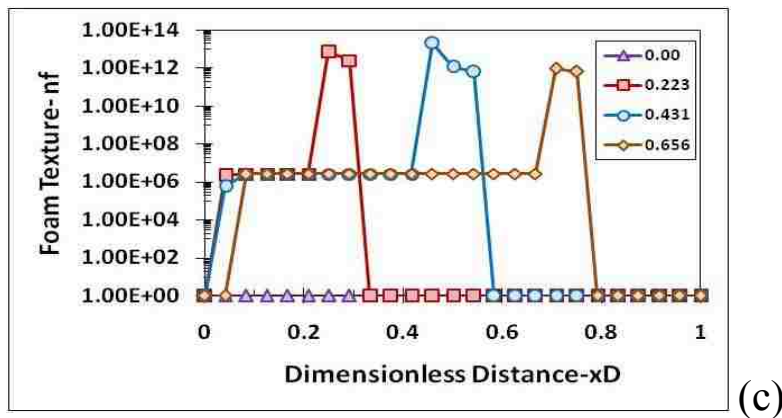
Figure C.7 Water saturation profile from mechanistic simulations: (a) $u_g = 5.3 \times 10^{-5}$ m/s, (b) $u_g = 7.0 \times 10^{-5}$ m/s, and (c) $u_g = 10.0 \times 10^{-5}$ m/s (from new simulation algorithm (Appendix B) in comparison with Fig. 4.16)



(a)



(b)



(c)

Figure C.8 Foam texture profile from mechanistic simulations: (a) $u_g = 5.3 \times 10^{-5}$ m/s, (b) $u_g = 7.0 \times 10^{-5}$ m/s, and (c) $u_g = 10.0 \times 10^{-5}$ m/s (from new simulation algorithm (Appendix B) in comparison with Fig. 4.17)

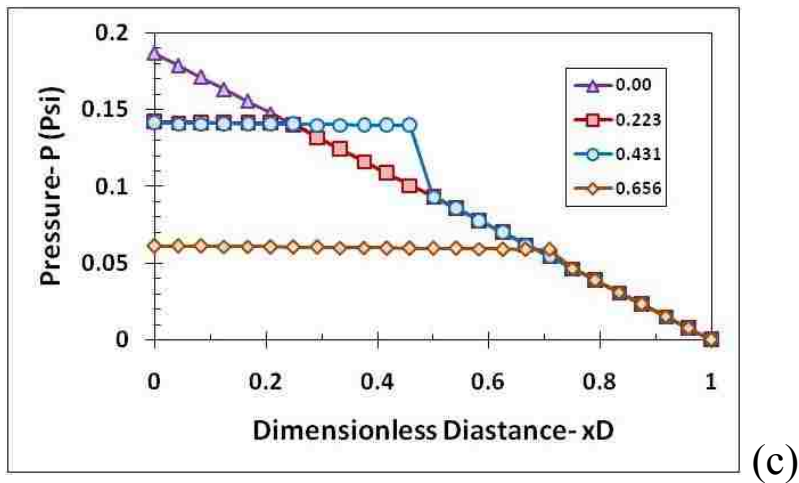
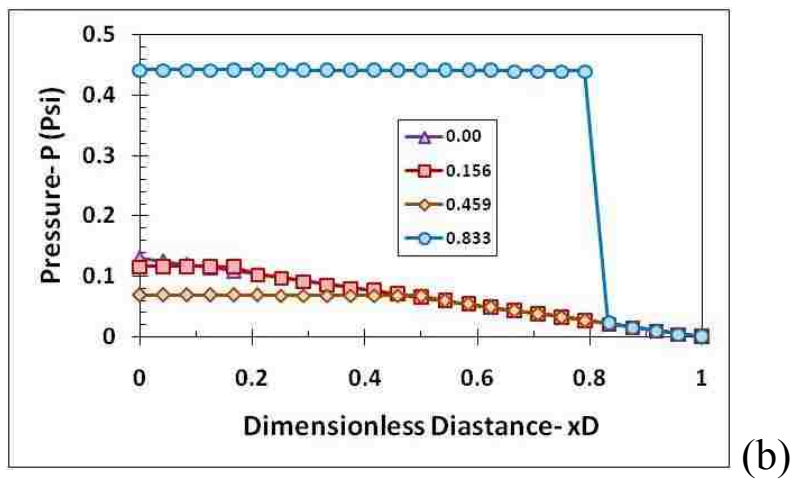
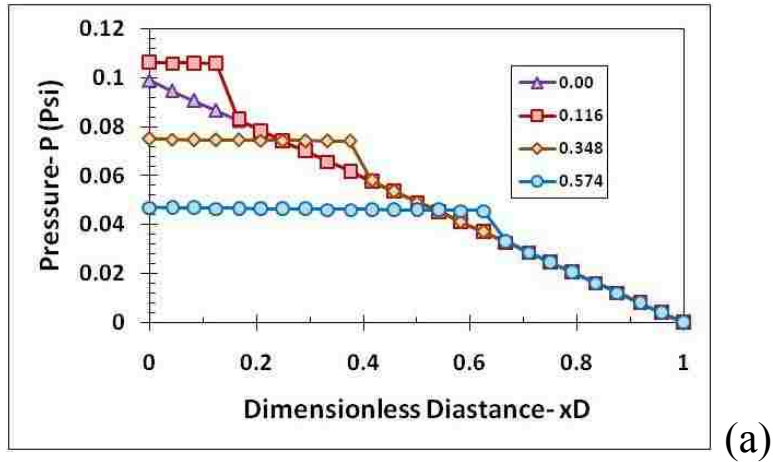


Figure C.9 Pressure profile without pressure modification from mechanistic simulations: (a) $u_g = 5.3 \times 10^{-5}$ m/s, (b) $u_g = 7.0 \times 10^{-5}$ m/s, and (c) $u_g = 10.0 \times 10^{-5}$ m/s (from new simulation algorithm (Appendix B) in comparison with Fig. 4.19

VITA

Ali Afsharpoor was born to Hassan Afsharpoor and Maliheh Kashefi in Tehran, Iran, in September 1984. He received his primary and secondary education in public schools in Tehran. To learn more about oil and gas industry, he decided to go to the Petroleum University of Technology (PUT), Ahwaz, where he received the Bachelor of Science degree in petroleum engineering-production from the Petroleum University of Technology, Iran in September 2006. He was accepted by the Craft and Hawkins Department of Petroleum Engineering at Louisiana State University and began his Master of Science in petroleum engineering in January 2007.

His interests include mathematical reservoir simulation, enhanced/improved oil recovery, and generally reservoir-engineering subjects.